High Energy Physics Laboratory,
Department of Physics,
Nara Women's University,
Nara 630-8263, JAPAN

NWU-HEP 99-01

Development of the CsI(Tℓ) Calorimeter for the Measurement of CP Violation at KEK B-Factory

Hitomi Ikeda

Human Life and Environmental Science Course,
Graduate School of Human Culture,
Nara Women's University
Nara 630-8263, JAPAN

January 1999

Ph.D Dissertation

Abstract

The understanding of the origin of the CP violation is one of the most important subjects in recent particle and high energy physics. In order to make an systematic study of the CP violation in the B meson system, the BELLE detector was constructed.

We completed the construction of the electromagnetic calorimeter in December 1998, which is one of the most important part of the BELLE detector. We put our best foot forward the design and the test of its performance, since we need a precise calorimeter for the energy measurement of electrons and γ's.

The calorimeter consists of 8,736 pieces of 30 cm long thallium doped cesium iodide (CsI(Tℓ)) crystals and we did the energy calibration of each crystal by using cosmic rays before the installation.

The beam test was carried out using a photon beam in the energy range of 20 MeV to 5.4 GeV at the Budker Institute of Nuclear Physics (BINP), Russia. The calorimeter system has been tested in almost the same configuration as the BELLE experiment. The energy equivalent noise is $\sim$200 keV for one counter. The measured energy resolution is 4 % at 20 MeV and 1.7 % at 5.4 GeV for 5×5 matrix with a threshold of 0.5 MeV. This is better than any other similar detectors constructed, or being constructed in the world. The energy linearity is -3 ± 2 % for whole energy region. This is the first measurement of the linearity for such a wide energy range with the photon beam.

In analyzing the beam test data, we established an analysis method to obtain a best energy resolution. It helps us to detect the electron, γ and π^0 with good efficiency. We checked the expected detection efficiency for γ's and π^0's from $B\bar{B}$ decays by the GEANT simulation.

Contents

Chapter 1

Introduction

The goal of the particle physics is to understand the nature by searching the ultimate constituent elements of matter and to explain the forces responsible for the interactions among them. We have a standard model[1],[2],[3], for the explanation of their forces. The standard model is the theory that six types of quarks; up(u), down(d), strange(s), charm(c), bottom(b), top(t) and six types of leptons; electron(e), muon(μ), tau(τ), and neutrinos(ν_e, ν_μ, ν_τ) interact through the agency of gauge particles; photons(γ) mediate the electromagnetic force, Z^0 and $W^\pm$ bosons mediate the weak forces and gluons(g) mediate the strong forces.

Prediction of the standard model has good agreements with the experimental results until 100 GeV, but many issues still await settlement. One of the most important issue is the origin of CP violation. The CP violation is believed to relates on the basic principle of the nature. For example, if we believe that the universe was born with the same amount of matter and anti-matter as explained in the Big-Ban model[4], the CP violation is a key issue to explain why the universe we live in consists predominantly of the matter.

Although the CP violation was first observed 35 years ago in the K meson system, we still do not understand how it occurs. In 1973, Kobayashi and Maskawa[5] noted that, with three quark generations, the CP violation could be accommodated in the standard model. In the KM model, the CP violation is caused by the imaginary phase of the rotation matrix of three generations of quarks. This is an elegant and economical manner of the explanation. We do not know, however, whether this explanation is quantitatively correct.

The magnitude of the CP violating asymmetry in the K meson system is in the order of 10^{-3}. It was pointed out that the CP violation in certain decay modes of B

mesons will be much bigger than that in K mesons. The CP violating asymmetry in the B mesons is expected to be an order of $\sim 10\%$ [6],[7],[8]. In addition to the magnitude of the CP asymmetry, the B meson system is also an ideal place for systematic studies of the KM matrix elements, since experimental results can be related to the theory more directly than that in the case of the K mesons, thanks for the large mass value of the bottom quark.

The observation of the CP asymmetry in B meson system, thus, is an important milestone to the full understanding of the mystery of the CP violation in the nature. For this purpose. the B factory project was initiated 5 years ago [9],[10] at the High Energy Accelerator Research Organization(KEK) in Tsukuba, Japan. The importance of this research is reflected in the number of competitors to this project. The SLAC-B[11],[12] project in USA and the HERA-B[13] project in Germany also started at almost the same time and all three projects are planning to start their experiments in 1999.

In order to measure the CP violation in the B meson system, several advanced techniques are required both for accelerator and detector components. The KEKB accelerator is under construction in the same TRISTAN tunnel to generate a large amount of B mesons. It is the colliding accelerator which has 2 rings. Electrons and positrons are accelerated with different energies (asymmetric accelerator) in order to detect the decay vertex of the B mesons. The center of mass energy is just set on the mass of the $\Upsilon(4S)$ state (10.580GeV), where a pair of B and $\bar{B}$ mesons is produced. The accelerator is designed to achieve the luminosity $10^{34}\mathrm{cm}^{-2}\mathrm{s}^{-1}$, which is 2 orders of magnitude larger than those of any existing e^+e^- machines.

In the interaction point of the KEKB accelerator, a large detector with high performance, BELLE is located. The construction of the detector itself is also the challenging task. It should be emphasized that the typical branching fraction of the decay modes of B which have a large CP asymmetry, is in the order of 10^{-4} to 10^{-5}. Therefore B mesons in this small branching fraction should be reconstructed exclusively by keeping backgrounds as low as possible. This requirement leads that the detector system should have highest possible resolutions and efficiencies in each subdetector component. We need precise tracking devices for momentum measurements of charged particles, precise calorimeters for energy measurements of electrons and photons, precise vertex detectors for the determination of decay vertices of the B mesons. The identification of leptons

(electron, muon), kaons, pions as well as K_L^0's is also required. And all of them should be integrated in one detector system.

I devoted 5 years of my life to study of the design and the construction of the BELLE electromagnetic calorimeter which is one of the most important parts of the BELLE detector. The calorimeter consists of 8,736 of 30 cm long, thallium doped, cesium iodide (CsI(Tℓ)) crystals. The function of the calorimeter is to measure the total energy of photons and electrons by detecting all activities in the electromagnetic showers in the calorimeter material. The reconstruction of π^0 (and η^0) mesons is the most important function of the BELLE calorimeter, since about one third of the decay products of B mesons include π^0 mesons and π^0 decays to two photons(γ). The calorimeter should cover a wide range of energies from 20 MeV to 8 GeV with a good energy resolution. The electrons (or positrons) can be identified by using informations of the calorimeter and the tracking device. An electron carries an important information to determine their mother particles as either B^0 or $\bar{B}^0$ mesons (B tagging). The tagging of the B mesons is essential for the measurement of the CP violation.

This thesis is a collection of all my works, which includes the design of the calorimeter in the early stage, the construction of the actual calorimeter and the test of the detector performance. The thesis is organized as follows:

- Physics motivations and theoretical backgrounds of the B-factory project are described in chapter 2.
- Overview of the KEKB accelerator and the BELLE detector are given in chapter 3.
- Design principles and the detailed design of the BELLE electromagnetic calorimeters are described in chapter 4. The description includes the design of each counter, the supporting system of crystals and the readout electronics. The results of R&D works which were done in the design stage are also described.
- Calibration of 8,736 crystals on crystal by crystal basis is the most elaborating and important work in the construction of the calorimeter. This has been carried out by using cosmic rays. The method and the system of the calibration with cosmic ray and the results are described in chapter 5.
- Results of the beam test, which was carried out using a tagged photon facility at the Budker Institute of Nuclear Physics (BINP), Russia, are presented in chapter

6. In this beam test, the calorimeter system has been tested in almost the same configuration of the real experiment. To our knowledge, the resolution shown here is better than any other similar detectors ever constructed, or being constructed all over the world. The linearity of the energy response is also checked in the ranges from 20 MeV to 5.4 GeV. This is the first measurement of the linearity for such a wide energy range with the photon beam. This chapter describes an important milestone of my work in the BELLE collaboration.

- Expected performance of the electromagnetic calorimeter in the BELLE detector is discussed based on the Monte Carlo simulations in chapter 7.

- The thesis is concluded in chapter 8.

The calorimeter was installed to the BELLE detector in September to December, 1998. All other detector components were successfully integrated into BELLE by the end of December 1998. We are now making a fine tuning of each subdetector by using cosmic rays.

A brief history of the construction of the calorimeter is summarized in appendix A. Although it is impossible to write all details in this thesis, the reader can see from this history how the calorimeter has been constructed. We met several serious troubles in the construction of the BELLE calorimeter, which is the biggest crystal calorimeter to date. Fortunately those problems were overcome and we completed the construction.

The physics experiment is expected to start in spring, 1999, a few months later from now.

Chapter 2

B Physics

2.1 Motivation of B Physics

2.1.1 CP Violation

One of the most important concepts in physics is the symmetry or invariance under the operation in space and time. The symmetry strongly relates to the conservation laws. The conservation laws limit the possible interactions. For example, a momentum is conserved under the translation in space and an angular momentum is conserved under the rotation in space. These are the examples of the continuous transformation.

On the other hand, discrete transformation include a charge conjugation C, a space reflection P and a time reversal T. The transformation of physical observables under the C, P and T operation is summarized in Table. 2.1.

The operation of the spatial reflection on the wave function $\Psi(\mathbf{r})$ is produced by the operator P, where

$$P\Psi(\mathbf{r}) \rightarrow \Psi(-\mathbf{r}). \tag{2.1}$$

A repetition of this operation gives;

$$P^2\Psi(\mathbf{r}) \rightarrow P\Psi(-\mathbf{r}), \tag{2.2}$$

$$P^2\Psi(\mathbf{r}) \rightarrow \Psi(\mathbf{r}), \tag{2.3}$$

$$P^2 = 1. \tag{2.4}$$

		transformation		
		C	P	T
coordinate	$\mathbf{r}$	$\mathbf{r}$	$-\mathbf{r}$	$\mathbf{r}$
momentum	$\mathbf{p}$	$\mathbf{p}$	$-\mathbf{p}$	$-\mathbf{p}$
angular momentum	$\mathbf{J}$	$\mathbf{J}$	$\mathbf{J}$	$-\mathbf{J}$
spin	σ	σ	σ	$-\sigma$
electric field	$\mathbf{E}$	$-\mathbf{E}$	$-\mathbf{E}$	$\mathbf{E}$
magnetic field	$\mathbf{B}$	$-\mathbf{B}$	$\mathbf{B}$	$-\mathbf{B}$
particle		antiparticle	particle	particle

Table 2.1: C, P, T transformation of physical observables.

We obtain the eigen value or the parity $P = \pm 1$ for the space reflection. The parity is a multiplicative number, then if $\Psi = \phi_1\phi_2 \cdots \cdot$, the parity is equal to the product of the parity of each part and $(-1)^l$ where l is the orbital angular momentum of the particles in the system.

The charge conjugation C reverses the sign of the charge and the magnetic moment of a particle. The C transformation means the interchange of a particle and an antiparticle. The T transformation replaces the time T with $-$t and makes the time to flow in opposite direction. All three discrete transformations C, P and T have their own eigen value (parity) $\pm$ 1.

The violation of the space reflection symmetry in the weak interaction (P violation) predicted by Lee and Yang [14] and was found by Wu *et al.* in ^{60}Co β decay (^{60}Co (J=5) $\rightarrow {}^{60}Ni^*$ (J=4) $+ e^-\ \bar{\nu}_e$) in 1957[15]. A high proportion of ^{60}Co nuclei spin was aligned at $0.01°K$. The relative electron intensities along and against the field direction were measured in the magnet. The polarization of ^{60}Co was determined from the angular distribution of γ's from ^{60}Co. The results for the electron intensity distribution is described;

$$I(\theta) = 1 + \alpha(\frac{\sigma\mathbf{p}}{E}) = 1 + \alpha\frac{v}{c}cos\theta, \tag{2.5}$$

where $\alpha = -1$, σ is a unit spin vector, $\mathbf{p}$ and E are the electron momentum and total energy, θ is the angle of emission of the electron. The observed asymmetry of (2.5) signified the P violation.

The weak interactions also violates the charge conjugation invariance. An exam-

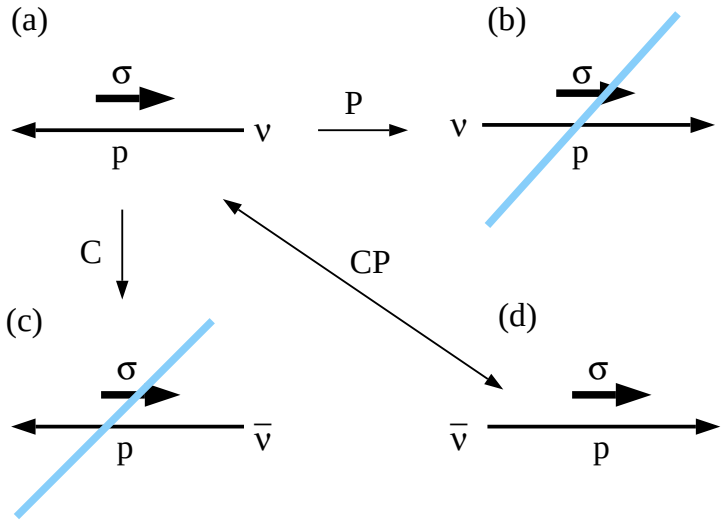

Figure 2.1: Results of C and P transformation on neutrino states. Only (a) and (d) are observed in neutrinos.

ple is a neutrino state. As shown in Fig. 2.1, neutrinos are 'left-handed'[16] and anti-neutrinos are 'right-handed'. But right-handed neutrinos and left-handed anti-neutrinos don't exist. It means that the weak interactions are not invariant under C and P transformation separately, but the CP invariance seems to be held.

The CP violation was first observed in K^0 system in 1964[17]. The K^0 particle decays by weak interaction into two pions of $CP = 1$ or three pions of $CP = -1$. The two pion decay has a decay time $\sim 9 \times 10^{-11}$ s and three pion decay has $\sim 5 \times 10^{-8}$ s. We may assume that the K^0 and $\bar{K^0}$ are composed of two particles K_1 and K_2, and each decays to two and three pions conserving the CP invariance;

$$|K^0 > \equiv \frac{|K_1 > + |K_2 >}{\sqrt{2}}, \tag{2.6}$$

$$|\bar{K^0} > \equiv \frac{|K_1 > - |K_2 >}{\sqrt{2}}, \tag{2.7}$$

where the CP of K_1 and K_2 is defined as follows;

$$CP|K_1 >= +|K_1 >, \tag{2.8}$$
$$(C = -1, P = -1, CP = +1),$$

$$CP|K_2 >= -|K_2 >, \tag{2.9}$$

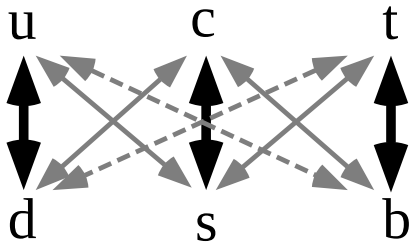

Figure 2.2: Weak transition of quarks.

$$(C = +1,\, P = -1,\, CP = -1).$$

If the CP invariance exists, K_1 should decay into two pions and K_2 should decay into three pions. But it was observed that K_2 decayed into two pions with the probability of 2×10^{-3}. This means the physical eigenstates K_S^0 and K_L^0 defined by their mass and decay time are different from the weak eigen states K^0 and $\bar{K^0}$. And they can be expressed by K_1 and K_2 as;

$$|K_S^0 >= |K_1 > +\varepsilon |K_2 >, \tag{2.10}$$

$$|K_L^0 >= |K_2 > +\varepsilon |K_1 >, \tag{2.11}$$

where $\varepsilon \neq 0$ signifies the CP violation. The origin of the CP violation is not at present established. The CP violation of K_0 is very small and was observed only in the K_0 and $\bar{K_0}$ system.

2.1.2 CKM Matrix

In the Standard Model (SM) of elementary particles, quarks interact with $W^{\pm}$ and Z^0 bosons and change in the flavor charge current weak interaction (see Fig. 2.2).

The interaction Lagrangian of this process is given by;

$$L_{int} = \frac{g}{\sqrt{2}} \left\{ (\overline{u}, \overline{c}, \overline{t})_L \, \gamma^{\mu} W_{\mu}^{+} \mathbf{V} \begin{pmatrix} d \\ s \\ b \end{pmatrix}_L + \left(\overline{d}, \overline{s}, \overline{b}\right)_L \gamma^{\mu} W_{\mu}^{-} \mathbf{V}^{\dagger} \begin{pmatrix} u \\ c \\ t \end{pmatrix}_{\mathbf{L}} \right\}, \tag{2.12}$$

g : coupling constant
$(\ )_L$: left handed quarks
γ^{μ} : γ matrix
$W_{\mu}^{\pm}$: $W^{\pm}$ boson

where $\mathbf{V}$ is a 3×3 unitary matrix called Cabbibo-Kobayashi-Maskawa (CKM) matrix. Kobayashi and Maskawa pointed out that the CP violation can be explained as a complex phase of the matrix $\mathbf{V}$ and it can be accommodated only if more than or equal to three pairs of quark flavors exist [5]. The Wolfenstein parameterization for the matrix is [18]

$$\mathbf{V} \equiv \begin{pmatrix} V_{ud} & V_{us} & V_{ub} \\ V_{cd} & V_{cs} & V_{cb} \\ V_{td} & V_{ts} & V_{tb} \end{pmatrix} = \begin{pmatrix} 1-\frac{\lambda^2}{2} & \lambda & A\lambda^3(\rho - i\eta) \\ -\lambda & 1-\frac{\lambda^2}{2} & A\lambda^2 \\ A\lambda^3(1-\rho-i\eta) & -A\lambda^2 & 1 \end{pmatrix} + O(\lambda^4). \tag{2.13}$$

The CKM matrix includes four parameters λ, A, ρ and η which have to be determined by experiments. As described below, the values λ and A are well constrained but the value of ρ and η are not determined well.

The free parameter λ is the sine of the Cabbibo angle $\sin\theta_c$ [20], and is well determined from strange particle decays such as $K \to \pi l^+ \nu$ [21], $\Sigma \to ne\bar{\nu}$ [22], nuclear β decay [23], and the production of the charm quark in ν interactions $\nu + d(s) \to \mu^- + c$, $\bar{\nu} + \bar{d}(\bar{s}) \to \mu^+ + \bar{c}$ [24] to be

$$\lambda = 0.221 \pm 0.002. \tag{2.14}$$

V_{cb} is determined from the measurement of the branching ratio for the decay $\bar{B}^0 \to D^+ \ell^- \bar{\nu}$, $\bar{B}^0 \to D^{*+} \ell^- \bar{\nu}$ and inclusive semileptonic decay $\bar{B}^0 \to X\ \ell^- \bar{\nu}$. The average value of V_{cb} is 0.0381 ± 0.0021, which gives the value of A to be [25]

$$A = 0.784 \pm 0.043. \tag{2.15}$$

The value of V_{ub} was obtained from both the exclusive and the inclusive analysis of the charmless b decay; $B \to \rho l \nu$ [26][27] and $B \to X_u l \nu$ [28]. The measurement of the parameter V_{ub} provides a constraint

$$(\frac{1}{\lambda^2})|\frac{V_{ub}}{V_{cb}}|^2 = (\rho^2 + \eta^2) = (0.36 \pm 0.07)^2. \tag{2.16}$$

Neutral B mesons can transform to their anti-particles before they decay. We will discuss the phenomenon of the $B - \bar{B}$ mixing in section 2.2. The probability of mixing is given by [29] [30] [31] [32] [33] [34].

$$x \equiv \frac{\Delta m}{\Gamma} = \frac{G_F^2}{6\pi^2} B_B f_B^2 m_B \tau_B |V_{tb}^* V_{td}|^2 m_t^2 F(\frac{m_t^2}{M_W^2}) \eta_{QCD}, \tag{2.17}$$

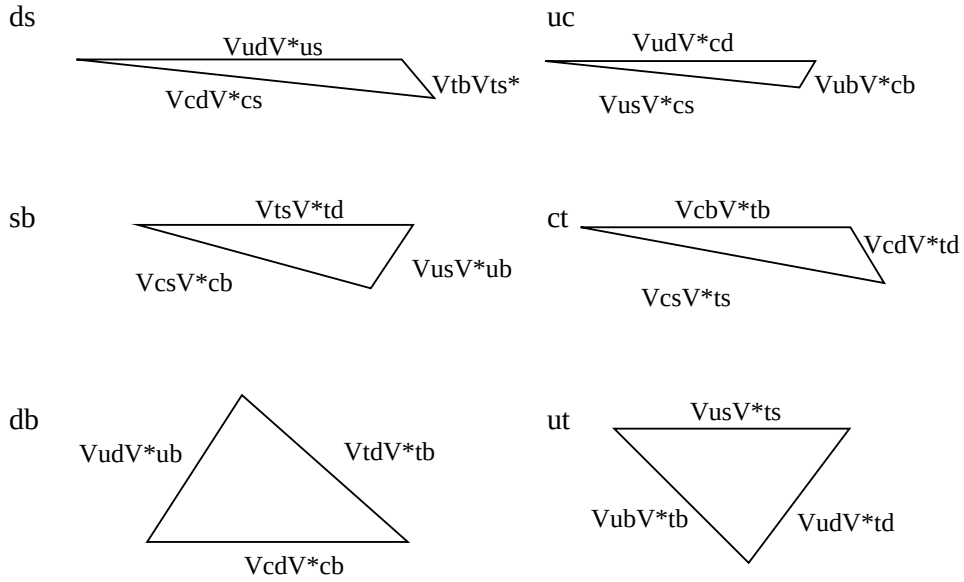

Figure 2.3: Six unitarity triangles following from the orthogonality of the CKM matrix.

where 'bag parameter' B_B is a parameter related to the probability of the d and $\bar{b}$ quarks forming a hadron, f_B is the decay constant, F is a known function which increases approximately as m_t^2 and η_{QCD} is a QCD correction with value about 0.8. Since

$$|V_{tb}^* V_{td}|^2 \propto |(1-\rho-i\eta)|^2 = (\rho-1)^2+\eta^2, \tag{2.18}$$

the value of x gives a constraint in the $\rho-\eta$ plane. There is also a constraint on ρ and η given by the K_L^0 CP violation measurement (ϵ), given by

$$\eta((1-\rho)A^2(1.4\pm0.2)+0.35)A^2\frac{B_K}{0.75} = (0.30\pm0.06). \tag{2.19}$$

The limit of $K^0 \to \pi\pi$ decay (ϵ') can be translated to limits on η given by [35],

$$Re(\epsilon/\epsilon') = (0.19\pm0.09)\times10^{-2}A^2\eta(1-0.46(\frac{m_t}{100GeV/c^2}-0.7)^2). \tag{2.20}$$

The theoretical constraint on the CKM matrix comes from the unitarity of the matrix as follows;

$$\mathbf{V}^\dagger\mathbf{V} = \begin{pmatrix} V_{ud}^* & V_{cd}^* & V_{td}^* \\ V_{us}^* & V_{cs}^* & V_{ts}^* \\ V_{ub}^* & V_{cb}^* & V_{tb}^* \end{pmatrix}\begin{pmatrix} V_{ud} & V_{us} & V_{ub} \\ V_{cd} & V_{cs} & V_{cb} \\ V_{td} & V_{ts} & V_{tb} \end{pmatrix} = I. \tag{2.21}$$

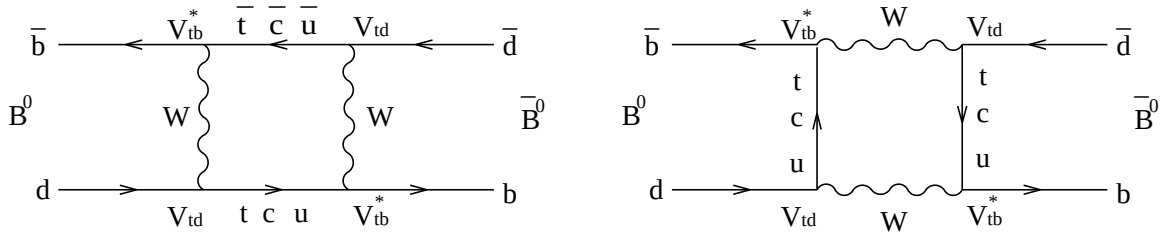

Figure 2.4: Feynman diagram of $B\bar{B}$ mixing.

The condition $\sum_i V_{ji}^* V_{ik} = \delta_{ij}$ gives 6 triangles in the complex plane as shown in Fig. 2.3. Each triangle is marked by a quark pair to which the triangle gives constraints on that transition. It is the flavor changing neutral current (FCNC) transitions between each quark pair. The direct (Born level) FCNC transition is forbidden in SM but it is possible through the box diagrams which is shown in Fig. 2.4. For example, (ds) triangle shows the constraint on the s $\rightarrow$ d transition which is observed in $K^0(\bar{K}^0)$ transition. By measuring three angles and three sides of the triangles, the CKM matrix elements can be determined with over constraint.

2.1.3 B-factory

The goal of the BELLE experiment is to perform definitive tests on the Kobayashi-Maskawa predictions for the CP violation in B meson decays [19]. This is related with the (db) triangle described by the following equation ;

$$V_{ud}V_{ub}^* + V_{cd}V_{cb}^* + V_{td}V_{tb}^* = 0. \tag{2.22}$$

The triangle shape which three sides are defined as $V_{td}V_{tb}^*$, $V_{ud}V_{ub}^*$ and $V_{cd}V_{cb}^*$ and three internal angles are defined as

$$\phi_1 \equiv arg(\frac{V_{cd}V_{cb}^*}{V_{td}V_{tb}^*}), \tag{2.23}$$

$$\phi_2 \equiv arg(\frac{V_{ud}V_{ub}^*}{V_{td}V_{tb}^*}), \tag{2.24}$$

$$\phi_3 \equiv arg(\frac{V_{cd}V_{cb}^*}{V_{ud}V_{ub}^*}). \tag{2.25}$$

The shape of the triangle is shown in Fig. 2.5 with the constraints for the CKM parameters.

The KEK B-factory is constructed for the measurement of three angles and three sides of this triangle. A large number of Υ(4S)'s are produced by KEKB collider

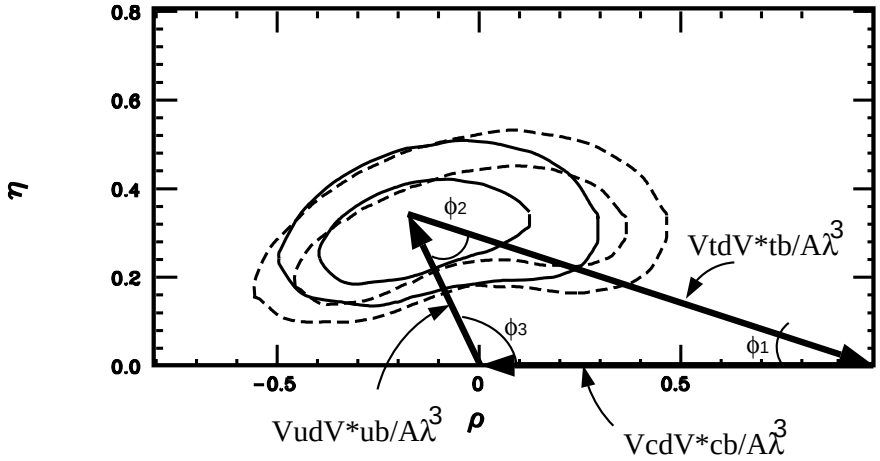

Figure 2.5: Allowed region in the $\rho - \eta$ plane estimated from presently available data. Solid curves : $|V_{cb}|$, $|V_{ub}|/|V_{cb}|$, ϵ, Re(ϵ'/ϵ), x_d and m_t as constraints; Dashed curves : without x_d and Re(ϵ'/ϵ). The inner (outer) curves denote 1σ (90% C.L.) regions.

through the collision of e^+e^- beams at the center of mass energy $\sqrt{S} = 10.58$ GeV. The Υ(4S) decays to a $B\bar{B}$ pair and specific decay modes of B will be reconstructed by the BELLE experiment. Various decay modes usefull for the determination of the side and the angle are tabulated in Table. 2.2.

2.2 Indirect CP Violation

When the B^0 and $\bar{B}^0$ mesons decay into the same CP; $B^0 \to f$ and $\bar{B}^0 \to f$, the CP violationg asymmetry A_f is given by

$$A_f = \frac{R(B^0 \to f) - R(\bar{B}^0 \to f)}{R(B^0 \to f) + R(\bar{B}^0 \to f)} = sin2\phi_{CP} sin(\Delta m \Delta t), \tag{2.26}$$

where Δm is the mass difference between two B^0's and Δt is the difference of proper time for B^0 and $\bar{B}^0$ decays. $R(B^0 \to f)$ is the decay rate of $B^0 \to f$.

The asymmetry is produced by the interference of two amplitudes (Fig. 2.4); a direct decay $B^0 \to f$ and a decay through the $B\bar{B}$ oscillation $B^0 \to \bar{B}^0 \to f$ which is called as the indirect CP violation. Experimentally the measurement of Δt is essential for the observation of the asymmetry. We can measure Δt using the Lorenz boost of the Υ(4S) state produced by the asymmetry of beam energies as described later. The angle ϕ_{CP} is the phase difference between two amplitudes, which is directly related to the internal angle of the unitarity triangle.

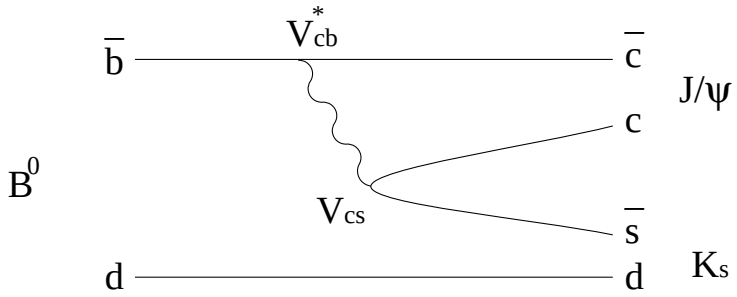

Figure 2.6: Feynman diagram for $B^0 \to J/\psi K_s^0$

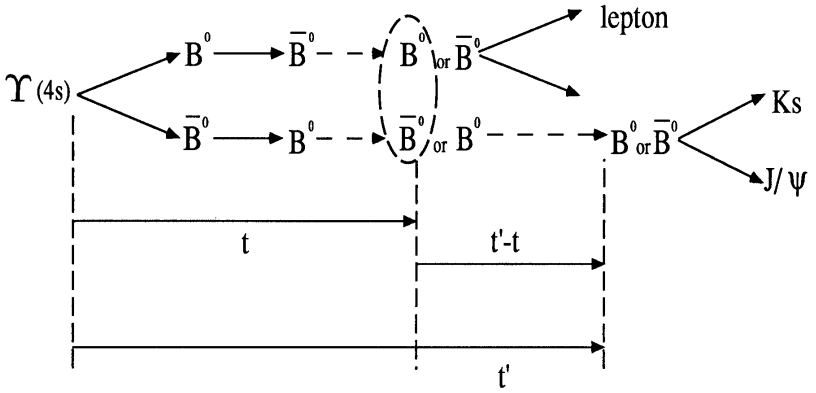

Figure 2.7: Measurement of time difference (t'-t) for $B^0 \to \mathrm{J}/\psi\ K_s$.

	λ^n	
ϕ_1	λ^2	$\eta_c K_s$ ψK_s $\psi' K_s$ $\psi'' K_s$ χK_s $\eta_c K^*$ $\eta_c K_s\pi^0$ $D_{1,2}\pi^0$ $D_{1,2}\omega$ $D_{1,2}\rho^0$ ψK^* $\psi' K^*$ $\psi'' K^*$ $\psi K_s\pi^0$ $\psi' K_s\pi^0$ $\psi'' K_s\pi^0$
	λ^3	$D^0\bar{D}^0$ D^+D^- D^*D D^0K_s $D^0K_s\pi^0$ $\eta_c\pi^+\pi^-$ $D^0\bar{D}^0\pi^0$ $D^+D^-\pi^0$ $\psi\pi^+\pi^-$ $\psi'\pi^+\pi^-$ $\psi''\pi^+\pi^-$ $D^*D\pi^0$
ϕ_2	λ^3	$\pi^+\pi^-$ $\pi^0\pi^0$ $\rho^0\pi^0$ $\omega\pi^0$ $\eta\pi^0$ $\pi^+\pi^-\pi^0$ $\eta\pi^+\pi^-$ $\eta\pi^0\pi^0$ $a_1^\pm\pi^\pm$ $\rho^\pm\pi^\mp$ $\rho^+\rho^-$ $\rho^0\rho^0$ $\rho^0\omega$ $\omega\omega$ $\rho^0\pi^0\pi^0$ $\rho^0\pi^+\pi^-$ $\omega\pi^+\pi^-$
	λ^4	$K^\pm\pi^-$
ϕ_3	λ^3	$B_s \to \rho K_s$ $B_s \to \phi K_s$ $B^0 \to K_s D^0$ $B^0 \to D^0 K_s\pi^0$ $B^\pm \to D^0 K^\pm$ $B^\pm \to D^0 K^\pm\pi^0$ $B^\pm \to D^0 K_s\pi^0$
$\lvert V_{ud}V_{ub}^*\rvert$		$B \to \rho\ell\nu$ $B \to \pi\ell\nu$
$\lvert V_{td}V_{tb}^*\rvert$		$B_d \leftrightarrow \overline{B}_d$,$B_s \leftrightarrow \overline{B}_s$ mixing
$\lvert V_{cd}V_{cb}^*\rvert$		$B \to D^*\ell\nu$

Table 2.2: Decay modes of B meson useful for the determination of unitarity triangle.

For example, a decay mode $B^0 \to J/\psi K_s^0$ (Fig. 2.6) can be used to measure the angle ϕ_1. The asymmetry in this decay is given by

$$\frac{R(B^0 \to J/\psi K_s^0) - R(\bar{B}^0 \to J/\psi K_s^0)}{R(B^0 \to J/\psi K_s^0) + R(\bar{B}^0 \to J/\psi K_s^0)} = sin2\phi_1 sin(\Delta m \Delta t). \tag{2.27}$$

A schematic view of the measurement is illustrated in Fig. 2.7. Since the $B\bar{B}$ pair produced from the Υ(4S) is a coherent state with $C = -$, when one of the pair decays as a B at the time t, the other one is determined as $\bar{B}$ at the same time. This phenomenon is a famous Einstein-Podolsky-Rosen's paradox. We know the flavor of the first decay at the time T from the lepton charge of the semileptonic decay as shown in Fig. 2.8. The flavor tagged $\bar{B}$ decays to $J/\psi K_s^0$ at the time t'. Then a nonzero value of A_f will be observed as the function of Δt = t' − t. The Monte Carlo simulation of the proper time for the expected asymmetry (sin2ϕ_1=0.6) is shown in Fig. 2.9.

The expected asymmetry ranges from 0.02 to 0.2 [36]. The CP asymmetry is observed with 3 σ significance if d × sin2ϕ_1 is larger than 0.37 with an integrated luminosity of 10 fb^{-1} [37] where d is a dilution factor.

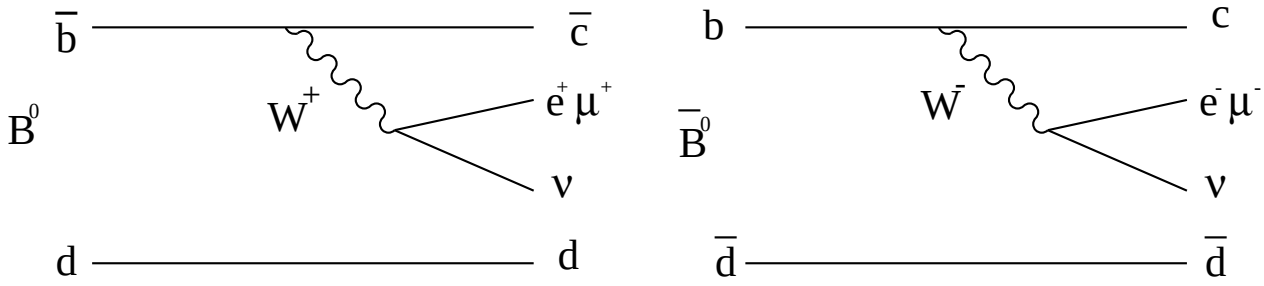

Figure 2.8: Feynman diagram for B tagging.

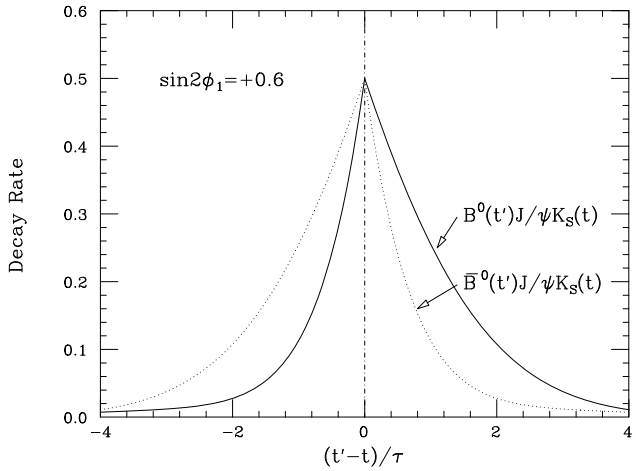

Figure 2.9: Proper time distribution of t'−t in $B \to J/\psi K_s^0$.

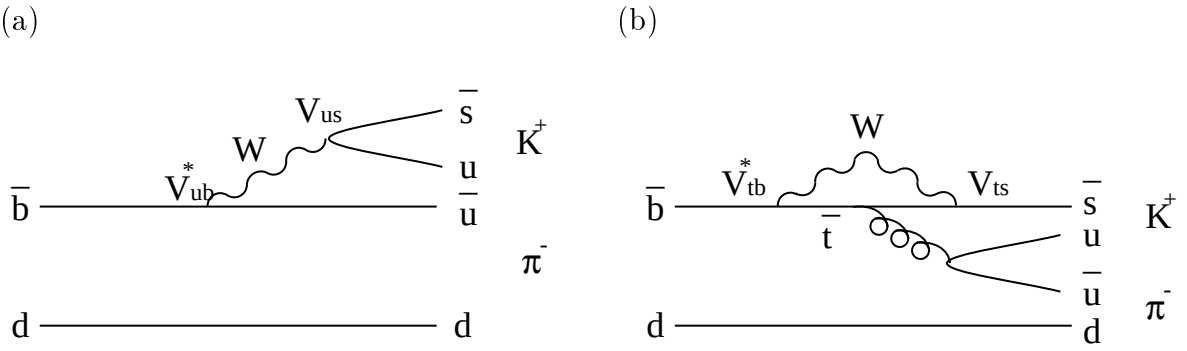

Figure 2.10: Feynman diagram for $B^0 \to K^+\pi^-$.(a)tree diagram and (b)penguin diagram.

2.3 Direct CP Violation

A direct CP violation means the difference between the decay rate of $B \to f$ and its charge conjugation decay rate of $\bar{B} \to \bar{f}$;

$$R(B \to f) \neq R(\bar{B} \to \bar{f}). \tag{2.28}$$

The direct CP violation occurs when there is an interference between two decay diagrams having different weak complex phases and different strong complex phases with the amplitudes of similar size. An example is shown in Fig. 2.10 for $B^0 \to K^{\pm}\pi^{\mp}$. In this decay mode, there are contributions from the tree and penguin diagrams and they have different phases.

Chapter 3

KEKB Accelerator and BELLE Detector

3.1 KEKB Accelerator

The KEKB accelerator is being constructed at KEK in Tsukuba, Japan, reusing the tunnel of decommissioned TRISTAN accelerator. The construction started in April of 1994 and it is completed in November, 1998. It is now under detailed tuning of the machine.

KEKB is an asymmetric energy electron positron collider to make the generated particles run along the beam axis by Lorenz boost. Electrons and positrons are stored in two separate rings. The electron energy is 8 GeV and the positron energy is 3.5 GeV. They collide at the center-of-mass energy of 10.58 GeV and the energy is used to produce $\Upsilon(4S)$ which decays into a $B\bar{B}$ mesons ($M_B = 5279$ MeV). The velocity of cms in the laboratory (β) becomes 0.39 and the Lorenz factor (γ) is $\gamma = \frac{1}{\sqrt{1-\beta^2}} = 1.09$. Since the kinetic energy of the B meson in cms is only 11 MeV, the produced B mesons fly in the direction of the electron with the velocity β. The life time τ of B^0 is 1.6 $\times$ 10^{-12} s, and B mesons run about 200 μm ($= \beta c\tau\gamma$) before it decays in the laboratory system. Specific decay channels of B meson will be studied for the CP violation and the measurement of CKM matrix element. Since many of interesting decay modes have a branching fraction of 10^{-4} or less, a very high luminosity is required. The goal of the luminosity is 10^{34} cm^{-2}s^{-1} and this corresponds to two orders of magnitude higher luminosity than those of the existing accelerators. The high luminosity is achieved mostly by increasing the beam current stored in many bunches. The number of bunches of electron and positron are 5000 and the beam current is 2.6 A and 1.1 A for electron

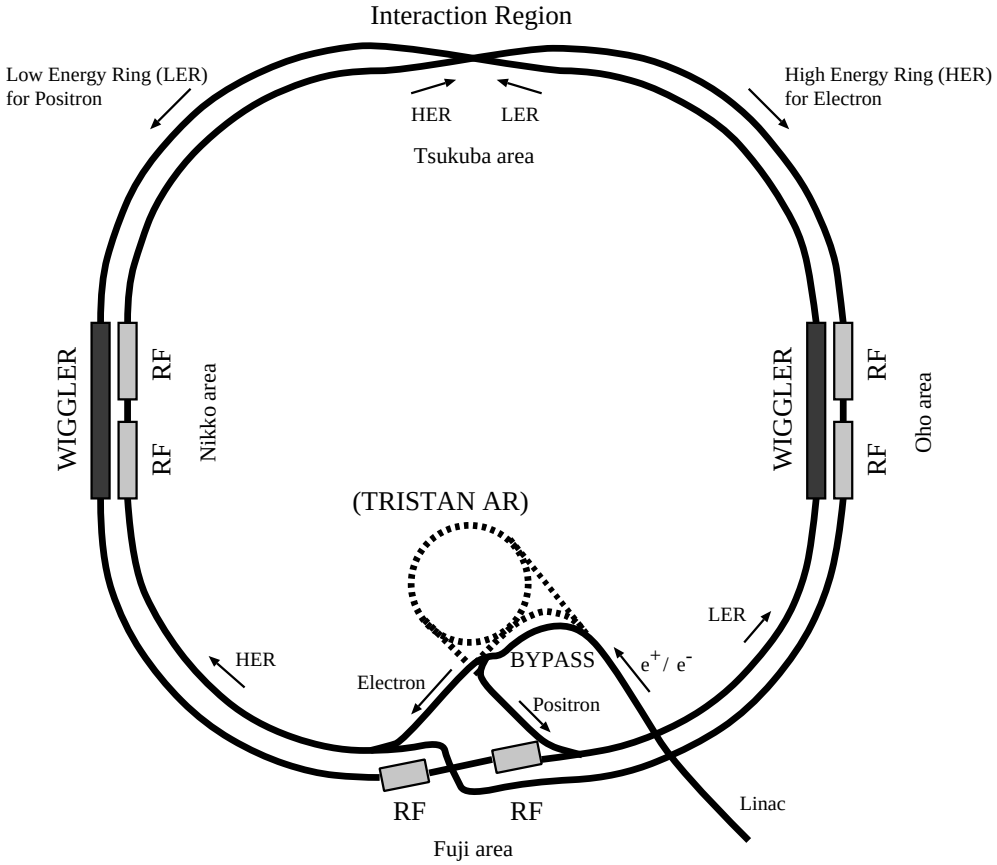

Figure 3.1: Configuration of KEKB accelerator system.

and positron beams. Fig. 3.1 shows the configuration of KEKB and Table 3.1 shows the parameter of the collider[38].

As shown in Fig. 3.1, the interaction point is only one in the Tsukuba experimental area where the BELLE detector is installed.

3.2 BELLE Detector

3.2.1 Overall Design

The BELLE is an international collaboration, which includes institutes and universities from many countries (Australia, China, India, Japan, Korea, Phillipines, Poland, Russia, Taiwan, U.S.A.). The collaboration started in 1994 and the detector construction is completed in December 1998. The BELLE detector is illustrated in Fig. 3.2. This is a combination of several detectors to detect many types of particles.

Ring	LER	HER	
Energy (E)	3.5	8.0	GeV
Circumference (C)	3016.26		m
Luminosity (L)	1×10^{34}		$\mathrm{cm}^{-2}\,\mathrm{s}^{-1}$
Crossing angle (θ_x)	± 11		mrad
Tune shifts (ξ_x/ξ_y)	0.039/0.052		
Beta function at IP (β_x^*/β_y^*)	0.33/0.01		m
Beam current (I)	2.6	1.1	A
Natural bunch length (σ_z)	0.4		cm
Energy spread (σ_E)	7.1×10^{-4}	6.7×10^{-4}	
Bunch spacing (s_B)	0.59		m
Particles/bunch	3.3×10^{10}	1.4×10^{10}	
Emittance ($\varepsilon_x/\varepsilon_y$)	$1.8 \times 10^{-8}/3.6 \times 10^{-10}$		m
Synchrotron tune (ν_s)	$0.01 \sim 0.02$		
Betatron tune (ν_x/ν_y)	45.52/45.08	47.52/46.08	
Momentum compaction factor (α_p)	$1 \times 10^{-4} \sim 2 \times 10^{-4}$		
Energy loss/turn (U_0)	$0.81^*/1.5^\dagger$	3.5	MeV
RF voltage (V_c)	$5 \sim 10$	$10 \sim 20$	MV
RF frequency (f_{RF})	508.887		MHz
Harmonic number (h)	5120		
Longitudinal damping time (τ_ϵ)	$43^*/23^\dagger$	23	ms
Total beam power (P_b)	$2.7^*/4.5^\dagger$	4.0	MW
Radiation power (P_{SR})	$2.1^*/4.0^\dagger$	3.8	MW
HOM power (P_{HOM})	0.57	0.15	MW
Bending radius (ρ)	16.3	104.5	m
Length of bending magnet (l_b)	0.915	5.86	m

* without wigglers †with wigglers

Table 3.1: Parameters of KEKB accelerator.

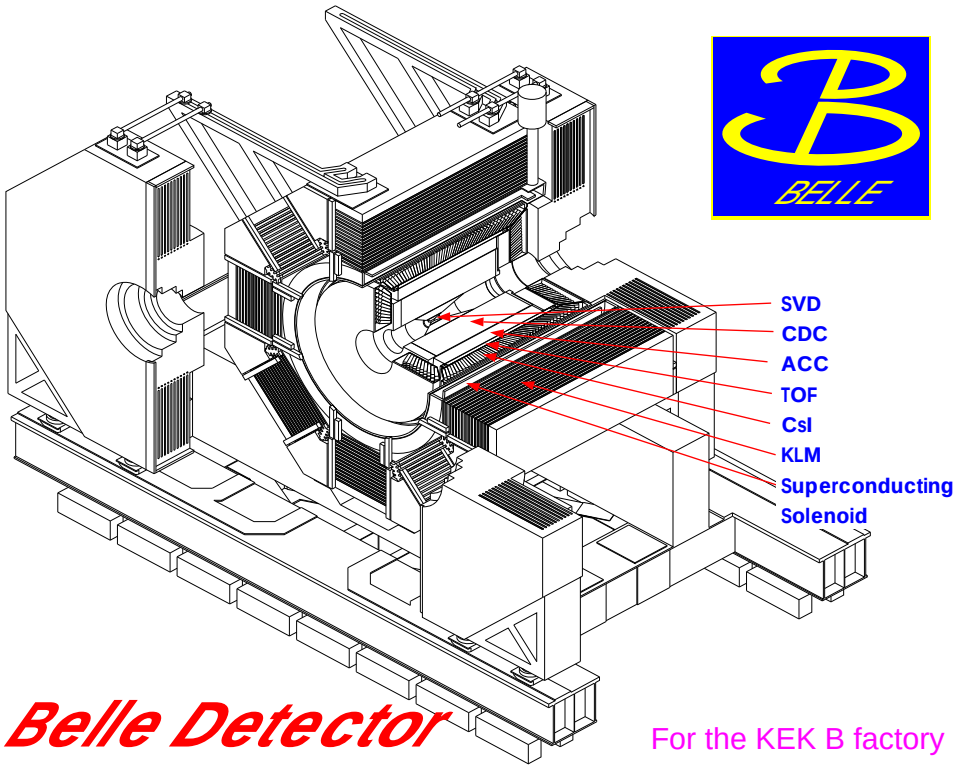

Figure 3.2: BELLE detector.

The following subdetectors are installed around the interaction point.

- A vertex detector to measure the decay point (SVD).
- A tracking detector to measure the momentum of charged particles in the magnetic field (CDC).
- A calorimeter to measure the particles in the extreme forward region(EFC).
- A particle identification detector for the separation of $\pi^{\pm}$ and $K^{\pm}$ (CDC,TOF,ACC).
- A calorimeter to measure the energy of gamma rays and electrons (CsI).
- A detector to identify muons and K_L^0 (KLM).

The BELLE detector is approximately 7 m in diameter and 7 m long. It's weight is about 2000 tons. The parameter of each detector is tabulated in Table. 3.2.

The requirement of the detector is to identify the type of each particle (e, μ, γ, $\pi^{\pm}$, $K^{\pm}$, K_L^0 etc.) and to measure their vectors as precise as possible. The reconstruction of the mother particles and their decay processes are achieved from the information of them. Since the momentum of detected particle is low, the material composing each detector should be as thin as possible to reduce the influence of scattering and particle interaction.

3.2.2 Beam Pipe

The BELLE beam pipe should be strong enough to stand the vacuum pressure and the heat generated by the high current beam. The configuration is shown in Fig. 3.3. Since the multiple scattering for the same thickness of the material is proportional to the atomic number Z, it is better to use a small Z material for the beam pipe. It is made by the double wall of 0.5 mm thick beryllium (Z = 4) cylinders separated by 2 mm [39]. The helium gas flows between two walls for cooling. Both ends of the beryllium cylinder are attached to the aluminum beam pipe. The cooling of this part is done with water.

3.2.3 Silicon Vertex Detector(SVD)

In the BELLE experiment, it is important to distinguish two decay points of B mesons. Because the difference of the decay time has to be measured as mentioned in the

Detector	Type	Configuration	Readout	Performance
Beam pipe	Berylium double-wall	Cylindrical, r = 2.3 cm 0.5 mm Be/ 2 mm He /0.5 mm Be		
SVD	Double sided Si strip	300 μm thick, 3 layers r = 3.0 - 5.8 cm Length = 22 - 34 cm	ϕ: 41k θ: 41k	$\sigma_{\Delta z} \sim 105$ μm
EFC	BGO	2 cm × 1.5 cm × 12 cm	θ : 5 ϕ : 32	
CDC	Small cell drift chamber	Anode : 52 layers Cathode : 3 layers r = 8.5 - 90 cm -77 $\leq$ z $\leq$ 160 cm	 A: 8.4k C: 1.5k	$\sigma_{r\phi} = 130$ μm $\sigma_z = 200 \sim 1{,}400$ μm $\sigma_{p_t}/p_t = 0.3$ % $\sqrt{p_t^2 + 1}$ $\sigma_{dE/dx} = 6$ %
ACC	n : 1.01 $\sim$ 1.03 Silica Aerogel	$\sim 12 \times 12 \times 12$ cm ^{3} blocks 960 barrel / 228 endcap FM - PMT readout	 1,788 ch	 $\mu_{eff} = \geq 6$ K/π 1.2 $\leq$ p $\leq$ 3.5 GeV/c
TOF	Plastic Scintillator	128 ϕ segmentation r = 120 cm, 3 m long	 128 × 2 ch	$\sigma_t = 100$ ps K/π =up to 1.2 GeV/c
ECL	CsI	Tower structure $\sim 5.5 \times 5.5 \times 30$ cm^3 crystals Barrel : r = 125 - 162 cm Endcap : z = -102 and +196 cm	 6,624(B) 1,152(FE) 960(BE)	σ_E/E $= \frac{0.066(\%)}{E} \oplus \frac{0.81(\%)}{E^{1/4}} \oplus 1.34(\%)$ $\sigma_{pos} = 0.5$ cm / $\sqrt{E}$ E in GeV
MAGNET	super conducting	inn.rad. = 170 cm		B = 1.5 T
KLM	Resistive plate counter	14 layers (5 cm Fe + 4 cm gap) 2 RPCs in each gap θ and ϕ strips	 θ: 16k ϕ: 16k	$\Delta\phi = \Delta\theta = 30$ mrad for K_L $\sigma_t = 1$ ns 1 % hadron fakes

Table 3.2: Performance parameters of the BELLE detector

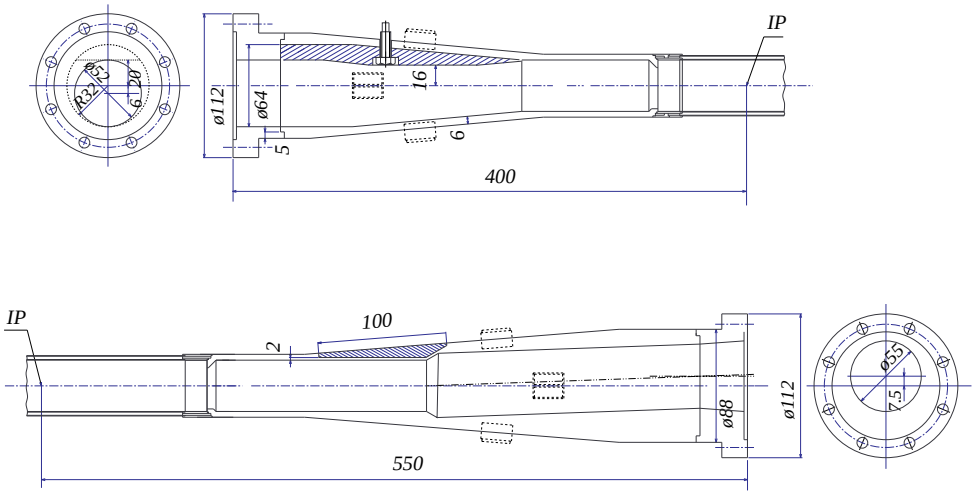

Figure 3.3: Beam pipe.

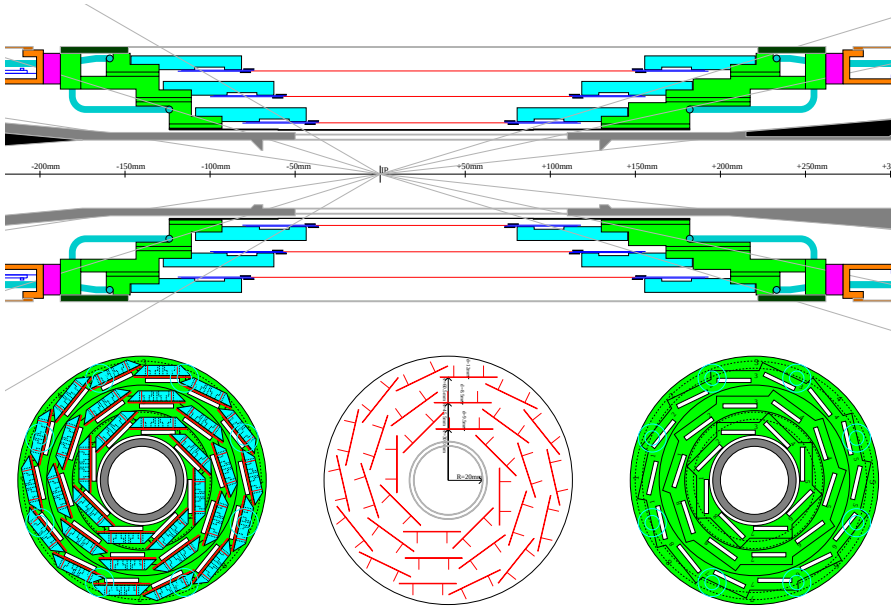

Figure 3.4: Silicon vertex detector.

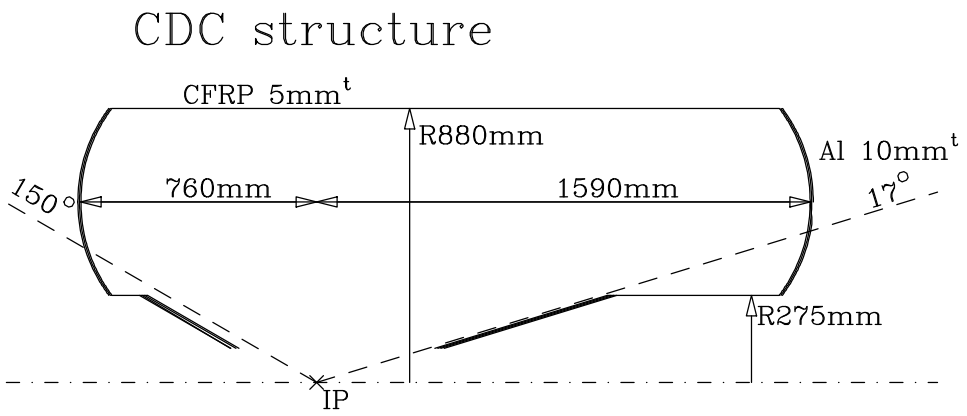

Figure 3.5: Central drift chamber.

previous chapter, the vertex detector is required to have a good position resolution of ~ 10 μm.

The configuration of the silicon vertex detector (SVD) is shown in Fig. 3.4. The SVD has three cylindrical detection layers consisting of 8, 10 and 14 units of the double sided silicon detectors (DSSD). Each DSSD width is 300 μm and the 2 dimensional position is measured in one layer. The vertex δz resolution is estimated to be 113 μm including the effect of the beam background [40].

3.2.4 Extreme Forward Calorimeter(EFC)

The extreme forward calorimeter (EFC) detects particles produced near the beam line ($6.4^\circ < \theta < 12.4^\circ$ and $162.2^\circ < \theta < 173.4^\circ$)[41]. It is attached to the front nose of the cryostat of the QCS magnet surrounding the beam pipe. The QCS magnet is the final focusing quadrupole of the KEKB accelerator. EFC is for the measurement of the energy of electrons and photons which can not be detected by large angle calorimeter. It is also used to detect the charged particles in this region. A radiation hard BGO crystals [42] are used for EFC. EFC measures scintillation light in the BGO crystal produced by the electromagnetic shower of electrons and photons as the CsI electromagnetic calorimeter.

3.2.5 Central Drift Chamber(CDC)

The charged particle makes a spiral motion in a uniform magnetic field and its radius is proportional to the transverse momentum of the particle. Then the transverse mo-

mentum is measured by the reconstruction of the track and the known strength of the magnetic fields.

The central drift chamber of BELLE is installed outside of the SVD. The size is shown in Fig. 3.5. It is asymmetric in z to cover $17° \leq \theta \leq 150°$. The sense wires are made of 30 μm diameter gold plated tungsten and the 126 μm diameter aluminum wire is used for field wires. A mixture of Helium 50 % and C_2H_6 50 % gas is used for the operation of the chamber. The use of low-Z Helium gas and the aluminum field wire is to reduce the multiple scattering and to obtain a good momentum resolution at low energy. The number of layers are 40 and it is possible to measure the momentum of the charged particles with $\frac{0.3\%}{p_t^2+1}$ resolution[39].

3.2.6 Aerogel Čerenkov Counter(ACC)

When the particle velocity becomes larger than the propagation velocity of the light (= light velocity in vacuum / refractive index) in the material, the Čerenkov light is emitted. The Aerogel Čerenkov Counter(ACC) of BELLE uses Čerenkov light to separate $\pi^{\pm}$ and $K^{\pm}$ in the momentum region between 1.2 GeV/c and $2.5 - 3.5$ GeV/c. The upper limit depends on the polar angle. The configuration is shown in Fig. 3.6. The Čerenkov light is detected using a fine-mesh photomultiplier to use inside the high magnetic field [39].

3.2.7 Time of Flight Counter(TOF)

The low momentum particle which is not identified by ACC is recognized by the timing of plastic scintillation counters. This counter measures the time of flight from the vertex point with 100 ps resolution. The π/K separation is possible up to 1.2 GeV. The signal from this counter is used as the clean event timing for BELLE trigger as well.

The counters dimension are given in Fig. 3.7. The number of counters is 128 and each counter has a dimension of 40 mm $\times$ 60 mm $\times$ 2550 mm. These counters are mounted on the inner wall of the CsI detector at 1175 mm radius.

3.2.8 Electromagnetic Calorimeter(CsI)

The energy measurement of electron and photon is done by the electromagnetic calorimeter. For this purpose, 8736 pieces of CsI(Tℓ) crystals are used. These crystals measure the scintillation light generated by electromagnetic shower and determine the energy of the particles. This detector is elaborated in the next chapter.

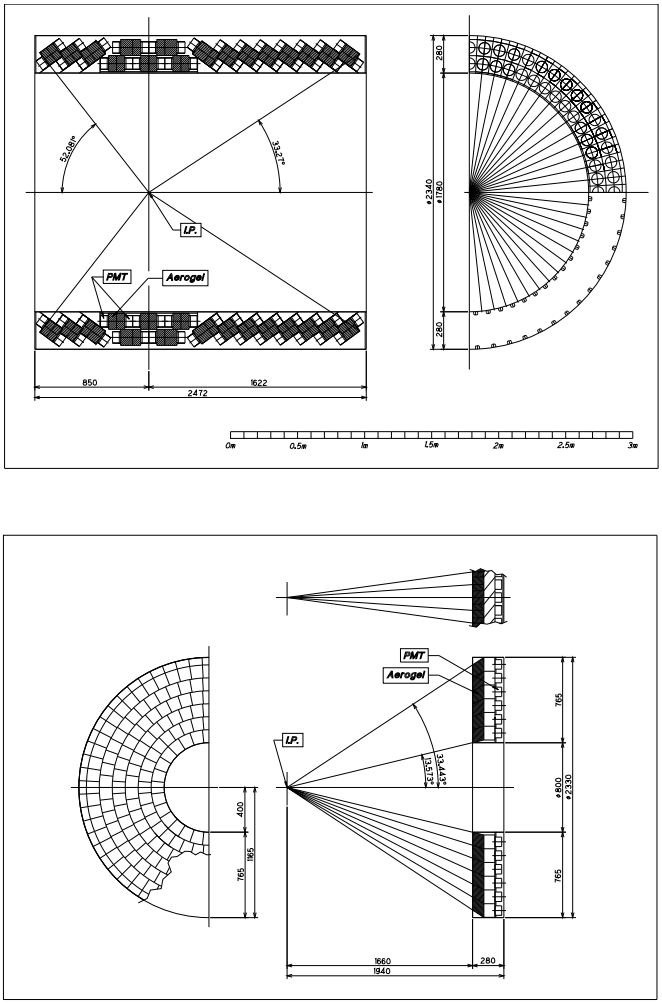

Figure 3.6: Aerogel Čerenkov counters. (a)barrel (b)endcap.

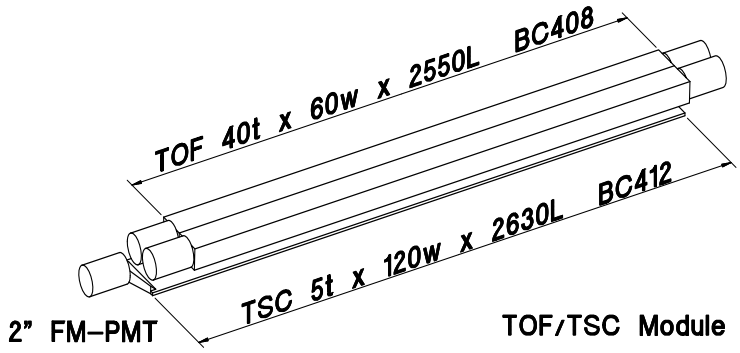

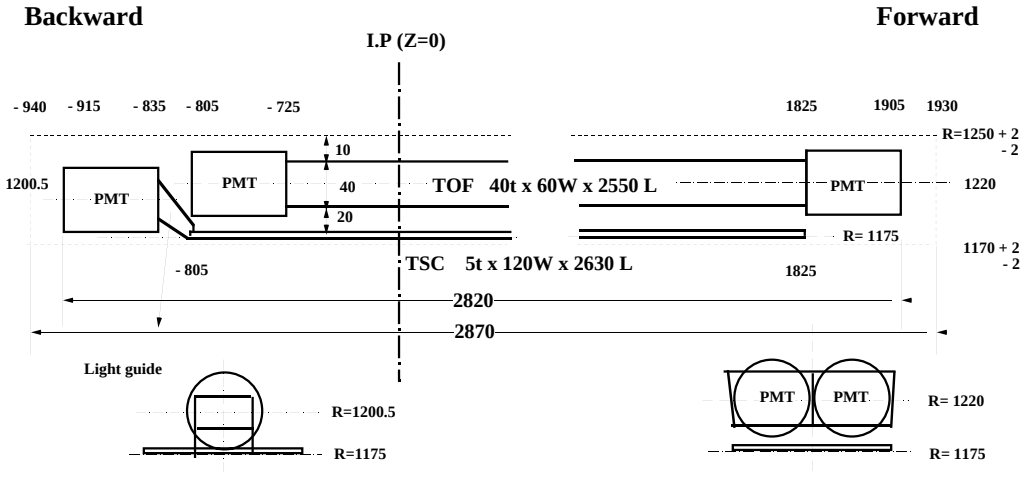

Figure 3.7: Time of flight counter and trigger scintillator.

3.2.9 Super Conducting Magnet

A super-conducting solenoid magnet has been designed to provide a 1.5 T magnet field in a cylindrical volume of 3.4 m in diameter and 4.4 m in length. The coil is surrounded by a multi layer steel return yoke to house the KLM detector.

3.2.10 K_L and Muon Detector(KLM)

The K_L particle makes a strong interaction with the material and emit the charged particles to be detected. The KLM is a sandwich of 14 layers 47 mm thick iron and 15 layers tracking device. The iron is the absorption material to generate the interaction of K_L. Resistive plate counter (RPC) modules which are planar spark counters made of glass are used as the tracking device.

High momentum muons ($\geq$ 600 MeV/c) which pass through the inner detector are also detected by KLM.

3.2.11 Trigger and DAQ System

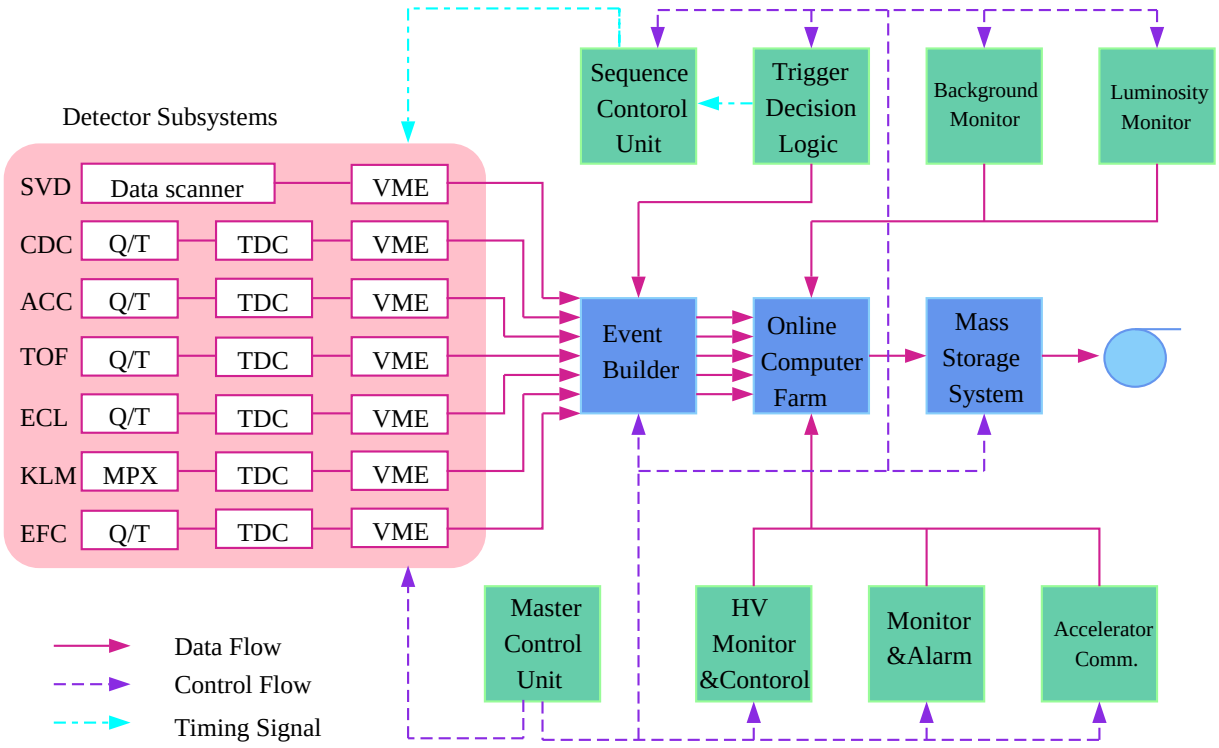

Figure 3.8: BELLE DAQ system

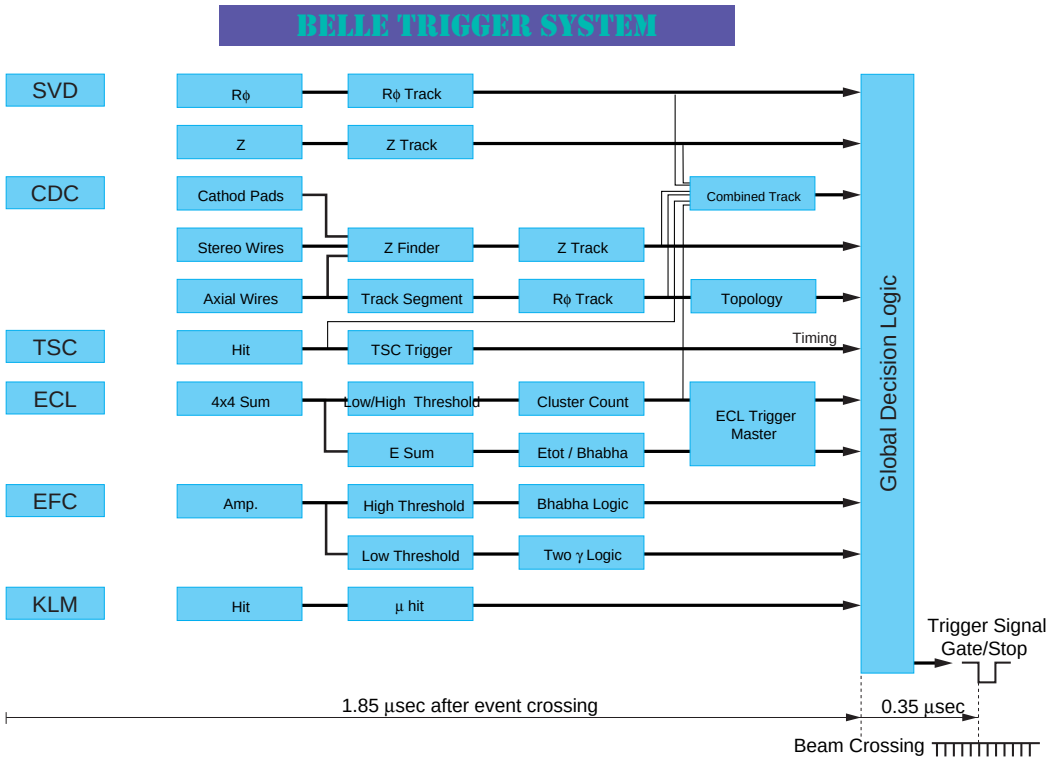

Figure 3.9: BELLE trigger scheme.

A schematic view of the BELLE data acquisition system is shown in Fig. 3.8. The readout of each sub-detector runs in parallel at 200 Hz. The signal from sub-detectors are converted to a time signal by Q-to-T converter except for KLM which provides the time-multiplexed information on a single line. All sub-detectors use TDC readout and it is controlled by VME and FUSTBUS. The SVD is an exception and its data is sent to flash ADC (FADC) and gathered to a memory module.

The readout data is transfered to the Event Builder and the detector-wise parallel data is sorted to event-wise parallel data here. The data is then shipped to each node of the online farm. The data passed the farm are sent to the computer center and stored in the Mass Storage system.

The trigger for the data acquisition is provided by several sub-detectors (see Fig. 3.9). There are two major types of triggers in BELLE system. One is provided by the tracking information from CDC and the other is provided by the energy information from the calorimeter. The global decision logic (GDL) combines the trigger signal from each sub-detector and makes a final decision to initiate a BELLE-wide data acquisition.

Chapter 4

CsI(Tℓ) Calorimeter

4.1 Introduction

We describe the BELLE calorimeter system in this chapter which include the design principle, mechanical structure and readout electronics in detail. As will be mentioned later, we use large number of counters to cover the wide polar angular region. In order to manage the quality of the counters, many kinds of items should be designed and tested carefully.

The BELLE electromagnetic calorimeter is used for the detection of γ rays and electrons. The detection of γ is important for the reconstruction of D and B meson decays including π^0's. The π^0 particle decays into two γ's. There are also such decays as $B \to K^*\gamma$ and $D^* \to D\gamma$ including a direct γ. The separation of $e^\pm$ from $\pi^\pm$ can be done by requiring that the momentum measured by CDC is equal to the energy measured by CsI. This is because nearly 100 % of electron energy is absorbed in the electromagnetic calorimeter but only a fraction of pion energy is deposited in the calorimeter. The electron identification is important to tag B^0 or $\bar{B}^0$ mesons through the semi-leptonic decays.

Since the final state of the Υ(4S) include 10 photons and 5 charged particles in average, the reconstruction of π^0 from two γ's in the multi particle environment is not an easy task. For the reconstruction of π^0 mass from two γ's, the following equation is used;

$$M^2_{\pi^0} = 2E_{\gamma 1}E_{\gamma 2}(1 - cos\theta_{12}), \tag{4.1}$$

where $E_{\gamma 1}$, $E_{\gamma 2}$ are the energy of γ's and θ_{12} is the opening angle of 2 γ's in the laboratory system. The opening angle θ_{12} is related with the π^0 velocity β and the

(a) (b)

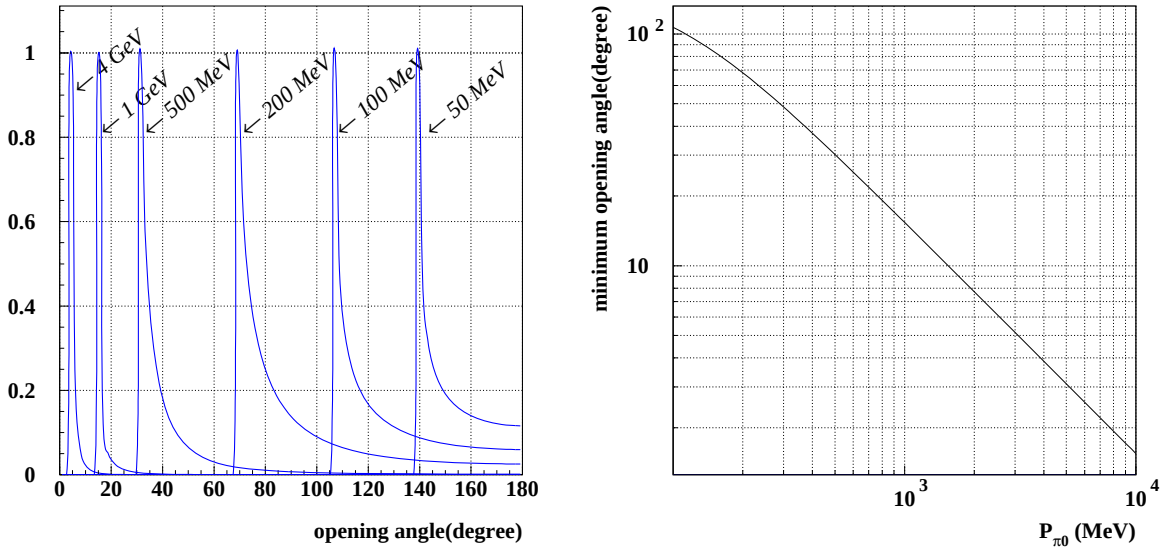

Figure 4.1: (a) Distribution of the opening angle of 2 γ's decaying from π^0 and (b)momentum dependence of the minimum opening angle.

decay angle (with respect to the π^0's flight direction) θ_1^* in the rest frame of π^0 as follows;

$$cos\theta_{12} = \frac{2\beta^2 - 1 - \beta^2 cos^2(\theta_1^*)}{1 - \beta^2 cos^2(\theta_1^*)}. \tag{4.2}$$

β : P_{π^0}/E_{π^0}.
P_{π^0} : momentum of π^0.
E_{π^0} : energy of π^0.

There is the minimum opening angle θ_{12}^* in the laboratory system which corresponds to $\theta_1^* = 90^\circ$ at the π^0 rest frame and the value is given by;

$$\theta_{12}^{min} = cos^{-1}(2\beta^2 - 1). \tag{4.3}$$

Fig. 4.1(a) shows the distribution of θ_{12} for several π^0 momenta. The value of θ_{12}^{min} is a function of the π^0 energy (P_{π^0} is given in Fig. 4.1(b)).

The mass resolution of π^0 is obtained from (4.1) by

$$(\frac{\delta M_{\pi^0}}{M_{\pi^0}})^2 = (\frac{\delta E_1}{2E_1})^2 + (\frac{\delta E_2}{2E_2})^2 + (\frac{\delta\theta_{12}}{2tan(\theta_{12}/2)})^2 \simeq \frac{1}{2}(\frac{\delta E_\gamma}{E_\gamma})^2 + (\frac{\delta\theta_{12}^{min}}{\theta_{12}^{min}})^2, \tag{4.4}$$

(a) (b)

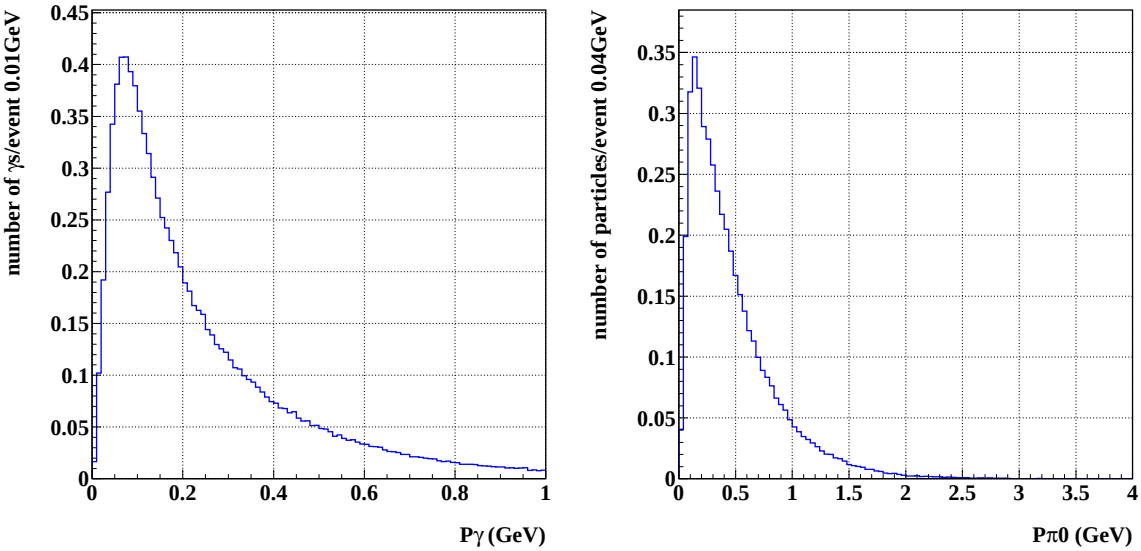

Figure 4.2: Momentum spectrum of inclusive (a)γ's and (b)π^0's from B meson decays.

where $E_\gamma = E_1 \simeq E_2$ is assumed. From the equation, we can see that the energy resolution of γ is essential to get the good π^0 mass resolution. Better angular resolution is also needed for high energy π^0's.

The energy range required for the BELLE electromagnetic calorimeter is very wide. The inclusive γ and π^0 spectrum from the B meson decay is shown in Fig. 4.2. Most of the γ's are produced with low energy because they are the final products of many decay chains. On the other hand, interesting rare decays such as $B \rightarrow K^* \gamma$ and $B^0 \rightarrow \pi^0 \pi^0$ generate γ's with near 4 GeV as shown in Fig. 4.3. The Bhabha events have electrons near 8 GeV as shown in Fig. 4.4. In order to cover all the processes, a good energy and position resolution is required from 20 MeV to 8 GeV with high detection efficiency.

4.2 Principle of Calorimetry

A detector measuring the total energy of particles is called 'calorimeter' in high energy experiments. When a high energy electron or photon is injected into a thick absorber material, it produces a cascade shower of electrons and photons in the material. The particle loses all the energies in the material if the size of the material is big enough.

The electromagnetic cascade shower develops as follows. The electron or positron

(a) (b)

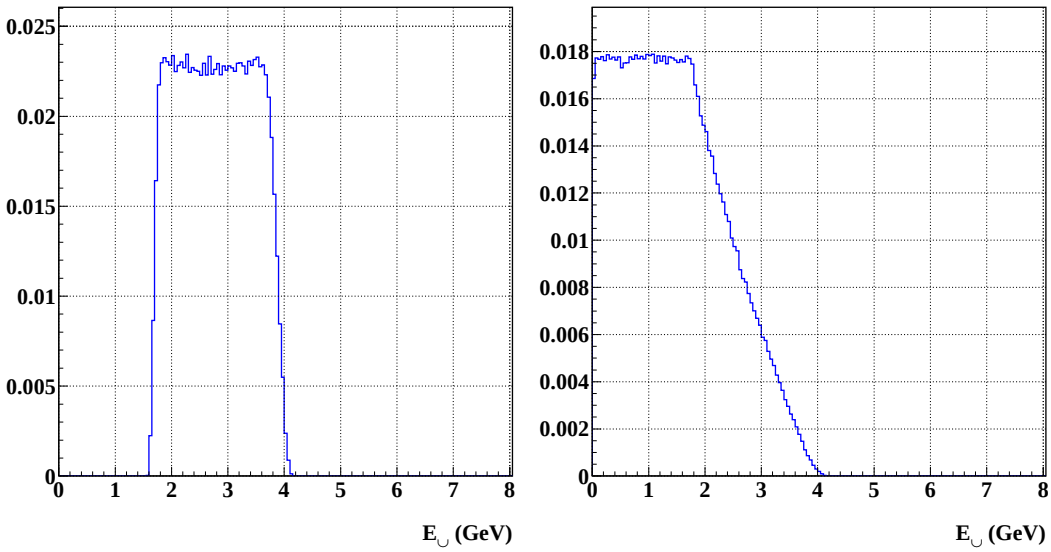

Figure 4.3: Energy spectrum of γ's in the process of (a) $B \to K^*\gamma$ and (b) $B \to \pi^0\pi^0$.

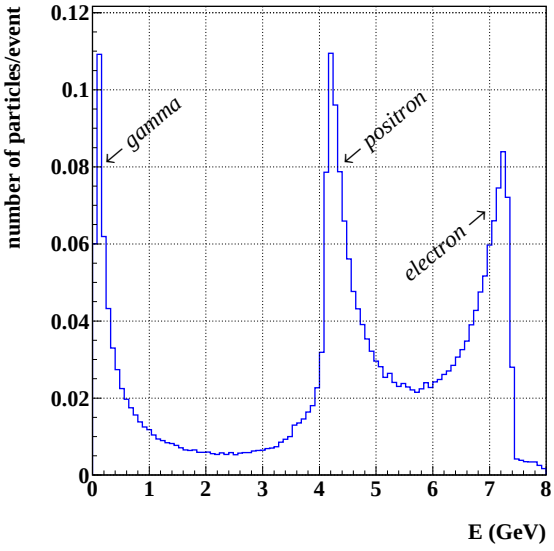

Figure 4.4: Energy spectrum of the e^+, e^- and γ from the Bhabha scattering.

(a)

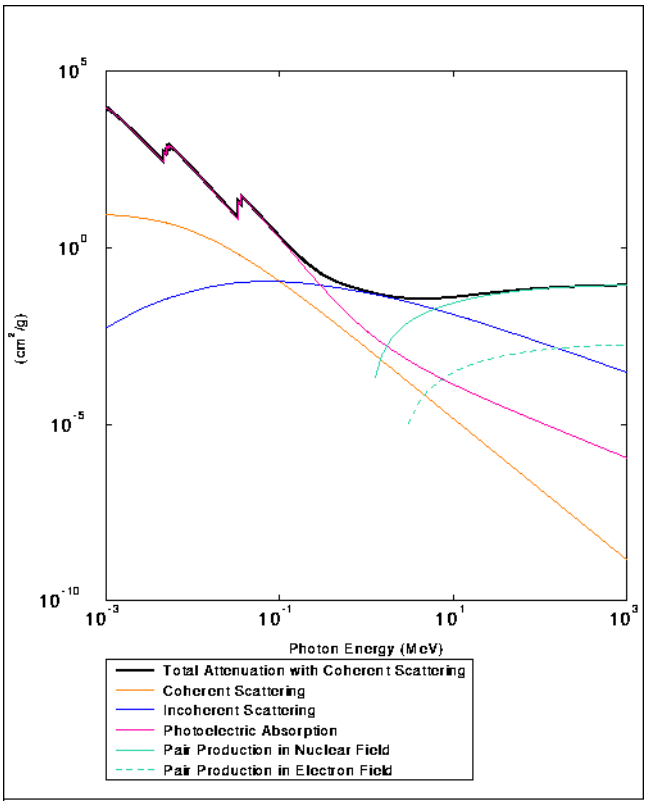

(b)

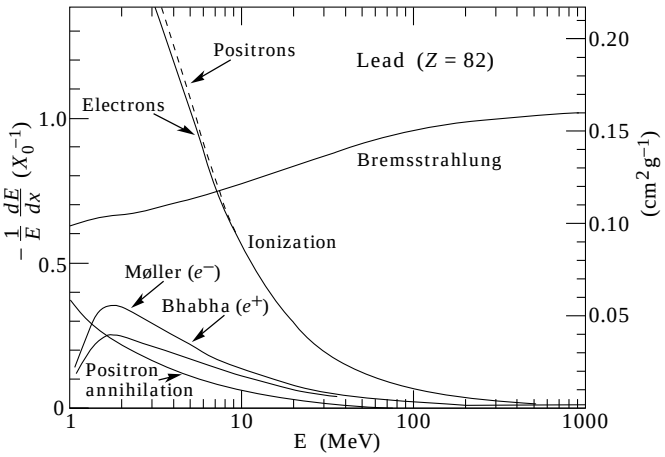

Figure 4.5: (a) Photon total attenuation as a function of energy in CsI. (b) Fractional energy loss of electrons and positrons per radiation length in lead as a function of energy.

generates a γ by the Bremsstrahlung and the γ creates an electron-positron pair in the material. Each process happens after passing one radiation length distance in average. The radiation length X_0 is defined as;

$$X_0 = \frac{716.4A}{Z(Z+1)\ln(287/\sqrt{Z})}[\text{g cm}^{-2}], \tag{4.5}$$

where Z is the atomic number and A is the atomic mass in the unit of g mol^{-1}. One radiation length is equal to the distance over which the electron energy is reduced to $\frac{1}{e}$ by the radiation loss only. The calorimeter depth defined by the radiation length is universal because the average number of interactions is one per 1 X_0 for all the materials. After several Bremsstrahlung and pair creations, the particle's energy goes down and other processes takes over. The γ's cause the Compton scattering or the photoelectric effect. The electrons and positrons below a critical energy E_c ($\sim 800/(Z + 1.2)$ MeV) lose most of their energy by the ionization. The critical energy E_c is defined as the energy at which the ionization loss per radiation length is equal to the energy loss by the Bremsstrahlung. After all the cascade shower processes are over, the incident electron or positron lose all the energies in the material mostly in the form of energy losses by the electrons and positrons below E_c. Fig 4.5 shows the photon cross section for CsI and the fractional energy loss for electrons and positrons in lead[51].

Many varieties exist for the electromagnetic calorimeter used for the detection of electrons and γ's. It is summarized in Table 4.1 together with a typical energy resolution. For NaI(Tℓ) and lead glass, a transparent bulk material is used for the absorber. The NaI(Tℓ) is a scintillator and the lead glass is a Čerenkov light radiator. A part of the absorbed energy in the shower is converted to a scintillation if we use a scintillator as the absorbing material. For the lead glass, electrons and positrons in the shower produce Čerenkov lights. Since the amount of produced photons are proportional to the total energy loss, we can determine the energy of incident particle by measuring the amount of light by the photodiode or photomultiplier.

For the rest of examples, the calorimeter is made by many layers of sandwiches. Each layer of the sandwich is a heavy metal absorber and a device to measure the energy deposit of shower particles. This type of device is called a sampling calorimeter. The energy measurement is done by the proportional wire chamber for (6) or ionization chamber for (3). But most popular types use the plastic scintillators ((4) and (5)).

For the electromagnetic calorimeter of BELLE, the detection of low energy photon is important. The detection efficiency of the photon decreases significantly, if the calorimeter is placed behind the thick solenoidal coil of the magnet. The calorimeter

placed inside of the solenoidal coil has to be operated in the magnetic field of 1.5 T. The calorimeter using phototube can not be used for BELLE.

For a good energy resolution at low energy, sampling calorimeters are not suited. For the bulk calorimeter, the scintillator is superior to the lead glass because the scintillator produces far more photons (typically $\times \sim 10^{2\sim3}$) than the Čerenkov radiator.

The use of bulk inorganic scintillator by the photodiode readout is therefore a unique choice for the BELLE calorimeter.

	Detector	Resolution
(1)	NaI(Tℓ) (Crystal Ball [69]; 20 X_0)	$2.7\%/E^{1/4}$
(2)	Lead glass (OPAL [44]; $24X_0$)	$5\%/\sqrt{E}$
(3)	Lead-liquid argon (NA31 [45]; 27 X_0)	$7.5\%/\sqrt{E}$
(4)	Lead-scintillator sandwich (ARGUS [46], LAPP-LAL [47])	$9\%/\sqrt{E}$
(5)	Lead-scintillator spaghetti (CERN test module [48])	$13\%/\sqrt{E}$
(6)	Proportional wire chamber (MAC [49]; 13 X_0)	$23\%/\sqrt{E}$

Table 4.1: Resolution of typical electromagnetic calorimeters. E is in GeV.

4.3 Crystal Calorimeter

4.3.1 Energy Resolution

There are many factors to determine the energy resolution of the calorimeter using the inorganic scintillator.

The shower fluctuation is an important factor. The generated shower leaks from the side and rear of the crystal, if the depth of the scintillator is not sufficient or the lateral size is limited. This leakage fluctuates from event to event and produces the uncertainty in the total energy loss in the crystal. The fluctuation is larger if the leakage is larger. The rear leakage is bigger in higher energy because the shower maximum increases logarithmically with energy. The side leakage becomes dominant at the low energy because the lateral size becomes larger. A special calorimeter configuration such as the staggered arrangement of the crystals and the gap between counters can enhance the problem of the shower leakage.

The light output from various parts of the crystal is not perfectly uniform. It has the longitudinal and lateral position dependence. The non-uniformity may come from

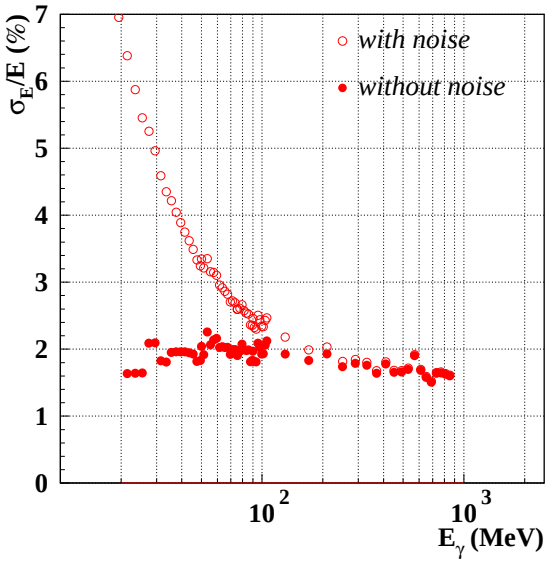

Figure 4.6: Effect of electronics noise on the energy resolution by MC simulation. Energy is obtained by the sum of 5×5 CsI(Tℓ) counters

the different scintillation efficiency caused by the dopant density fluctuation. It may also come from the different light collection efficiency determined by the transparency of the crystal and the surface quality for the reflection of the light etc.. The non-uniformity of the light output does not influence the energy resolution significantly, but it affects the energy linearity and it is checked by the GEANT simulation (see section 6.8.2).

The electronics noise is the dominant effect at low energy for the calorimeter using a photodiode readout. It is demonstrated by the Monte Carlo study shown in Fig. 4.6 where the energy resolution is plotted with and without the noise contribution. The solid circle is the original resolution of the generated energy deposit which is determined by the shower leakage fluctuation. The open circle represents a quadratic sum of the original resolution and the electronics noise estimated for the prototype CsI calorimeter of BELLE. It is apparent that the resolution is strongly affected by the electronics noise below 100 MeV. It should be noted that the effect of electronics noise is always relative to the average light output. When the light output increases, the relative noise effect decreases.

The stability and non-linearity of the electronics, the calibration of the counters and the pile-up effect under the high background condition are the other factors to influence the energy resolution.

Some of the adverse effects described above can be eliminated by the proper calibration method and the clever clustering software.

4.3.2 Position Resolution

The position resolution is determined by the transverse dimension of the shower and the number of calorimeter segmentation.

The transverse dimension of the shower profile scales with the Molière radius R_M in the same manner as the longitudinal dimension scales with the radiation length X_0. The R_M is defined as ;

$$R_M = \frac{E_s}{E_c} X_0. \tag{4.6}$$

where E_s is $m_e c^2 \sqrt{4\pi/\alpha} = 21.2$ MeV.

A finer segmentation and a small R_M are advantageous for a good position resolution, but it has no meaning to divide the calorimeter much smaller than the shower dimension itself. If the shower is spread over many crystals, the energy resolution could be worse because the leakage of the shower through the gap between crystals increase. The electronics noise is also higher because the same amount of light is collected by more number of electronics channels.

4.3.3 Detection Efficiency

The dominant effect on the detection efficiency is the amount of materials in front of the calorimeter. All the detectors for the tracking and the particle identification (SVD, CDC, ACC and TOF) installed between the interaction point and the calorimeter will be the source of photon conversion. The electron and positron produced by the photon conversion will be separated by the magnetic field. The reconstruction of the photon from such e^+e^- pair is difficult and the converted photon is practically lost. The loss of efficiency will be higher if the conversion point is far away from the calorimeter. The amount of materials of the inner detector was minimized but it still poses a limit to the detection efficiency of the calorimeter.

If the crystal length is too short, the reconstructed energy tends to have a low energy tail due to the rear shower leakage. Such a tail is usually long due to the large fluctuation of the shower leakage. The event in the long tail often gives a lower π^0 mass and will be rejected in the reconstruction. The thicker calorimeter is more

advantageous but the total volume of the crystal quickly increases and the construction of such a large calorimeter becomes unrealistic.

When the reconstructed shower is overlapped with the charged track, the γ is misidentified as the charged particle and rejected in the reconstruction. This also causes the inefficiency.

4.3.4 Choice of Crystal

Table 4.2 shows the property of several inorganic scintillators. The CsI(Tℓ) and Na(Tℓ) crystals have higher light output than other crystals and the photodiode can be used instead of the photomultiplier. The BELLE calorimeter is given a limited radial space. It is r = [1250mm, 1540mm] and the thickness (in radiation length) of the calorimeter has to be as large as possible for better resolution and efficiency. If we use NaI(Tℓ), we can put 11.6 radiation lengths in 300mm space and it is 16.2 radiation lengths for CsI(Tℓ). Since the Molière radius of CsI(Tℓ) is smaller than NaI(Tℓ), the separation of 2γ's is easier in CsI(Tℓ). The hygroscopicity of NaI(Tℓ) also makes the construction and operation of the calorimeter difficult. The BGO and CsI(pure) can be used with photomultiplier. But both sintillators are expensive and the system with fine-mesh photomultiplier which is operative under 1.5 T magnetic field becomes too big and too expensive. Then we chose the CsI(Tℓ) crystal for the BELLE calorimeter with the photodiode read out.

We decided the basic size of one CsI(Tℓ) segment is 6 $\times$ 6 cm^2 in cross section and 30 cm in length. The area of 6 $\times$ 6 cm^2 is equivalent to a circle with a radius of 3.4 cm, which is close to R_M = 3.8 cm of CsI(Tℓ). According to GEANT simulation, about 80 % of incident energy is deposited in one segment when a γ ray enters at the center of the segment. This rate is approximately same for photons with energies 100 MeV $-$ 2 GeV. The length of 30 cm corresponds to 16.2 X_0 and it is sufficient for low energy photons.

4.4 Layout of the BELLE Calorimeter

4.4.1 Overall Arrangement

An overall layout of the BELLE calorimeter is shown in Fig. 4.7. The plus direction is the electron direction. It is composed of a barrel and two endcaps and covers the regions of $\theta = 17^\circ - 150^\circ$. The barrel has an inner radius of 1.25 m and a length of

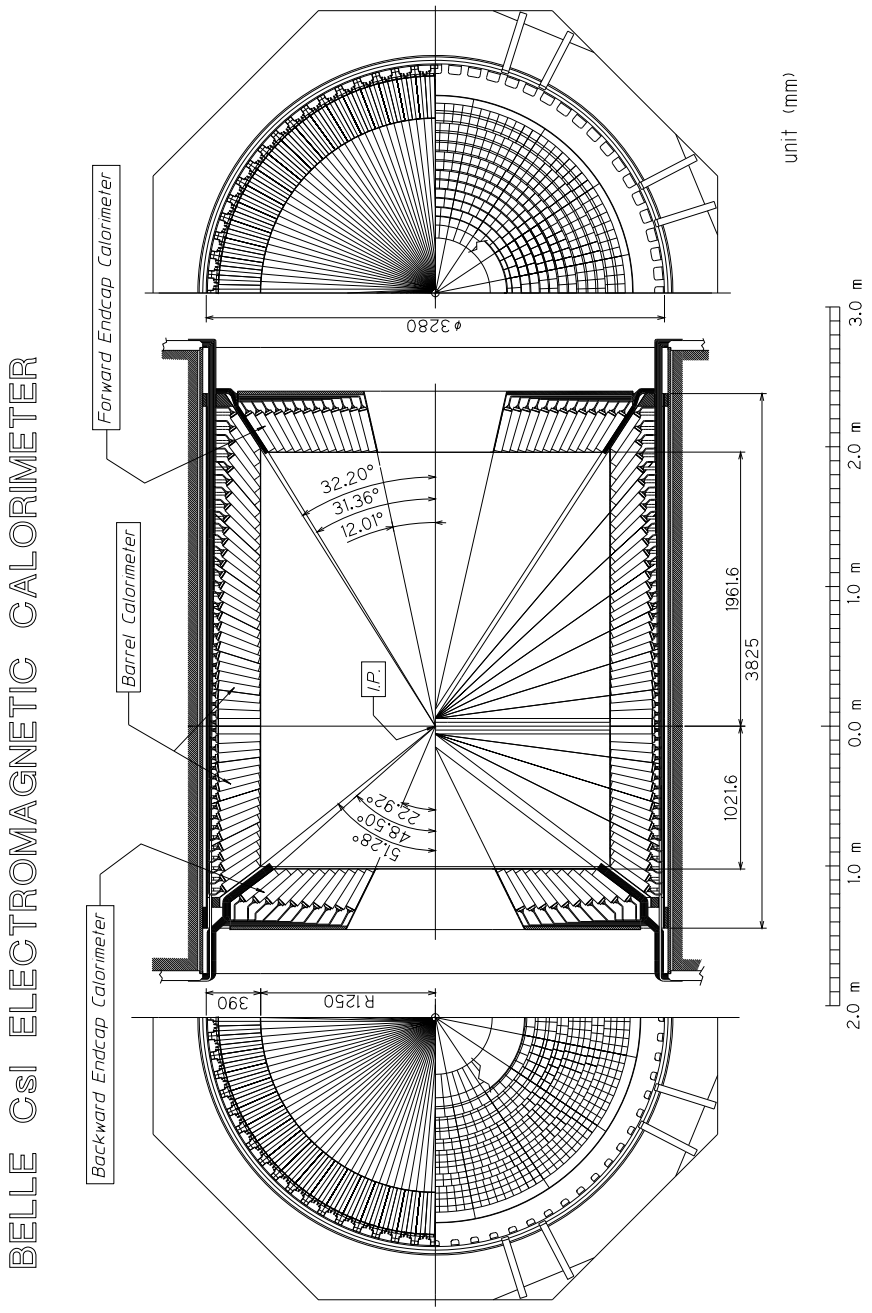

Figure 4.7: Overall design of the CsI(Tℓ) calorimeter.

	NaI(Tℓ)	BGO	BaF_2	CsI(Tℓ)	CsI(pure)	$PbWO_4$	CeF_3
Density (g/cm^3)	3.67	7.13	4.89	4.53	4.53	8.28	6.16
Radiation length (cm)	2.59	1.12	2.05	1.85	1.85	0.89	1.68
Molière radius (cm)	4.5	2.4	3.4	3.8	3.8	2.2	2.6
dE/dx (MeV/cm)	4.8	9.2	6.6	5.6	5.6	13.0	7.9
(per mip)							
Nucl. int. length (cm)	41.4	22.0	29.9	36.5	36.5	22.4	25.9
Decay time (ns)	250	300	0.7^f	1000	$10,36^f$	5-15	10-30
			620^s		$\sim 1000^s$		
Peak emission λ (nm)	410	480	220^f	565	305^f	440-500	310-410
			310^s		$\sim 480^s$		
Refractive index	1.85	2.20	1.56	1.80	1.80	2.16	1.68
Relative light output$*$	1.00	0.15	0.05^f	0.40	0.10^f	0.01	0.10
			0.20^s		0.02^s		
Relative light output$\star$	1.00	0.21	0.26	1.37	0.44	-	-
Hygroscopic	very	no	slightly	somewhat	somewhat	no	no

f = fast component, s = slow component

$*$ For standard photomultiplier tube with bialkali photocathode. [51]

$\star$ For photodiode S 1790-02. [50]

Table 4.2: Properties of several inorganic crystal scintillators.

3 m, The endcaps are placed at z=+2m and z=−1m from the interaction point. The acceptance in the laboratory frame is 91 % of 4π. There are small gaps between endcap and barrel to be used for the cabling and piping. The geometrical parameters are given in Table. 4.4.1.

Each crystal segment points to the interaction point with a small tilt angle of $1 \sim 2^\circ$ in both θ and ϕ directions. This is to avoid the photon escaping through the gap between crystals. This tilt angle was not implemented for the endcap ϕ direction due to the difficulty of the mechanical construction.

A total of 8,736 CsI(Tℓ) crystals are used for the electromagnetic calorimeter. The total weight of all is 43 tons.

	θ coverage	θ segments	ϕ segments	# of counters
Forward Endcap	12.01° - 31.36°	13	48 - 144	1152
Barrel	32.2° - 128.7°	46	144	6624
Backward Endcap	131.5° - 155.03°	10	64 - 144	960

Table 4.3: The geometrical parameters of the CsI Calorimeter.

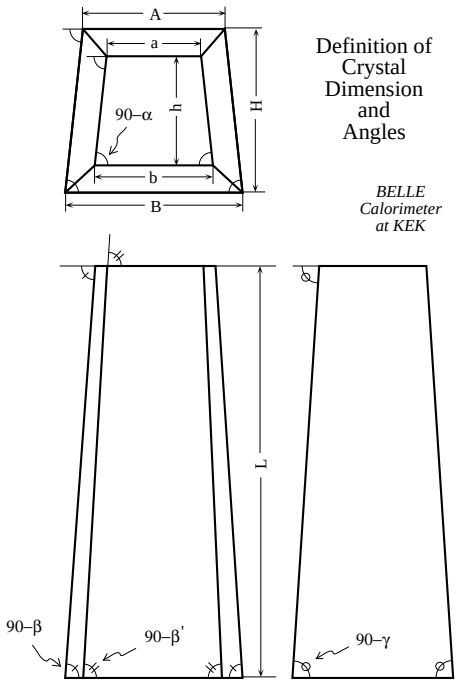

Figure 4.8: Dimension of the barrel CsI(Tℓ) crystal.

4.4.2 Shape of the Crystals

The shape of the barrel crystal is illustrated in Fig. 4.8. Its cross section is trapezoid due to the pointing structure and its side is about 5.5 cm in the front face and about 6.5 cm in the back face. The length of all the crystals is 30 cm. The average weight is 5 kg for one crystal. There are 29 types of barrel crystal in total.

The shape of the endcap crystal is more complicated because the number of ϕ segmentation decreases near the beam line. The arrangement of the crystals for the forward and the backward endcap is shown in Fig. 4.9 and Fig. 4.10. Typical crystal shapes are shown in Fig. 4.11. The cross sections is a quadrilateral type for the most of them and one pentagonal type is used for the forward endcap. There are 36 different

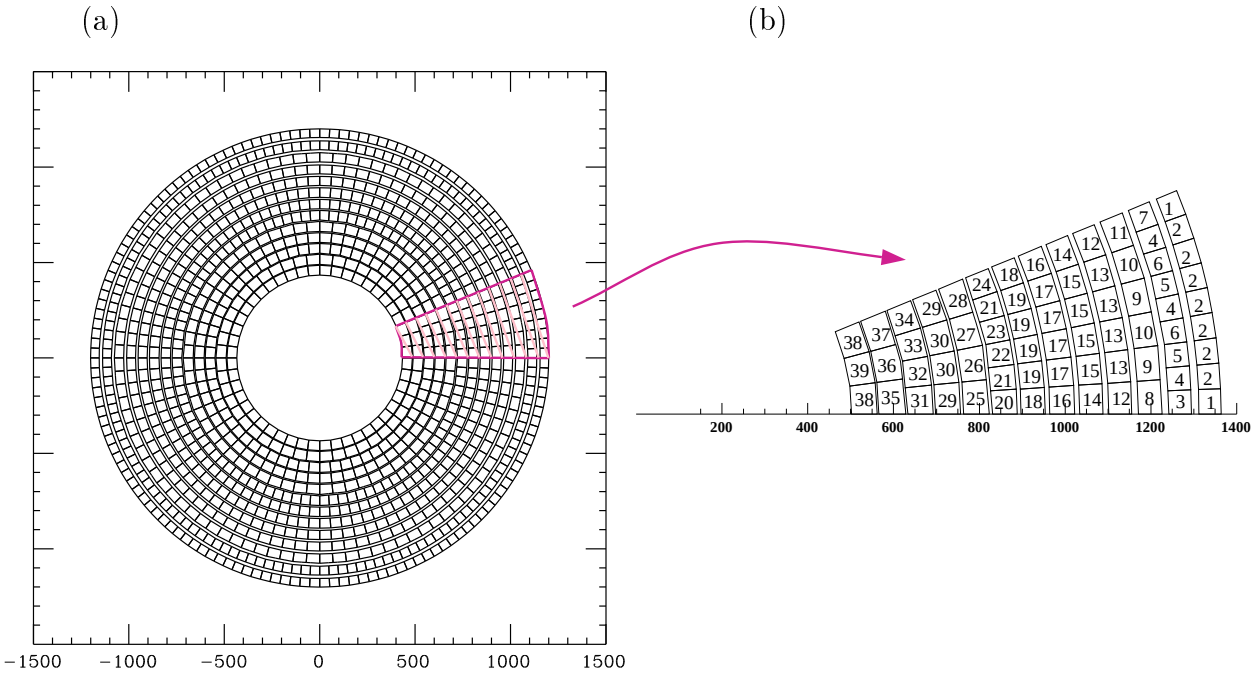

Figure 4.9: (a)Layout of the forward endcap CsI(Tℓ) calorimeter and (b) expanded view of its 1/16. The crystal front face projected to a plane perpendicular to the beam is drawn. There are no gaps between crystals.

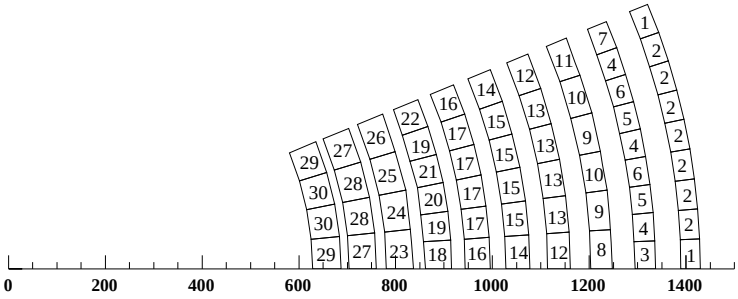

Figure 4.10: Expanded view of 1/16 of the backward endcap CsI(Tℓ) calorimeter.

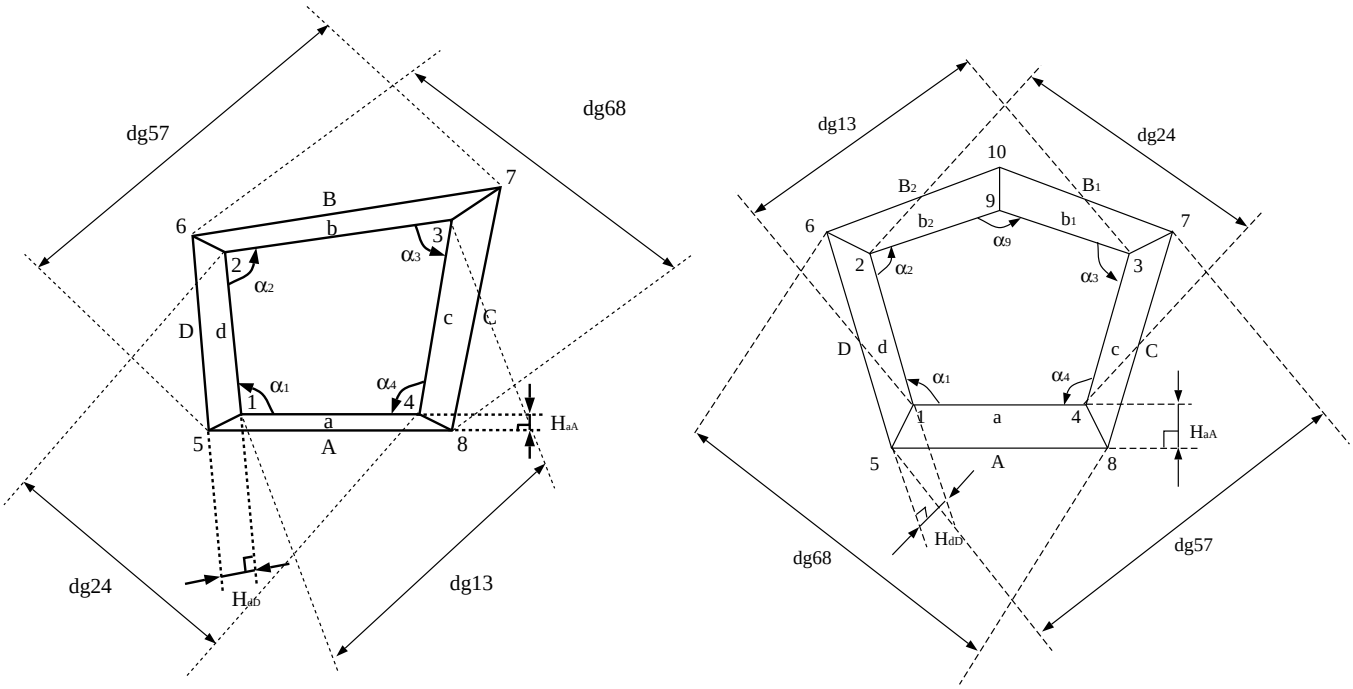

Figure 4.11: Dimensions of the endcap CsI(Tℓ) crystal. (1,2,3,4) or (1,2,3,4,5) is top plane and (5,6,7,8) or (6,7,8,9,10) is bottom plane. The top and bottom planes are in parallel.

types for the forward endcap and 30 types for the backward endcap. The size of all the crystals is given in APPENDIX B.

4.5 CsI(Tℓ) Crystal

4.5.1 Production

The CsI(Tℓ) crystals were supplied from three sources;

- 4463 pieces for barrel and 1506 pieces for endcap from BINP (Budker Institute of Nuclear Physics, Russia) and ISC (Institute for Single Crystals, Kharkov, Ukraine),
- 1153 pieces for barrel and 690 pieces for endcap from SIC (Shanghai Institute of Ceramics, China),
- 1008 pieces for barrel from Crismatec (France).

Principal parameters of the CsI(Tℓ) crystal to be controlled during the production are;

1. light output,
2. uniformity of the light output,
3. dimension,
4. radiation hardness.

These parameters were initially controlled by the producers. All the crystals were checked once more at KEK after the delivery.

4.5.2 Light Output and Uniformity

The measurement of light output and its uniformity was made using a setup shown in Fig. 4.12. A 2 inch bialkali phototube (Hmamatsu R1847S) was attached at one end of the crystal. No optical compound was used between the crystal and the phototube for the ease of measurement. The output of the phototube was shaped by the ORTEC 570 amplifier with 1 μs shaping time and digitized by a peak sensitive ADC. The γ-rays from a ^{137}Cs source was collimated by 5 cm thick lead and scanned along the crystal axis. The photopeak position of 662 keV γ-ray was measured at 9 locations (see Fig. 4.12).

The position of the photopeak was normalized to the photopeak of the small reference crystal to make the result independent of phototube and electronics gain. The reference crystal is 25 mm in diameter and 25 mm in length. Several reference crystals were calibrated at KEK and sent to each producer to be used as a standard.

The light output of the crystal is defined as the average of 9 measurements. We specified that the light output should be more than 0.27 of the reference crystal for all of the delivered crystals and it should be more than 0.29 for at least 90 % of the delivered crystals. The result of the measurement at KEK is shown in Fig. 4.13(a). The Crystals which did not satisfy the specification were rejected.

The non-uniformity of the light output H is defined as follows;

$$H \equiv \frac{P_{max} - P_{min}}{P_{ave}} \times 100. \tag{4.7}$$

P_{max} : maximum of 9 measured points,
P_{min} : minimum of 9 measured points,

(a)

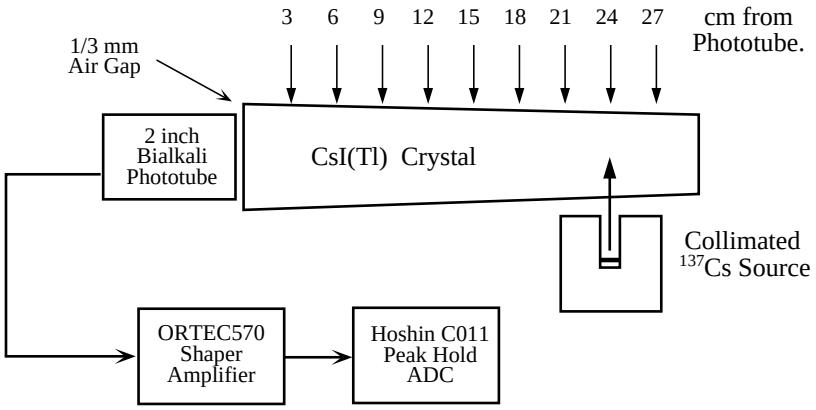

(b)

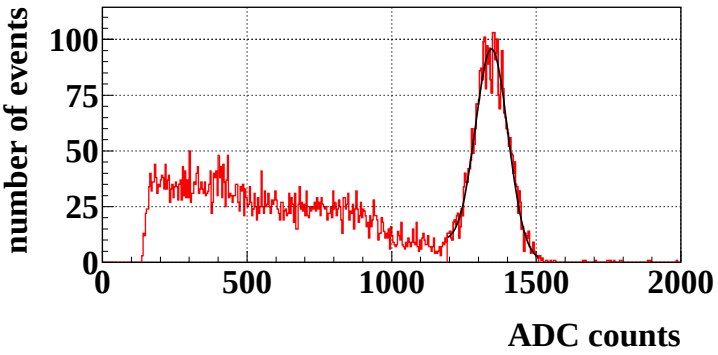

(c)

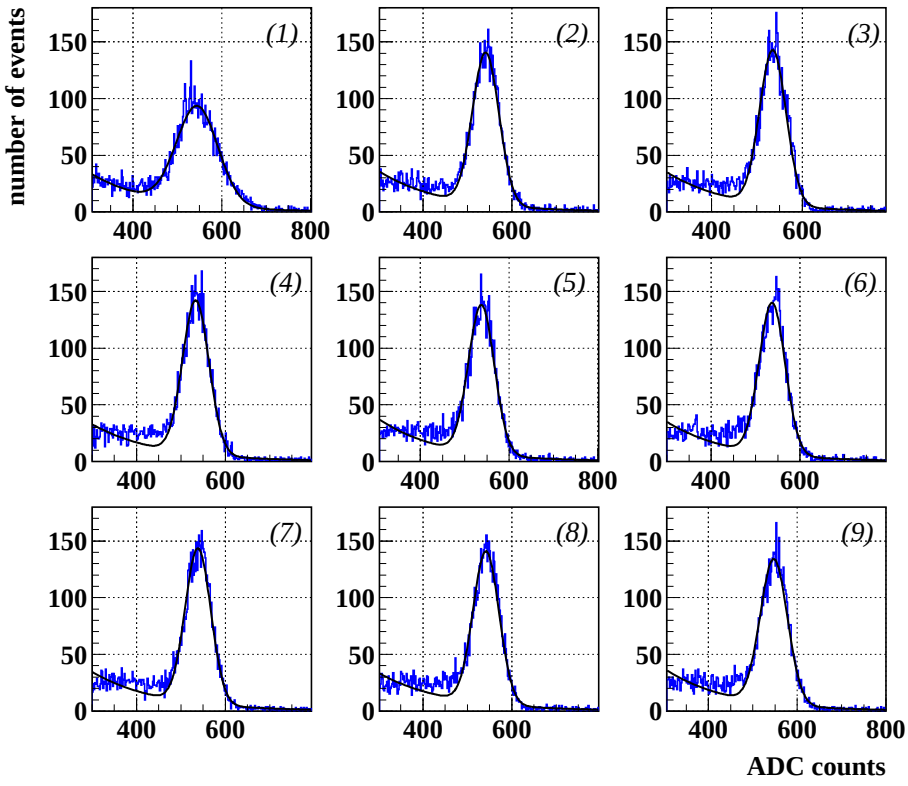

Figure 4.12: (a)Setup of the ^{137}Cs source test, (b)the ADC distribution of reference crystal and (c)the typical ADC distribution of 9 subparts in a large crystal.

(a) (b)

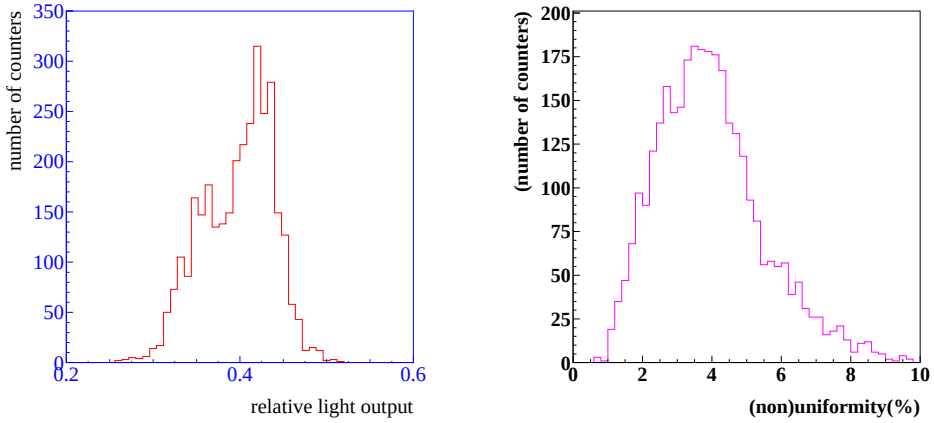

Figure 4.13: Results of ^{137}Cs source test. (a)average light output and (b)non-uniformity for sample counters.

P_{ave} : average of 9 measured points.

We specified that H $\leq$ 9 % for all the crystals and H $\leq$ 7 % for more then 90 % of all the produced crystals. The result of uniformity is shown in Fig. 4.13(b). It is also satisfied by most of the crystals.

4.5.3 Size Measurement of the CsI(Tℓ) Crystal.

The crystal dimensions are measured by an automatic device shown in Fig. 4.14. Eight linear gauges measure the position of the crystal surface with 10 μm accuracy. By moving the crystal downward in 3 cm step, nine points along the crystal axis are measured. The crystal shape is reconstructed from the measurement and compared with the specification. The same device was delivered to all the producers to control the dimension at the production stage. The measurement at the supplier was made for bare crystal and the measurement at KEK was done with wrapping.

We originally planned to set the tolerance of the crystal dimension as +0, −300 μm from the design value. Due to the difficulty in fabrication, we later increased the tolerances. Fig. 4.15 shows the results of the measurement at KEK for all the crystals used for the barrel calorimeter. The size is controlled within 100 μm in the standard deviation.

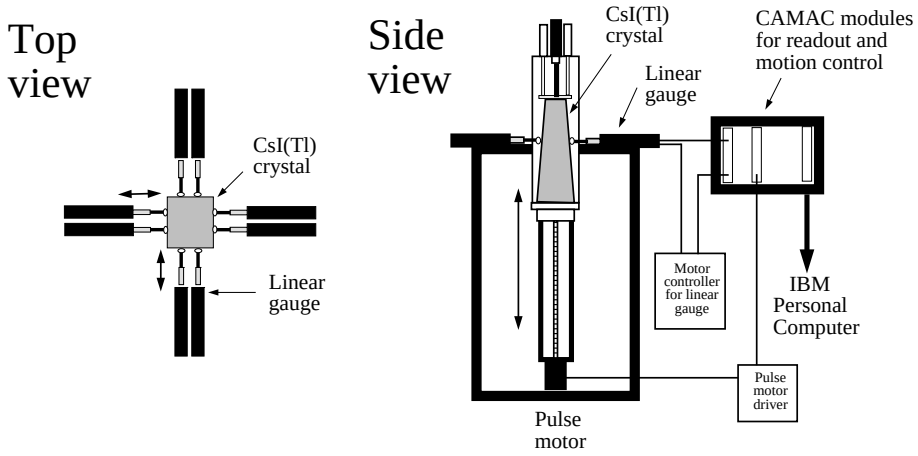

Figure 4.14: Size measurement device for CsI(Tℓ) crystals.

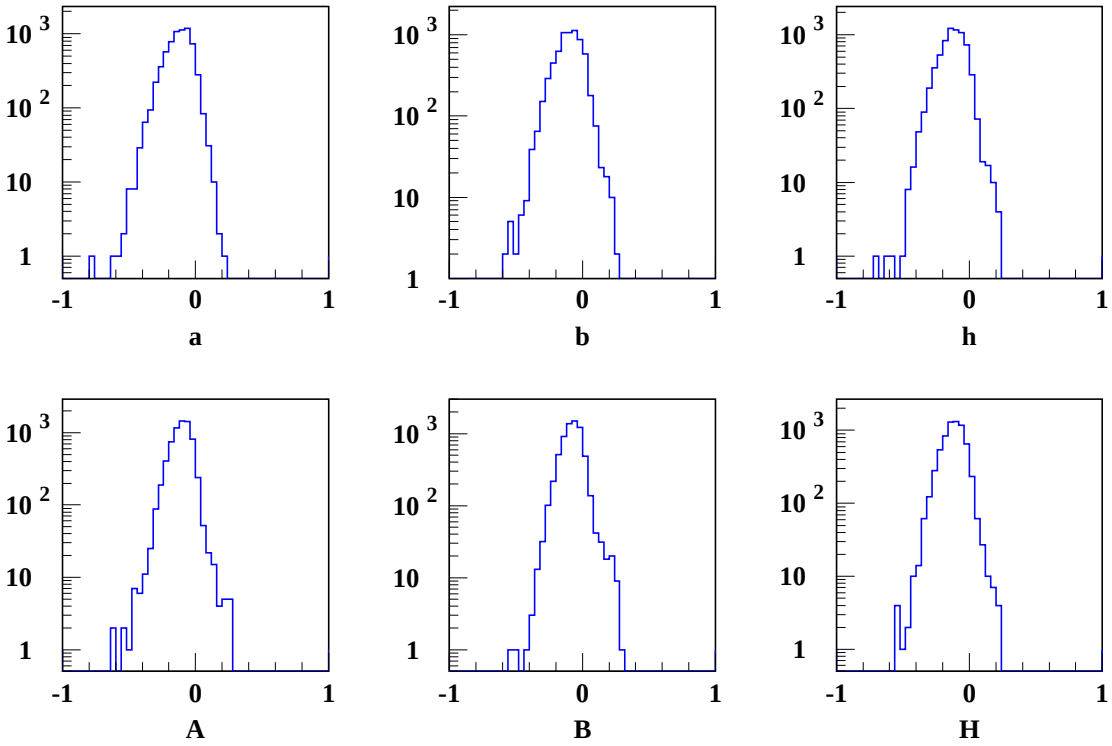

Figure 4.15: Results of the size measurements for all the barrel crystals. Each histogram is the difference (in mm) between the specified size and the measured size. For definition of parameters, see Fig.4.8.

(a)

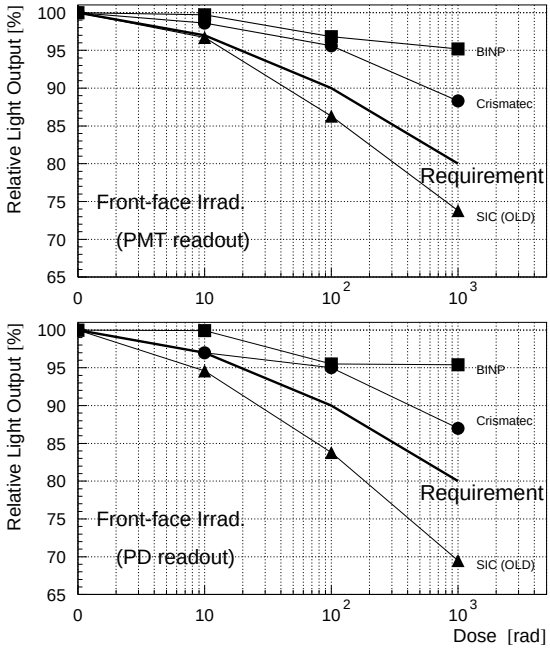

(b)

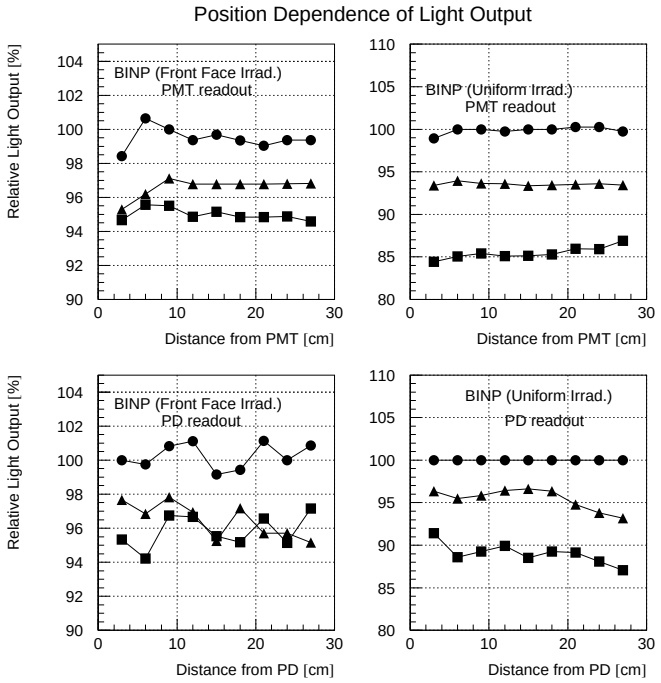

Figure 4.16: (a)Light output as a function of the dose for front-face irradiation. Upper: PMT-readout, Lower: PD-readout; The thick line represents the requirement for the radiation hardness of BELLE-ECL. (b)Position dependence of the light output measured by the PMT and PD readout. The data for front-face irradiation and uniform irradiation are shown; the circles, triangles, and squares stand for the data of 10, 100 and 1000 rad irradiation, respectively. All the values of the light output are normalized to those before irradiation.

4.5.4 Radiation Hardness

In order to estimate the effect of radiation damage, several CsI(Tℓ) crystal are irradiated by the ^{60}Co source and the difference of light output before and after the irradiation is measured [53]. The γ-ray of energy about 1 MeV from ^{60}Co corresponds to the expected mean background which was checked by BELLE Monte Carlo. The result of background become 4 krad in barrel calorimeter and less than 15 krad in most forward part. Two irradiation methods are used. One is the 'uniform irradiation' from side of the crystal. Another is the 'front face irradiation' which simulates the real case. The light output is measured by two methods; one with photodiode (PD) and cosmic muons, the other with photomultiplier (PMT) and ^{137}Cs source.

The read out system for the PMT is the same with what is described in section 4.5.2. The PD system is described in section 5.1 in detail. The measurement of light output was done after 10, 100 and 1000 rad irradiation.

The light output of CsI(Tℓ) decreased immediately with the irradiation but a part of the loss recovered slowly after a few weeks. Some crystals became slightly yellowish or pinky after the irradiation. We think that the reason of the decrease is caused by the absorption of the scintillation light. The alkali-halide crystal is known to form a color center by irradiation and it reduces the absorption length of the crystal. The average light output after the recovery is shown in Fig. 4.16(a) as a function of the radiation dose. The crystal from BINP and Crismatec satisfied the requirement, which is indicated by a thick line in Fig. 4.16(a). The test piece from SIC failed but its quality improved after introducing a scavenger material in the crystal growth process and it finally satisfied the requirement. The results of PMT and PD show similar behavior.

The position dependence of the light output is shown in Fig. 4.16(b) for the front face irradiation and the uniform irradiation. The result shows the light output decreases almost uniformly even for the front face irradiation case. This means only an overall correction factor will be needed to cope with the radiation damage. We do not expect a large performance degradation after the radiation damage.

4.6 CsI(Tℓ) Counter Module

The assembly of a single CsI(Tℓ) counter module is shown Fig. 4.17. The crystal is first wrapped by a porous teflon sheet. This teflon sheet makes a diffuse reflection of scintillation light with high efficiency and helps to collect light to the photodiode glued at the bottom of the crystal. We tested the light output as a function of the

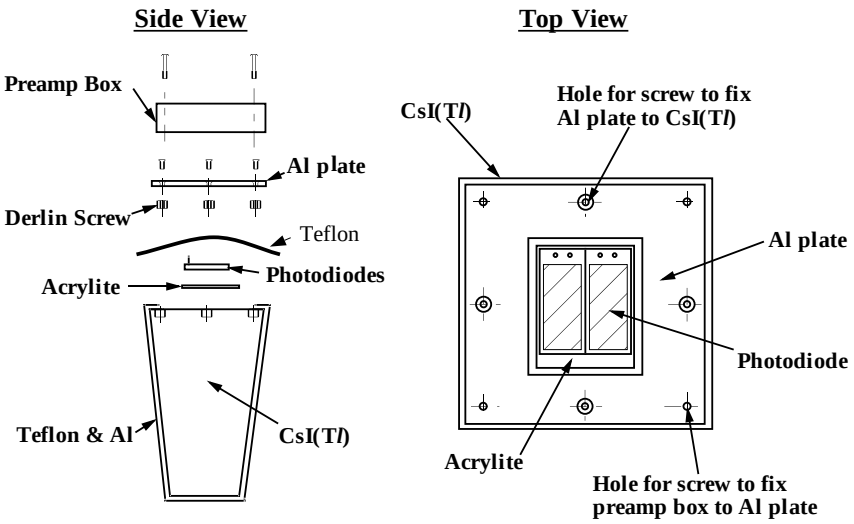

Figure 4.17: Assembly of CsI(Tℓ) counter module.

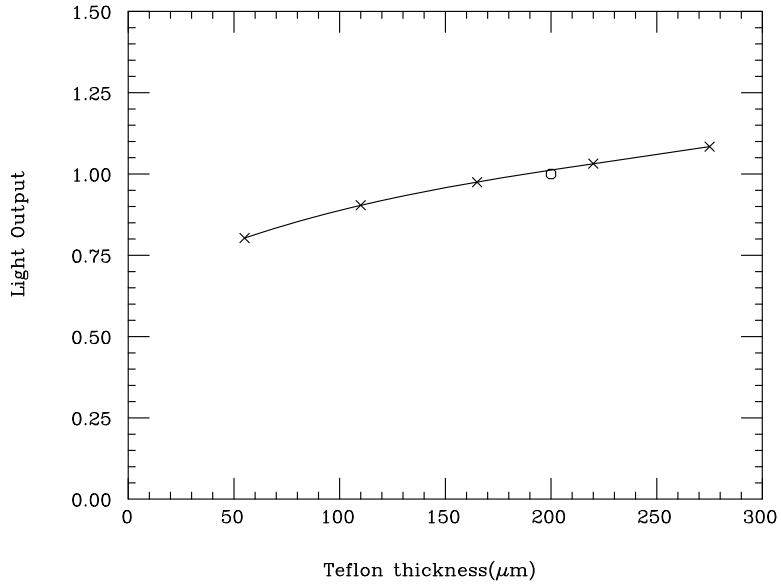

Figure 4.18: Change of light output as a function of teflon thickness.

thickness of the teflon sheet. A test crystal was wrapped by $1 \sim 5$ layers of 55 μm thick teflon sheet and the light output was measured by ^{137}Cs source. The result is shown in Fig. 4.18. The light output increases with the teflon thickness. But we decided to use one layer of 200 μm thick sheet (Goretex film) for the production because thicker one will cause lager gap between crystals and the resolution may become worse in the gap region. Then the crystal is wrapped by a laminated sheet of 25 μm thick aluminum and 25 μm thick mylar. The aluminum layer works for the shielding against the electric noise and the stray light. The mylar layer is used to isolate the counter electrically from the support structure.

Two pieces of PIN photodiodes are glued at the bottom of the crystal via 1 mm thick lucite. An epoxy glue (ECCOBOND 24)[52] is used both for CsI-lucite and lucite-photodiode joints. The CsI is lightly hygroscopic and gluing on the surface is difficult. The lucite also absorbs humidity in the air and changes its size. In order to make a stable joint, the surface of the CsI is cleaned by acetone and the lucite and the photodiode surface was cleaned by ethanol. They were kept in a dry room with humidity less than 15 % for more than one day before gluing. The gluing was also done in the dry room.

It is important to have a stable glue joint because the light detected by the photodiode decreases largely if the optical contact between CsI and lucite is broken. We tested the stability of the glue joint by cycling the temperature between 0 and 50 °C

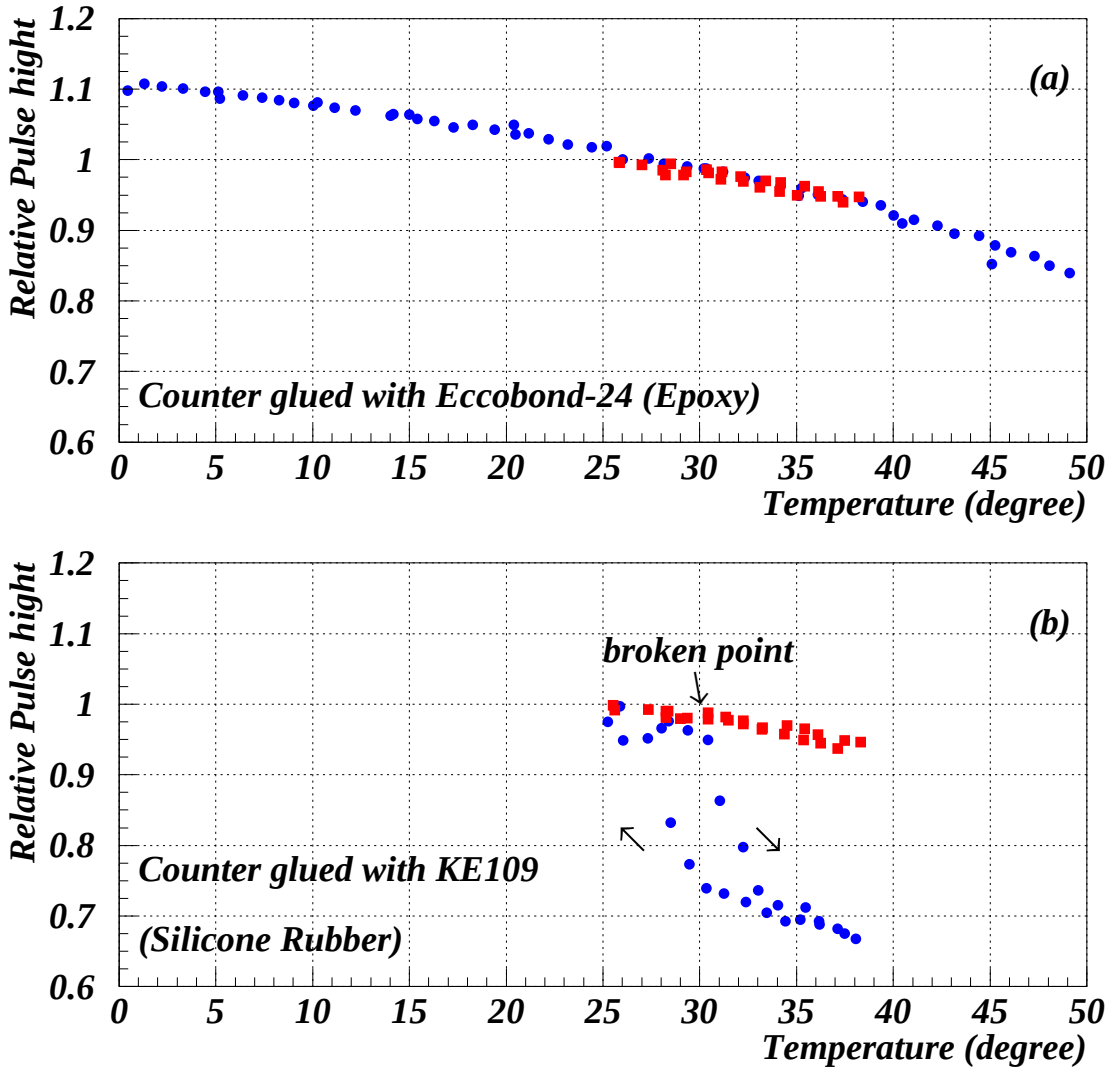

Figure 4.19: LED light output by changing the temperature with (a) epoxy (EC-COBOND 24) and (b) silicone rubber(KE109). The circles show the light output from photodiode with crystal. The squares show the photodiode and preamplifier results without crystal. In the case of KE109, the glue joint was broken around 31 degree and recovered after increasing the temperature to lower than the broken point. For the case with crystal, the temperature cycle is 27 °C → 50 °C → 27 °C → 0 °C → 20 °C.

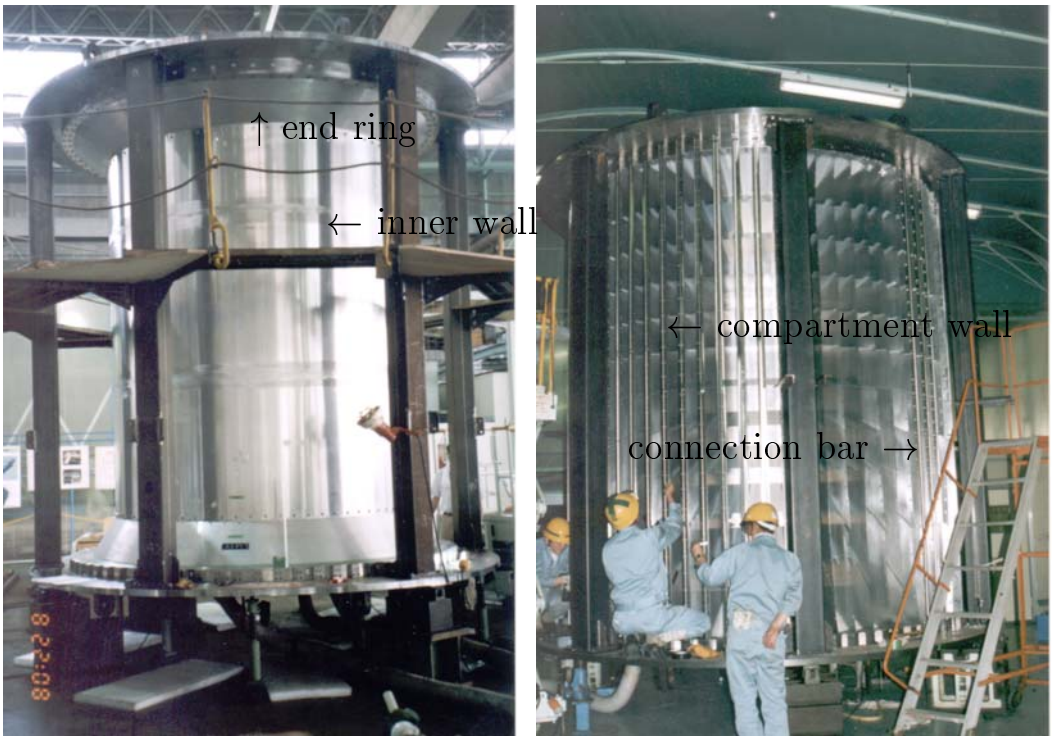

Figure 4.20: Mechanical structure for holding the CsI(Tℓ) counters. (Left) Before and (Right) after attaching the compartment wall to the inner wall.

and observing the LED test signal at the same time. The result is shown in Fig. 4.19. The observed temperature dependence is mostly coming from the variation of the LED output and no indication of broken joint is observed.

Four tapped holes are made on the bottom surface of the crystal by a robotic drilling machine. Small derlin pieces are screwed into the tapped hole and a sheet of 500 μm thick porous teflon was placed over the bottom surface for better hermeticity of the scintillation light. Then an aluminum base plate is fixed to the derlin piece via tapped holes made at the center of the derlin piece. A preamplifier is attached to each photodiode with a short lead. An aluminum shielding case is placed over the preamplifier and is fixed to the aluminum base plate with four screws. The electrical ground of the preamplifier is connected to the case. Together with the aluminum wrapping sheet, it formed a complete shielding cage against external noise pickups.

4.7 Mechanical Structure

Fig. 4.20 shows a photograph of the barrel crystal container. The container needs to fix each counter at the correct position and support a weight of 6624 counters ($\sim$ 35

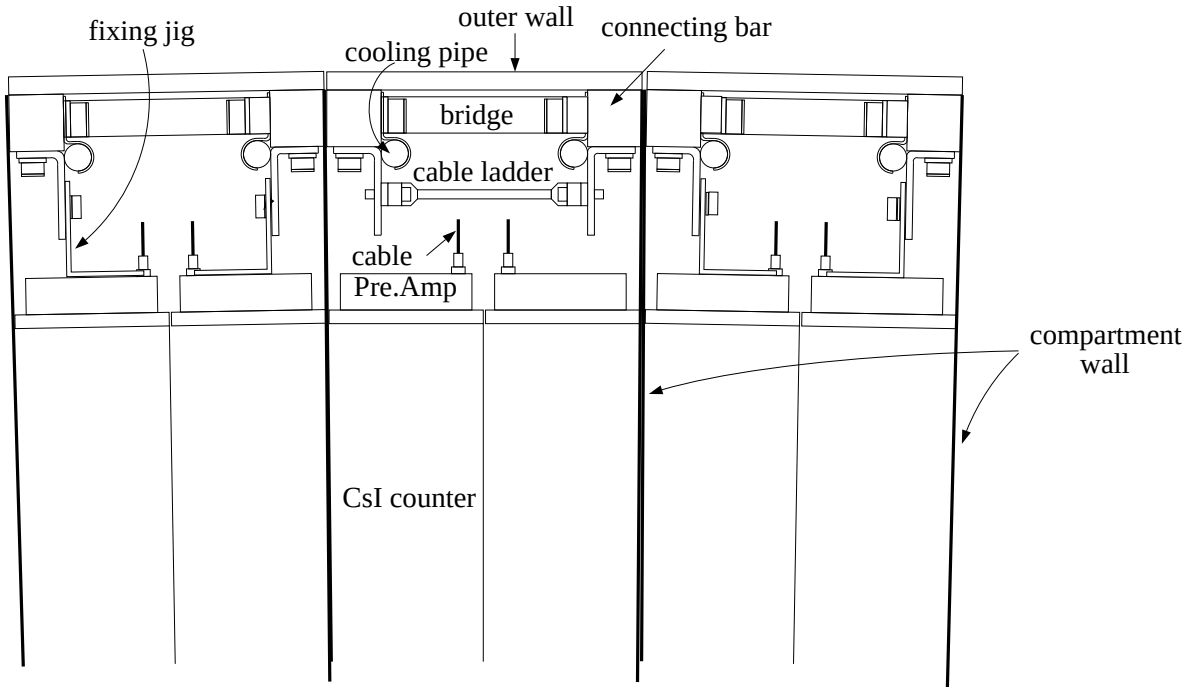

Figure 4.21: Illustration of installed counters in the compartment.

ton). Two end rings are connected with 144 connecting bars. An outer wall and a bridge is fixed between two bars. These parts are made by stainless steel and form a rigid cylindrical structure to support the weight of crystals. The CsI(Tℓ) counters are installed in a compartment structure made by the 0.5 mm thick aluminum wall. One end of the wall is fixed to the connecting bar and the other end is screwed to an inner cylinder made by 1.5 mm thick aluminum. The material and the thickness was chosen to minimize the photon conversion. The whole container is divided into 72 (in ϕ) times 11 (in θ) compartments. One compartment contains 8 $\sim$ 10 counters (4 $\sim$ 5 in θ direction and 2 for ϕ direction). A mylar sheet of 100 μm thick is inserted between the compartment wall and the counter for the electrical isolation of the counter from the container. A set of spacers in a triangular shape is laid at the bottom of the compartment to support the crystal weight uniformly by the inner wall. It is made by the acrylic foam of density 0.1 g/cm^3.

Each counter in the compartment is fixed to the connecting bar by a jig as shown in Fig. 4.21. This fixing jig is made by Cu-Be and allowed a shift of the counter position within a few mm. This was necessary for the safety of the counters when the container was rotated during the installation of the counters. A copper cooling pipe is attached to the connecting bar to remove the heat from the preamplifier through the fixing jig. Purified water of 20 °C will be used for the cooling. Dry air of humidity less than 5 %

(a) (b)

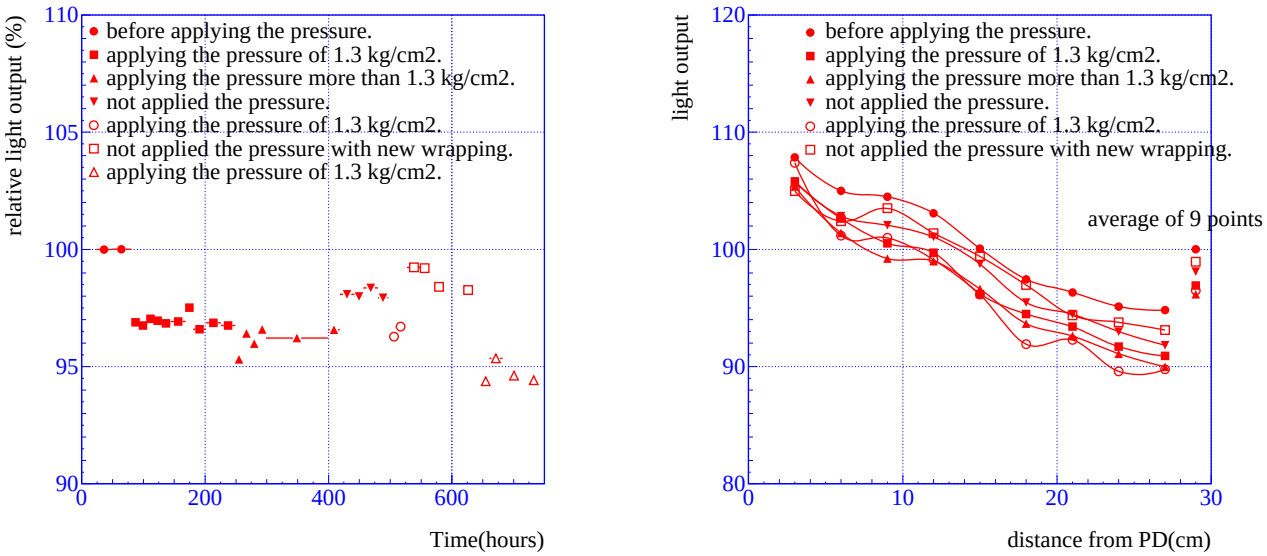

Figure 4.22: (a) Change of light output with pressure applied on the crystal surface. (b) Uniformity of light output with pressure.

will be flushed into the compartment as well.

The weight of the individual crystal in the compartment is not entirely supported by the inner and outer walls. Since the wall thickness of the compartment is only 0.5 mm, a part of the weight is transmitted to the crystals below. This may be applied to the crystal surface at the bottom of the container. It is therefore needed to check whether the light output changes or not under the pressure. The pressure of 1.3 kg/cm^2 which corresponds to the weight of 40 crystals was applied to two opposing faces of one counter. We monitored the light output of this counter for one month by changing the conditions. The measurement was done using the cosmic ray stand described in section 5.2. The results are shown in Fig. 4.22. Under the pressure, the light output decreased by $\sim$ 3 % and didn't recover even after removing the pressure. The light output recovered after re-wrapping by the new teflon sheet. The position dependence did not change by the pressure. The light output of the counters may decrease by $\leq$ 3 % by installing them to the container but that value will stay constant and can be corrected by the calibration.

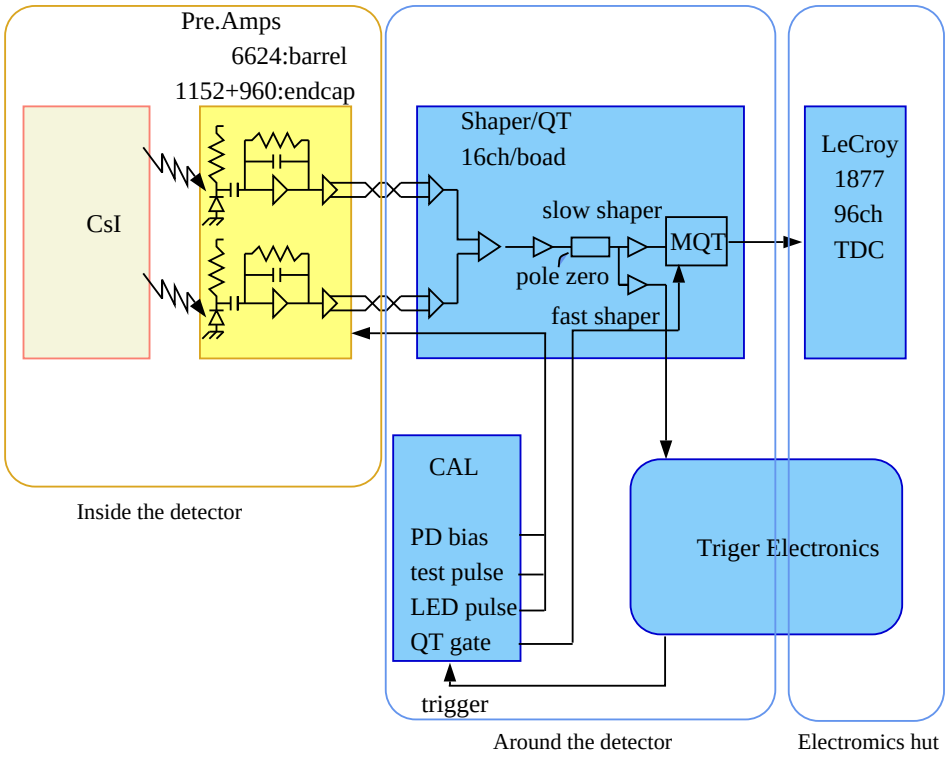

Figure 4.23: Block diagram of the CsI(Tℓ) readout electronics.

4.8 Readout Electronics

4.8.1 Overall Design

Each CsI(Tℓ) counter is read out by a pair of silicon PIN photodiodes and charge sensitive preamplifiers. The preamplifier output is transmitted on a $\sim$13 m long, 50 Ω twisted pair cable to the shaper/QT module placed near the detector. In the shaper/QT module two signals are summed up and then split into two streams; one is for the main data acquisition and the other is for the trigger. The signal for the main data acquisition is shaped with $\tau = 1$ μs time constant and fed into a charge-to-time (QT) conversion chip. After the conversion the time signal is sent to the TDC in the electronics hut for digitization. The trigger signal is shaped with a shorter time constant of about $\tau = 200$ ns and sent to the trigger system.

The energy equivalent noise of the readout electronics is defined as ENC/N_e where ENC is the equivalent noise charge in the unit of number of electron-hole pairs and N_e is the number of electron-hole pairs created by 1 MeV energy deposit in the crystal. The CsI readout system with a photodiode, a charge-sensitive preamplifier and a shaper is shown in Fig. 4.24. The ENC for this system is estimated as follows [55];

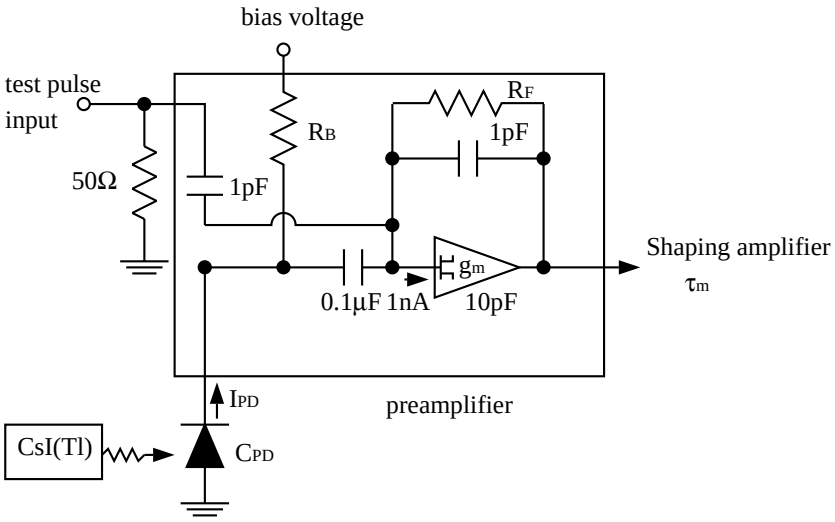

Figure 4.24: Schematics of the photodiode, preamplifier and shaper system.

$$ENC^2 \approx 4kT\frac{0.7}{g_m}\frac{C_{PD}^2}{\tau_m} + \frac{1}{3}(2eI_{PD} + 4kT(R_F^{-1} + R_B^{-1}))\tau_m \quad (4.8)$$

$$\approx \frac{3.9\times10^{-1}C_{PD}^2}{\tau_m g_m} + 1.2\times10^4\tau_m I_{PD} + 6.0\times10^5(R_F^{-1} + R_B^{-1})\tau_m, \quad (4.9)$$

with the following parameters:

- electron charge (absolute value) e.
- Boltzmann constant k.
- temperature T of the system in unit of °K.
- peaking time τ_m in unit of μs where the shaping function $(\tau/\tau_m)\exp(1\text{-}\tau/\tau_m)$ is assumed.
- transconductance g_m of the JFET used in the preamplifier in unit of S.
- junction capacitance of the photodiode C_{PD} in pF.
- leakage current of the photodiode I_{PD} in nA.
- feedback resistance R_F of the preamplifier in MΩ.
- bias resistance R_B for the photodiode in MΩ.

The three components in (4.9) are the thermal noise of the voltage generator, the shot noise and the thermal noise of the current generator. Typical values of parameter are T = 300 °K, $\tau_m = 2\mu$s, $g_m = 25$ mS, $C_{PD} = 100$ pF, $I_{PD} = 4$ nA and $R_F \approx R_B = 200\text{M}\Omega$. The ENC calculated by using the above parameters is 412 electron-hole pairs. The contribution of the first term and the second term are approximately equal and the 3rd term is negligible.

4.8.2 Photodiode

The following relations are important for the choice of the photodiode [54].

- N_e is proportional to the sensitive area S when S is small compared to the total crystal surface.
- The junction capacitance of the photodiode C_{PD} is proportional to S/d for fully depleted photodiode where d is a wafer thickness.
- The leakage current is proportional to $d \cdot S$.

If we chose a larger S, N_e increases linearly but C_{PD} and I_{PD} also increase. If the shot noise is dominant, the larger S may contribute to improve ENC/N_e through following relations;

$$\text{ENC by thermal noise ; } \sqrt{\frac{TC_{PD}^2}{\tau_m g_m}} \propto C_{PD} \propto S/d, \tag{4.10}$$

$$\text{ENC by shot noise ; } \sqrt{\tau_m I_{PD}} \propto \sqrt{Sd}. \tag{4.11}$$

On the other hand, a larger d causes better thermal noise and worse shot noise, and the total ENC would improve if the ENC by thermal noise is dominant. We tested several values of S and d of the photodiode but the noise level did not change so much.

Finally we chose two pieces of $S = 2$ cm^2 and $d = 300$ μm photodiode each equipped with an independent preamplifier. The system with two photodiodes gives us a good safety for the long term operation because the counter can be used even with only one photodiode if we tolerate the inner of ENC/N_e by a factor of $\sqrt{2}$. The two photodiode system also gives us better noise performance. The ENC can be written as

$$ENC^2 = x_c + x_i, \tag{4.12}$$

Sensitive Area	10×20 mm	
Thickness of Wafer	300 μm	
Supplied Reverse Voltage	$\leq$ 70 V	
Capacitance	average $\leq$85pF max $\leq$105pF	
Sensitivity(λ=560nm)	average $\geq$320mA/W min $\geq$310mA/W	
temperature dependence	$\leq$0.01%	
Dark current	average $\leq$4nA max $\leq$15nA	
temperature dependence	average $\leq$10%/°C	
Radiation Hardness	at 6 Gy	at 68 Gy
change of dark current	$\leq$8%	$\leq$40%
change of capacitance	$\leq$0.4%	$\leq$1%
change of sensitivity	$\leq$0.3%	$\leq$0.3%

Table 4.4: Specifications of photodiode.

where x_c is the component from the thermal noise of the voltage generator and x_i is from the shot noise. The total ENC of the two photodiode and two amplifier system is

$$ENC^2 = 2(x_c + x_i) = 2x_c + 2x_i, \tag{4.13}$$

The ENC of one photodiode with twice larger S would be

$$ENC^2 = 4x_c + 2x_i, \tag{4.14}$$

For a given total area of S, it is more advantageous to split the S and equip each photodiode with independent preamplifier.

The specification for the used silicon PIN photodiode (Hamamatsu S2744-08) is listed in Table. 4.8.2 [10]. The thickness of the photodiode is 300 μm and the photo-sensitive area is 10 mm × 20 mm. A reverse bias of 60 V will be supplied. The dark current (I_d) and the capacitance (C_j) of 14000 pieces delivered were checked at 25 ± 1°C. The measurement was done comparing with the standard capacitor of 97.9 pF to monitor the drift of the offset. The small offset value correction was applied. The average values of the measurement are

$$I_d = 3.31 \pm 0.92 \text{ [nA]},$$
$$C_j = 82.8 \pm 0.7 \text{ [pF]},$$

and the results well satisfy the specification [56].

4.8.3 Preamplifier

Each of the photodiode signal is sent to a charge sensitive preamplifier and integrated independently.

The circuit of the preamplifier is designed to keep ENC below 700 electron-hole pairs for a detector capacitance of 100 pF[57]. The integral nonlinearity of the preamplifier was less than 0.15 % for the maximum output voltage of 5 V.

Fig. 4.25 shows the photograph of the preamplifier parts. It is connected to the photodiode with a short lead and is put in an aluminum shielding case to suppress the pickup noise. A heat conductive rubber sheet is placed between the case and the mother-board to remove the heat without having an electrical contact.

A light emission diode (LED : CL-140YG) is put on the preamplifier mother-board to monitor the calorimeter performance. The wave length of this LED is 570 nm and is similar with the peak emission length of CsI(Tℓ) (565 nm).

All preamplifiers were tested using the test pulse, ^{241}Am source and LED. The schematic view of the setup is shown in Fig. 4.26. The reference photodiodes were used for all the tests. As shown in the figure, two output signals can be checked independently. The feedback capacitance (C_f) was obtained from the peak position of X-ray 60 keV from ^{241}Am using the following relation;

$$C_f = N_{Am}e/V_{Am}, \tag{4.15}$$

where e is 1.6×10^{-19} [c], and N_{Am} and V_{Am} are the number of electron-hole pairs generated by the 60 keV photon and the corresponding output voltage of the preamplifier. The N_{Am} is obtained by

$$N_{Am} = 60\text{keV}/3.62\text{eV} = 16.6 \times 10^3 \tag{4.16}$$

since 3.62 eV is needed to create an electron-hole pair. The test pulse capacitance was also calculated from the result. Fig. 4.27 shows the results of the preamplifier performance test for 7000 pieces. Table 4.5 shows the calculated results from the measurement [58].

4.8.4 Shaper/QT

Two preamplifier outputs from each crystal are summed in a shaper/QT module located near the BELLE detector. The summed signal is shaped with two different shaping times after passing through a pole-zero cancellation circuit. The fast output goes to

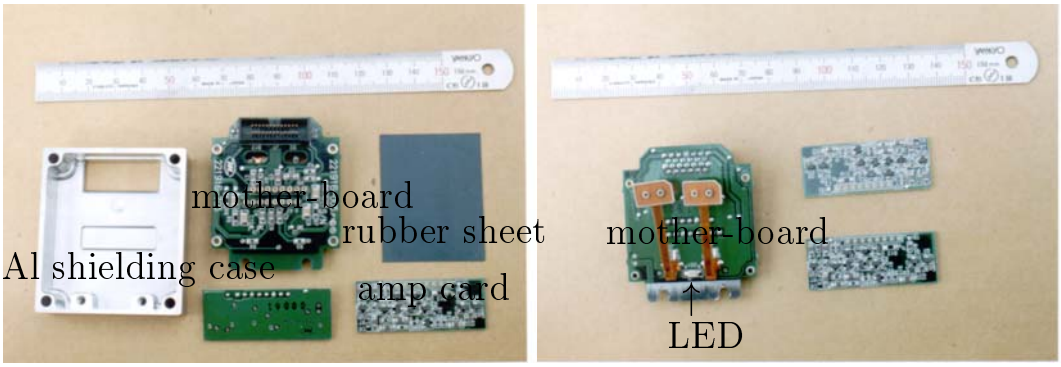

Figure 4.25: Each parts of the preamplifier.

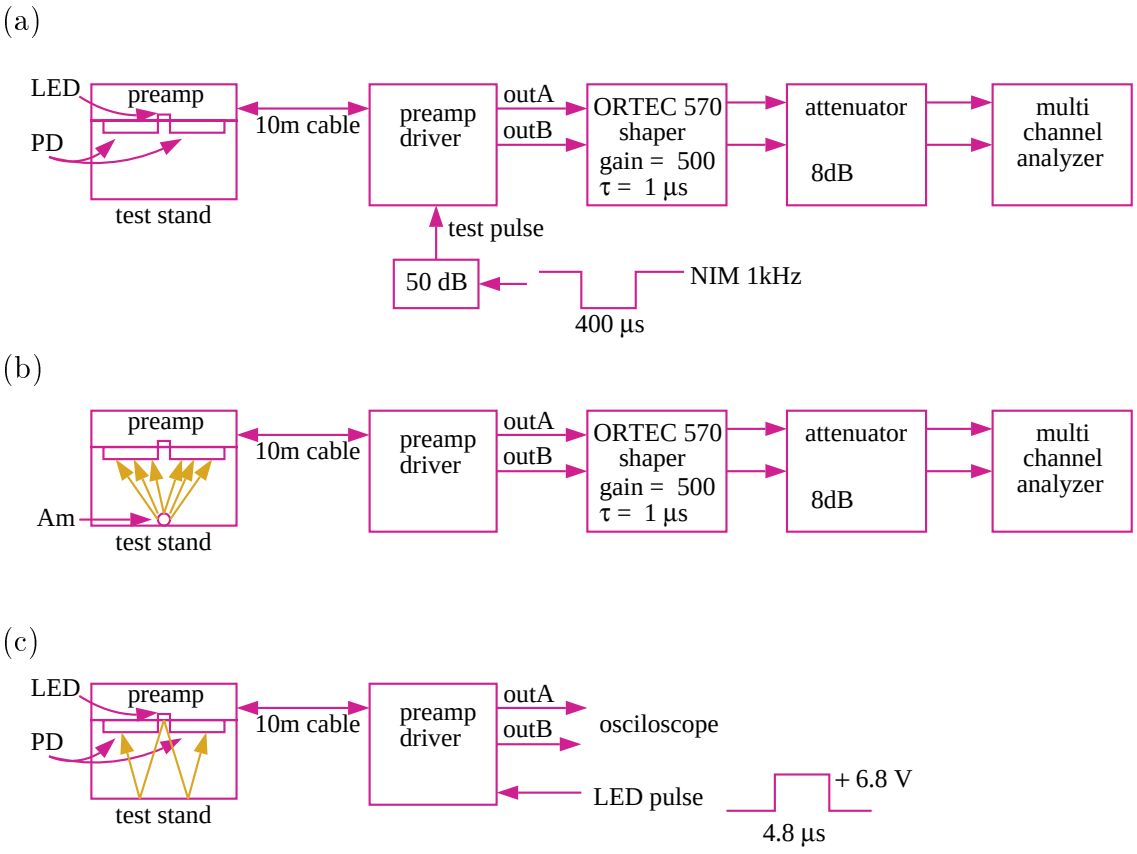

Figure 4.26: Preamplifier test setup for (a) test pulse (b) ^{241}Am source and (c) LED.

	average	maximum	minimum	
Feedback capacitance	1.28 ± 0.02	1.39	1.21	(pF)
Test pulse capacitance	1.94 ± 0.03	2.06	1.85	(pF)
ENC with one photodiode (τ=1μs)	690 ± 18	740		(electrons)
standard deviation of LED	7			(%)
preamplifier saturation voltage	5.01 ± 0.05	5.4	4.8	(V)

Table 4.5: Results of the preamplifier performance measurements.

the trigger system and the slow output is sent to a charge to time converter chip (MQT300A).

The MQT chip splits the input signal into three ranges, low/middle/high, approximately with the ratio of 1/8/64 [59]. After integrating the input charges of each range for the duration of externally supplied gate (100 ns), the signal is converted to the timing signal with the resolution of 12 bits as shown in Fig. 4.28. The timing signal of each range is shifted by $\sim$ 100 ns and overlaid into one signal line together with the time reference signal. By using this three-range method, the signal can be measured in 18-bit dynamic range. The output of MQT is an ECL differential signal and transmitted over 30 m to the TDC in the electronics hut by the twisted pair cable. The preamplifier power is also supplied by the same cable. There are 16 channels in one TKO* shaper/QT module.

4.8.5 Time to Digital Converter (TDC)

We used a 16-bit FASTBUS multi-hit TDC (LRS1877S) for the digitization of the MQT output signal. The module contains MTD133B chips which record the timing of MQT output with 0.5 ns resolution[60].

Two examples of the MQT output signal are illustrated in Fig. 4.29; one corresponding to the pedestal and the other corresponding to the small signal. It has 4 edges and each represents the reference timing, H, M, and L range output of the MQT. A timeout signal is also supplied to the TDC to set a full scale of the TDC. Its timing is set at about 7 μs after the MQT reference edge. It is slightly shorter than the MQT timeout of 8 μs and is well within the MTD133B full scale of 32 μs. The MTD133B

*KEK standard for modular electronics.

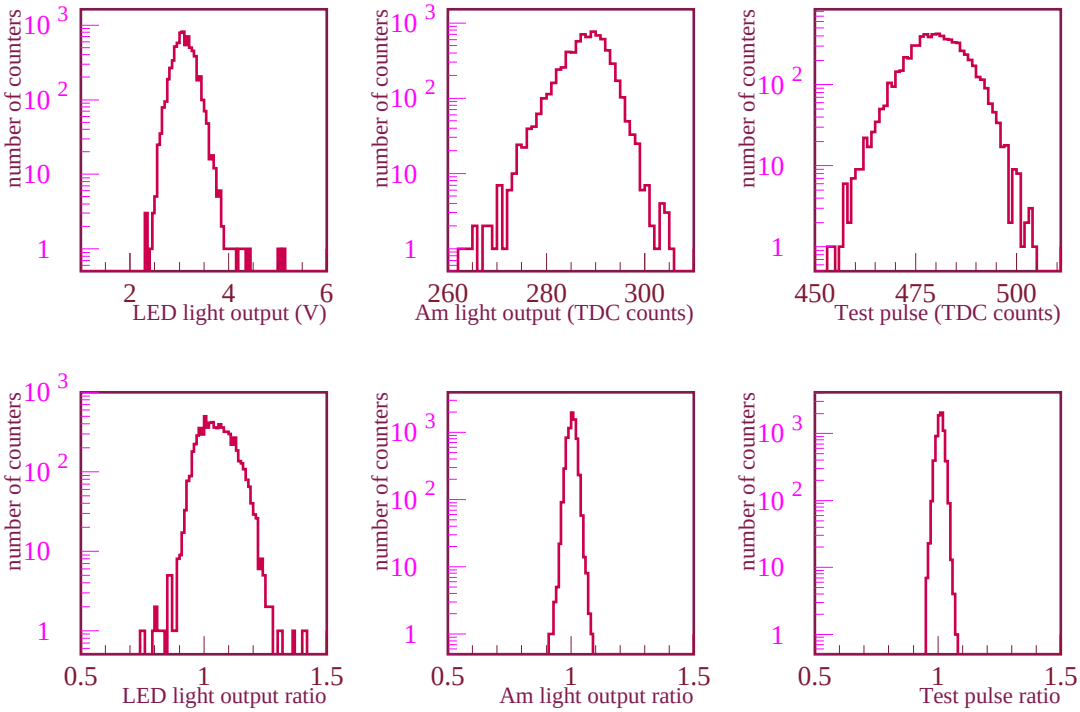

Figure 4.27: Results of the preamplifier test.

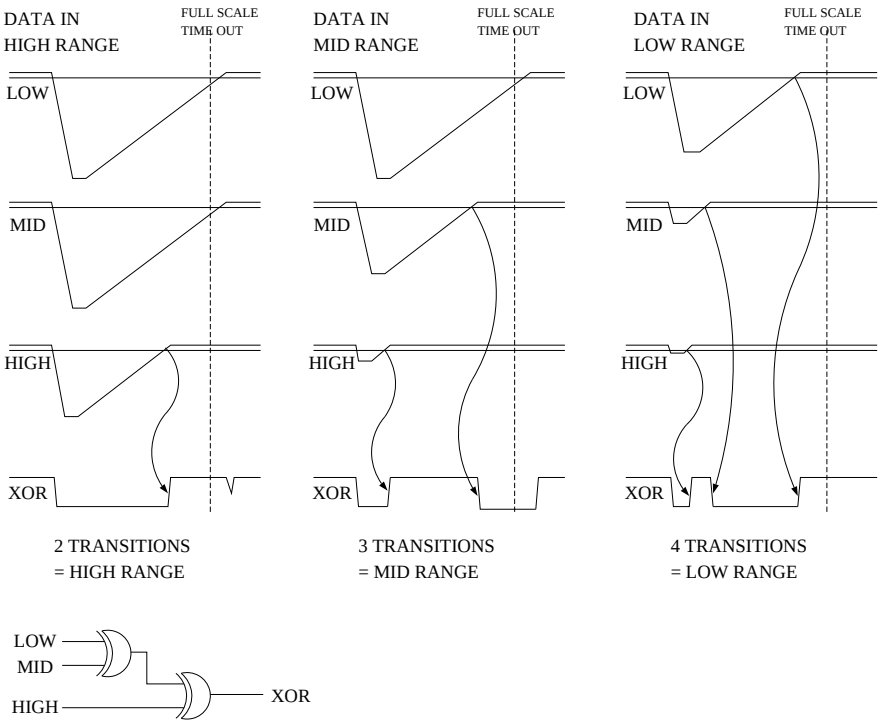

Figure 4.28: Operation of the three range of MQT300.

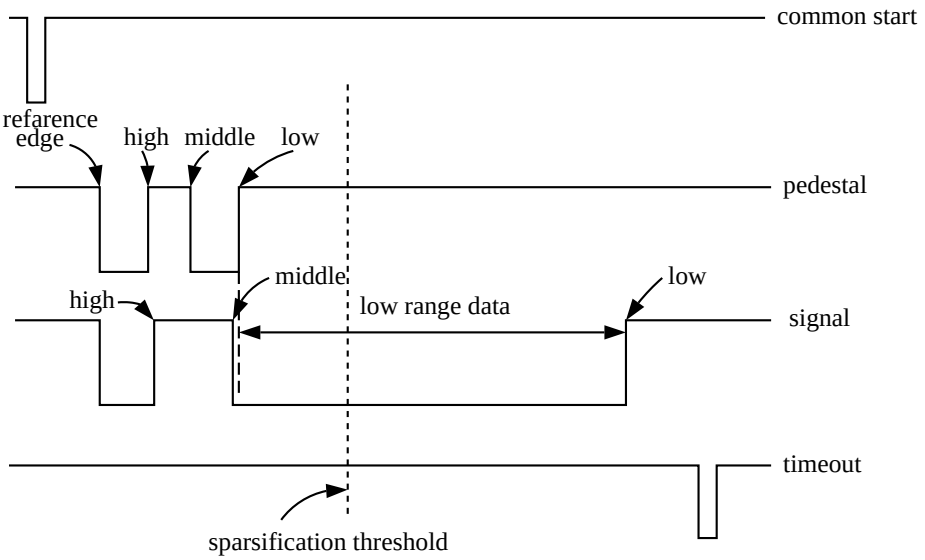

Figure 4.29: Signals supplied to the TDC. Two examples are given for MQT300 output to TDC; one for the pedestal and the other for the small pulse height.

chip can be programmed such that only one nearest edge before the timeout to be recorded and all other edges to be discarded. It also keeps a record of how many edges are received before the timeout. In this way, we obtain only one edge timing in the most appropriate range together with the information which range this timing belongs to. This is the mechanism of auto range selection.

The output of MTD133B goes through a digital comparator and it is compared with the pedestal value stored in the memory. The data is read out by FASTBUS only when it is significantly larger than the pedestal value. This sparcification mechanism saves a data taking time and reduces the amount of data to be recorded.

The energy region covered by each range of the MQT depends on the light output of the CsI(Tℓ) crystal. The low and middle ranges are used from 0 to 850 MeV and 850 MeV to 6.7 GeV approximately. The high range is used above 6.5 GeV.

The TDC contains 96 channels in one module and 107 TDC modules occupy six FASTBUS crates in the electronics hut.

4.8.6 Calibration Module

A calibration modules (CAL) is used to supply the photodiode bias voltage, the test pulse, the LED pulse and the gate for MQT. Each TKO crate contains 12 shaper/QT modules and one CAL module. The test signals are transmitted from CAL to shaper/QT

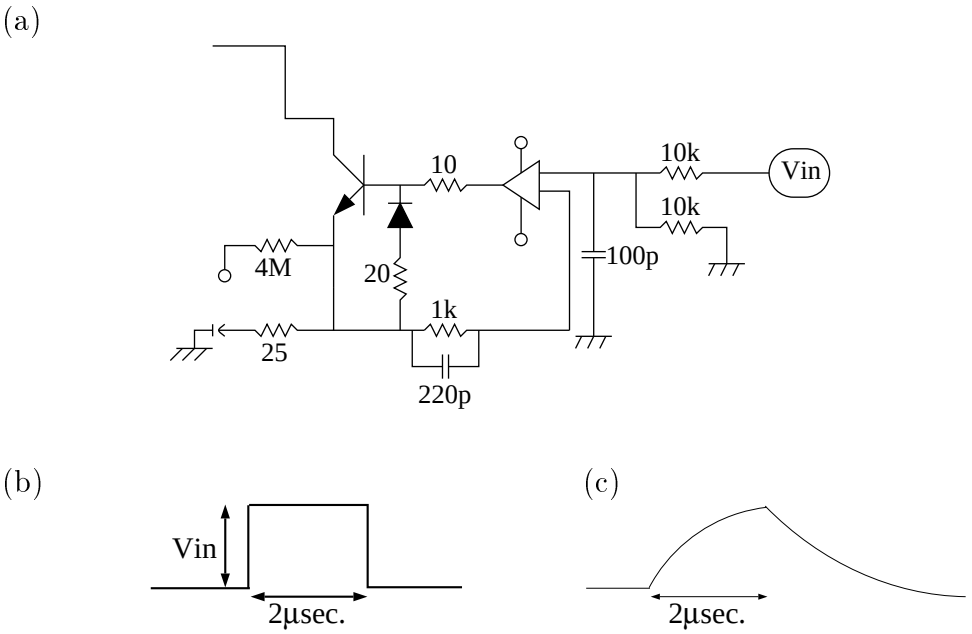

Figure 4.30: (a)LED driving circuit in shaper/QT module, (b)the signal to trigger the driver and (c)the signal supplied to LED.

by the daisy chain on the front panel. The test pulse is generated in the CAL module by 16-bit DAC in the range between -5 V $\sim +1$ V. The shape of test pulse is shown in Fig. 4.32. The rise time is set about 1 μs to reproduce the shape of preamplifier output for the scintillation light from the CsI(Tℓ) crystal.

The LED signal is 2 μs wide and the pulse height ranges from 0 to 4 V. The signal shape is shown in Fig. 4.30 with the circuit configuration. The LED linearity is shown in Fig. 4.31. The maximum output voltage is 4 V and it roughly corresponds to a 30 GeV energy deposit in the crystal. The output is somewhat non-linear in the low energy region, but it has enough linearity to be used in the high energy region. The stability of LED is $\pm$ 0.4 % at 22.5 $\pm$ 0.1 degrees [61].

A 100 ns wide gate signal for MQT is generated in a programmable gate generator and distributed to the shaper/QT module through the CAL module.

4.8.7 Trigger

Fig. 4.33 shows the schematics of the calorimeter trigger. The calorimeter trigger consists of two methods. One is by counting the number of isolated clusters (ICN) and the other is by measuring the total energy (E_{tot}). Two triggers are redundant and they are designed to select $B\bar{B}$ events with high efficiency. The fast shaping output from the

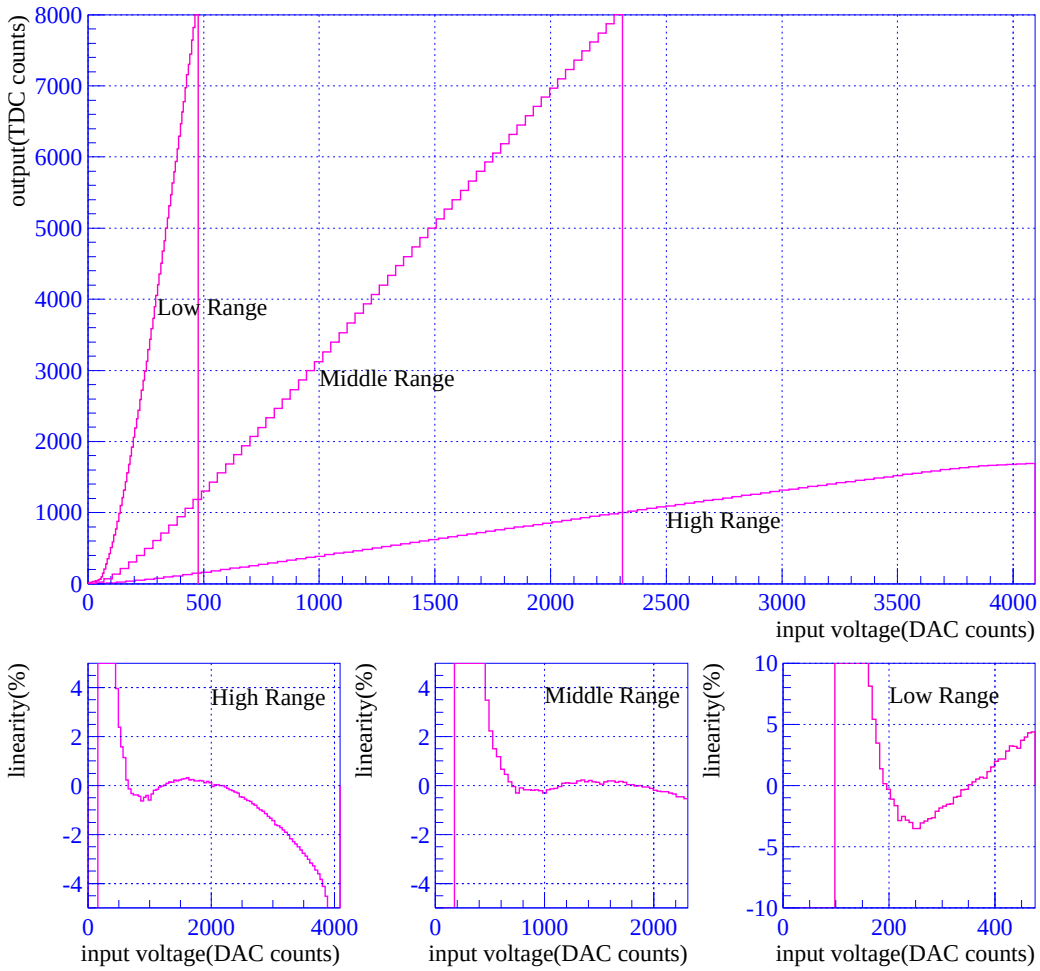

Figure 4.31: LED light output and the linearity for three ranges as a function of driving pulse height.

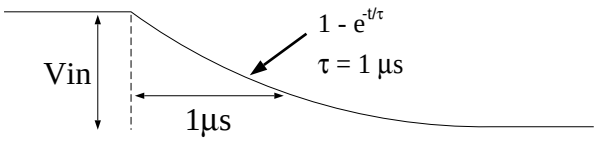

Figure 4.32: Shape of test pulse.

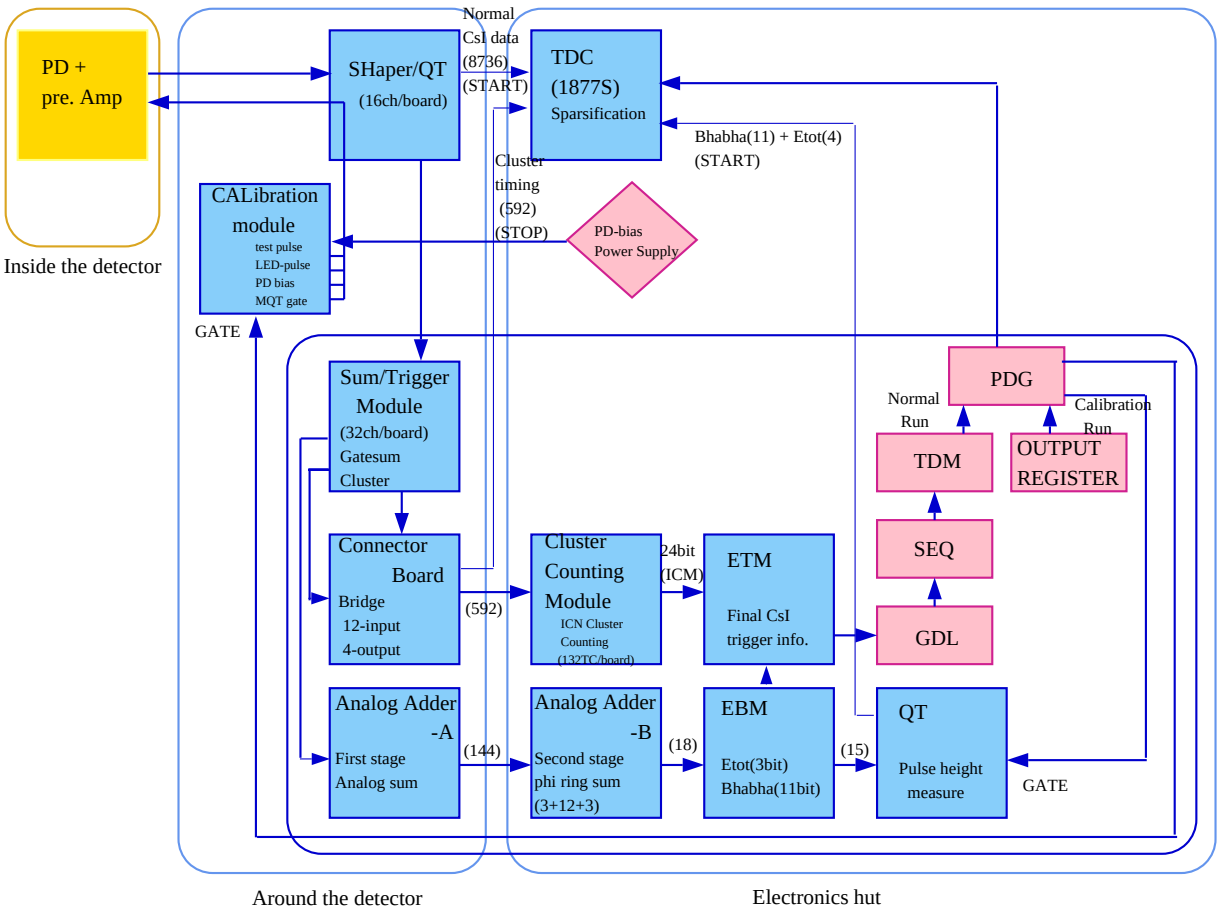

Figure 4.33: Block diagram of the CsI(Tℓ) trigger system.

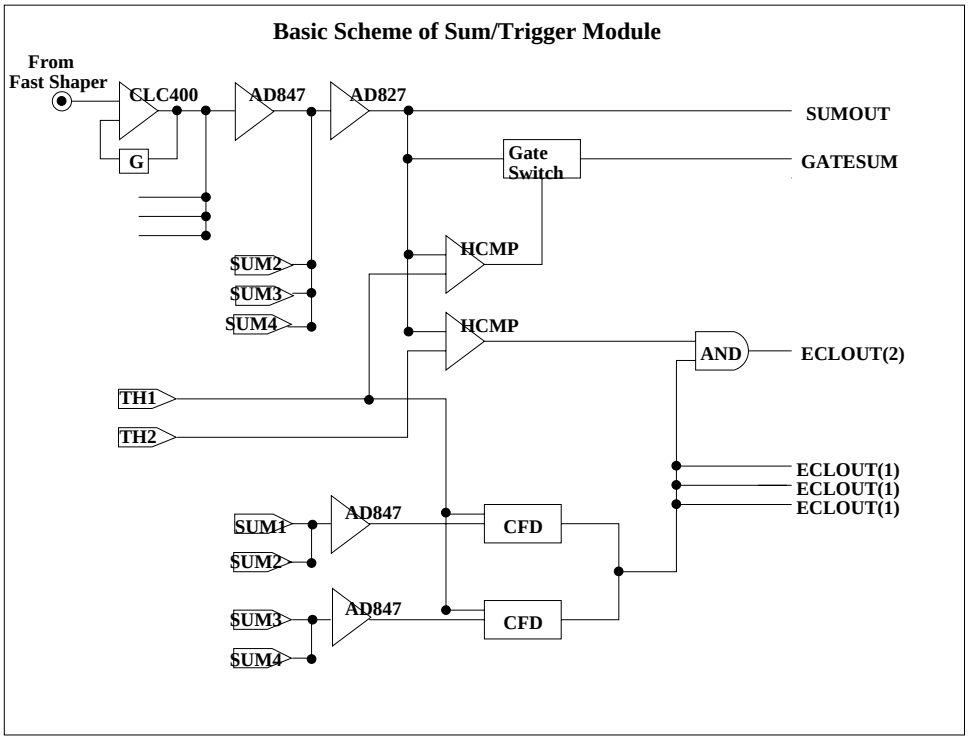

Figure 4.34: Schematic diagram of STM module.

shaper/QT module is sent to a sum/trigger module (STM) where an analog sum of 4 × 4 crystals and its discriminated logic signal are generated. The schematics of the STM module is shown in Fig. 4.34. A constant fraction discriminator is used to reduce the time jitter of the logic output. Approximately 20 ns resolution is obtained for energies above 100 MeV. The discriminated output is also used to gate the analog sum. This will exclude many analog sum channels below threshold from the subsequent summation and reduce the total noise level. The noise of the fast shaping signal is about 1.3 MeV for one counter. The threshold for the analog sum may be set around 50 MeV.

The gated analog sum signals are added in cascade by analog-adder-A and analog-adder-B modules to get E_{tot}. The E_{tot} is discriminated and generates a total energy trigger. Bhabha events will satisfy the E_{tot} trigger condition and its trigger rate will be too high. We will separate the Bhabha events and remove most of them from the trigger. Partial analog sums in θ are produced (see Fig. 4.35) for this purpose. All the analog sums with the same θ but different ϕ are added together. A back to back condition of the Bhabha event in cms is translated to 11 combinations of the partial analog sum as given in Table 4.6.

The logic signal is sent to a cluster counting module (CCM) and the number of

cut number	CUTS		
cut 1	($\sum$F1+$\sum$F2+$\sum$B1+$\sum$B2)	$>$ 9.0GeV	
cut 2	($\sum$F2+$\sum$F3+$\sum$B1+$\sum$B2+$\sum$C11)	$>$ 9.0GeV	
cut 3	($\sum$F2)	$>$ 6.5GeV	backward gap
cut 4	($\sum$F3+$\sum$C11+$\sum$C10)	$>$ 9.0GeV	
cut 5	($\sum$C1+$\sum$C9+$\sum$C10)	$>$ 9.0GeV	
cut 6	($\sum$C1+$\sum$C2+$\sum$C9)	$>$ 9.0GeV	
cut 7	($\sum$C2+$\sum$C8+$\sum$C9)	$>$ 9.0GeV	
cut 8	($\sum$C3+$\sum$C7+$\sum$C8)	$>$ 9.0GeV	
cut 9	($\sum$C4+$\sum$C6+$\sum$C7)	$>$ 9.0GeV	
cut 10	($\sum$C5+$\sum$C6)	$>$ 9.0GeV	
cut 11	($\sum$C10)	$>$ 3.5GeV	forward gap

Table 4.6: Conditions to trigger Bhabha events. The numbers are (2+11+3)-fold ϕ-ring sums depending on θ direction.

isolated clusters is counted. The condition on ICN only will produce a high trigger rate for the cosmic rays. Following additional condition is given to the ICN to veto the cosmic-rays;

$$(ICN_A \geq 1 \otimes ICN_D \geq 1) \oplus (ICN_B \geq 1 \otimes ICN_C \geq 1), \tag{4.17}$$

where ICN_i is the number of isolated clusters in the i-th region. The definition of the region is shown in Fig. 4.36.

Two kinds of triggers then go to ECL trigger master (ETM) module to generate a CsI trigger, which is transferred to the BELLE trigger system. The condition for the physics trigger will require;

$$(E_{tot} > 1GeV) \oplus (ICN > 3). \tag{4.18}$$

The trigger efficiency for the generic $B\bar{B}$ event was simulated by the Monte Carlo[62]. The condition $E_{tot} \geq 1$ GeV gives $\sim$ 99 % efficiency and ICN ≥ 3 gives $\sim$ 99.5 % efficiency. The trigger efficiency will be significantly higher for the OR ($\oplus$) of two conditions.

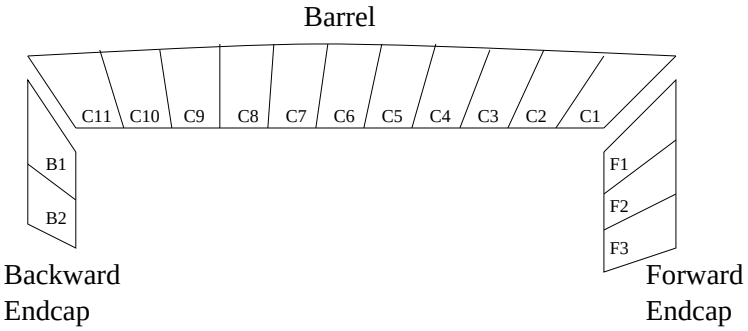

Figure 4.35: Calorimeter division for Bhabha event selection.

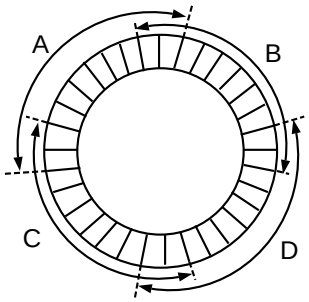

Figure 4.36: Segmentation for cosmic ray veto.

Chapter 5

Energy Calibration of CsI(Tℓ) Counters

5.1 Introduction

Although CsI(Tℓ) calorimeter has an excellent intrinsic energy resolution as will be discussed later, the crystals have variation of the light output. Therefore we need to know the response of each counter for a fixed amount of energy deposit in order to convert a signal from the CsI(Tℓ) to an energy measured in that counter. This is called a calibration and is important to get a good energy resolution from the whole system of the electromagnetic calorimeter.

We calibrated all produced counters by cosmic ray muon before installing the counter into the container. This served as a final test of the counter before installation, and gave us a pre-calibration of light output to be used at the beginning of the experiment.

In the BELLE experiment, the CsI(Tℓ) counters will be calibrated by the electrons from the Bhabha scattering. We expect it will replace the cosmic-ray calibration and become the final and the most reliable calibration *in situ*.

The uniform light output from the CsI(Tℓ) crystal is important to the linearity of energy response. The good linearity is important for BELLE because the calibration obtained by Bhabha scattering at high energy must be used in much lower energy region where most of the gamma rays from B meson decay exist.

The uniformity of the light output along the crystal, which can not be measured by the Bhabha scattering, is also measured by the cosmic rays.

5.2 Setup

The layout of the cosmic ray stand which is used for the calibration is shown in Fig. 5.1. It consists of two sets of scintillation counters for triggering, an aluminum container box on the moving table to hold the crystals during the calibration, 8 layers of drift chambers for tracking cosmic ray and a layer of 5 cm thick lead for absorbing soft component of the cosmic ray. Twenty CsI(Tℓ) counters are placed horizontally at the predefined positions in the aluminum box and the box is inserted between the drift chambers for the measurement.

Each drift chamber has a sensitive area of 1.2 $\times$ 1.2 m^2 and consists of 12 drift cells with the cross section of 5 cm $\times$ 10 cm and the length of 1.2 m. It is made of 3 mm thick extruded aluminum. A Copper-Beryllium anode wire of 100 μm diameter was strung at the center of the cell. Two sets of four layer drift chambers sandwiched the aluminum container box with a configuration of X-X-Y-Y and Y-Y-X-X for the optimum tracking. The X and Y direction is defined in Fig. 5.1.

The chamber was operated with PR gas (Ar 90% + CH_4 10%) flushed at the rate of 100 cc/min. The signal from the anode wire is amplified and discriminated and the drift time was measured by LRS2277 CAMAC TDC's. The position resolution of 1.2 mm is obtained, which is sufficient to track the cosmic ray muon through the CsI(Tℓ) crystal and determine the path length inside the crystal.

The signal from the preamplifier was shaped with 1 μs time constant and converted to a time signal by HOHSHIN-HE2550 shaper/QT module. The time was digitized by LRS2277.

A complete electronics channel from the shaper/QT to the TDC was calibrated for each channel by using a reference counter. The difference between channels were approximately 1.5% and was corrected in the subsequent analysis. The sensitivity and linearity were routinely checked by sending a test pulse to the preamplifier. A calibration module which was the prototype for the real experiment was used for the purpose.

The electronics noise was estimated by the width of the pedestal and the average value was 216 keV.

The cosmic ray event was triggered by the coincidence of upper and lower layer of the scintillation counters. The pulse height of CsI(Tℓ) counter and the timing information of the drift chamber were recorded by the Sun workstation[64]. The event with no hit in the CsI(Tℓ) counter was immediately discarded and the rest was used for the tracking. The vector of the muon was passed to the GEANT program and the

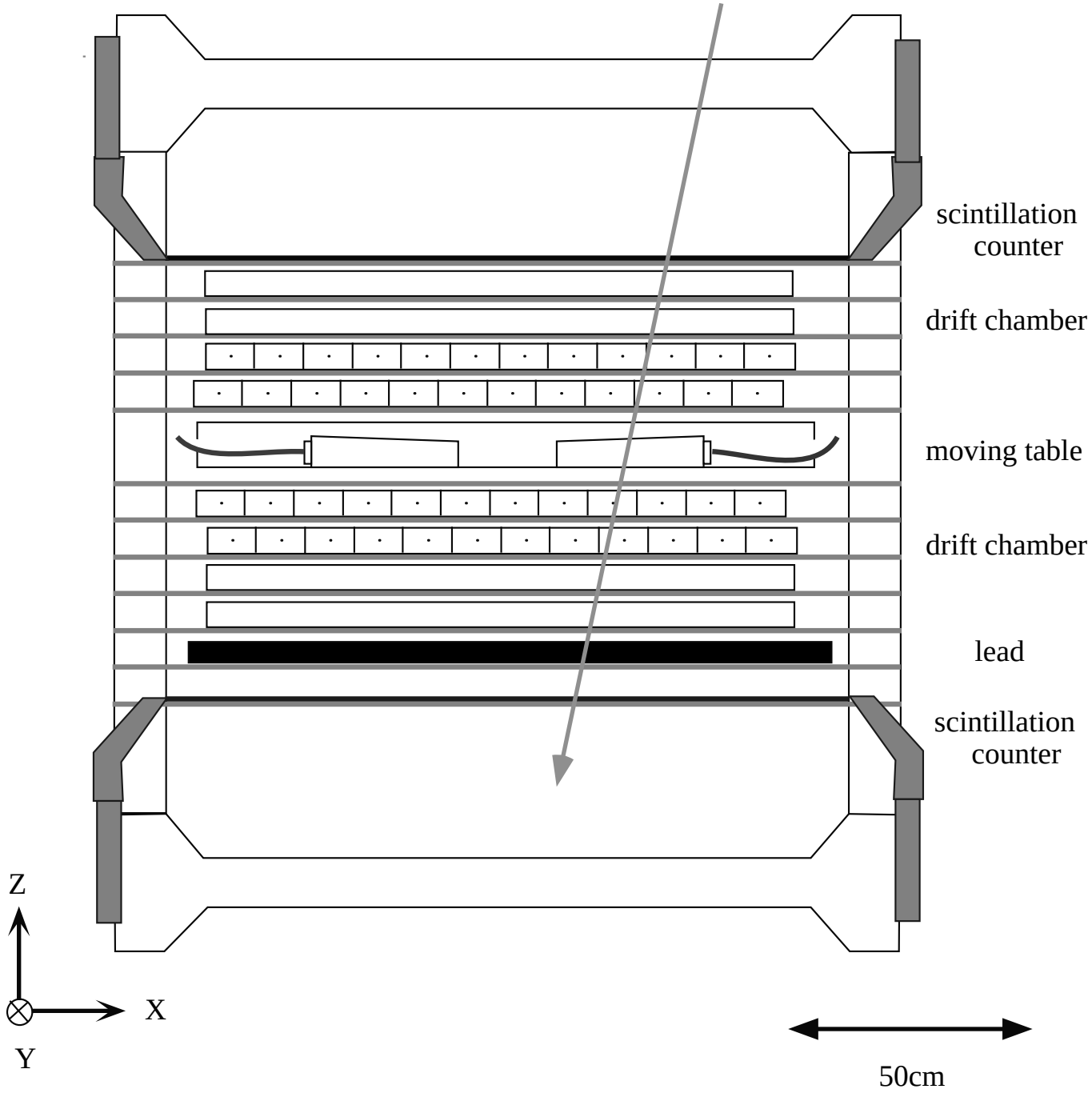

Figure 5.1: Cosmic ray stand.

path length in CsI was calculated on line using the GEANT tracking package. The value of pedestals are measured every 30 minutes and the most recent one was used for the analysis. The system covered a solid angle of 0.79 steradian at the center of the container box. The system was placed in an underground experimental hall and the trigger rate of the scintillation counter was 50 Hz, out of which about 5 % was useful for the calibration. The dead time for the data acquisition was approximately 75 %.

5.3 Analysis

In order to measure the uniformity of light output along the long axis of the crystal (z-axis), events were split into 9 subparts according to the z-value of impact point in the median plane (y=0) of the crystal. Each subparts has 3 cm wide acceptance in z. 1.5 cm at both ends of the crystal were not used (Fig. 5.2(a)). The cosmic ray which entered into the subpart with the polar angle more than 45 degrees or the one with less than 3 cm path length were excluded from the analysis. We plotted the pulse height of each subpart after correcting the difference of path length inside the crystal. An example of the pulse height normalized to the 1 cm path length is shown in Fig. 5.2(b).

The most probable channel (peak) of this distribution was obtained by fitting with the logarithmic Gaussian function $F(x)$ defined as follows;

$$F(x) = N \exp(-\frac{1}{2\sigma_0^2}\ ln^2(1 - \frac{x - x_p}{\sigma_E}\eta) - \frac{\sigma_0^2}{2}) \tag{5.1}$$

where x_p is peak value, η is asymmetry parameter, N is normalization factor and and σ_0 is $\frac{2}{\xi} sinh^{-1}(\frac{\eta\xi}{2})$. From this formula, the resolution of σ_E is calculated as the full width at half maximum (FWHM) divided by $\xi = 2\sqrt{ln4}$;

$$\sigma_E = \frac{FWHM}{\xi} \tag{5.2}$$

The number of cosmic rays used to determine the peak was about 500 events for each subpart. We estimate the error of light output in each subpart is approximately 2 % from the fluctuation among 9 subparts (see Fig 5.3). The statistical error is $\sim$ 0.5 %.

5.4 Energy Scale

The distribution obtained so far is in the unit of TDC counts/path length (counts/cm) in CsI. We will now scale it to a more general unit of N_{eh}/MeV, which is the number of

(a)

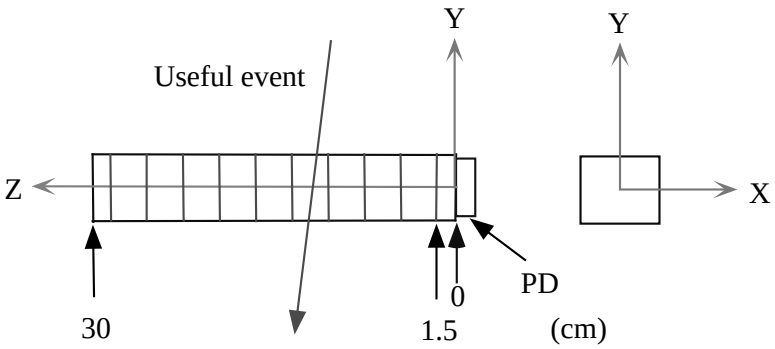

(b)

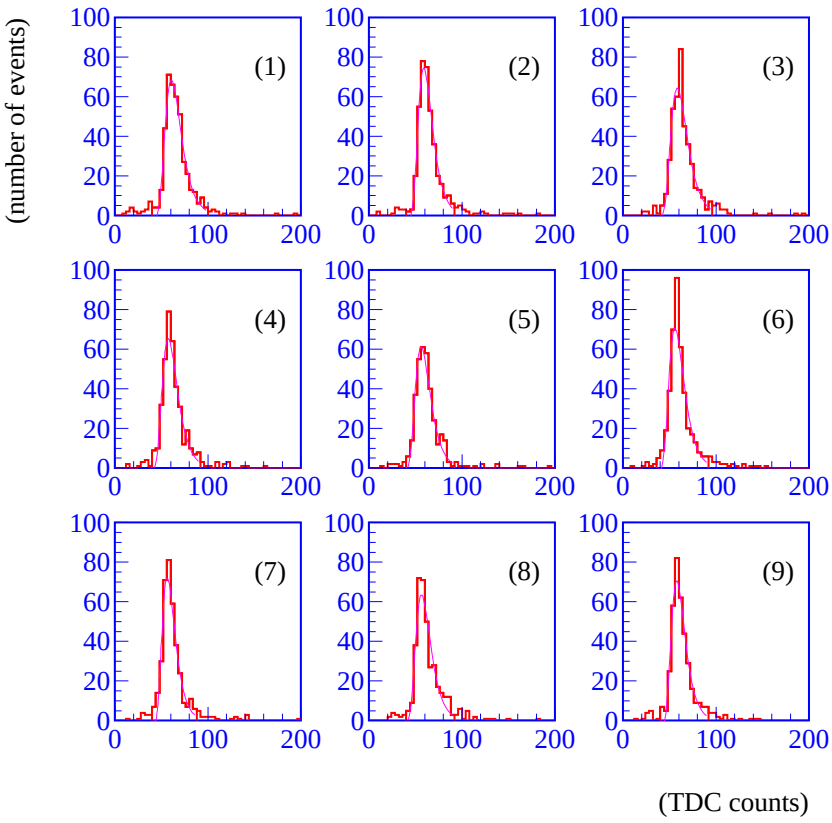

Figure 5.2: (a)Definition of CsI(Tℓ) crystal subparts and (b)the distribution of TDC counts/cm in 9 subparts.

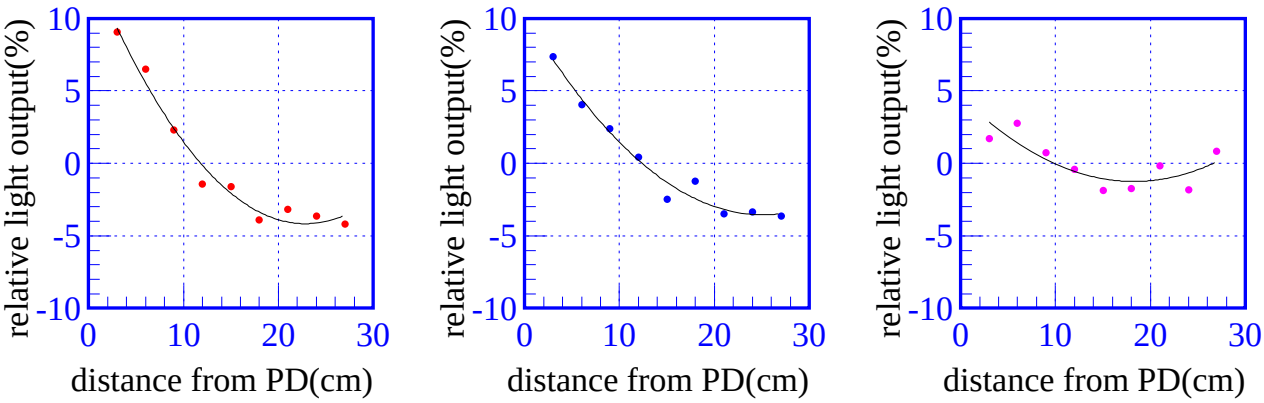

Figure 5.3: Examples of the uniformity of the light output for 9 subparts. The solid line is the fitting by the 3rd order polynomial.

electron-hole pairs detected in the photodiode for 1 MeV energy deposit in the crystal.

We first estimate an average energy deposited by the cosmic ray when cosmic muon passes through the CsI(Tℓ) crystal by using GEANT simulation. The energy loss of μ^- impinging perpendicularly to the 5.4 cm thick flat CsI plate was calculated at 22 energy points between 0.2 GeV and 1 TeV and its peak value was tabulated. Fig. 5.4(a) shows the results. The expected distribution of the energy loss by cosmic ray was calculated by weighting the tabulated energy loss by the measured momentum distribution of the cosmic ray [63] (see Fig. 5.4(b)). The result is 5.76 MeV for 1 cm path length in CsI.

We next find the relation between the TDC count and the number of photoelectrons. We detached the photodiode and preamplifier from the crystal and measured the TDC distribution of cosmic rays directly passing through the photodiode. The result is shown in Fig. 5.5(a). A corresponding GEANT simulation is shown in Fig. 5.5(b). The thickness of 300 μm is assumed for the photodiode and the effect of injection angle of the cosmic ray is included in the simulation. The peak of GEANT distribution is converted to electron-hole pairs as;

$$0.08363(\mathrm{MeV}) \div 3.6(\mathrm{eV}) = 23.23 \times 10^3(\text{electron hole pairs}) \tag{5.3}$$

where 3.6 eV is the necessary energy to create one electron-hole pair in Si photodiode. The conversion factor between the TDC counts and the electron-hole pairs is calculated from the above calculation and the peak value of the TDC distribution.

Another method is to use ^{241}Am radioactive source. We irradiated the photodiode directly by the 60 keV X-rays from ^{241}Am and recorded its pulse height. The mean

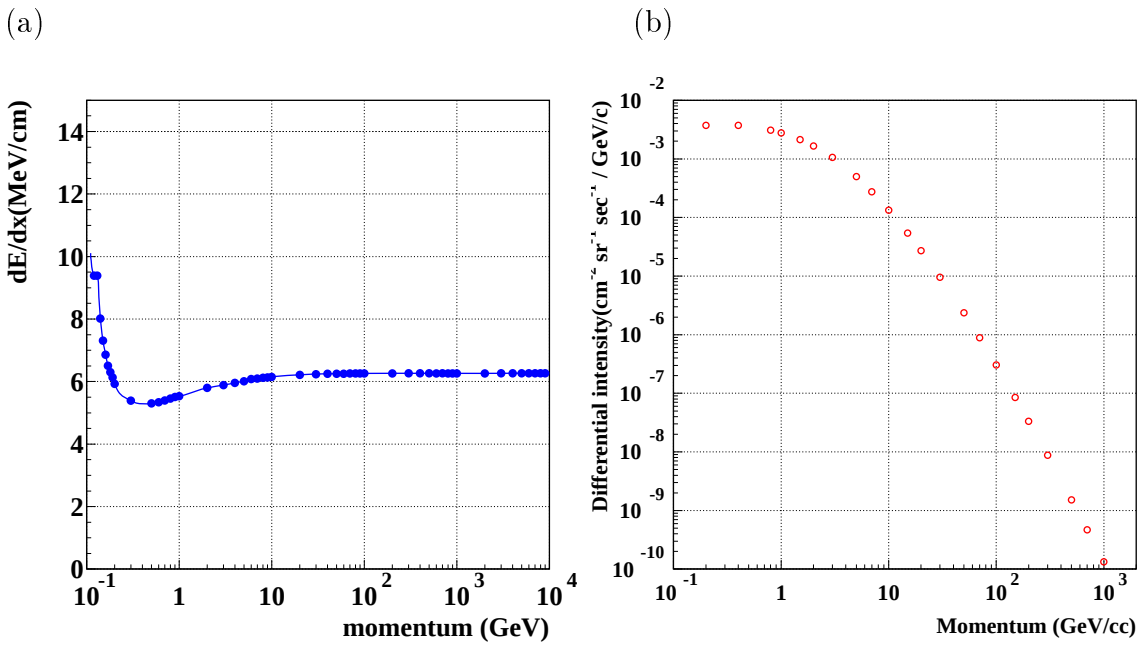

Figure 5.4: (a)Most probable energy deposit of cosmic ray in CsI counter (GEANT simulation). (b)The differential intensity of the cosmic ray.

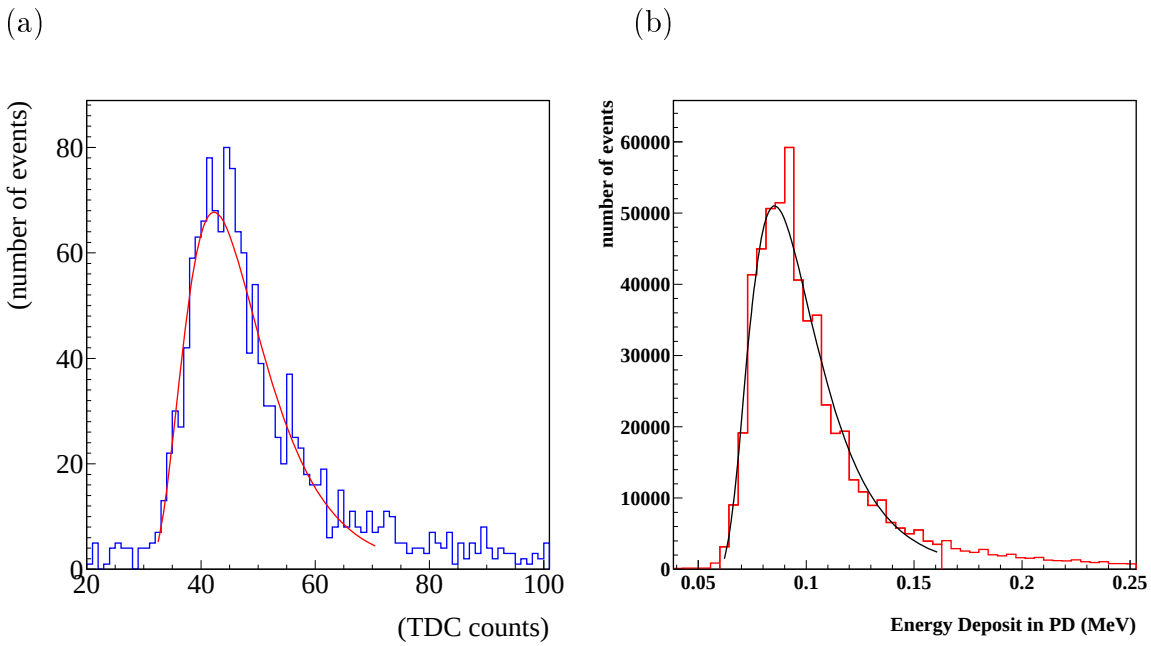

Figure 5.5: Energy deposit of cosmic rays in a photodiode (a)data and (b)GEANT simulation.

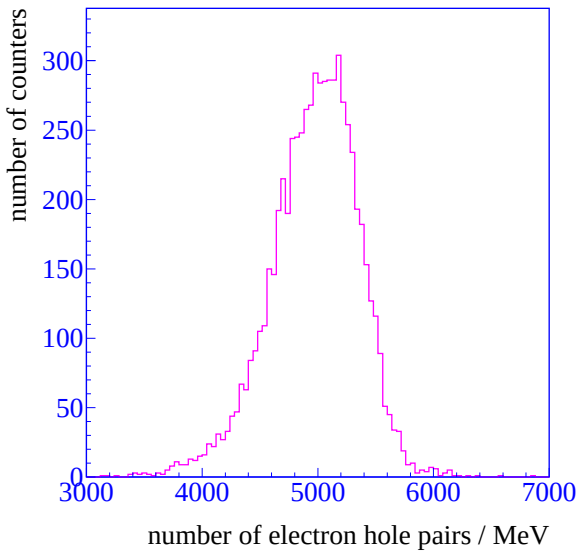

Figure 5.6: Results of the light output for all CsI(Tℓ) counters

value of this distribution corresponds to the number of electron-hole pairs of 16.7 $\times$ 10^3. This result was consistent within 4 % with the cosmic ray measurement.

5.5 Light Output Result

We measured the light output of all the barrel CsI(Tℓ) crystals (6,624 pieces). These were delivered from Budker Institute of Nuclear Physics (BINP), Russia, Shanghai Institute of Ceramics (SIC), China and Crismatec, France.

We defined the average of 9 subparts as the average light output of the crystal. The distribution of average light output for 6,624 barrel crystals is shown in Fig. 5.6. It is given in the unit of electron-hole pairs per 1 MeV of energy deposit in the crystal. The mean and rms of this distribution are 4,969 and 381 electron hole pairs. No significant difference was observed among the crystals of Crismatec, SIC and BINP.

In order to estimate the long term stability of the measurement, sample counters were measured again after 6 months from the first measurement. Fig. 5.7 shows the results. The peak shifts 1.4 % but the difference of light output is small within 1 % and the position dependence of light output also remain unchanged.

The result was compared with the average light output measured by ^{137}Cs. The data was obtained from the crystal acceptance test (see section 4.5.2). The comparison is shown in Fig. 5.8(a). There is a good agreement and the rms deviation of the ratio

(a) (b)

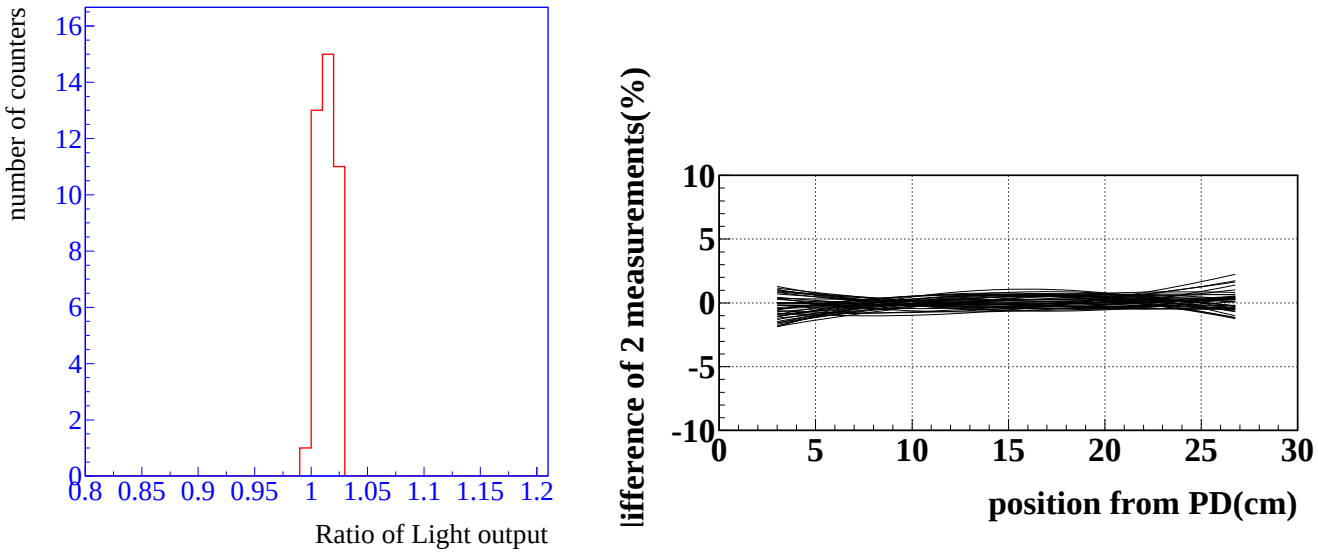

Figure 5.7: Reproducibility of (a)the light output and (b)position dependence after 6 months.

(a) (b)

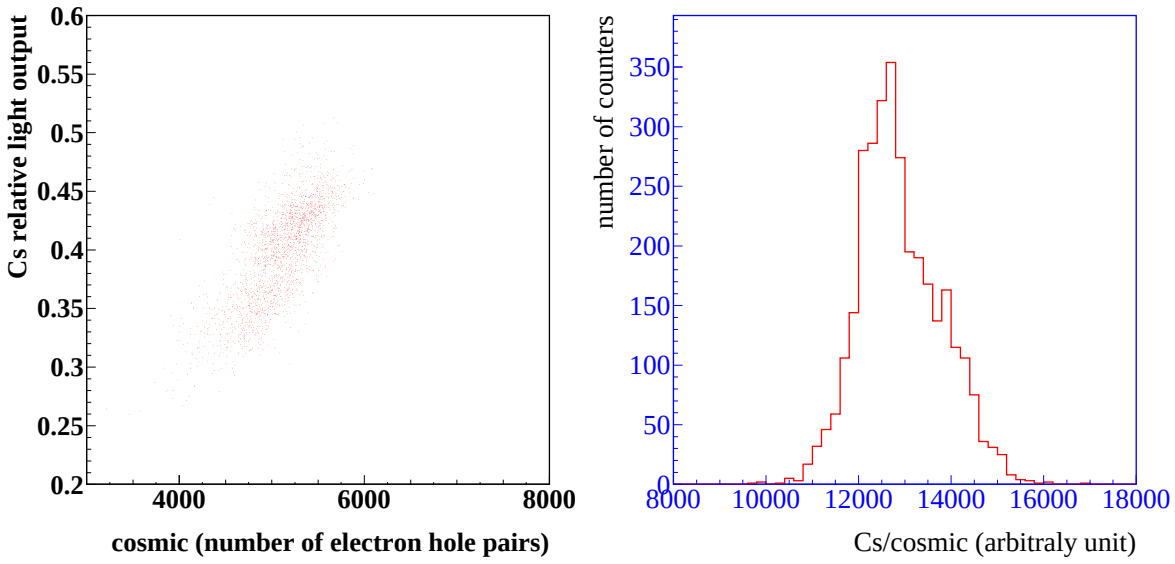

Figure 5.8: (a)Comparison between the calibration by cosmic rays and the ^{137}Cs source. (b)Ratio between two calibrations.

of two measurements is about 7 % (Fig. 5.8(b)).

5.6 Uniformity of Light Collection

The position dependence of the light output obtained from above measurements is shown in Fig. 5.9(a)-(c). The measurement of each subpart is normalized to the average light output and it is fitted by the 3rd order polynomial. The behaviors BINP crystal and Crismatec crystal are similar and the light output increases near the photodiode. The SIC crystals are separated in two types; one is similar with BINP/Crismatec and the other is almost flat over all regions of the counter.

The result of the measurement by the photomultiplier which is described in the previous chapter is shown in Fig. 5.9(d)-(f) for comparison. The difference between two measurements is shown in Fig. 5.9(g)-(i). A systematic shift between two measuring techniques is apparent. It is probably caused by the difference of optical contact; the photodiode is glued to the crystal and has a good optical contact, and in the phototube case, the light has to pass through the air layer and the rate of reflection at the boundary region is larger.

The distribution of uniformity parameter H (see 4.7) for barrel counters is shown in Fig. 5.10. The average was 9 %.

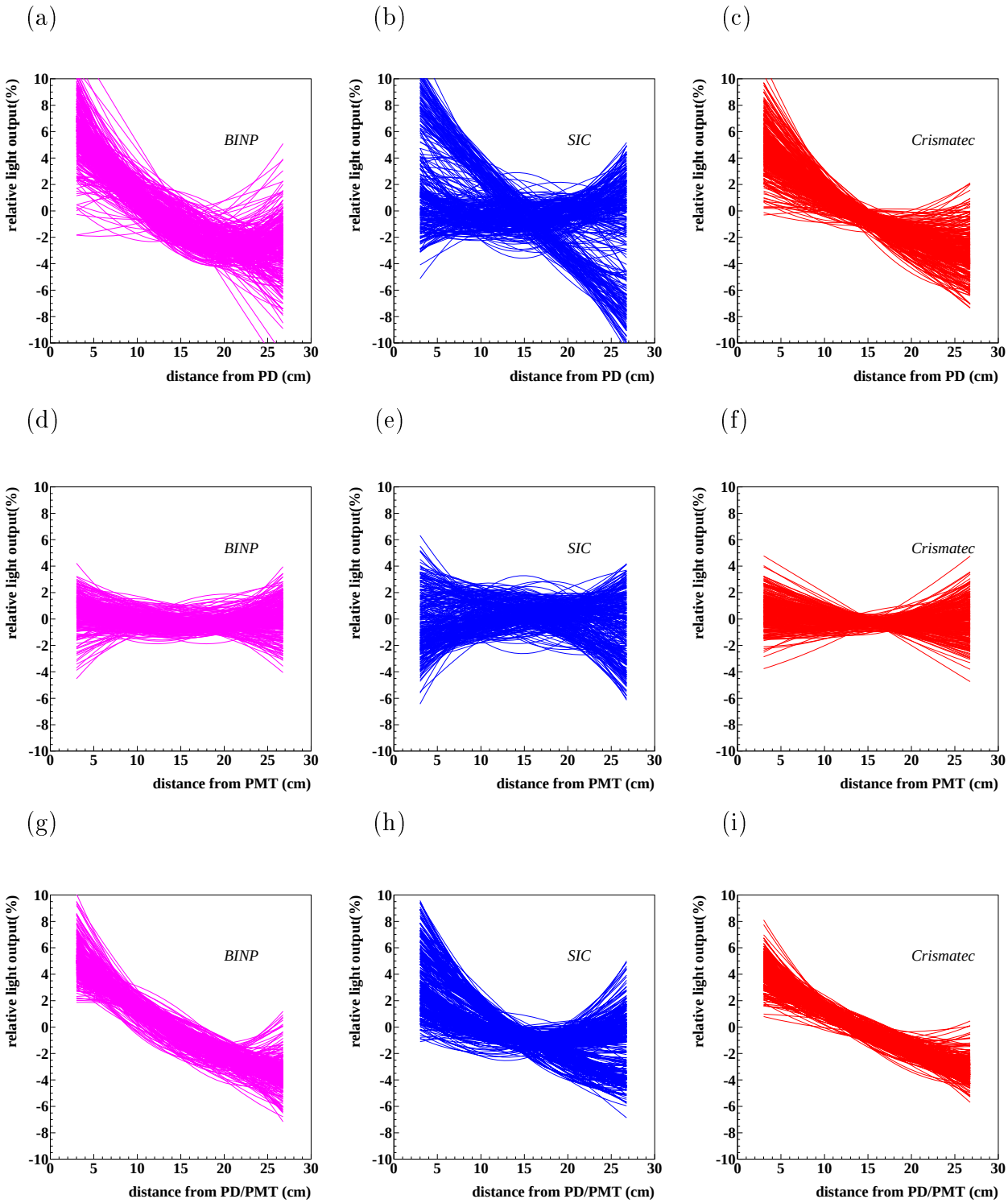

Figure 5.9: Position Dependence of light output. (a-c): Measurement by photodiode glued on the crystal. (d-f): Measurement by phototube with air gap. (g-i): Difference between two methods.

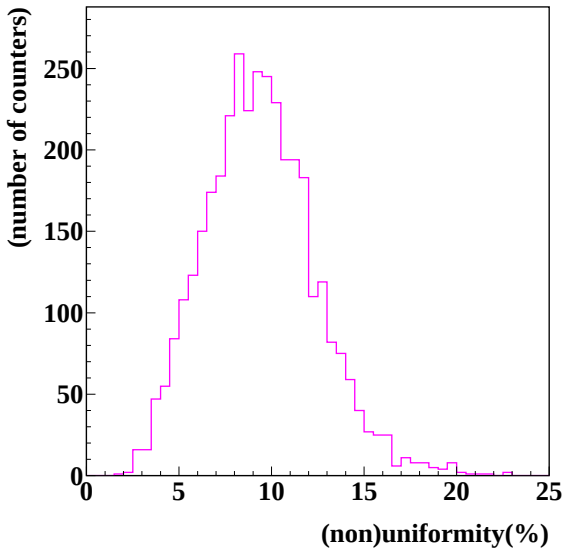

Figure 5.10: Distribution of uniformity.

Chapter 6

Test of the CsI(Tℓ) Calorimeter Performance by Photon Beam.

6.1 Motivation

In the BELLE experiment, the electromagnetic calorimeter is responsible for the detection of photons and electrons in a wide energy range. The minimum energy is 20 MeV for photons from π^0 decay and the maximum energy is 8 GeV for electrons from Bhabha scattering. A good energy resolution, linearity and position resolution is required to detect such photons in a wide energy range.

We used a wide energy range photon beam of the VEPP-4M collider at Budker Institute of Nuclear Physics (BINP), Russia to measure the performance of 6 $\times$ 6 matrix of CsI(Tℓ) counters. The aims of the experiment are

- tests of the counters performance as well as final electronics,
- development of the calibration procedure, clustering and analysis method,
- investigation of the properties of the Monte Carlo simulation programs by comparing with real data.

6.2 Photon Beam

We used two sources of photon beam in this measurement. One is a backward scattered laser light by an ROKK-1M electron beam in VEPP-4M electron-positron storage ring in a Compton scattering process; $\gamma(2.33\text{ eV}) + e^- \to \gamma + e^-(\text{tagged})$ (Fig 6.1)(a). The

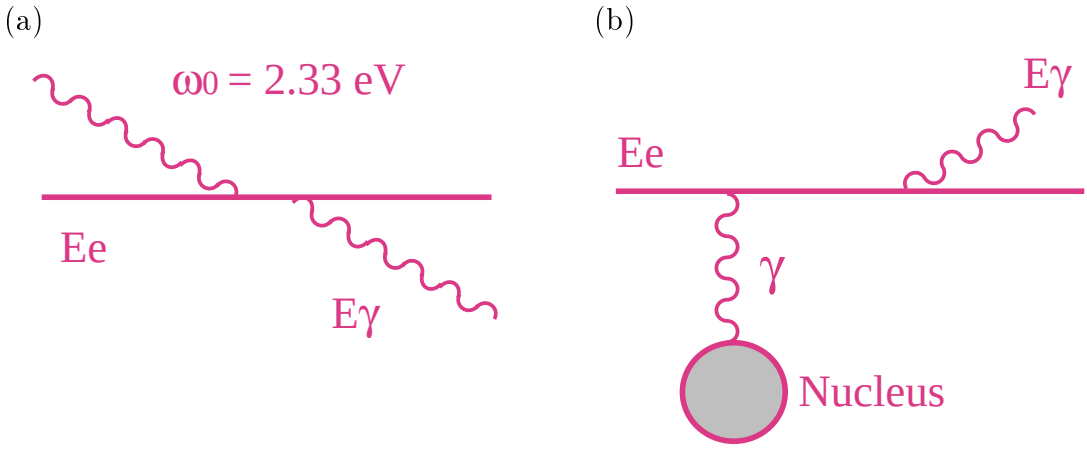

Figure 6.1: (a) Compton scattering and (b) Bremsstrahlung scattering.

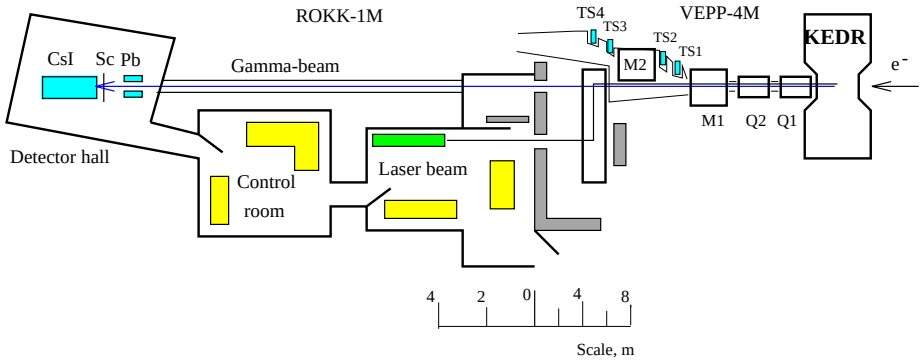

Figure 6.2: Layout of the photon beam line.

energy of the photon is calculated by measuring the energy of the scattered electron using the tagging system. The other source is the Bremsstrahlung photon generated by the collision of the electron beam and the residual gas nuclei in the vacuum chamber of the accelerator; $e^- + \text{Nucleus} \rightarrow \gamma + e^- + \text{Nucleus}$(Fig 6.1).

A schematics of the photon beam line at ROKK-1M is shown in Fig 6.2 [65]. Primary photons with an energy of 2.33 eV are generated by Nd:YAG pulse laser. The photon is guided to the interaction point of VEPP-4M by a set of mirrors and makes a head-on collision with the electron beam. By the backward Compton scattering with electron, the laser photon receives a significant part of the electron energy E_{beam} and boosted back in the direction of initial electron beam. The energy of the photon is calculated in each event by measuring of the electron energy in the tagging system

(TS) placed in the straight section of the storage ring.

The tagging system consists of TS_1 to TS_4, each of which is consists of six double layers of drift tubes. The deflection of electron by the machine component magnet, Q1 and Q2 quadruples and M1 and M2 dipoles, is used to analyze the momentum. The resolution of the tagging system is determined by the magnetic structure of the interaction region of accelerators, electron beam parameters such as the angular and energy spread and the transverse size at the interaction point, the space resolution of the drift tube. The energy spectrum of the Compton scattered photon $F(E)$ is approximated for $E_c \ll E_{beam}$ by;

$$F(E) = N((E - \frac{E_c}{2})^2 + \frac{E_c^2}{4}). \tag{6.1}$$

where N is the normalization factor and E is the photon beam energy. The Compton edge energy E_c is calculated from the primary photon energy ω_0 and the electron beam energy as follows;

$$E_c = 4\gamma^2\omega_0/(1 + \frac{4\gamma\omega_0}{m_e}). \tag{6.2}$$

where γ is the relativistic factor of incoming electron and m_e is the electron mass.

The Bremsstrahlung cross section is described by the following formula [66];

$$d\sigma = 4Z^2 r_e^2 \alpha \frac{d\nu}{\nu}((1+\varepsilon^2)(\frac{\phi_{1(\xi)}}{4} - \frac{1}{3}lnZ - f(Z)) - \frac{2}{3}\varepsilon(\frac{\phi_2(\xi)}{4} - \frac{1}{3}lnZ - f(Z))), \tag{6.3}$$

Z : atomic number of the material,
r_e : electron classical radius (e^2/mc^2),
α : 1/137,
ε : E/E_0,
E_0 : total energy of the incident electron,
E : total energy of the scattered electron,
$f(Z)$: Coulomb correction factor,
$\phi_1(\xi)$, $\phi_2(\xi)$: screening function,

ξ is the screening parameter and given by the formula,

$$\xi = \frac{100 m_e c^2 h\nu}{E_0 E Z^{1/3}}, \tag{6.4}$$

$h\nu$: energy of photon

In the case of complete screening ($\xi = 0$), the cross section becomes

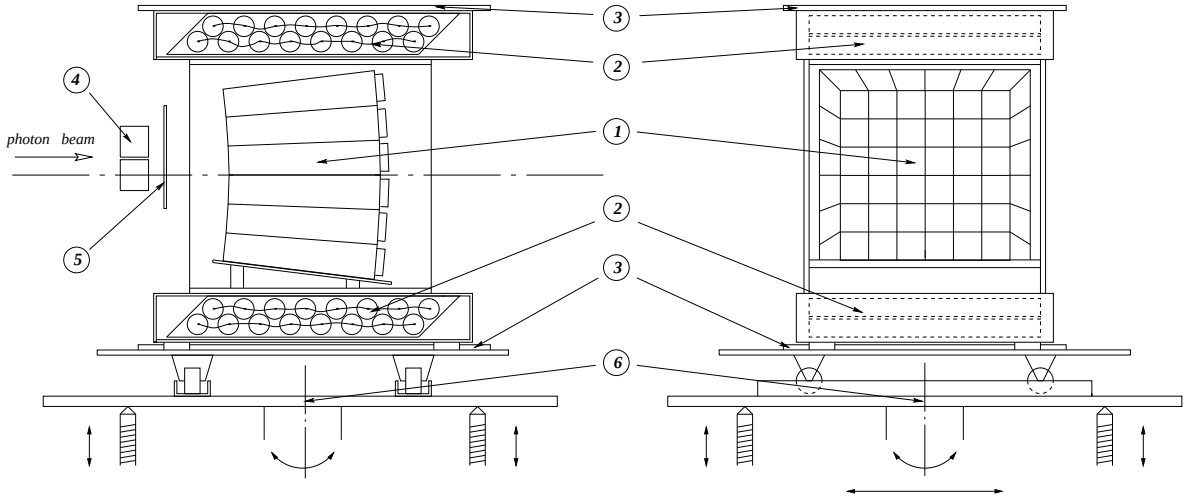

Figure 6.3: Experimental setup − 1. CsI(Tℓ) counters; 2. drift tube hodoscopes; 3. plastic scintillation counters for cosmic trigger; 4. lead collimator; 5. veto counter; 6. movable platform for the position adjustment.

$$d\sigma = 4Z^2 r_e^2 \alpha \frac{d\nu}{\nu}((1+\varepsilon^2 - \frac{2\varepsilon}{3})(ln(183Z{-}1/3) - f(Z)) + \frac{\varepsilon}{9}). \tag{6.5}$$

The spectrum is inversely proportional to the photon energy ν. The maximum energy of the photon in Bremsstrahlung is near to the incident electron energy. For the Bremsstrahlung photon, the edge value of the spectrum was used for the analysis but the tagging system was not used.

The rate of the Compton photon is proportional to the beam current, laser intensity and laser frequency. The laser was set at the maximum intensity and frequency (10kHz) and the timing is synchronized with a beam phase signal of $\sim$ 800 kHz. The electron beam current was limited at around 1 μA such that the number of interacted photons is kept less than 0.1 for each laser pulse. The transverse size of the photon beam is 2-4 cm at the CsI matrix and it is mainly determined by the electron beam parameters. The photon beam is injected to the front face of the CsI matrix.

6.3 Experimental Setup

The experimental setup is shown in Fig 6.3 and Fig. 6.4. The CsI(Tℓ) counters are piled in a 6 $\times$ 6 matrix and installed in a light shielded box. The box is placed on a

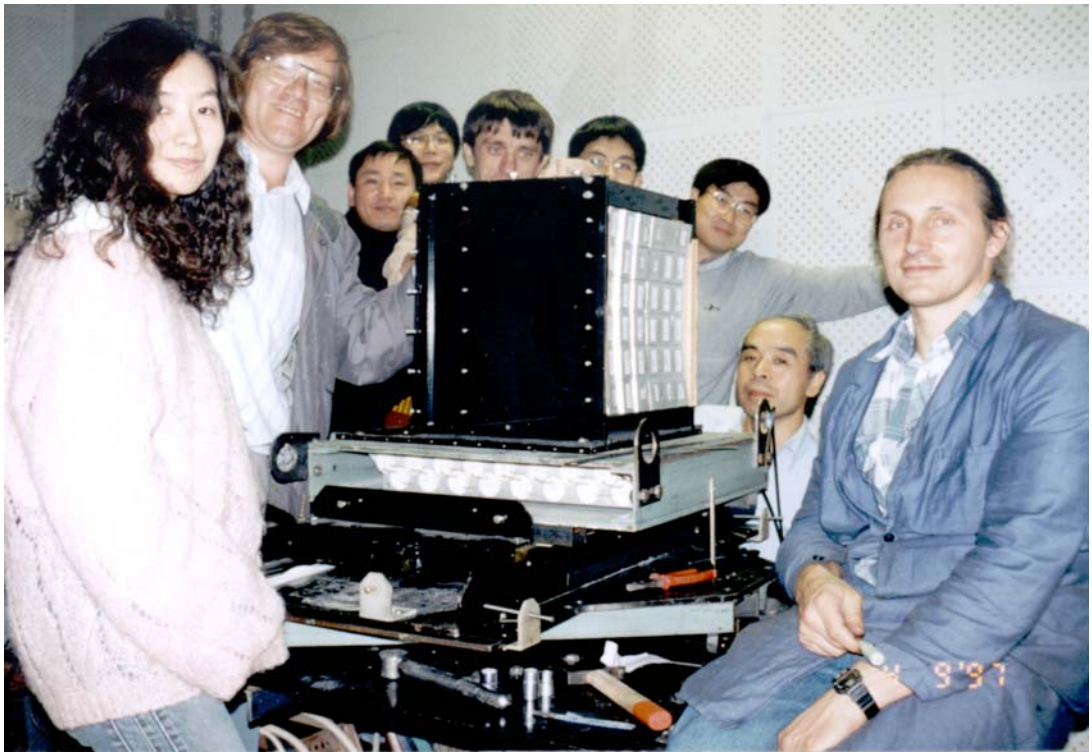

Figure 6.4: Beam test setup and crews.

movable table for the alignment to the photon beam. A plastic scintillation counter was installed in front of the matrix to veto photons converted in the output window of VEPP-4M and in the upstream air.

We used 36 crystals of the standard BELLE type produced at BINP. The dimension of the crystals is approximately 55 × 55 mm at the front end and 60 × 60 mm at the rear end. The length is 300 mm. The structure of the counter is described in Chapter 4. Aluminum sheets of 0.5 mm thickness are placed between the crystals to simulate the effect of compartment walls of the crystal container (see section 4.7).

For most of the data taking, the photon beam is injected to the center of the four central counters ((3,3)(3,4)(4,3)(4,4)). Then the signals from 3 × 3 or 5 × 5 counters are summed for the analysis. The heavily shaded area in Fig. 6.5 shows the region of 3 × 3 summation and the lightly shaded area is for 5 × 5 summation with the photon beam injected at the center of (4,4) crystal. All the counters are calibrated by the cosmic ray *in situ* and the central 16 counters are calibrated by the photon beam.

Two sets of drift tube hodoscopes are installed at the top and bottom of the matrix for the cosmic-ray calibration. Each set is composed of two layers of eight tubes, which are connected in sequence. The radius of the tube was 40 mm and the position along

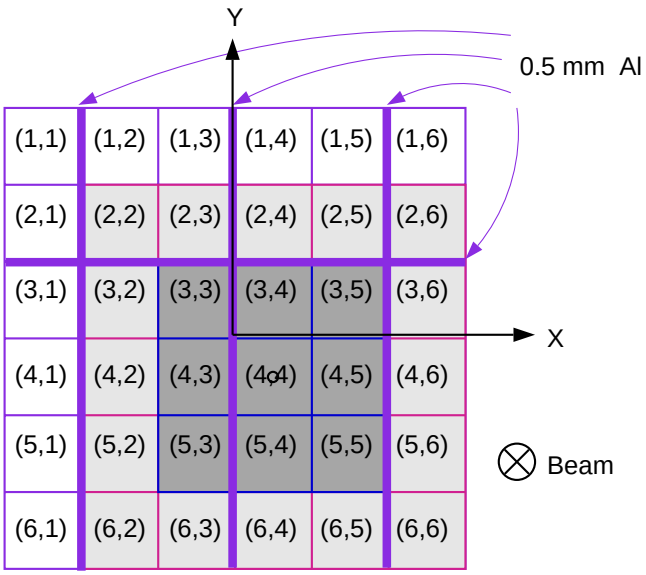

Figure 6.5: 6 × 6 CsI(Tℓ) matrix and crystal numbering (Front view).

the wire was determined with an accuracy of 15 mm by measuring the difference of the arriving time of the signal at the both ends of the wire. The plastic scintillation counters are used for triggering cosmic rays.

A schematics of the trigger and data acquisition system is shown in Fig. 6.6. For Compton runs, a trigger was produced by the coincidence of the scintillation counter signal placed behind of the TS drift tubes and the anti-signal from the veto counter And the signals from the CsI(Tℓ) matrix is used only for low energy. A beam crossing marker and a laser gate pulse are also required. The signal from the matrix is defined when an analog sum of the central 15 counters* produced by the STM module is above certain energy threshold. For Bremsstrahlung runs, the TS scintillator and the laser gate pulse were not required. A gate signal of 100 ns wide is generated by the trigger and is distributed to the shaper/QT module through the calibration module (CAL). The CAL module also generated the test pulse for the calibration of the electronics, LED driving pulse and supplied 60 V bias of the photodiode.

All the electronics used in the test beam are same as the production version except STM and CAL module. The two modules were CAMAC version prototype. The data acquisition from the FASTBUS TDC and the control of CAMAC modules are done by one-board SUN computer in VME system. The data taking rate was about 100 Hz for

*central 16 counters except (5,5).

the usual Compton runs. The temperature was continuously monitored also by SUN computer system.

6.4 Data Collection

Analysis	E_{beam}(MeV)	Compton Edge(MeV)
Energy calibration	4036.	508.3
Energy resolution and linearity	921.	29.4
	1206.	49.8
	1506.	76.8
	1810.	109.8
	3007.	291.5
	4036.	508.3
	5441.	884.7

Table 6.1: Summary of the beam setup in the beam test.

We took the data in September and October, 1997. All the data were collected at seven different settings of the electron beam energy. Both Compton photon and Bremsstrahlung photon data were obtained for each energy setting. Used electron beam energy and the corresponding Compton edge energy are listed in Table. 6.1. About 50k to 200k events were collected for each energy setting of Compton and Bremsstrahlung runs. The Compton photon of 508 MeV was used for the beam calibration. For this purpose, the beam was injected at the center of central 16 counters. The same photon energy was used for the measurement of the position dependence.

The pedestal and test pulse runs were done once every few hours during the beam time. The cosmic data were taken during the beam off time. The number of triggered events was 100k in average and it took 8 hours. The pedestal, test pulse and LED runs were also made regularly during the beam off time to check the electronics performance.

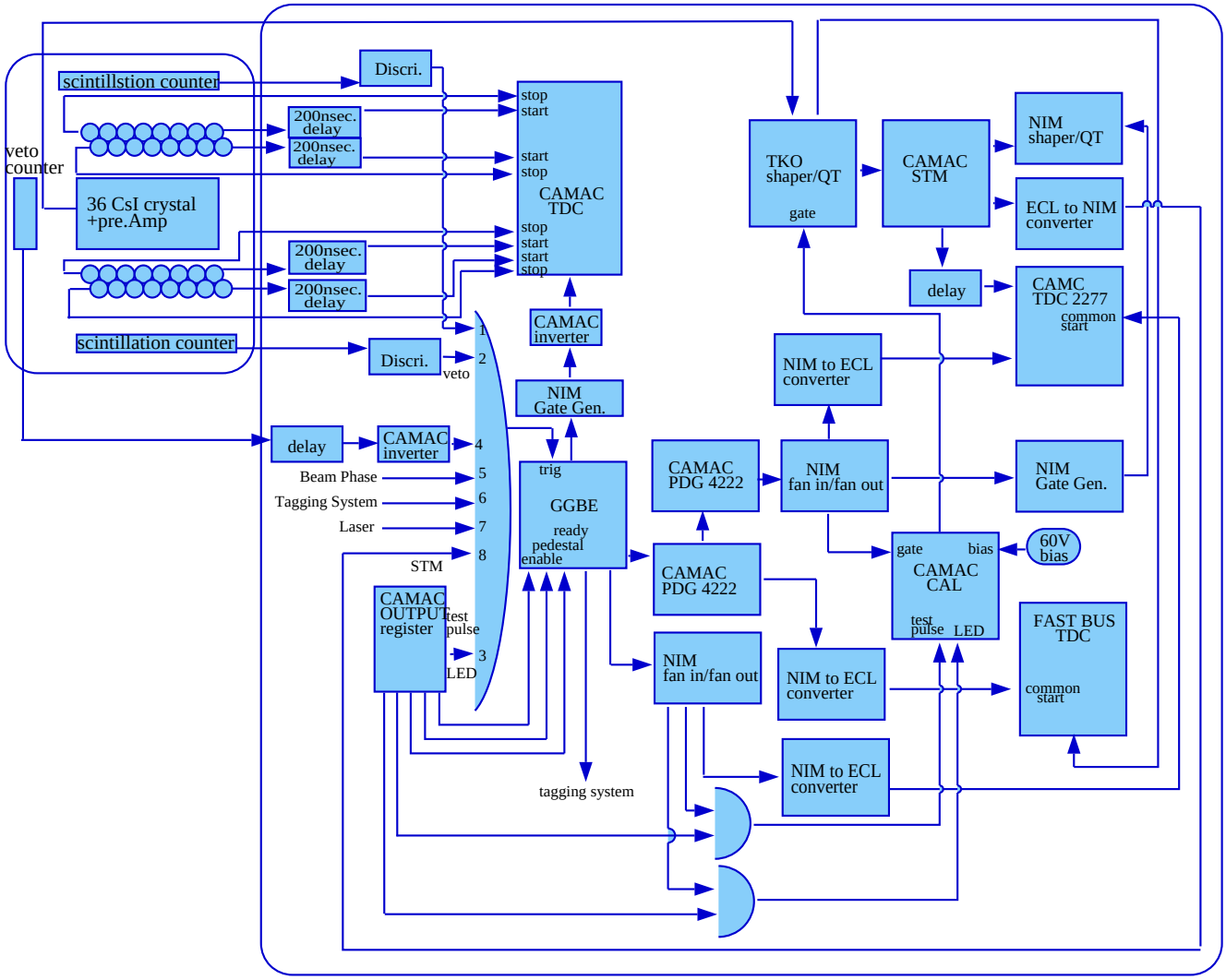

Figure 6.6: Schematics of trigger and data acquisition for the beam test.

(a) (b)

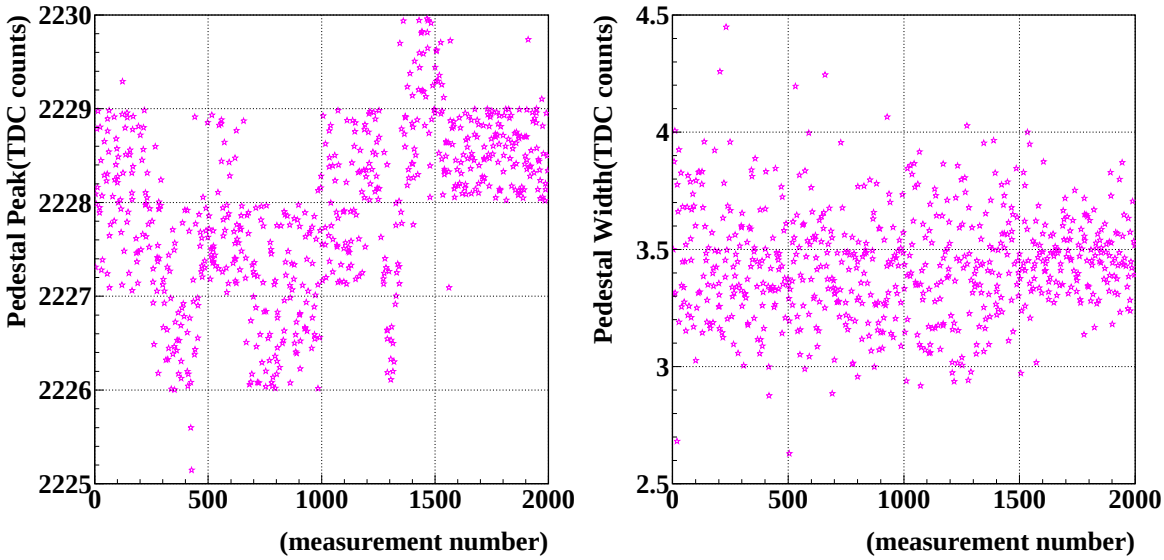

Figure 6.7: History of (a)pedestal and (b)it's width over 2 months.

6.5 Electronics Performance

6.5.1 Noise Level

Fig. 6.7 shows the history of the peak and the width of the pedestal distribution obtained by the Gaussian fitting. The horizontal axis is the time scale and the full scale corresponds to 2 months. The pedestal value was stable ($\pm$ 1 counts) over long time.

A typical distribution of the pedestal run in the low range for single channel is shown in Fig. 6.8(a). The distribution of the pedestal after summing all 36 channels are shown in Fig. 6.8(b). The width of the pedestal distribution corresponds to the electronics noise level. The electronics noise consists of the preamplifier internal noise and external pickup noise. The former is independent in each channel (incoherent) and the latter happens at the same time for all channels (coherent). From the fitting of the pedestal distribution of the single channel $\sigma_{i,0}$ and the sum of n channels σ_n, coherent noise and incoherent noise are separated using the following formula;

$$\sigma_{i,0}^2 = \sigma_{i,in}^2 + \sigma_{i,ch}^2 \tag{6.6}$$

where $\sigma_{i,in}$ and $\sigma_{i,ch}$ stand for incoherent and coherent noise component of i-th channel, respectively. The total noise is given by using σ_{in} and σ_{ch} of all channels and separated

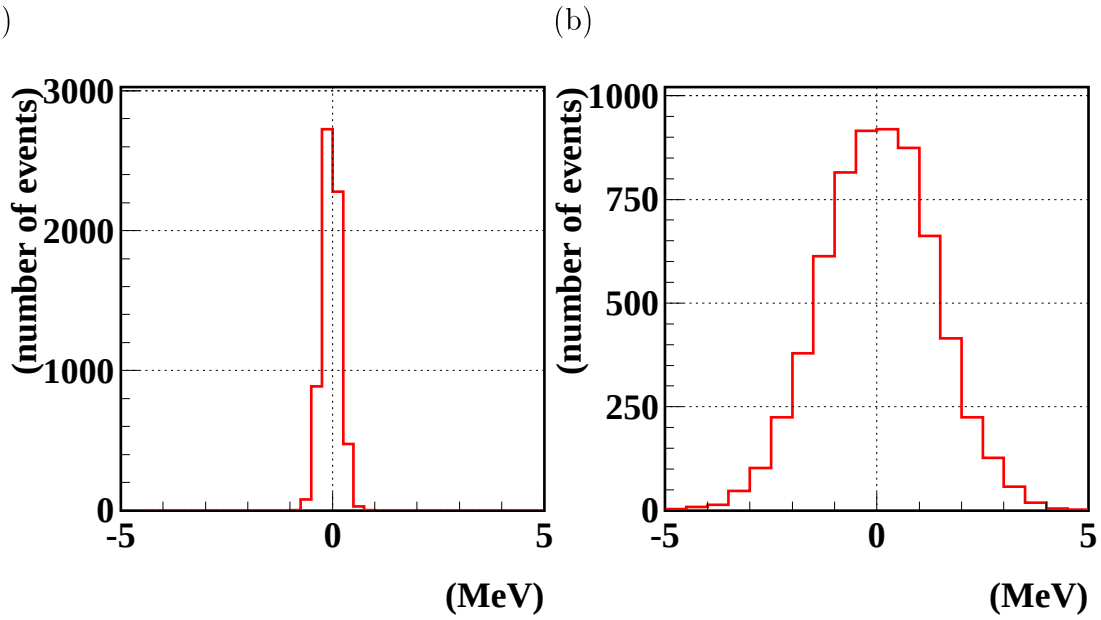

Figure 6.8: Typical pedestal distribution of (a) one channel and (b) the sum of 36 channels after conversion to energy unit.

to two components as follows;

$$\sigma_n^2 = \sum_{i=1}^{n} \sigma_{i,in}^2 + (\sum_{i=1}^{n} \sigma_{i,ch})^2 \tag{6.7}$$

$$< \sigma_{i,ch}^2 >= \frac{\sigma_n^2 - \sum_{i=1}^{n} \sigma_{i,0}^2}{n^2 - n} \tag{6.8}$$

$$< \sigma_{i,in}^2 >= \frac{(\sum_{i=1}^{n} \sigma_{i,ch})^2 - \sigma_n^2}{n^2 - n}. \tag{6.9}$$

From the above equation, the coherent and incoherent noise are calculated to 16.5 keV and 189 keV in average for n = 36 counters. They correspond to 75 and 950 electron hole-pairs in ENC.

6.5.2 Electronics Linearity

The electronics linearity is checked by a test pulse. Fig. 6.9 is an example of the results of test pulse run. The input voltage are $0 \sim 0.8$ V (corresponding to $0 \sim 1$ GeV) for MQT low range, $0 \sim 2.4$ V ($0 \sim 3$ GeV) for MQT middle range, and $0 \sim 4$ V ($0 \sim 5$ GeV) for MQT high range. The full scale in each range was equally split in 20 steps.

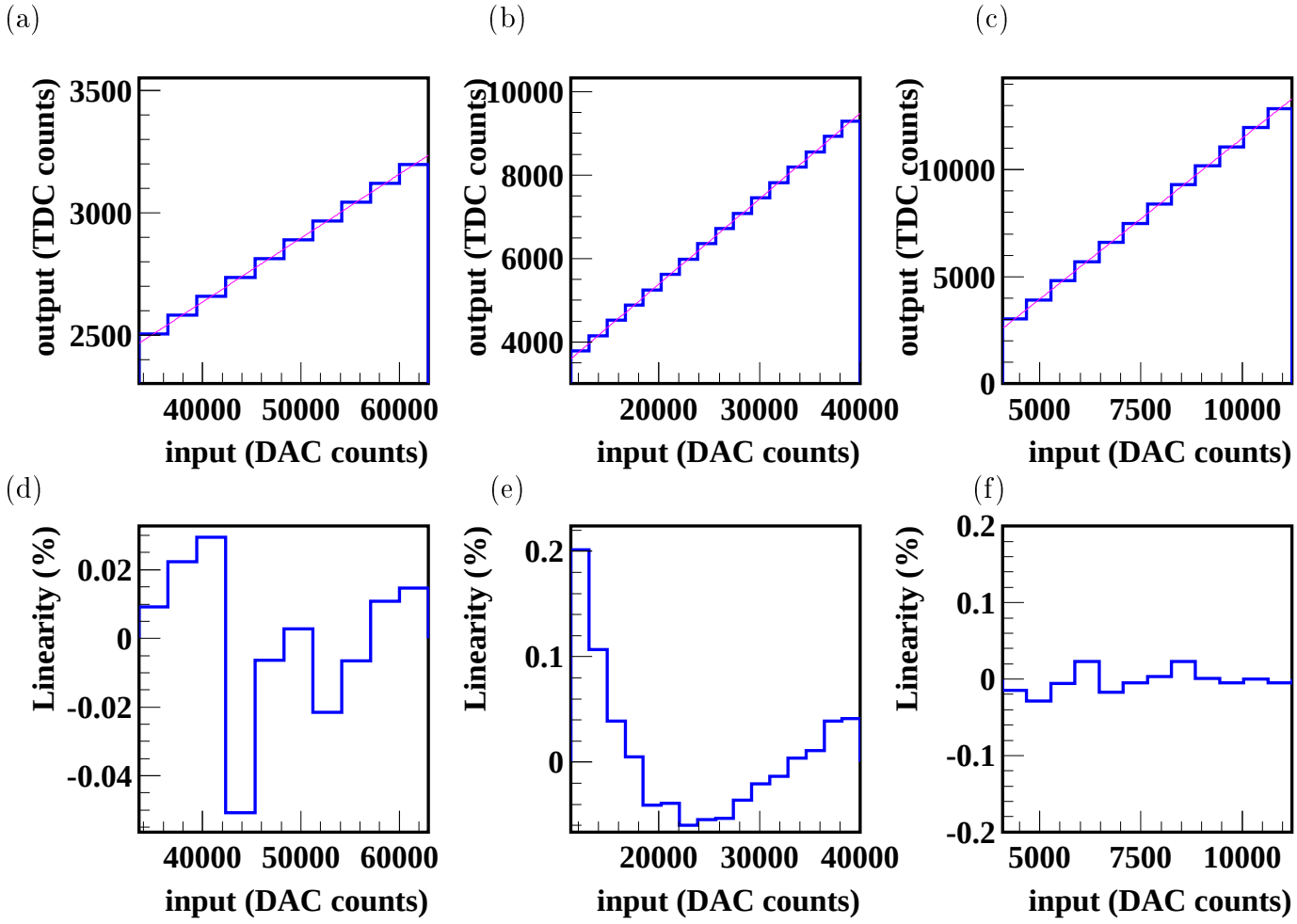

Figure 6.9: Test pulse calibration for (a) High, (b)Middle and (c)Low ranges. (d)-(f) shows the deviation from the linear fitting in % for each range.

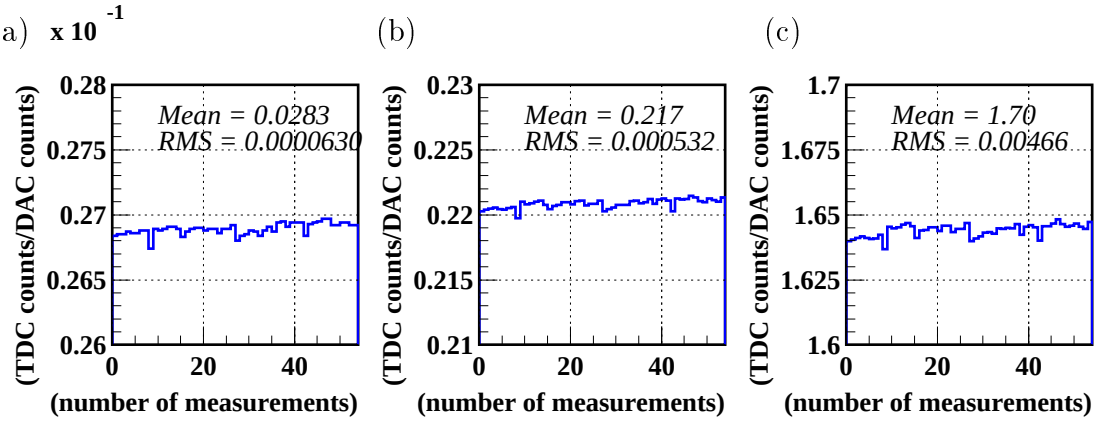

Figure 6.10: Stability of the test pulse slope in (a) High, (b)Middle and (c)Low range of MQT.

In Fig. 6.9, about 4000 DAC channels correspond to 0 V and 100 DAC channels are equivalent to 1 MeV. In each step, the peak channel was determined by the Gaussian fit and is plotted in Fig. 6.9 (a),(b) and (c).

Fig. 6.9 (d),(e) and (f) show the deviation of each point from the linear fitting line as defined bellow;

$$\frac{y_i - f(x_i)}{f(x_i) - f(x_0)} \times 100\ (\%). \tag{6.10}$$

$f(x_i)$: linear fitting function
x_i : i-th input DAC channel
x_0 : input DAC channel which corresponds to 0 V.
y_i : i-th output TDC channel

We used the low range for $0 \sim 700$ MeV and the middle range for higher than 700 MeV in the data analysis. The electronics linearity was measured for low range and it was less than 0.1% for higher energies than 10 MeV. The high range of MQT was not used. Since the electronics was proved to have a good linearity, we did not have any correction of the linearity.

6.5.3 Electronics Calibration

The output of MQT has three ranges to have a good resolution over a wide dynamic range. The ratio of slopes obtained by the test pulse run is used as the conversion factor between different ranges. The ratio was 6.98 to 7.87 between low and middle range and 7.67 to 8.32 for middle and high ranges. A long term stability of the slope

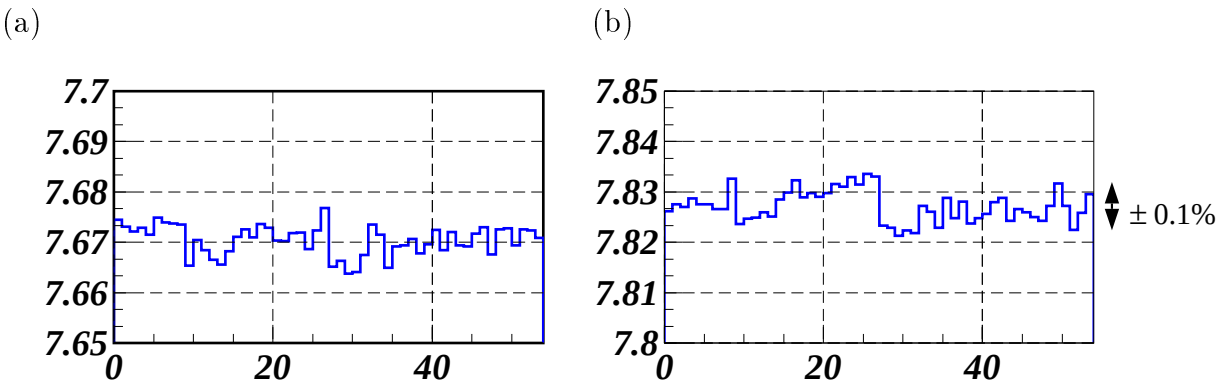

Figure 6.11: Stability of the test pulse ratio for (a)H/M and (b)M/L for a typical channel. The stability is within 0.1 %.

for a typical read out channel is shown in Fig. 6.10. The stability of the ratio is also shown in Fig. 6.11. As shown in the figures, the slope was stable within ± 0.3 % over 2 months of data taking period. The ratio was stable within ± 0.1 % for the same period.

6.6 Energy Calibration

The energy of the injected photon is calculated by the following formula for each event by summing the output of crystals in a 3 × 3 or 5 × 5 region around the central crystal.

$$E = A \times \sum_{i=1}^{9,25} (T_i^j - P_i^j) \times C_i \times R_i^j, \tag{6.11}$$

T_i^j : TDC counts of i-th counter in j-th MQT range,
P_i : Pedestal value of i-th counter in j-th MQT range,
C_i : Calibration constant of i-th counter,
R_i^j : MQT range factor,
$R_i^L \equiv a_i^L / a_i^L = 1$,
$R_i^M \equiv a_i^M / a_i^L$,
$R_i^H \equiv a_i^H / a_i^L$,
A : Overall correction factor,
a_i^j : test pulse slope of i-th counter in j-th MQT range,

where i is the index of the counter and j is the index of the MQT sensitivity range (j = L, M, H). For each counter, a most appropriate MQT range is chosen from j = L,

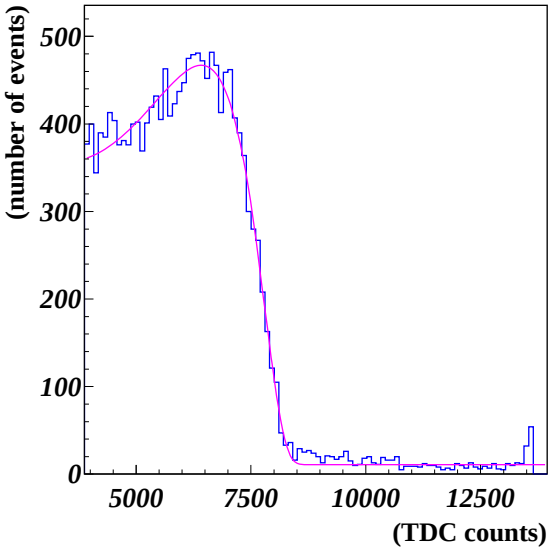

Figure 6.12: Pulse height distribution for the back scattered Compton photons for 1 counter. The theoretical Compton edge is at 508 MeV.

M, H. Such T_i^j is the TDC count of the lowest (most sensitive) range not exceeding the overflow count of the corresponding range.

In order to get the calibration constant C_i, Compton photon beam and cosmic muons were used. The calibration with the photon beam was done only once during the beam time for the central 16 counters at the center of the matrix. The cosmic-ray calibration was done once every few days for all the counters during the measurement time. Two calibration were related using the ratio of the calibration constant for the central 16 counters. The average of 36 counters by the cosmic-ray calibration was also used to correct a time dependence of the calibration.

For the cosmic-ray calibration of each counter, we selected events in which the above and below counter are both fired. This was to make sure a muon passes through the entire thickness of the counter. The track of the muon was reconstructed by the streamer tubes and the inclination of the muon track was determined. The track length inside the crystal calculated in this way has an accuracy of 1.5 %. The mean energy loss of the cosmic muon is 5.67 MeV per cm in CsI if we approximate it by a minimum ionizing particle. With this value and the path length inside the crystal for each event, we plotted the distribution of the TDC channel per MeV energy loss by the cosmic ray. The calibration constant C_i is the inverse of the peak position of this distribution. It has the unit of MeV/TDC count.

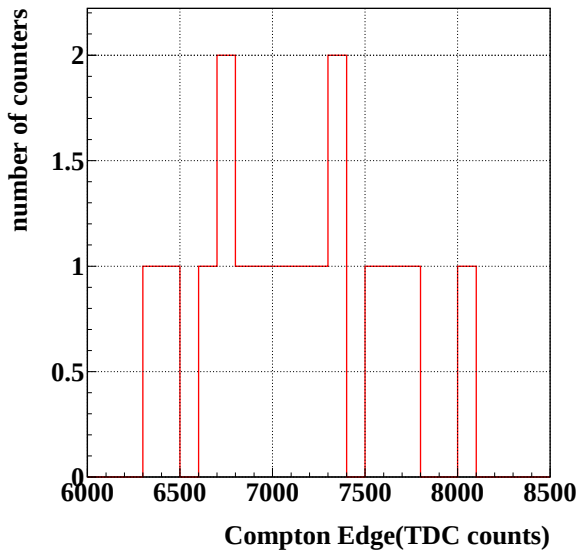

Figure 6.13: Distribution of beam calibration constants for central 16 counters.

The photon beam calibration used 4036 MeV electron beam setting. The Compton photon beam with 508 MeV maximum energy was injected at the center of each counter by adjusting the position and angle of the moving table which is supporting the crystal matrix. Due to the limitation of the moving table, twenty counters in the outer layers of the matrix were not measured by this method. An example of the low range TDC distribution after pedestal subtraction is shown in Fig. 6.12. This is the distribution for one counter at which the photon beam was aimed.F The calibration constant is obtained from the TDC edge value and calculated Compton edge energy.

Fitting function used is the same as that used in the normal Compton run which will be explained in APPENDIX C. The fitting was done in 2 steps to obtain a stable fitting result. In the first fitting, the TDC channels corresponding to the Compton edge and asymmetry parameter η are determined for each counter. In the second step, the fitting region is limited to 50 $\sim$ 180 % of the Compton edge and the asymmetry parameter was fixed as the average of 16 counters obtained in the first step. The distribution of the fitted Compton edge which is proportional to the inverse of the calibration constant C_i, is shown in Fig. 6.13. In order for two sets of calibrations to be consistent, we multiplied all the photon beam calibration constants by a constant S ($\equiv$ average of C_i obtained by cosmic rays / average of C_i obtained by photon beam).

Fig. 6.14 shows the comparison between the scaled beam calibration constant and

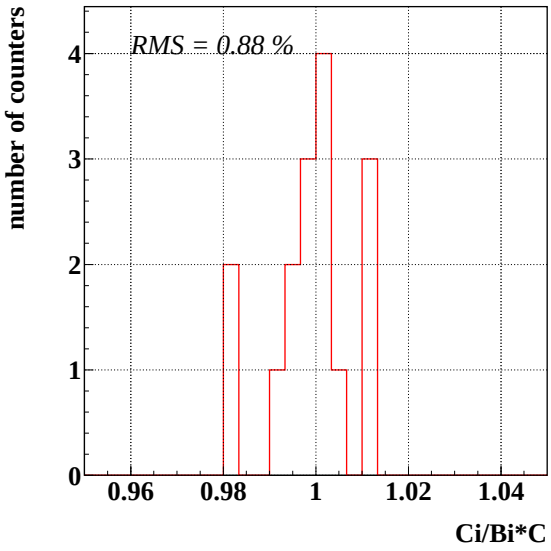

Figure 6.14: Ratio of the cosmic-ray calibration to the beam calibration.

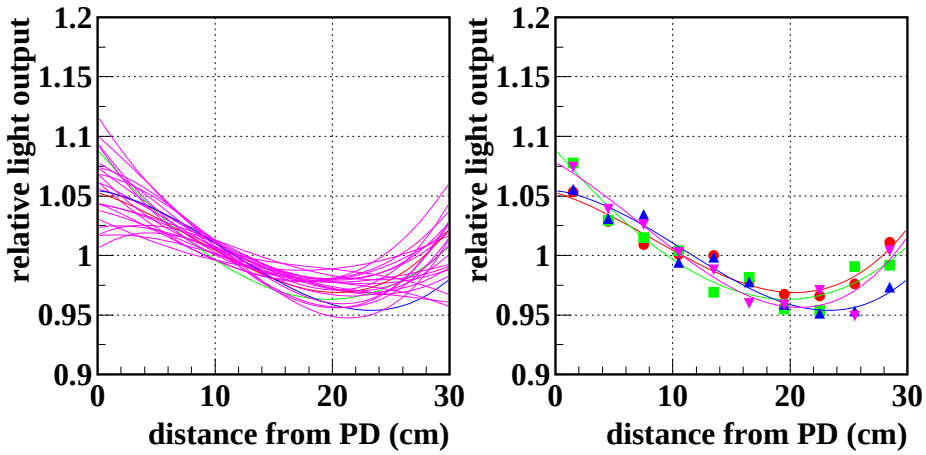

Figure 6.15: Position dependence of the light output measured by cosmic rays for (a) all counters and (b) central four counters after scaling to the average light output of each counter.

the original cosmic-ray calibration constant for the central 16 counters. Both of beam calibration and cosmic-ray calibration are consistent within a rms of 0.88 %. For the subsequent analysis of energy resolution and linearity, we use the scaled photon beam calibration for the central 16 counters and the original cosmic-ray calibration constants for the outer 20 crystals. The gain variation of 36 different electronics channels, which amounts to ± 10 % at maximum, are automatically corrected in this process.

In order to determine the value of correction factor A, the effect of longitudinal non-uniformity has to be considered carefully. The position dependence of the cosmic ray pulse height is shown in Fig. 6.15. The light output is higher near the photodiode and the behavior is similar for all the counters. On the other hand, the energy deposit by the photon is heavily weighted at the front part of the crystal. Fig. 6.16 shows the energy deposit in each 3 cm slice of the CsI crystal obtained by GEANT simulation when the Compton photon beam of 508 MeV is injected from the front face of the crystal. It is clear from the figure that the most of the energy is deposited in the first half of the crystal which has the lower light output.

The cosmic-ray calibration constants are calculated as the average of all subparts and the effect of non-uniform energy deposit by the photon is not included. In order to correct that effect, GEANT simulation was done for the Compton photon beam. The non-uniformity function used in GEANT is described later in section 6.7.7. We made four Monte Carlo simulations by injecting the 508 MeV Compton photon beam at the center of one of the (3,3)(3,4)(4,3)(4,4) crystals. The fitted Compton edge of 5 × 5 counters was 497.0 MeV for the Monte Carlo contrary to the Compton edge of 508 MeV. The value of 497.0 MeV is the estimate of energy deposit by the Monte Carlo with shower leakage taken into account. We determined the value of A such that the 5 × 5 energy deposit calculated by the formula (6.11) for data gives the same edge value of 497.0 as the Monte Carlo simulation. We found the value of $A = 1.021$ and the absolute energy scale given by the cosmic-ray calibration seems fairly accurate.

We used only one set of C_i described above to analyze all the data taken over 2 months of beam period. But a small time dependent factor is applied on C_i. Fig. 6.17 shows the history of the temperature of the crystal and electronics together with the relative shift of cosmic-ray calibration constant averaged over 36 counters. The correlation between two parameters indicates that the light output of CsI crystal is affected by the temperature and this is to be corrected. We used this relative shift to represent the variation of C_i with temperature. In the analysis of the data, we took the correction from the most nearby cosmic-ray calibration in time. The maximum of this correction was 0.8 %.

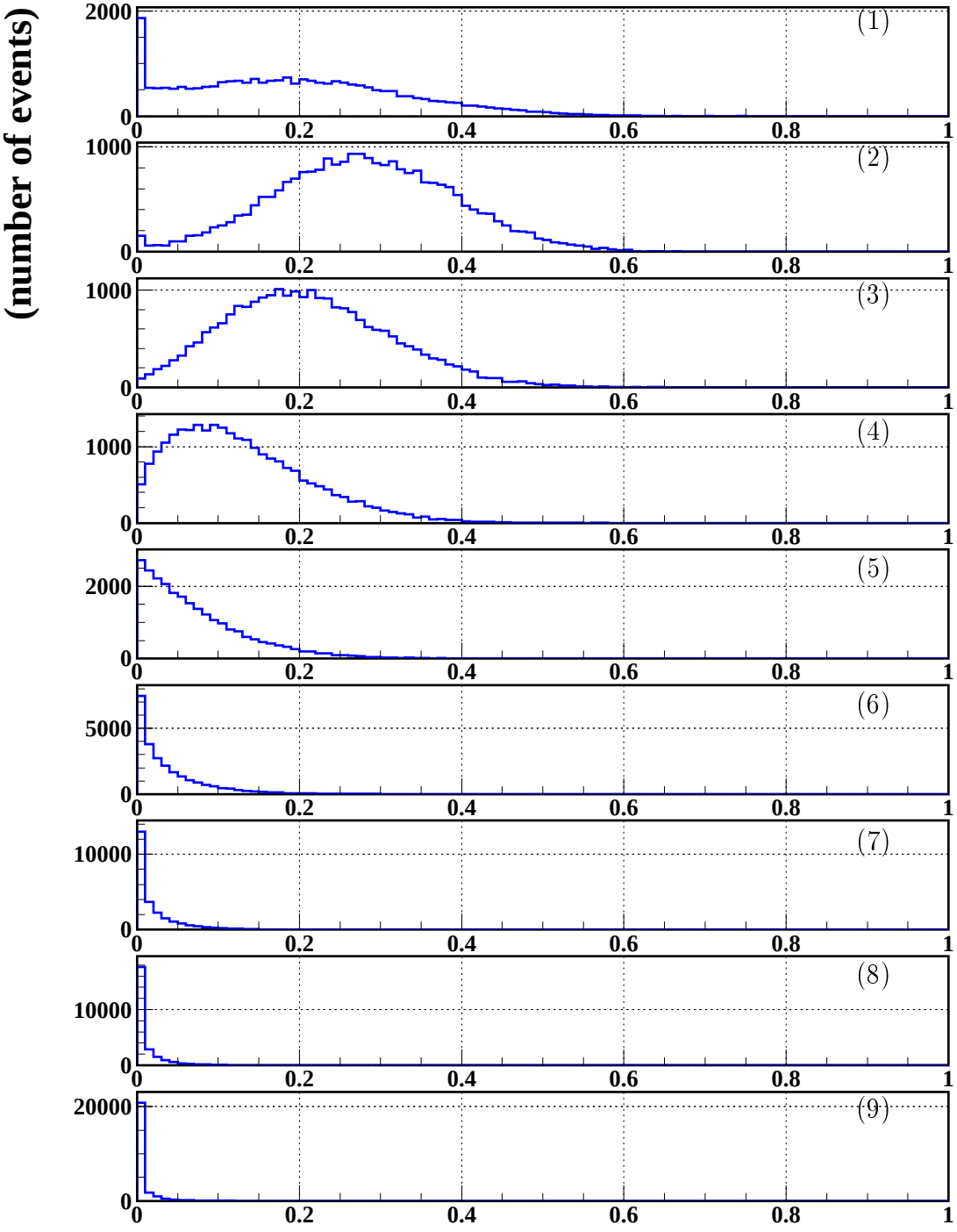

Figure 6.16: Energy deposit in longitudinal slices of the CsI(Tℓ) crystal for 508 MeV Compton beam. The depth of each slice is 3 cm.

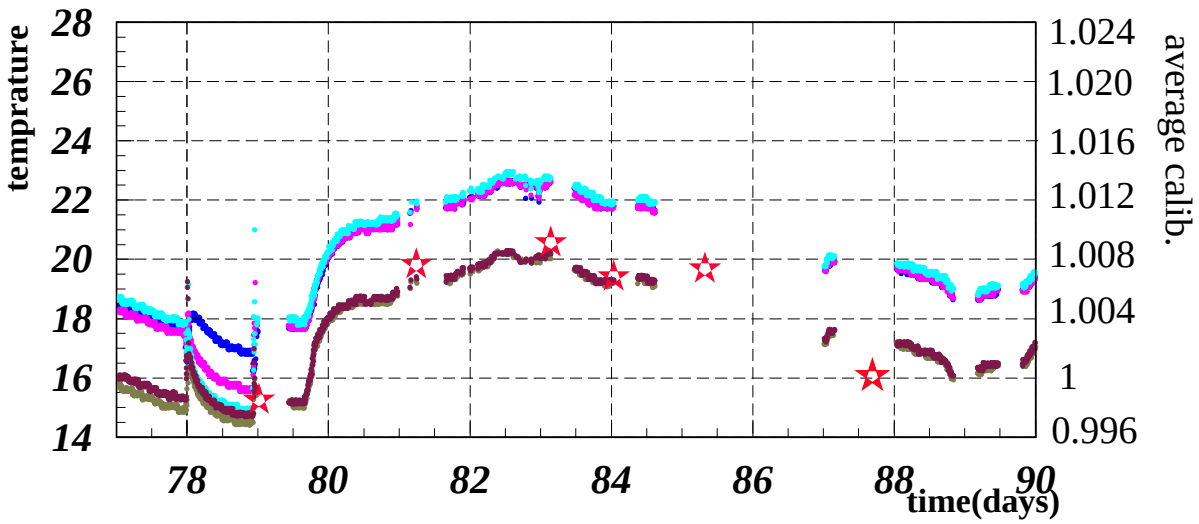

Figure 6.17: Temperature dependence of cosmic-ray calibration. Lines indicate the temperature at several locations in the data taking room, and stars are the average of the cosmic-ray calibrations of 36 counters.

6.7 Energy Resolution

6.7.1 Tagged Photon Analysis

There are two methods to get the energy resolution of the CsI(Tℓ) counter from Compton photon beam. The first method uses the tagging system (TS) to estimate the photon beam energy event by event. Fig. 6.18(a) shows the correlation between the energy obtained by CsI counters (E_{CsI}) and by the tagging system (E_{tag}). Using the tagged photon energy, the energy dependence of the energy resolution can be studied from the lowest limit of the tagging system acceptance up to the Compton edge. We divided the whole energy range of E_{tag} into several subparts and plot the ratio of E_{CsI} and E_{tag} in each subpart. Fig. 6.18(b) shows a typical distribution of the ratio $R_E \equiv E_{CsI}/E_{tag}$ together with the fitting function of a logarithmic Gaussian. The upper and lower tail regions of R_E with histogram contents below 20 % of the peak value were removed from the fitting to suppress the uncertainty in the fitting procedure. For this method, the resolution of E_{CsI} is obtained by subtracting the resolution of E_{tag} from the resolution of R_E in quadrature as follows,

$$\sigma_{E_{CsI}} = \sqrt{\sigma^2_{R_E} - \sigma^2_{E_{tag}}}. \tag{6.12}$$

(a) (b)

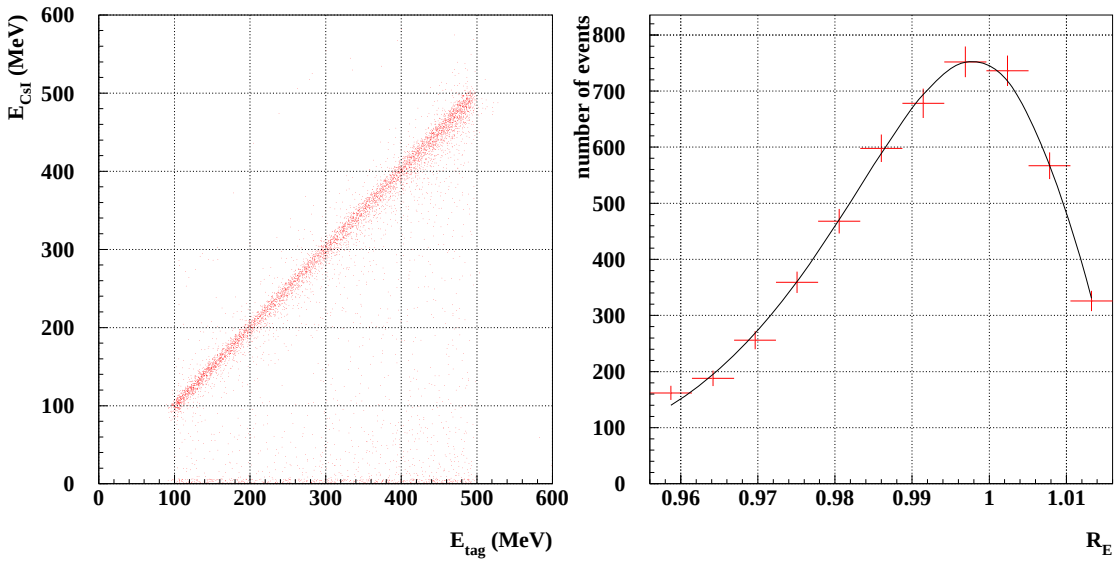

Figure 6.18: (a)Correlation between the energies E_{CsI} and E_{tag} for 508 MeV Compton run. (b)Distribution of R_E with fitting . The fitting region is 410 $\sim$ 510 MeV.

6.7.2 Compton Edge

The second method is the fitting of the shape of the Compton edge. The convolution of Compton spectrum (6.1) and the resolution function (5.1) is used for the fitting (APPENDIX C). The examples of the fitting is shown in Fig. 6.19. To avoid the systematic shift of the fitting results by the different fitting region, the fitting was done in two steps. An approximate position of the edge E_{edge} and the resolution σ_E were determined in the first step. The fitting region was limited to [$E_{edge} \pm 5\sigma_E$] in the second step.

The fitting function includes a background term coming from the overlapping of two Compton photons in a single laser pulse. The distribution of the background was analyzed by Monte Carlo simulation. If 20 % of the event has a contribution from the second photon, the energy spectrum looks like Fig. 6.20. From the figure, the background distribution of triangular shape in the fitting function is justified.

6.7.3 Bremsstrahlung Edge

The Bremsstrahlung photon spectrum edge also used for the estimation of the energy resolution using the same way as used for the Compton spectrum edge. The fitting

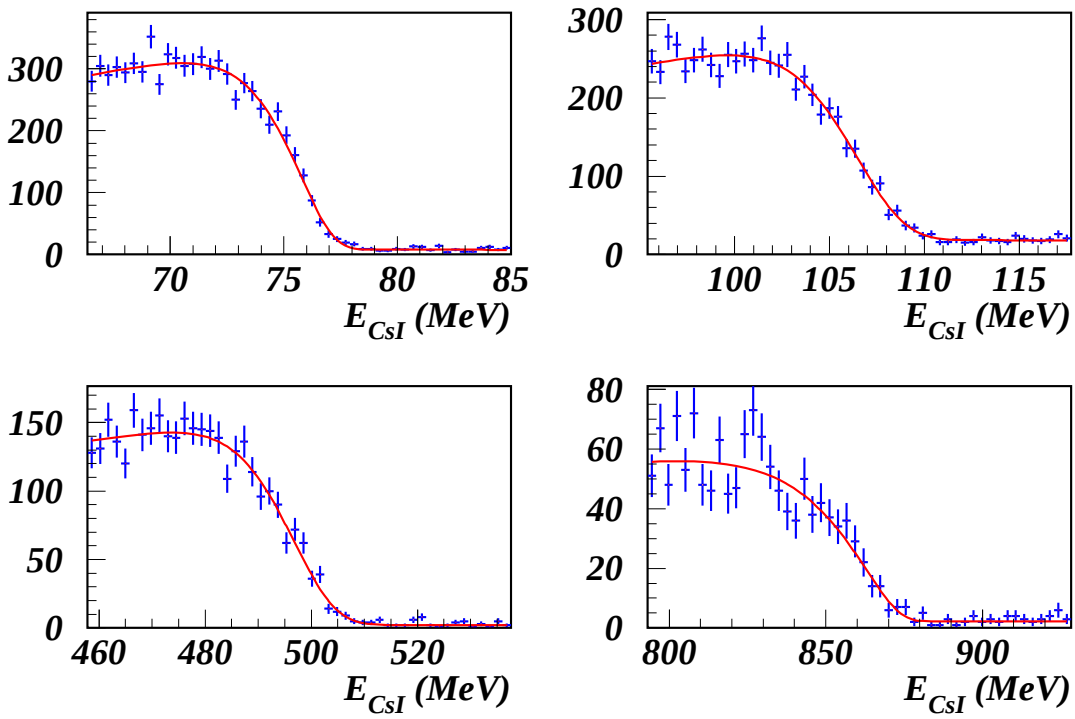

Figure 6.19: Typical Compton edge distributions. The solid line in each figure is the fitting results.

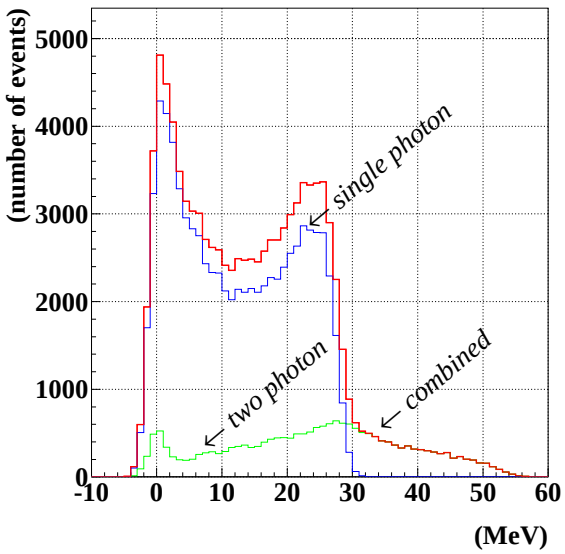

Figure 6.20: Compton photon distribution with two photon background by Monte Carlo simulation. The percentage of 2 photon is 20 % of the single photon.

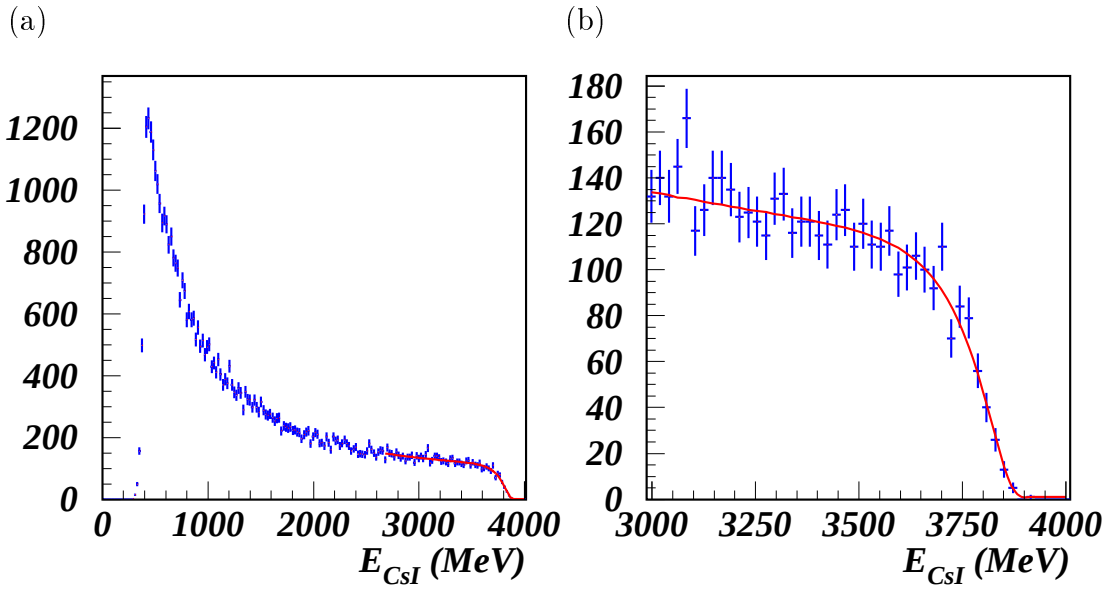

Figure 6.21: (a)Typical Bremsstrahlung distribution for 4036 MeV electron beam and (b)the expanded view of the edge region with fitting result.

function is the convolution of the theoretical Bremsstrahlung function and the CsI response function. The distribution is shown in Fig. 6.21. Fitting region is taken from 67 % to 100 % of the incident electron beam energy.

6.7.4 Asymmetry Parameter

For all three methods, the asymmetry parameter η of the fitting function affects the estimate of the resolution. Both of the edge fittings need special care because the asymmetry parameter tends to be unstable in the fitting. In Fig. 6.22, we show the energy dependence of the asymmetry parameter η obtained from the fitting of the R_E. In fitting the Compton and Bremsstrahlung edges, we fixed the asymmetry parameter η at the values represented by the solid curve in Fig. 6.22.

6.7.5 Energy Resolution for Simple Sum

The result of the energy resolution for a simple sum is shown in Fig. 6.23(a)(b) for the 3×3 and 5×5 matrix, respectively. The simple sum means the sum of all signals from the 3×3 or 5×5 crystals around the beam injected crystal. The solid line shows the tagging system resolution which is quadratically subtracted from the resolution of R_E.

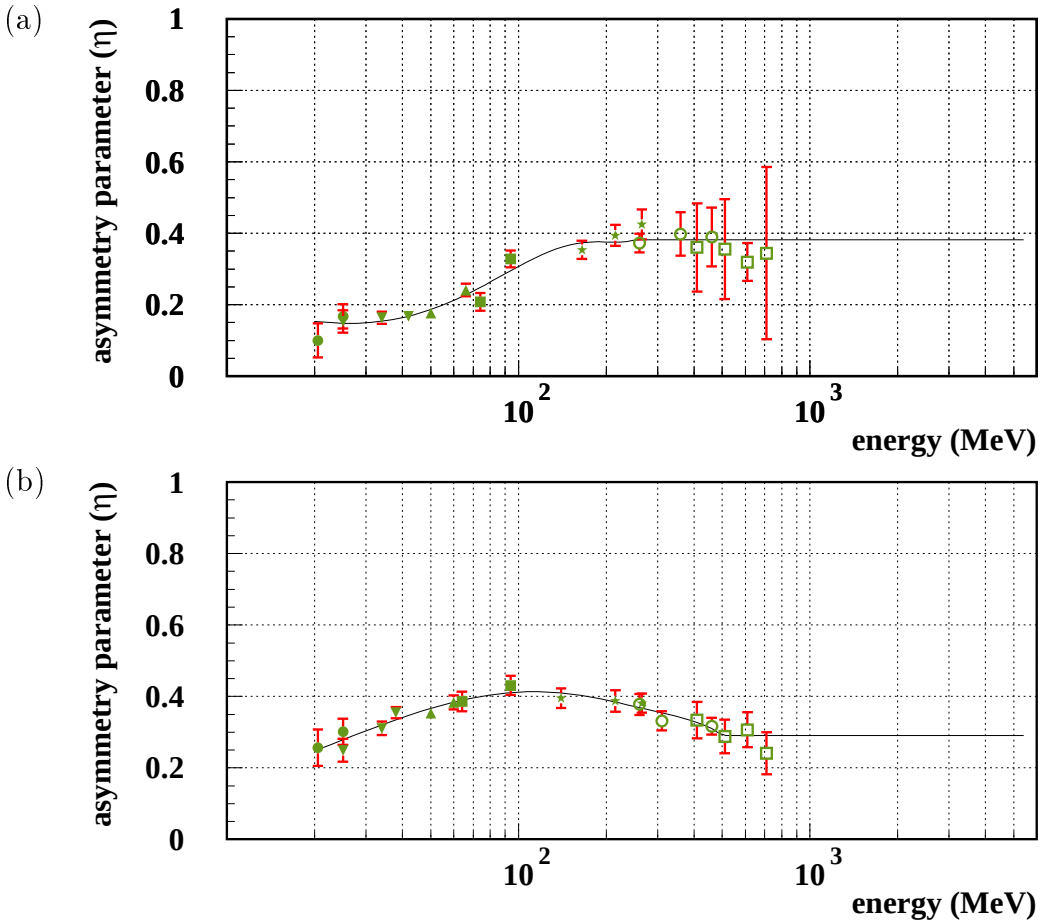

Figure 6.22: Energy dependence of asymmetry parameter η obtained from the fitting of R_E for (a)5x5 and (b)3x3 matrix with fitting.

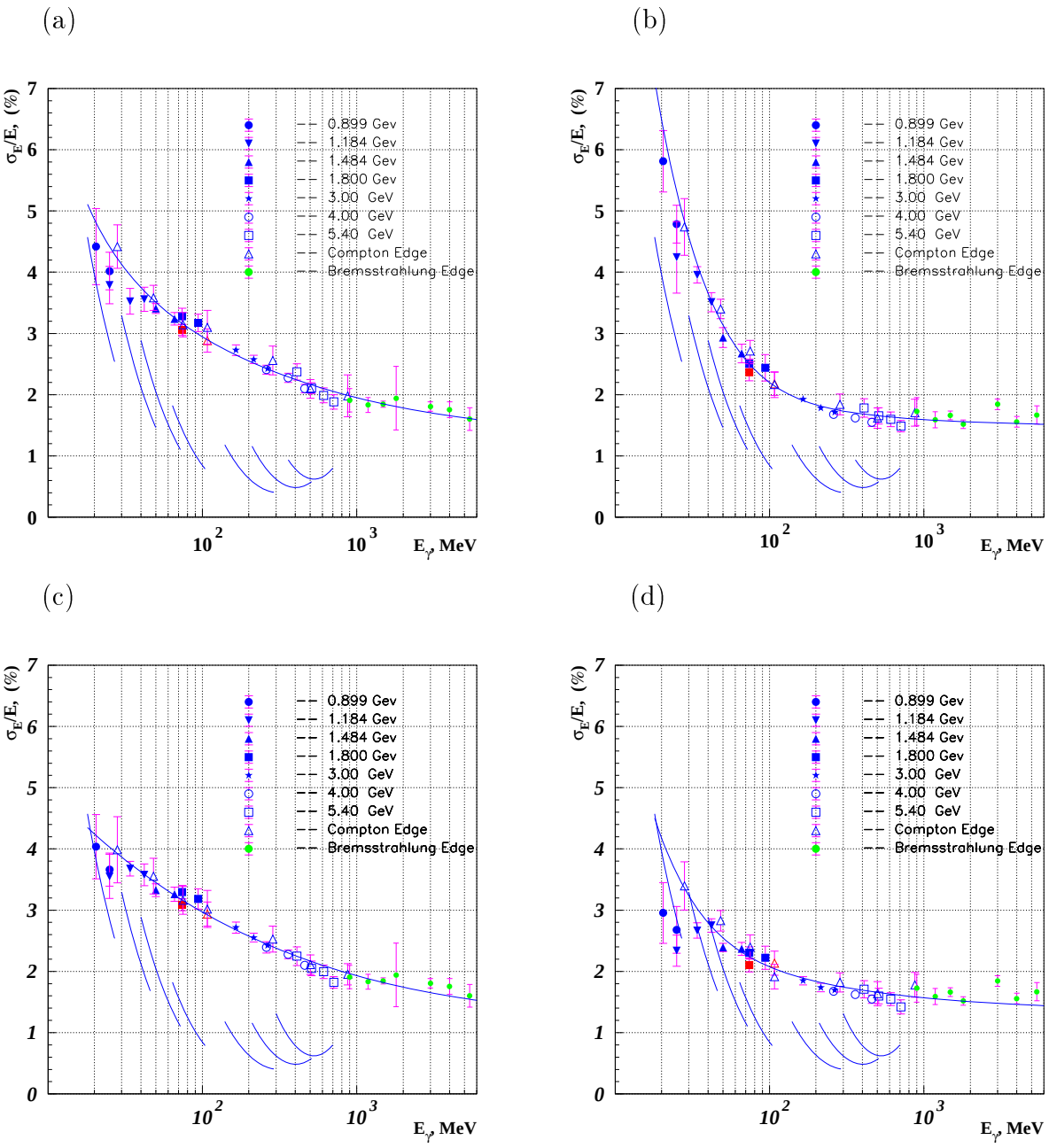

Figure 6.23: Energy resolution as a function of incident photon energy for (a)3 × 3 and (b) 5 × 5 matrix by the simple sum. The energy resolution of (c)3 × 3 and (d)5 × 5 matrix with the threshold of 0.5 MeV. Solid lines are results of the fitting. The resolution of the tagging system is given in seven separate lines below the data points.

The resolutions obtained by three methods (i.e. R_E, Compton edge, Bremsstrahlung edge analysis) are in good agreement each other for an energy range from 20 MeV to 5.4 GeV. The result of 3×3 matrix is better than 5×5 in the region below 40 MeV where the electronics noise makes a dominant contribution to the resolution.

The resolution can be fitted by the quadratic sum ($\oplus$) of the following three terms. The first term is from the contribution of electronics noise, the second term and a part of the third term represent the shower leakage fluctuation and the third term also includes the systematic effects such as the calibration uncertainty of the crystals.

The results are

$$\frac{\sigma_E}{E} = \frac{0.053(\%)}{E} \oplus \frac{1.46(\%)}{E^{1/4}} \oplus 1.30(\%), \quad E \text{ in GeV} \tag{6.13}$$

for 3×3 matrix and

$$\frac{\sigma_E}{E} = \frac{0.127(\%)}{E} \oplus \frac{0.55(\%)}{E^{1/4}} \oplus 1.47(\%), \quad E \text{ in GeV} \tag{6.14}$$

for 5×5 matrix.

The solid lines in Fig. 6.23 are the results of the fitting.

6.7.6 Energy Resolution with Threshold

Fig. 6.24 shows the number of counters which have the energy deposit greater than certain threshold value in 5×5 matrix. The number depends on the incident photon energy. We note that the number of counters with significant energy deposits is much less than 25 at low energy. We expect the energy resolution at low energy improves if we remove counters with no significant energy deposit.

Fig. 6.25 shows the energy resolution v.s. number of summed counters for several energy points. All the energy deposits in 5×5 matrix are arranged in energy decreasing order and only the first n counters were used for the summation of energies.

As seen in Fig. 6.25, the energy resolution for low energy photon starts deteriorating with more number of counters because the electronics noise effect goes up when the number of summed counters increase. The contribution of electronics noise is small above 100 MeV. When we limit the number of summed crystals to less than 10, the resolution is worse again due to the leakage of the shower.

In order to determine the optimum threshold for selecting the counters to be added, we plotted the threshold dependence of the energy resolution in Fig. 6.26. The best resolution is obtained at around 0.5 MeV.

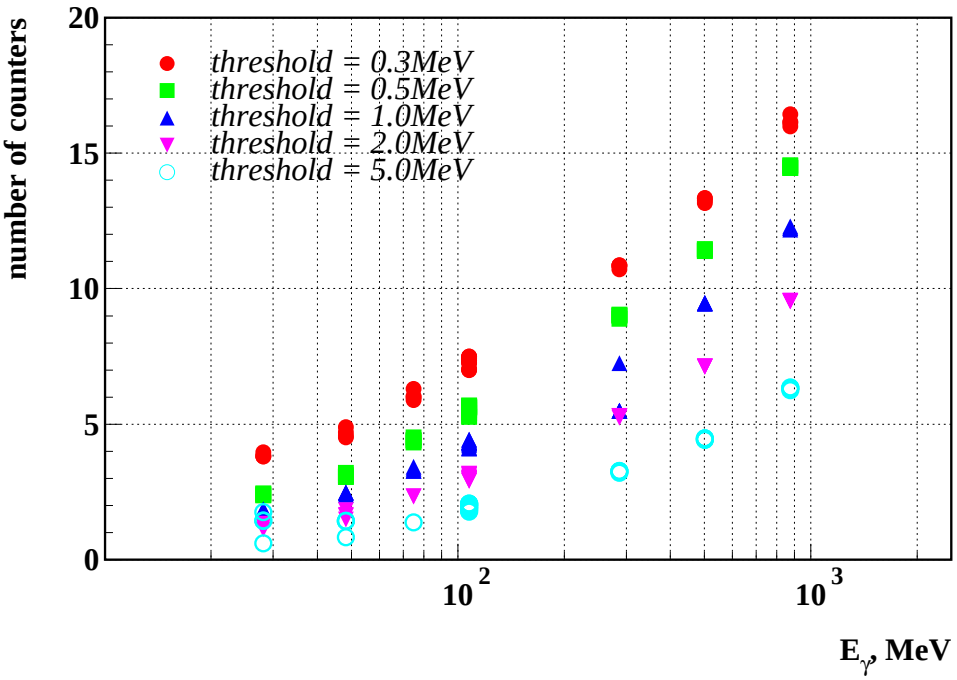

Figure 6.24: Most probable number of counters with energy deposit greater than the threshold.

The energy resolution of 3 × 3 and 5× 5 matrix obtained with the threshold of 0.5 MeV is shown in Fig. 6.23(c)(d) together with the fitting result in solid line. The result of fitting is

$$\frac{\sigma}{E} = \frac{0.0066(\%)}{E} \oplus \frac{1.53(\%)}{E^{1/4}} \oplus 1.18(\%), \quad E \text{ in GeV} \tag{6.15}$$

for 3 × 3 matrix and

$$\frac{\sigma}{E} = \frac{0.066(\%)}{E} \oplus \frac{0.81(\%)}{E^{1/4}} \oplus 1.34(\%), \quad E \text{ in GeV} \tag{6.16}$$

for 5 × 5 matrix.

The contribution of electronics noise and the resolution decreased as expected.

6.7.7 Comparison with Monte Carlo Simulation

The Monte Carlo simulation was done using GEANT program package. CsI crystals are piled up in 6 × 6 matrix as in the real experimental setup. The wrapping material of the crystal and 0.5 mm thick aluminum sheet in between crystals are also included.

The Compton photon beam is generated with the energy distribution described in

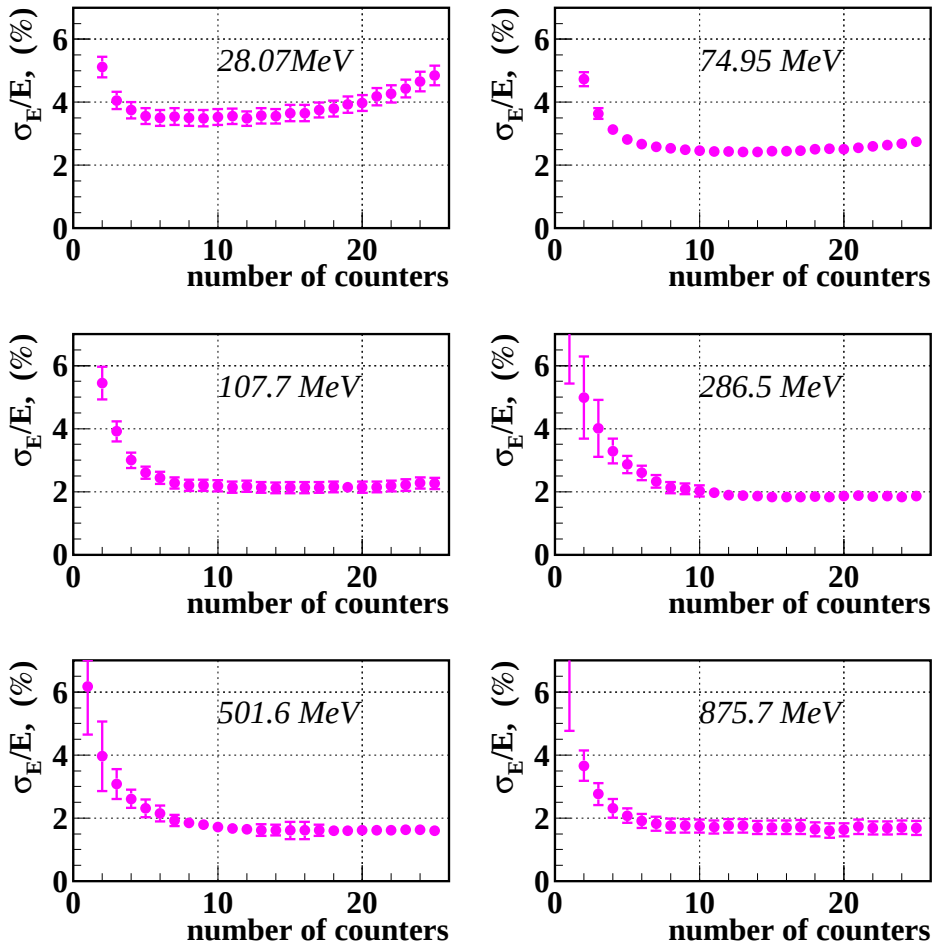

Figure 6.25: Number of counters used in the summation of energy vs energy resolution.

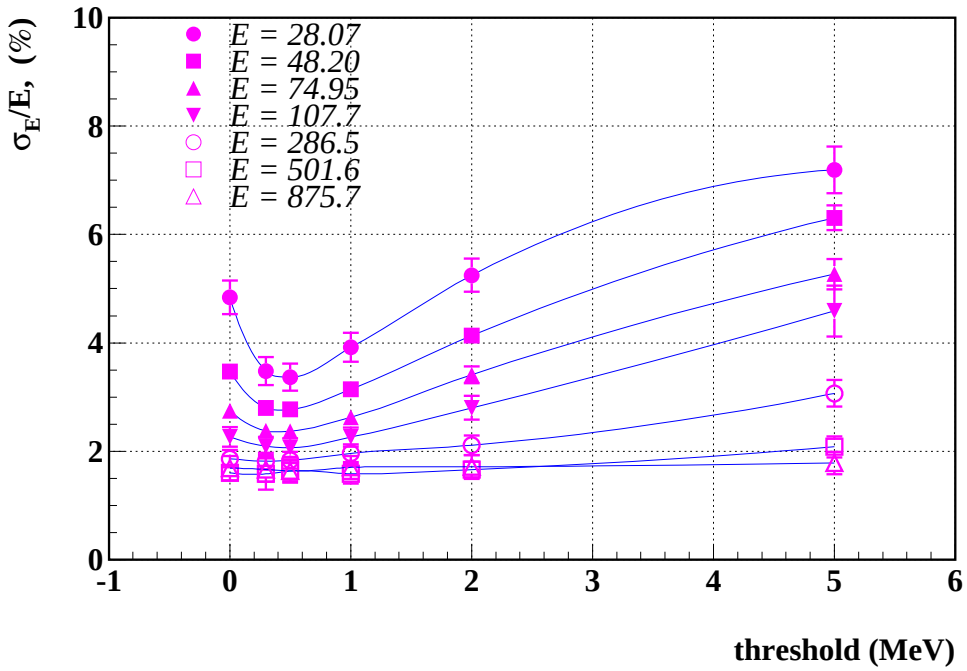

Figure 6.26: Threshold dependence of the energy resolution.

(6.1). For the Bremsstrahlung beam, monochromatic photons with energy corresponding to the Bremsstrahlung edge are used.

The spread of the beam at the matrix front face was simulated with the following formula (6.17), (6.18) with $S_x = 1$ cm, $S_y = 1$ cm for both Compton and Bremsstrahlung runs. All the photons were injected normal to the matrix front face with no angular spread.

$$f(x) = \frac{1}{1 + (\frac{x - x_0}{S_x})^2}. \tag{6.17}$$

$$f(y) = \frac{1}{1 + (\frac{y - y_0}{S_y})^2}. \tag{6.18}$$

x_0, y_0 : peak of the fitting
S_x, S_y: width of the fitting

The photon and electron in the shower was tracked down to 10 keV[‡]. Every energy deposit in each tracking step was weighted by the non-uniformity function obtained by the cosmic ray calibration. The 3rd order polynomial function was used to represent the measured non-uniformity. After summing all the energy deposits in one crystal,

[‡]CUTGAM = CUTELE = 10 keV in GEANT parameter.

smearing by the incoherent electronics noise of 189 keV and the coherent noise of 16.5 keV was added.

In order to correct the energy shift caused by the arbitrary scale of non-uniformity, the energy deposit is simulated without non-uniformity. The simulated Compton edge of the perfectly uniform crystal is 489.4 MeV in 5×5 sum for 502 MeV Compton beam. When the original scale of the non-uniformity is used, the Compton edge became 480.6, 476.9, 476.3, 477.7 MeV for the central four counters. We multiplied the uniformity function by 1.024 such that the average of four Monte Carlo simulations becomes equal to the uniform simulation result.

The distribution of the beam incident position for the Compton beam is shown in Fig. 6.27 for the data and Monte Carlo simulation. The scatter plot shows the X position v.s. Y position of the beam calculated by the center of gravity method by the following equation.

$$X_c = \frac{\sum_{i=1}^{36} X_i E_i}{\sum_{i=1}^{36} E_i}, \tag{6.19}$$

$$Y_c = \frac{\sum_{i=1}^{36} Y_i E_i}{\sum_{i=1}^{36} E_i}. \tag{6.20}$$

where X_i and Y_i are coordinate of the center of the i-th counter and E_i is the energy deposit in the i-th counter.

The histograms are the distributions of X_c and Y_c with fitting results. In the Monte Carlo, X_c and Y_c became similar value.

Fig. 6.28 and Fig. 6.29 show the comparison between the real data and the simulation result on R_E and the Compton spectrum, respectively for various energy of photons. Inefficiency of the lower part of real data are caused by the trigger threshold in STM module and the acceptance of the TS trigger counter. The data are well reproduced by the simulation for all the distributions.

Fig. 6.30 show the results of the Monte Carlo on the energy resolution. For the R_E analysis in Monte Carlo simulation, the energy deposit in CsI crystal was calculated at first. The TS resolution generated by Gaussian was then added to the 3×3 and 5×5 sum. After the fitting of R_E, the TS resolution was subtracted quadratically in the same way as for the data. The results of the simulation are consistent with the data.

In order to make a clear comparison, Fig. 6.31 shows the overlay of the data and simulation for the resolution of 5×5 sum with 0.5 MeV threshold. In the figure, the dot with error bar reproduces the real data plotted in Fig. 6.23(d) and the solid line shows the fitting result of simulation shown in Fig. 6.30(d). They are in excellent

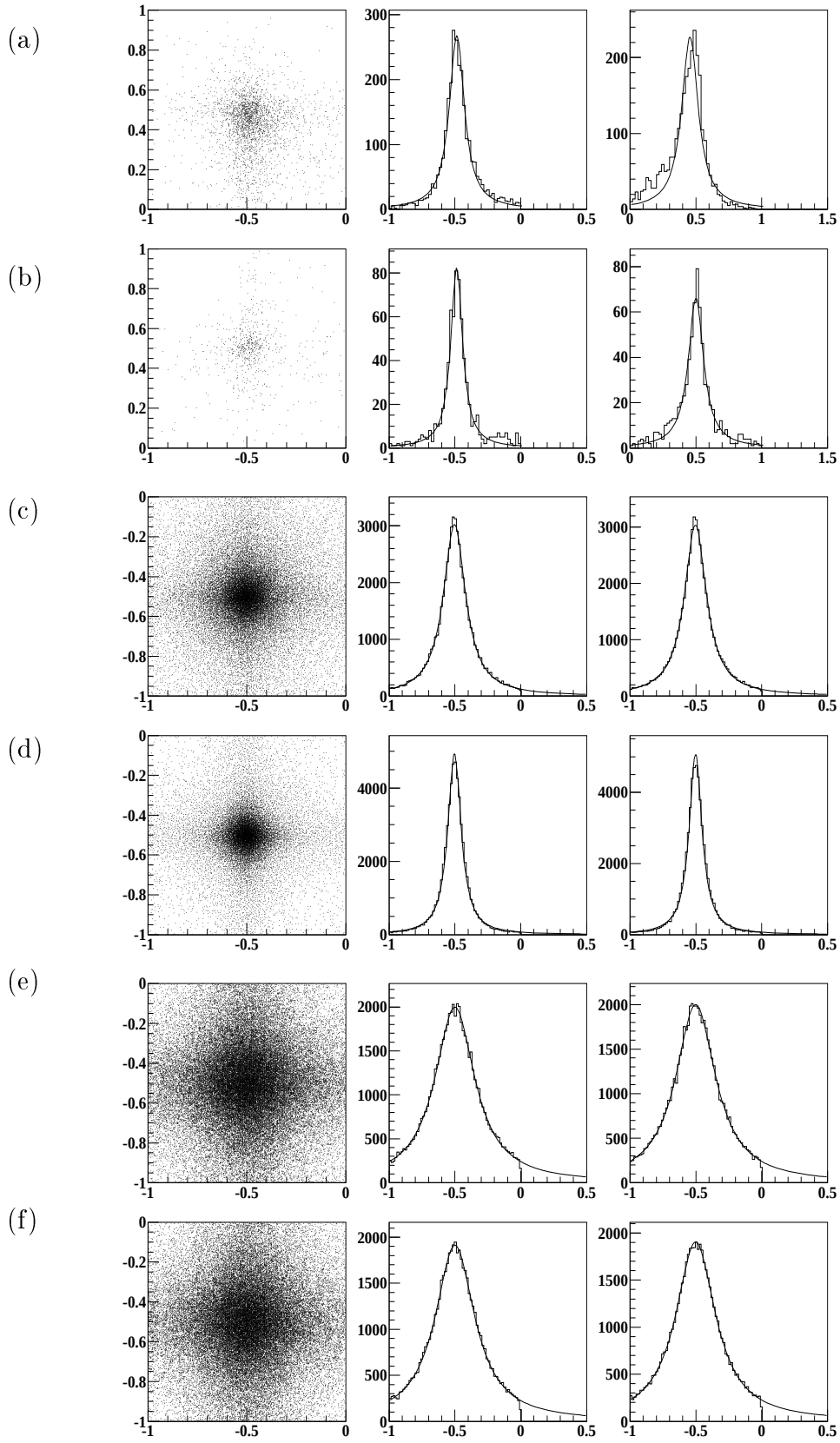

Figure 6.27: Position of beam injection point by the center of gravity method for (a)(c)1810.MeV (b)(d)5441.MeV. (a)(b) are data and (c)(d) are Monte Carlo simulation (MC) results. (e)(f) are the real beam injected points in MC. Left figures show X_c vs Y_c , middle figures show X_c distribution and right figures show Y_c distribution. The unit is the edge length of one crystal.

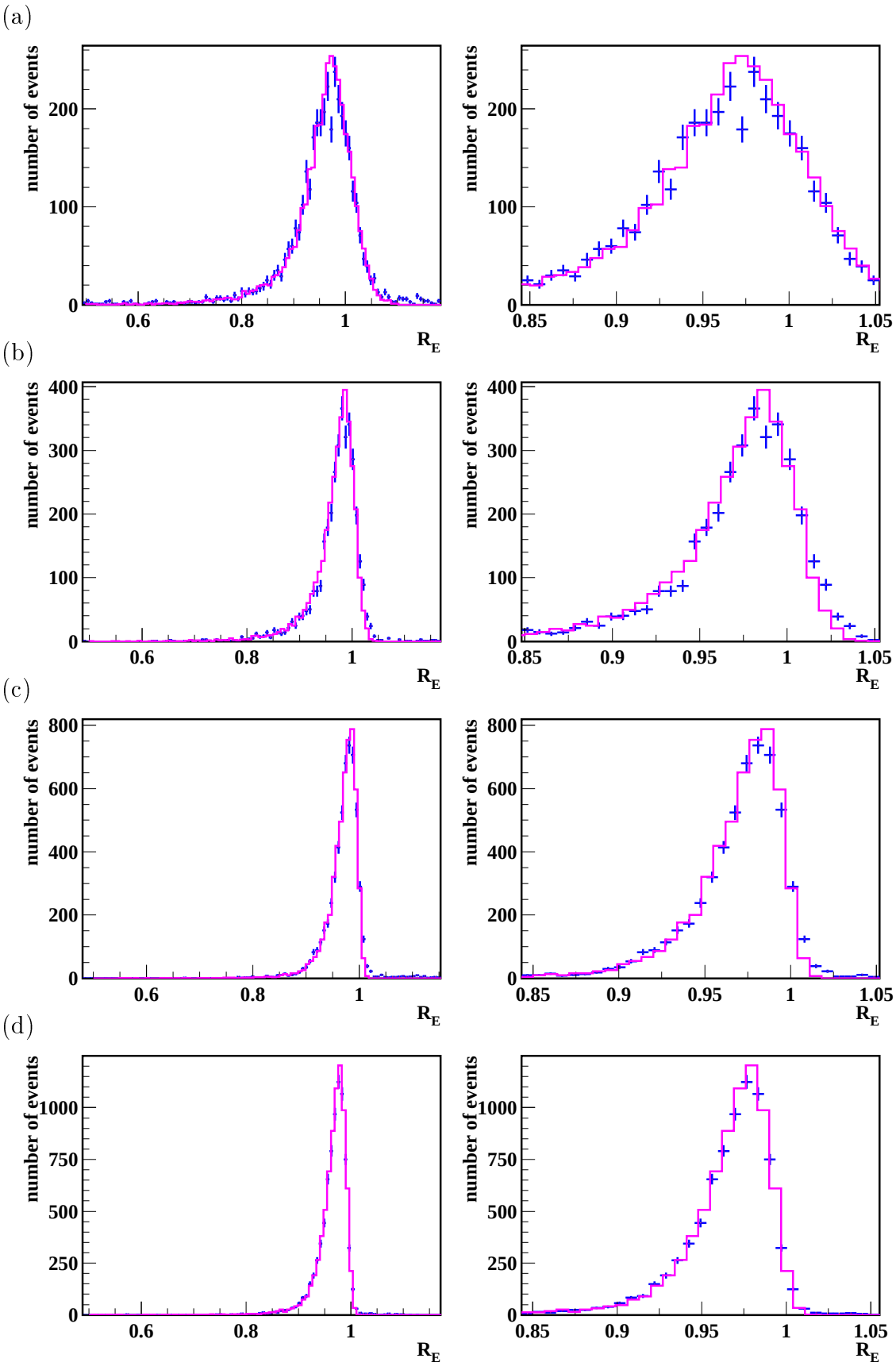

Figure 6.28: Comparison between data (cross) and simulation (histogram) of the R_E distribution for (a)27.5, (b)75, (c)300 and (d)500 MeV photon. The right figures are expanded view near the peak.

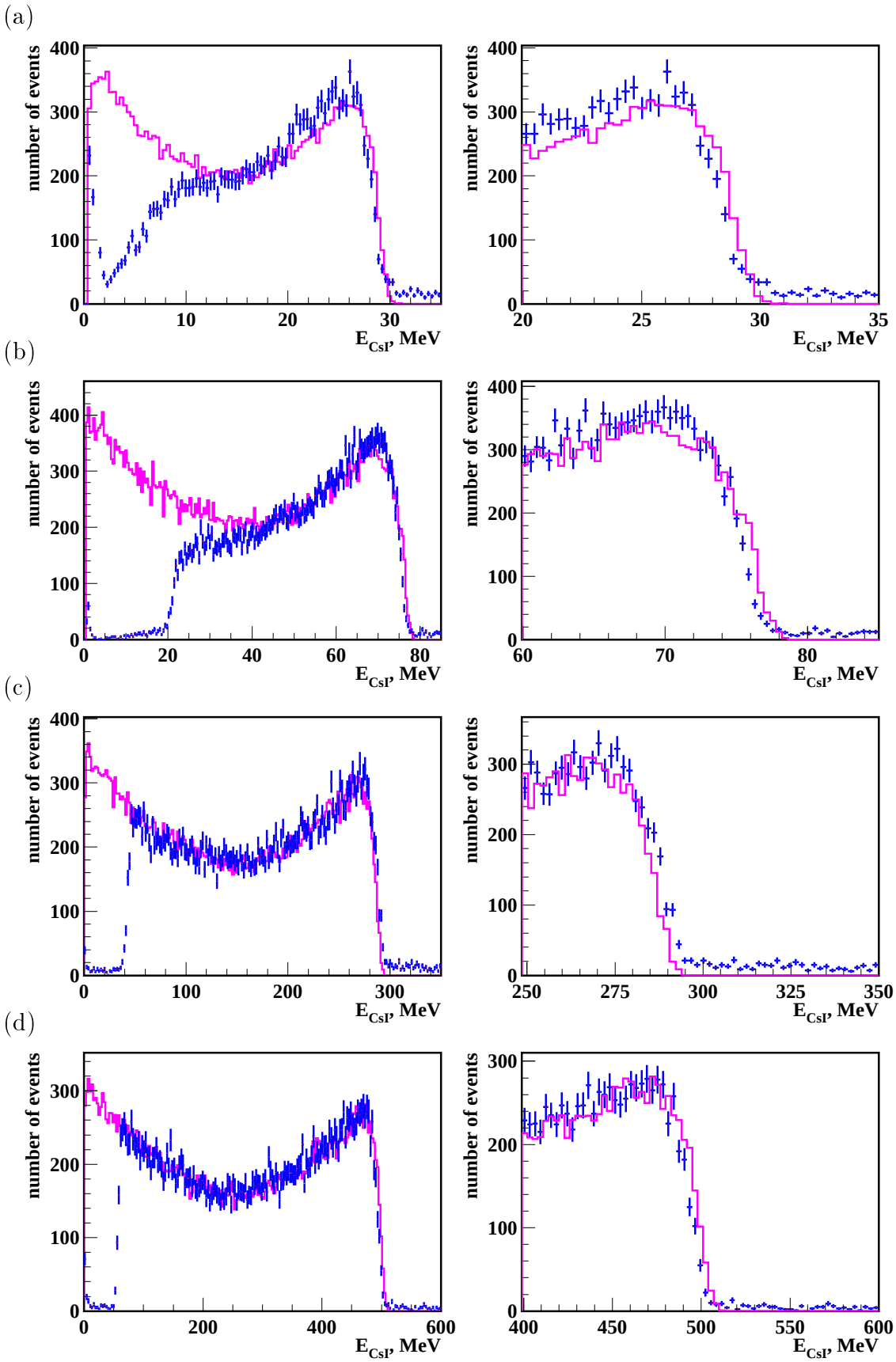

Figure 6.29: Comparison between real data (cross) and simulation(histogram) of the Compton edge of (a)29.4, (b)76.8, (c)291.5 and (d)508.3 MeV. The right figures are expanded view of the edge part.

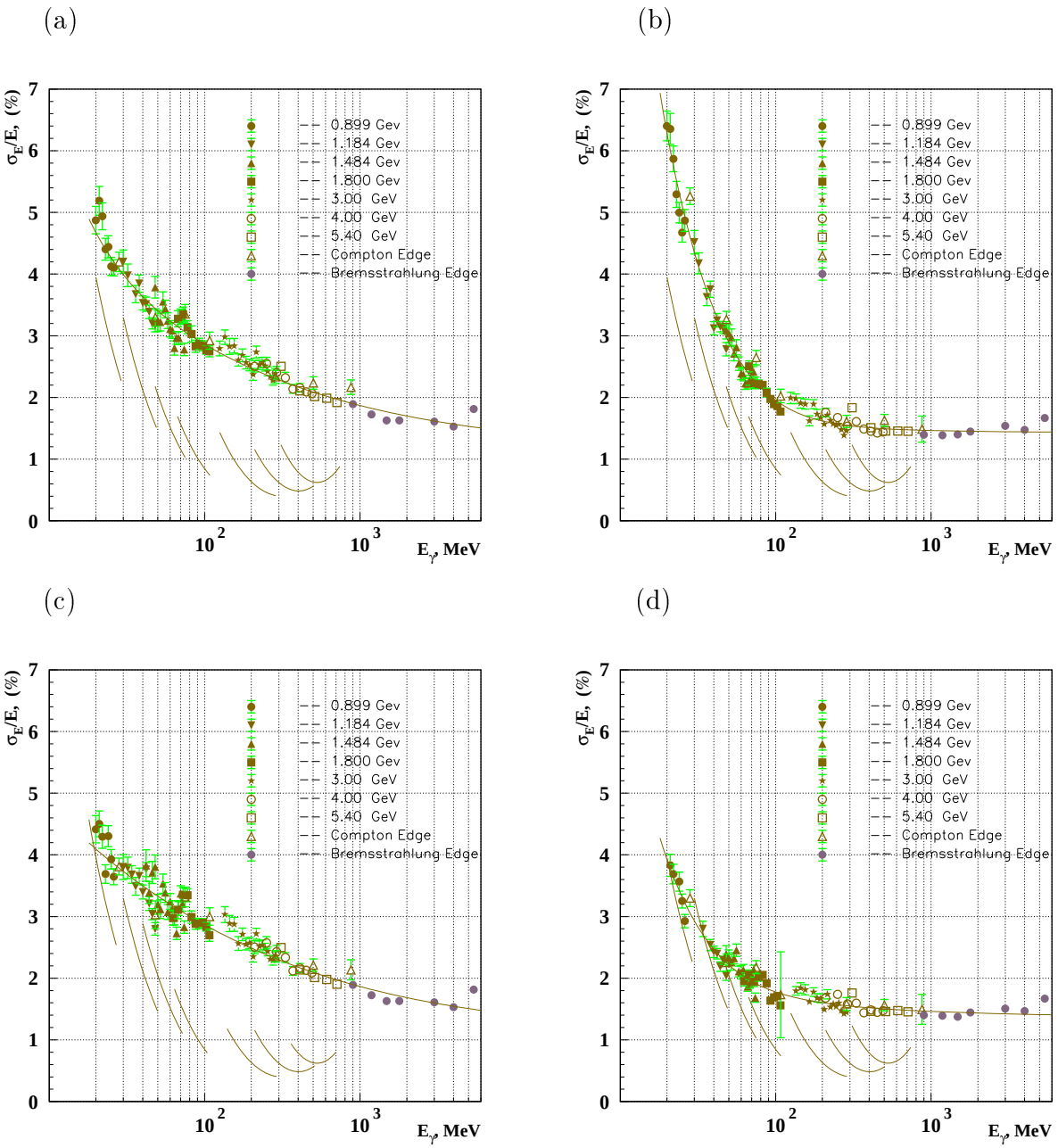

Figure 6.30: Monte Carlo simulation (MC) results of energy resolution of (a)3 × 3 and (b)5 × 5 counters, and energy resolution of (c) 3 × 3 and (d) 5 × 5 with threshold = 0.5MeV. Tagging System resolution which are drawn by solid line is included in MC and subtracted after fitting.

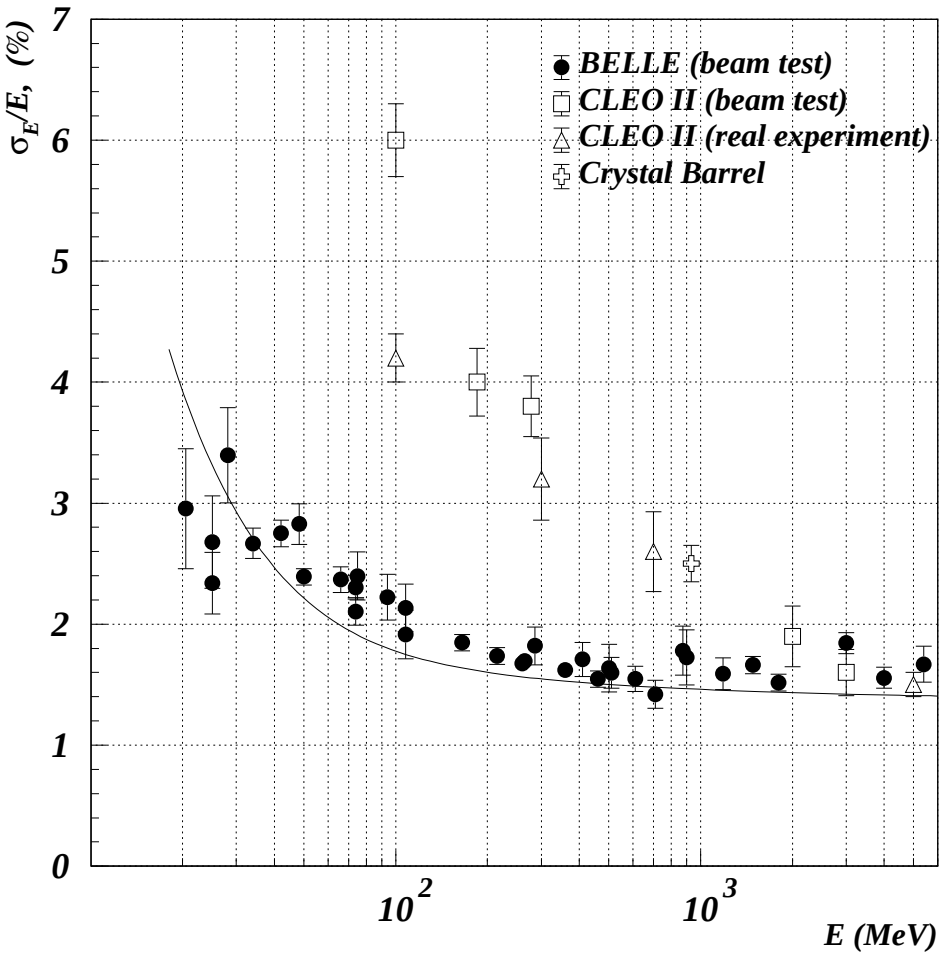

Figure 6.31: Energy resolution of 5 × 5 matrix with threshold of 0.5 MeV. The solid line is the fitting to the Monte Carlo resolution (see Fig. 6.30d). CLEO II beamtest results are obtained for 3 × 3 matrix.

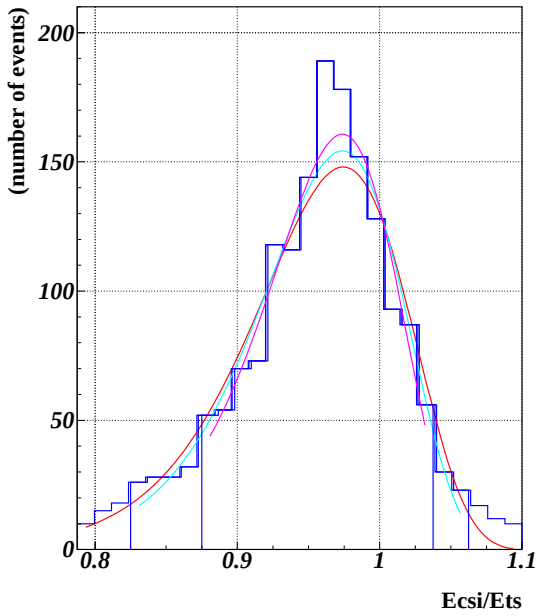

Figure 6.32: R_E distribution with different fitting regions for $E_\gamma = 25$ MeV. Different fitting regions correspond to removing histogram bins less than 5, 10, 20 % of the peak bin.

agreement. The results from CLEO and Crystal Barrel are also plotted for comparison [67] [68] [69].

6.7.8 Error in Resolution

The statistical error given by the fitting program MINUIT is at the level of 0.1 % and negligible for most of the results.

For the tagged photon analysis, the resolution of TS used for the subtraction is estimated from the expected accelerator parameters. In Fig. 6.23(b), we only used the region of tagged photon energy where the TS resolution is smaller than 60 % of the CsI resolution. The same energy region determined this way was applied to all subsequent plots on energy resolution. The fitting method also has an influence on the result. They are, for example, the fitting region, the initial parameter setting, the value of fixed asymmetry parameter and the shape of background contribution. The effect from these factors were checked by varying the parameter and by applying different procedures for the fitting. The effect was mostly negligible except for one described below.

For the fitting of R_E, the cut off is set at 20 % of the peak value to remove the tail part from the fitting. The χ^2 of the fitting usually became best at that value.

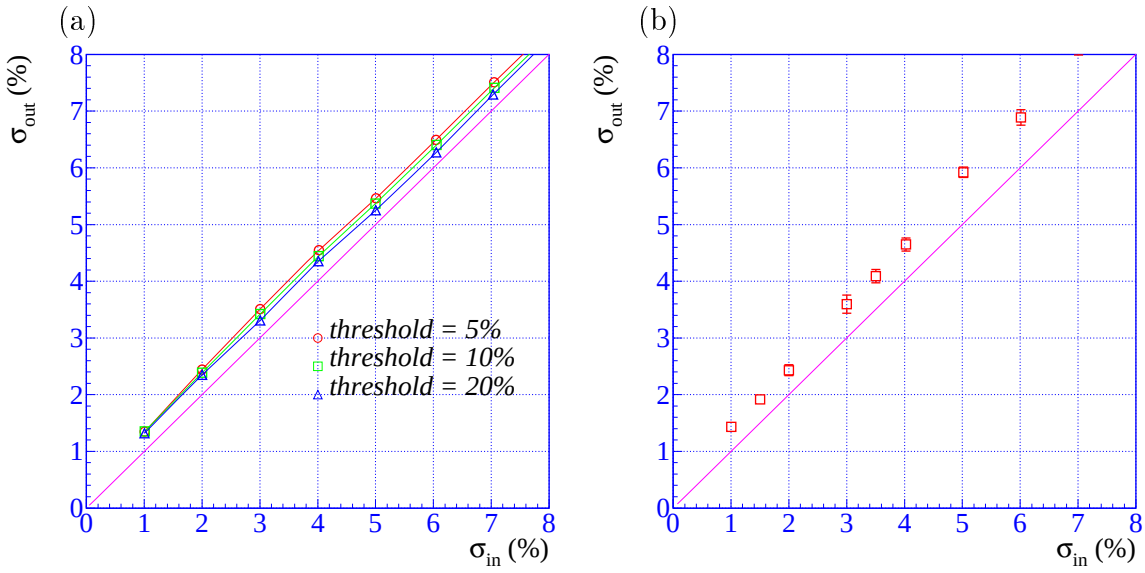

Figure 6.33: (a)Correlation of the generated R_E resolution σ_{in} and obtained resolution σ_{out} after fitting and subtraction of the TS resolution with $\sigma_{TS} = 3.3\%$. (b)Results of the same practice for the Compton edge resolution.

The variation of the fitting for different cut off value are shown in Fig. 6.32 for the R_E distribution at $E_\gamma = 25$ MeV. When the cut off value was changed, the result of resolution changed between 4.5 % and 5.3 %.

For the purpose of checking the fitting procedure, we made a simple Monte Carlo program. We produced the distribution of R_E $(= \frac{E_{CsI}}{E_{TS}})$ by generating E_{CsI} by the logarithmic Gaussian and E_{TS} by the Gaussian. Then we fitted R_E by the logarithmic Gaussian and subtracted the resolution of E_{TS} quadratically from the resolution of R_E to obtained the resolution of E_{CsI} (see section 6.7.1). This is the same procedure as we used to get σ_E from the data. Fig. 6.33 shows the result with $\eta = 0.47$ and $\sigma_{TS} = 3.3$ % corresponding roughly to the photon energy of 30 MeV. The different marks mean the different cut-off thresholds used to determine the fitting region. If our fitting procedure is perfect, the E_{CsI} resolution obtained after fitting $(=\sigma_{out})$ should be equal to the E_{CsI} resolution used for the generation $(=\sigma_{in})$. The results have some systematic deviation from $\sigma_{out} = \sigma_{in}$ line. This is because the energy spectrum of CsI is not Gaussian and the tagging system resolution is not perfectly subtracted.

The same study is done to the Compton edge fitting. Theoretical Compton distribution (6.1) is generated and convoluted with the CsI response function. The fitting result given in Fig. 6.33 shows a similar systematic shift.

For every photon beam setting, we repeated the measurement four times, and for

each time the beam was injected at the center of one of the four central crystals. The error bars in Fig. 6.23 is not statistical error but the rms deviation of four measurements. We note that the results obtained by three methods (R_E, Compton and Bremsstrahlung edge) are in good agreement each other. The results of R_E from different electron beam settings overlaps in the same energy region. Considering different methods have different systematics, we think the error bars assigned to the Fig. 6.23 from the rms deviation of four measurements are realistic. An estimate of additional systematic error is difficult, but the simulation study of fitting procedure described above suggests it is at the level of 0.5 %.

6.8 Energy Linearity

6.8.1 Compton Edge and Bremsstrahlung Edge

The energy linearity is analyzed by using the edge values of the Compton and Bremsstrahlung distribution. The information of the tagging system was not used for this analysis to avoid additional complication from the non-linearity of the TS response.

The Compton edge and Bremsstrahlung edges are fitted with the convolution of the theoretical distribution and the CsI response function as explained in the previous section. The values obtained from the fitting of the data E_{CsI} and the theoretical edge value E_{TH} calculated from the electron beam energy are plotted in Fig. 6.34(a). The value of E_{CsI} is calculated as the 5×5 matrix sum with 0.5 MeV threshold. The deviation from the linear response, $(E_{CsI} - E_{TH})/E_{TH}$, is plotted in Fig. 6.34(b). The error is estimated in section 6.8.3. For all the energy ranges, the deviations are negative because of the shower leakage from the central 5×5 counters. The leakage from the back of the crystal becomes dominant at high energy and makes a larger negative deviation.

6.8.2 Comparison with Monte Carlo Simulation

The same GEANT setup is used for the resolution analysis. The deviation from the linear behavior is shown in Fig. 6.35. The error bar is the rms of four different runs. The shower leakage effect found in the higher energy data is well reproduced by the Monte Carlo. The deficiency of energy deposit in the lower energy is caused by the non-uniformity of CsI crystals. The results with perfectly uniform crystal is shown in Fig. 6.36 to demonstrate this effect.

(a)

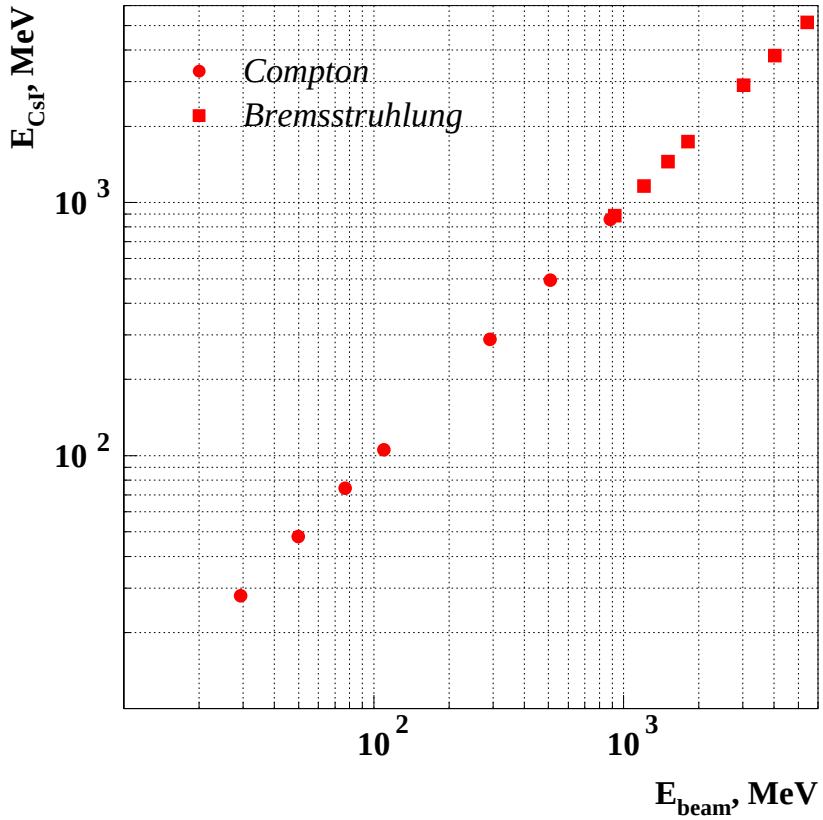

(b)

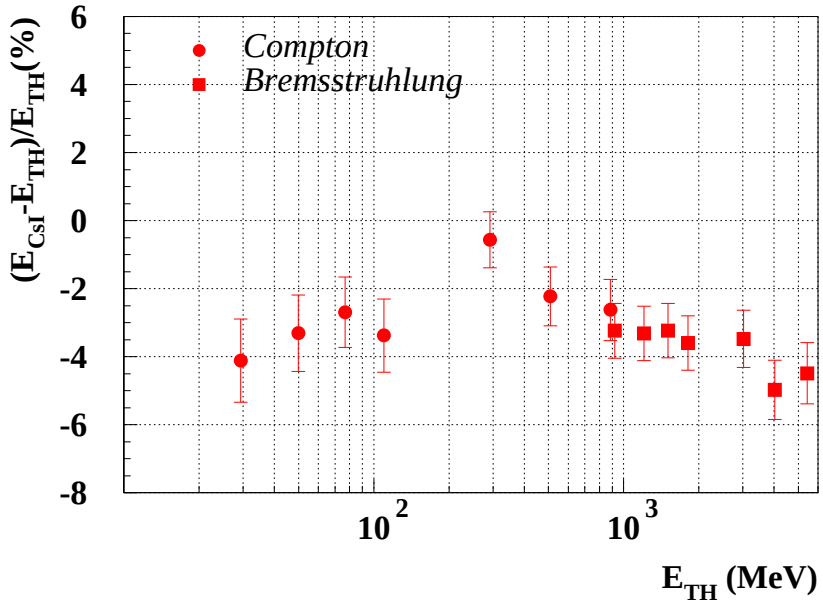

Figure 6.34: (a)Incident photon beam energy vs measured energy in CsI for data. (b)Energy linearity for data.

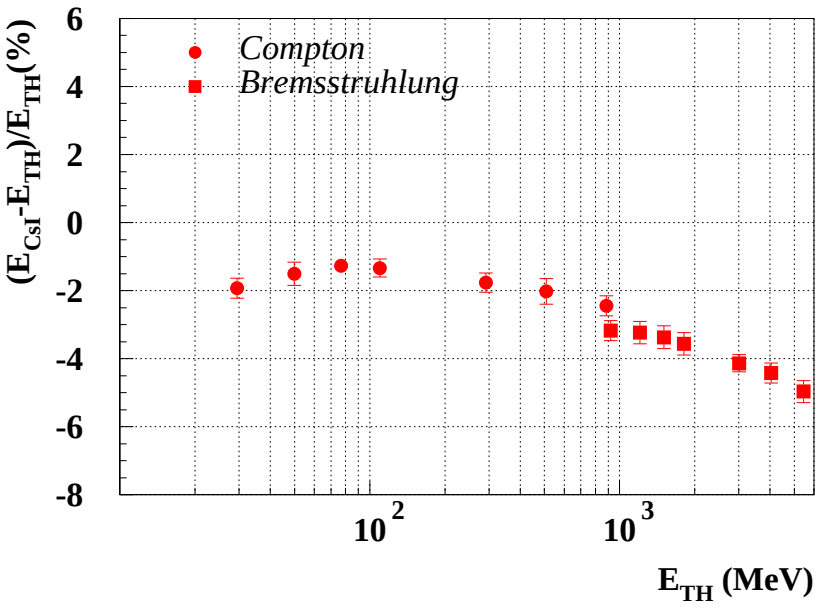

Figure 6.35: Energy linearity for MC.

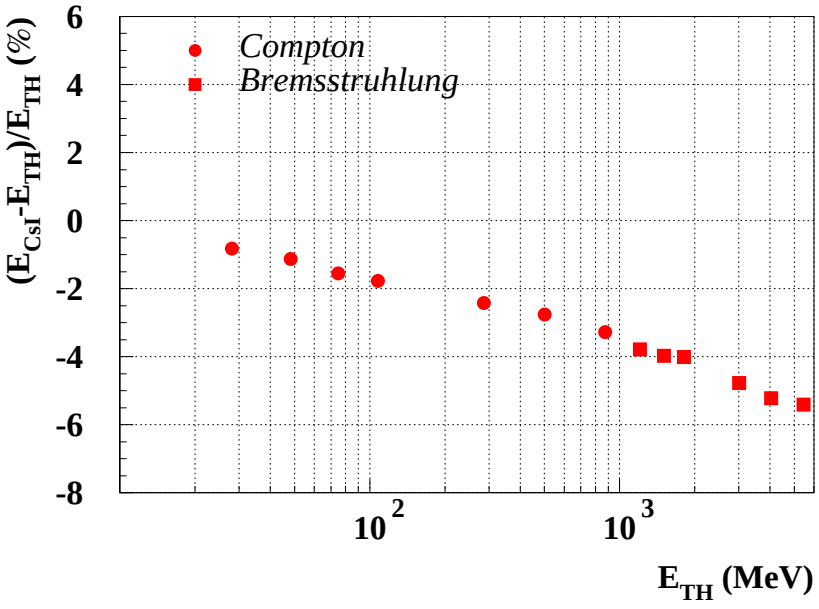

Figure 6.36: Energy linearity for Monte Carlo simulation. Perfectly uniform light output is assumed.

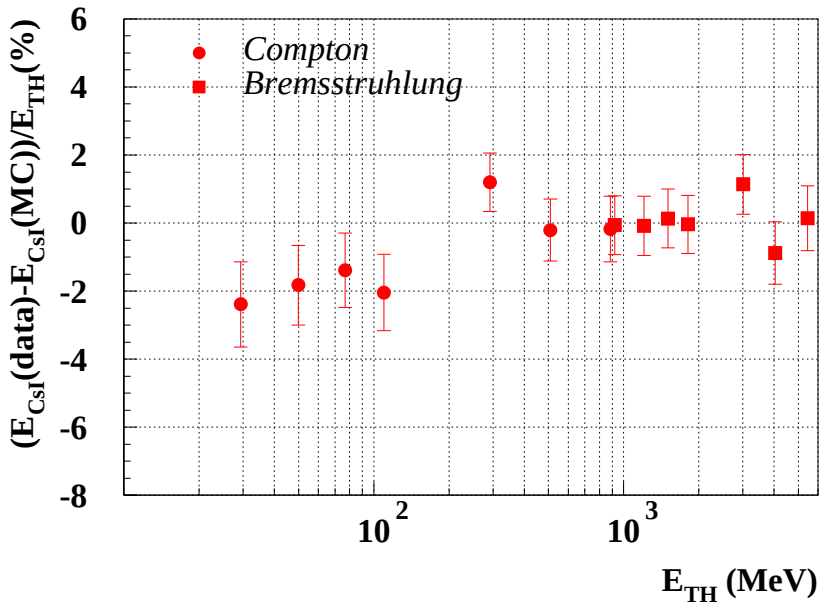

Figure 6.37: Difference of energy linearity between data and M.C.

Fig. 6.37 show the difference between real data (Fig. 6.34) and simulation results (Fig. 6.35). The differences are within ± 2 % for all energy range.

6.8.3 Discussion

An estimate of errors for the linearity plot is tabulated in Table. 6.2. We explain each source of errors in the following.

The statistical error is obtained by the MINUIT routine of the fitting. It is larger at low energy but is still at the negligible level.

All counters are calibrated at the photon beam energy of 508 MeV. Different light collection uniformity can make a different linearity behavior for the four counters tested. The rms deviation of four counters becomes larger in the low energy region and it seems to support this idea. Some of the data points were measured more than once and the rms in the Table. 6.2 also includes the effect of time dependent factor.

As discussed in section 6.6, the time dependence of the calibration constant is followed by the cosmic-ray calibration. Fig. 6.38 shows the correction factor applied for the Compton photon run. The deviation is less than 1% and we guess it is mainly the temperature effect. We assign 0.5 % error to the temperature dependence of the calibration constant.

The incident beam position also affects the energy deposit in the crystal. The beam was targeted at the center of the crystal for all runs in all the energy ranges. But it

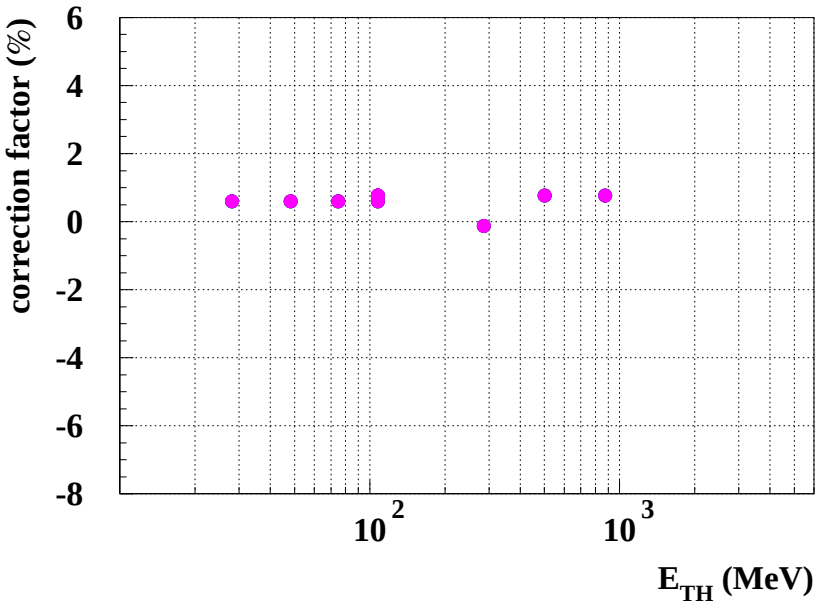

Figure 6.38: Time dependent correction factor determined by cosmic calibration. The reference point is the cosmic data nearest to the beam calibration run, which is not included in this plot.

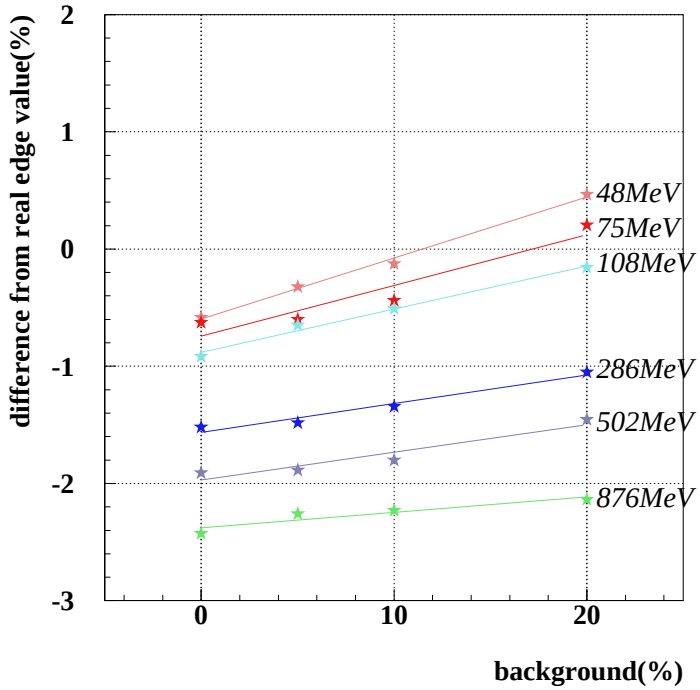

Figure 6.39: Variation of fitted Compton edge with different amount of 2 photon background simulation study.

(a)

Error source vs. Beam Energy	29.4	49.8	76.8	109.8	291.5	508.3	884.7
statistical error from MINUIT	0.13	0.06	0.03	0.02	0.006	0.003	0.002
variation among 4 counters	0.84	0.80	0.77	0.74	0.19	0.15	0.13
temperature	0.5	0.5	0.5	0.5	0.5	0.5	0.5
incident point	-	0.03	0.015	0.015	-	-	-
background	0.4	0.4	0.28	0.31	0.18	0.08	0.09
fitting procedure	0.25	0.15	0.10	0.11	0.07	0.05	0.12
electronics linearity	0.3	0.3	0.3	0.3	0.3	0.3	0.3
pedestal measurement	0.30	0.21	0.21	0.18	0.11	0.079	0.057
Electron beam energy estimation	0.33	0.21	0.13	0.36	0.50	0.60	0.66
quadratic sum	1.22	1.12	1.04	1.08	0.82	0.86	0.90

(b)

Error source vs. Beam Energy	921.	1206.	1506.	1810.	3007.	4036.	5441
statistical error from MINUIT	0.08	0.08	0.05	0.05	0.11	0.09	0.11
variation among 4 counters	0.53	0.53	0.53	0.53	0.53	0.53	0.53
temperature	0.5	0.5	0.5	0.5	0.5	0.5	0.5
incident point	-	-	-	-	0.008	-	-
background	-	-	-	-	-	-	-
fitting procedure	0.05	0.10	0.10	-	0.05	0.15	0.20
electronics linearity	0.3	0.3	0.3	0.3	0.3	0.3	0.3
pedestal measurement	0.01	0.008	0.007	0.005	0.003	0.002	0.001
Electron beam energy estimation	0.16	0.10	0.07	0.04	0.26	0.32	0.36
quadratic sum	0.81	0.80	0.80	0.80	0.84	0.87	0.90

Table 6.2: Systematic error estimation of (a)Compton photon and (b)Bremsstrahlung photon(unit : %).

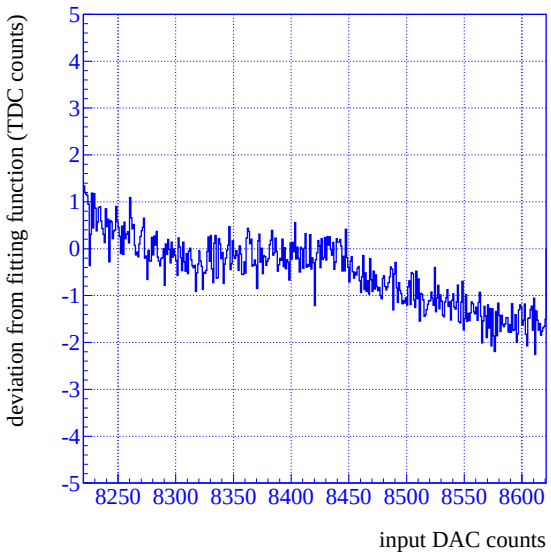

Figure 6.40: Electronics linearity measured by the test pulse for $0 - 100$ MeV.

sometimes shifted a few mm in the center of gravity position (X_c,Y_c). The displacement of δX_c or $\delta Y_c \equiv 0.1$ causes the 0.03 % energy shift. From the beam position of each run, we calculated the amount of energy shift and listed them in the Table. 6.2.

The Compton distribution has the 2 photon background and it is modeled as a triangular shape in the fitting routine (see Fig. 6.20). If the background estimation is not correct, the Compton edge value has some shift. By using a simple Monte Carlo program, we generated smeared Compton spectrum with different amount of 2 photon backgrounds. They are fitted by the flat and triangular shape of background and the values of obtained Compton edge are compared. The results are shown in Fig. 6.39. The difference also depends on energy. The real background of the data was different run by run but it was less than 10 %. The estimated error is listed in the Table. 6.2.

The Compton edge value obtained by the fitting varies with the fitting region. For the values shown in Fig. 6.34, the fitting region is limited to $\pm$ 5 σ around the Compton edge obtained by the first preliminary fitting. In order to estimate the effect, the fitting region was changed to 50 $\sim$ 180 % and 90$\sim$ 120 % of the edge value. The difference is 0.1 $\sim$ 0.5 MeV in all the energy ranges and its effects listed in the Table. 6.2.

The electronics linearity is good as mentioned in section 6.5.2. However, a special electronics calibration was done to check the linearity especially in low energy range. Fig. 6.40 shows the result corresponding to the energy region of 0 $\sim$ 100 MeV. In the energy region lower than 50 MeV, the deviation was $\pm$ 1 TDC count and it corresponds

to 100 keV.

We also made a special source test of the electronics to confirm the linearity below 2.5 MeV. We prepared a small CsI(Tℓ) crystal and attached the photomultiplier and the photodiode at both ends of the crystal as shown in Fig. 6.41(a). A ^{137}Cs was placed on the crystal and a ^{60}Co was buried in the crystal. The spectra obtained are shown in Fig. 6.41(b) and (c) for photomultiplier and photodiodes. The photopeaks at 0.662 MeV for ^{137}Cs, 1.173 and 1.333 MeV for ^{60}Co are clearly seen for the phototube in Fig. 6.41(b). The peak produced by the sum of 2 γ's (2.506 MeV) is also seen. We selected the event in the photopeak region by the photomultiplier data and plotted the distribution of the photodiode data. The photodiode data correspond to 0.662 MeV photopeak is shown in Fig. 6.41(e). The peak of this distribution corresponds to the energy deposit of 0.662 MeV in the crystal detected by the photodiode.

We collected two more sets of data by reducing the amount of light collected by the photodiode by a factor of $\sim$2 and $\sim$4. All three sets of data are fitted by a line keeping the ratio of four peak positions within one set constant (0.662 : 1.173 : 1.333 : 2.506) and only changing the scale between three sets. The result is shown in Fig. 6.42. The linearity is $\pm$ 0.5 % from 0 to $\sim$2.5 MeV*. This proves the good linearity of the electronics in the low energy region, independently from the test pulse measurement.

For the linearity analysis, we obtained the pedestal value for each run from the empty trigger mixed in the usual data taking trigger. In this way, we avoided the effect of drift from the pedestal values taken by the pedestal run. This was necessary because the Compton edge at low energy is sensitive to a small shift of the pedestal value. We estimate the error of the pedestal is 0.5 TDC counts and it corresponds to $\sim$ 35 keV.

The theoretical energy of the Compton or Bremsstrahlung edge E_{TH} also has a systematic error coming from the uncertainty of the electron beam energy. The nominal electron beam energy of VEPP4 storage ring was calibrated by using the harmonics of Nd:YAG laser. The laser can produce two harmonics ; the first harmonic corresponds to w = 1.1654 eV and the second harmonics is at w = 2.3308 eV. We can produce the some Compton spectrum by the 2nd harmonic with electron beam energy E_1 and by the 1st harmonic with electron beam energy E_2 ($E_1 < E_2$). As the ratio E_1/E_2 for the same Compton edge energy can be exactly calculable, we can measure the electron beam energy E_2 if we know the energy of E_1 exactly. Experimentally, the energy of E_1 was calibrated by the J/ψ observation by the KEDR experiment where VEPP4 was operated in e^+e^- collision made. We used our CsI matrix to check the Compton edge

*The energy scale of Fig. 6.42 is consistent within 10 % with the large crystal to be used in the BELLE experiment.

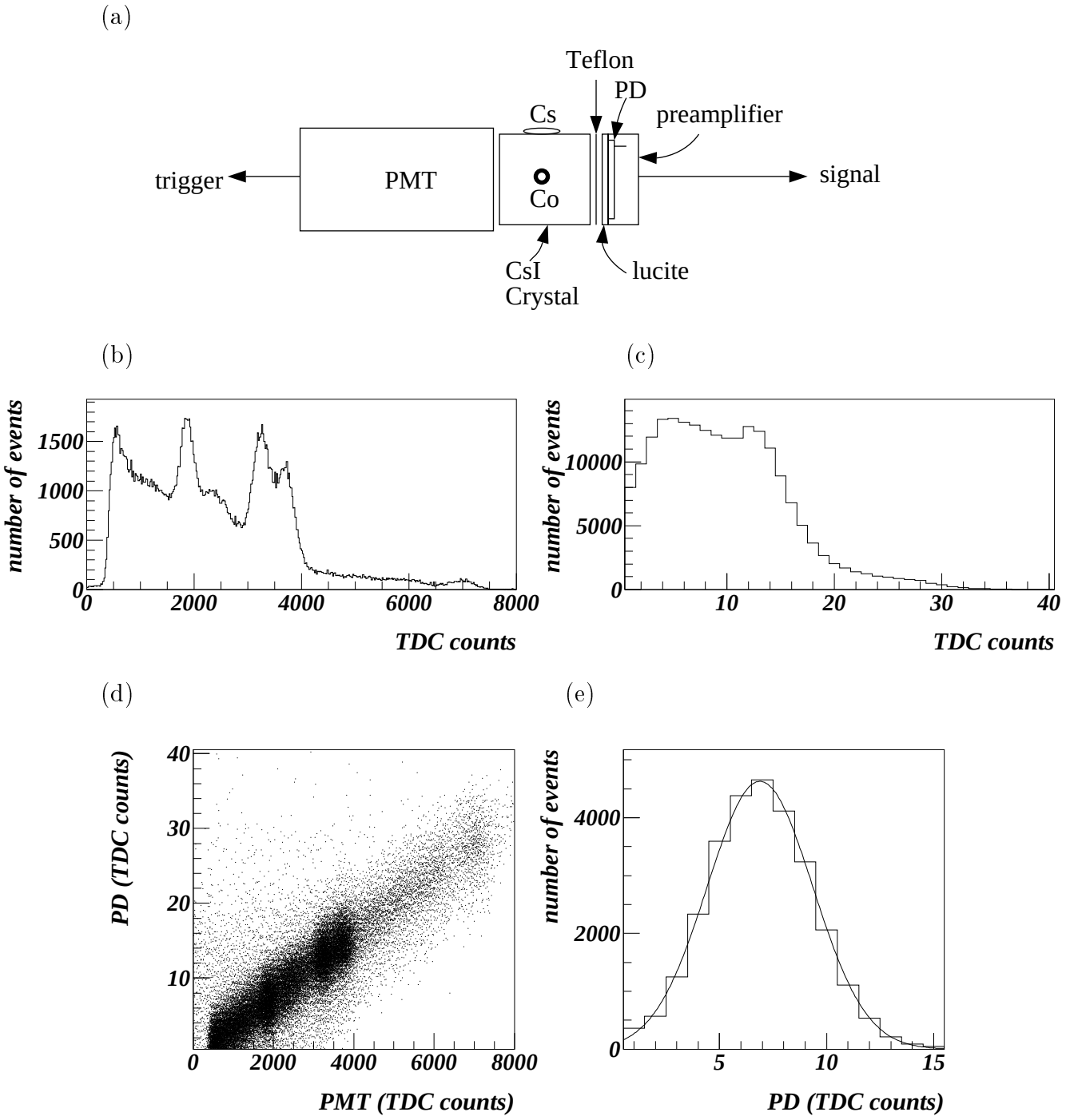

Figure 6.41: (a)Setup of the linearity measurement by using the ^{137}Cs and ^{60}Co sources and the spectrum with (b)photomultiplier and (c)photodiodes. (d)Correlation between photomultiplier data and photodiode data. (e)Photodiode spectrum corresponding to 662 keV ^{137}Cs photopeak selected by the photomultiplier data.

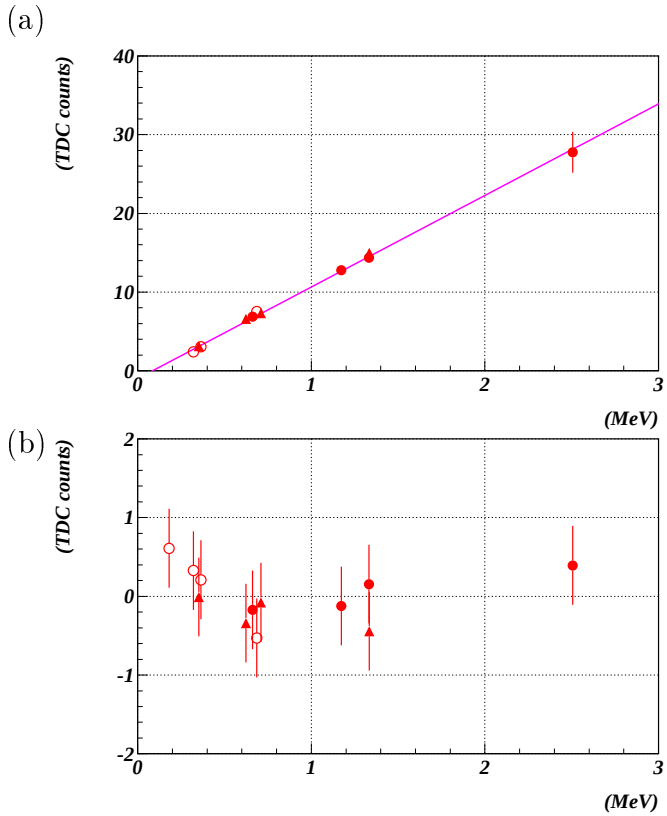

Figure 6.42: (a)Energy linearity measured by using the ^{137}Cs and ^{60}Co and (b)deviation from the linear response.

of E_1 is the same as the Compton edge E_2. As two edge energies could not be adjusted exactly, we applied a small correction on E_2 calculated from the energy difference of two edge energies. The electron beam energy was calibrated between $1090 \sim 4269$ MeV in 5 steps by this method and corrections of $20 \sim 30$ MeV were made. From the error of this correction, the E_{TH} error is calculated. It is larger at high energy because the beam energy was successively calibrated from J/ψ energy upward [70].

6.9 Summary and Conclusion

The performance of the BELLE calorimeter prototype based on 6×6 matrix counters was studied with tagged Compton photon and Bremsstrahlung photon beam in the energy range from 20 MeV to 5.4 GeV. The energy resolution is 5.8 % at 20 MeV and 1.8 % at 5.4 GeV when the energy deposit in 5×5 counters are summed up. We found the resolution improves significantly when 0.5 MeV threshold is applied. The result with threshold is 5×5 counters is 4 % at 20 MeV. The measured Compton spectrum and the resolution of CsI are in excellent agreement with the GEANT Monte Carlo.

The energy deposit in 5×5 matrix with 0.5 MeV threshold is -3 ± 2 % of the injected photon energy for 20 MeV $\sim$ 5.4 GeV. The energy dependence of the energy deposit (linearity) is well reproduced by GEANT above 300 MeV. Below 100 MeV the data shows $\sim$ 2 % lower energy deposit than GEANT expects. The observed non-linearity can be corrected by the response function and by the use of GEANT simulation in BELLE experiment.

The electronics noises are 16.5 keV and 189 keV for the coherent and incoherent noise. The performance of the electronics designed for BELLE was thoroughly tested by the photon beam and was proven to be excellent.

Chapter 7

Expected Performance

7.1 Simulation of γ and π^0 Detection

7.1.1 BELLE Simulation

The performance of the calorimeter is influenced strongly by the materials in front of the calorimeter. For example, if a γ is converted to an e^+e^- pair by the CDC or ACC wall materials, the γ can not be measured properly by the calorimeter. Fig. 7.1 shows the first interaction point of 100 MeV γ's generated uniformly in 4π and went through the GEANT simulation of the BELLE detector. The electron and positron produced by the interaction will be deflected by the magnetic field and many of them will be lost in the reconstruction. The detection efficiency become lower and the resolution becomes worse. It is important to check the performance of the calorimeter as a part of the whole BELLE detector. Since the whole detector is inside the magnetic field and each component has a complicated shape the simulation is the only possible method of checking.

The BELLE full simulation package is used for this study. This includes the $B^0\bar{B}^0$ and B^+B^- event generator and the GEANT simulator to track the decay and the interaction of produced particles in the detector. The $B^0\bar{B}^0$ and B^+B^- are produced from the $\Upsilon(4S)$ and each B meson decays with the known branching fraction. After the decay, the particles are boosted to the laboratory system and passed to the GEANT simulator. All inner detectors except the endcap ACC are installed in the used version. All the energy deposits of the CsI(Tℓ) crystals are smeared with the electronics noise. The energy deposits in the crystal are combined into an electromagnetic shower using a clustering program developed for the BELLE data analysis, and the energy of the

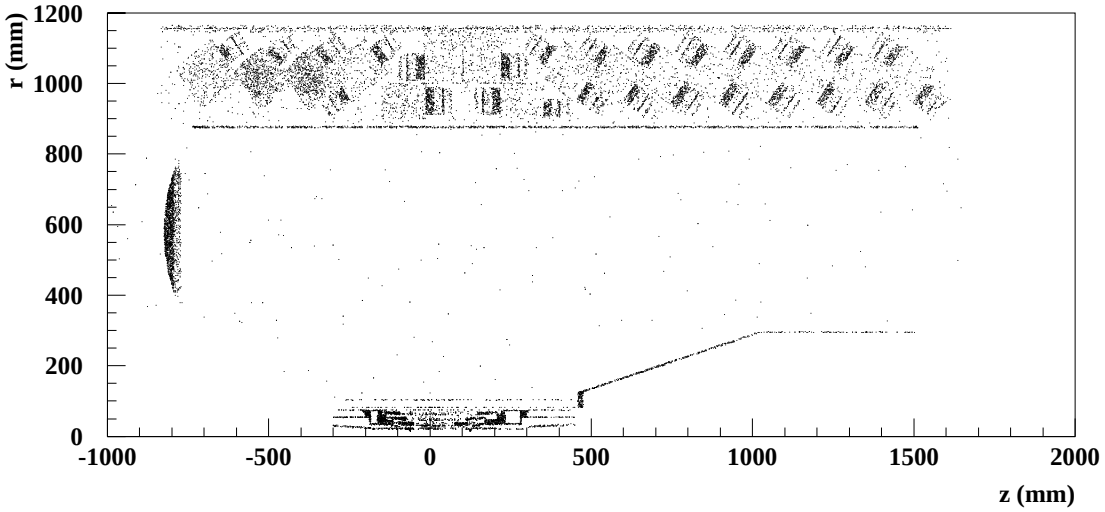

Figure 7.1: First interaction points of 100 MeV γ's generated uniformity in the detector.

shower is determined. The π^0 is reconstructed from any combination of 2 clusters by calculating an invariant mass. The number of generated events are 25k with inner detectors (detector ON) and 30k without inner detectors (detector OFF).

In the following sections, the performance of γ and π^0 detection is discussed from the reconstruction results.

7.1.2 γ Detection

A cluster is formed first by finding a seed counter. The energy of the seed counter should be more than a certain threshold value and 5 MeV for this analysis. When a seed counter is found, the energy of 5 $\times$ 5 counters around the seed are summed up and a cluster is formed. The threshold for each counter is 0.5 MeV. If there are two seed counters in the 5 $\times$ 5 matrix, two clusters are reconstructed so far as there is at least one counter between two seeds and its energy is lower than any of the seeds. Such a case happens for two γ's from a high momentum π^0 or by accidental overlap of two γ's. After the cluster is formed, the energy deposit is corrected for the shower leakage effect. The cluster position by the center of gravity is corrected by the correction curve.

We selected good γ clusters by applying following 3 cuts;

1. opening angle between generated γ and the reconstructed cluster $\leq 2.5°$.
2. $E_9/E_{25} \geq 0.9$.
3. $\hat{R_\gamma} - 3\sigma^L_{R_\gamma} \leq R_\gamma \leq \hat{R_\gamma} + 3\sigma^H_{R_\gamma}$

The each parameter will be explained later.

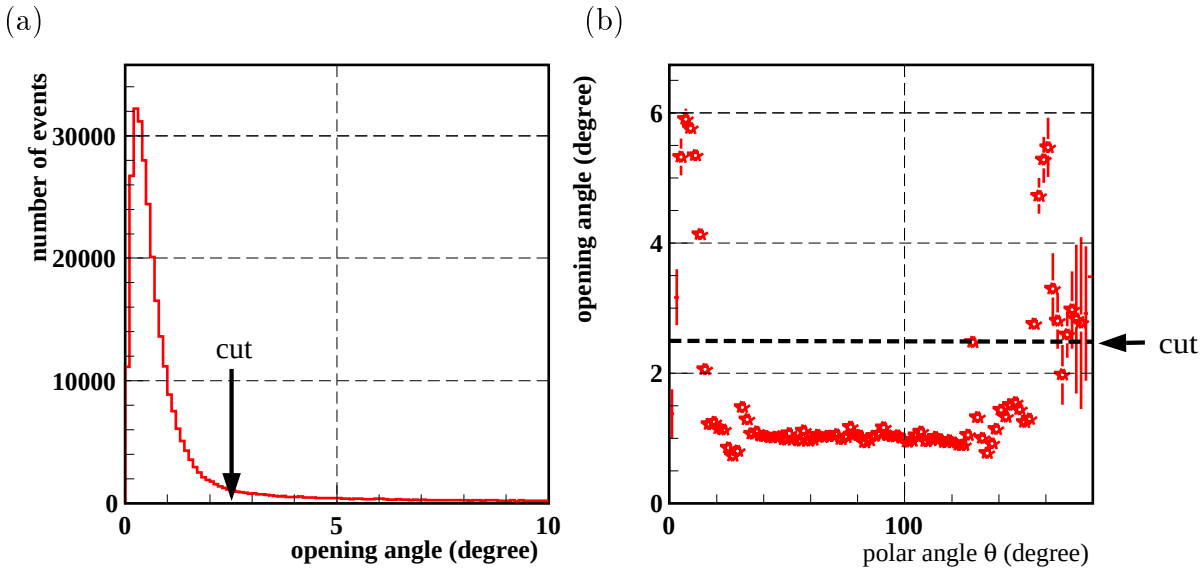

Figure 7.2: (a)Opening angle between CsI cluster and the generated γ and (b) Polar angle dependence of the average opening angle.

The 1st cut was applied to find a matching between the generated γ and the reconstructed cluster. For each generated γ, we calculated the opening angle with any of the clusters and selected the nearest one. If the opening angle is less than 2.5°, the matching is taken. The distribution of the opening angle is shown in Fig. 7.2.

The second cut is applied to check whether the shape of the cluster is consistent with the γ-ray. The γ makes an electromagnetic shower and most of the energy is deposited near the center of the cluster. On the other hand, the shower generated by hadrons tends spread over many clusters. When a γ is converted into an e^+e^- pair before entering the calorimeter, it also tends to produce a 'fat' shower due to the magnetic deflection of e^+e^-. We used the energy deposit of 3 $\times$ 3 counters (E_9) and 5 $\times$ 5 counters (E_{25}) around the seed to implement this cut. The clusters are rejected if the ratio E_9/E_{25} is less than 0.9. The distribution is shown in Fig. 7.3(a).

For these events after E_9/E_{25} cut, we plotted $R_\gamma \equiv E_\gamma^{REC}/E_\gamma^{GEN}$ where E_γ^{REC} is the energy reconstructed by the cluster program and E_γ^{GEN} is the generated γ energy. The distribution is then fitted by the logarithmic Gaussian and the peak $\hat{R}_\gamma$ and its width $\sigma_{R_\gamma}^L$ for the low energy side and $\sigma_{R_\gamma}^H$ for the high energy side are determined. We selected the events within $\pm$ 3 σ as good reconstructed γ's as shown in Fig. 7.3(b).

The results are shown in Fig. 7.4 and Table 7.1 for both cases of inner detector ON and OFF. The efficiency given here is calculated for all the γ's generated in the $B\bar{B}$ decay including the ones which is generated along the beam line and not covered

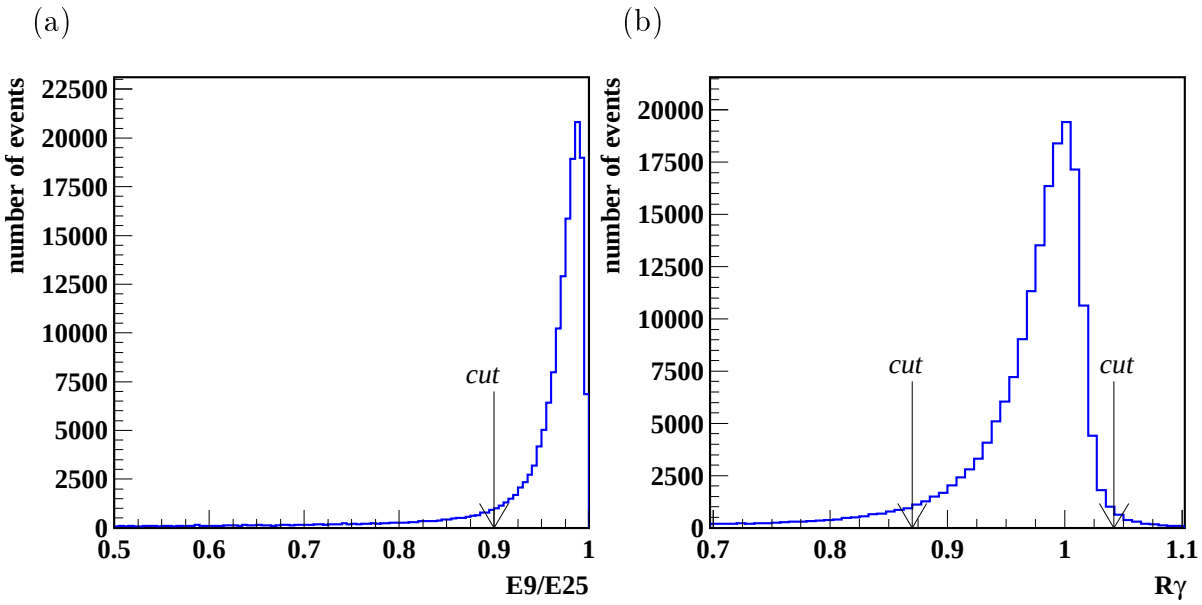

Figure 7.3: (a)E_9/E_{25} distribution after 'cut 1' (opening angle $\leq 2.5°$), and (b)R_γ distribution after 'cut 2' ($E_9/E_{25} \geq 0.9$).

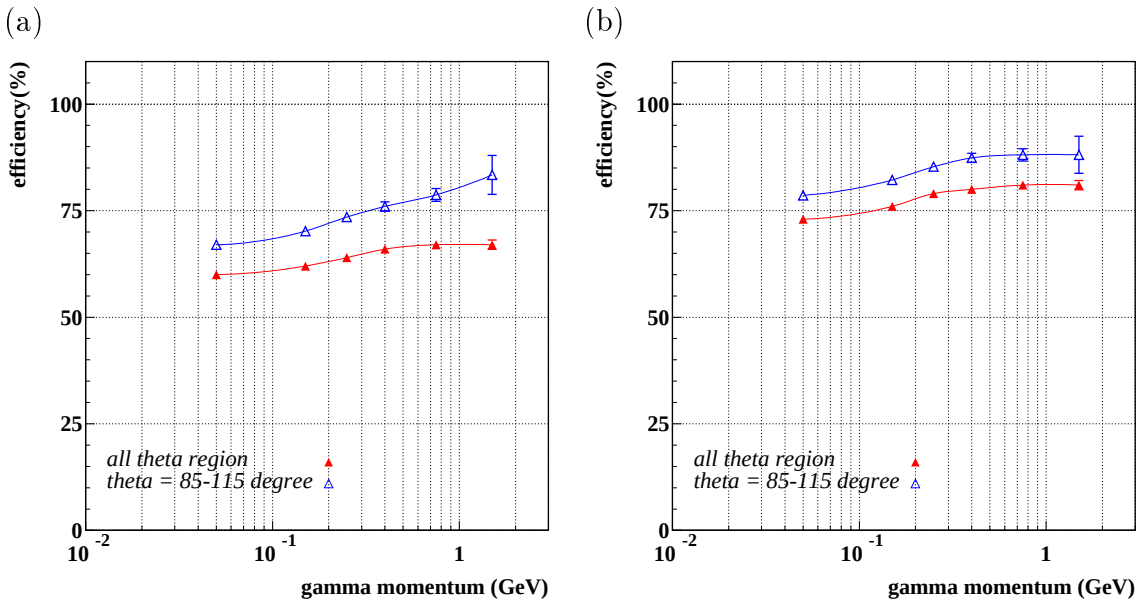

Figure 7.4: Momentum dependence of γ detection efficiency for (a)inner detector ON and (b)OFF after applying all selection cuts.

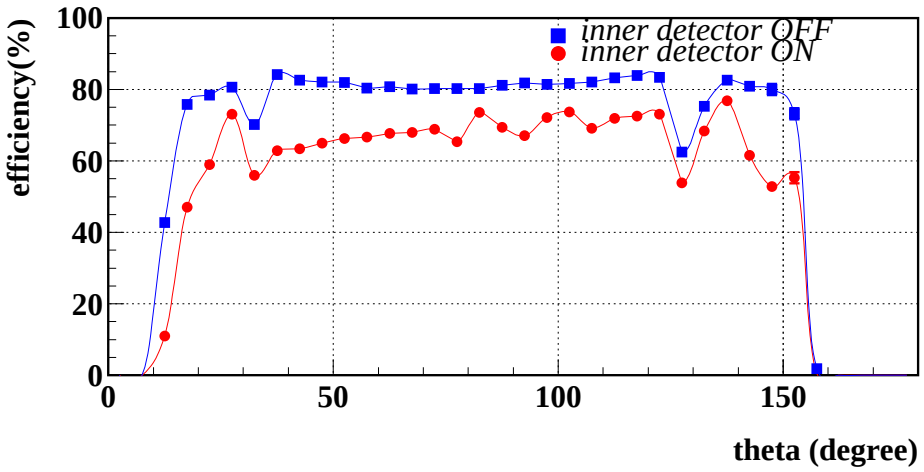

Figure 7.5: Polar angle (θ) dependence of γ detection efficiency.

by the CsI(Tℓ) calorimeter. The γ detection efficiency of BELLE is 60 $\sim$ 65 %, and it depends on the angle and energy of γ's. In the middle of barrel (85° $\sim$ 115°), the efficiency becomes higher than 80 %. Both of them are the results of the detector ON case. The loss of efficiency by the material in front of the calorimeter is about 10 %.

	Inner detector OFF (%)	Inner detector ON (%)
cut 1	93	83
cut 2	85	74
cut 3	76	63

Table 7.1: Cut dependence of the γ detection efficiency for $B\bar{B}$ events. Detector geometrical acceptance is included in the efficiency.

The theta dependence in Fig. 7.5 shows the low efficiency at the gap between barrel and endcap. But the efficiency still stays at more than 50 %.

7.1.3 π^0 Mass Resolution

We selected the clusters originating from the γ by applying the opening angle and E_9/E_{25} cuts described in the previous section. When we analyze the real data, the opening angle cut will be replaced by the CDC track - CsI cluster matching cut. This cut will select only 'neutral' clusters which have no matched charged tracks nearby. For the time being, we proceed for the analysis of π^0 using the γ clusters selected by the opening angle and E_9/E_{25} cuts.

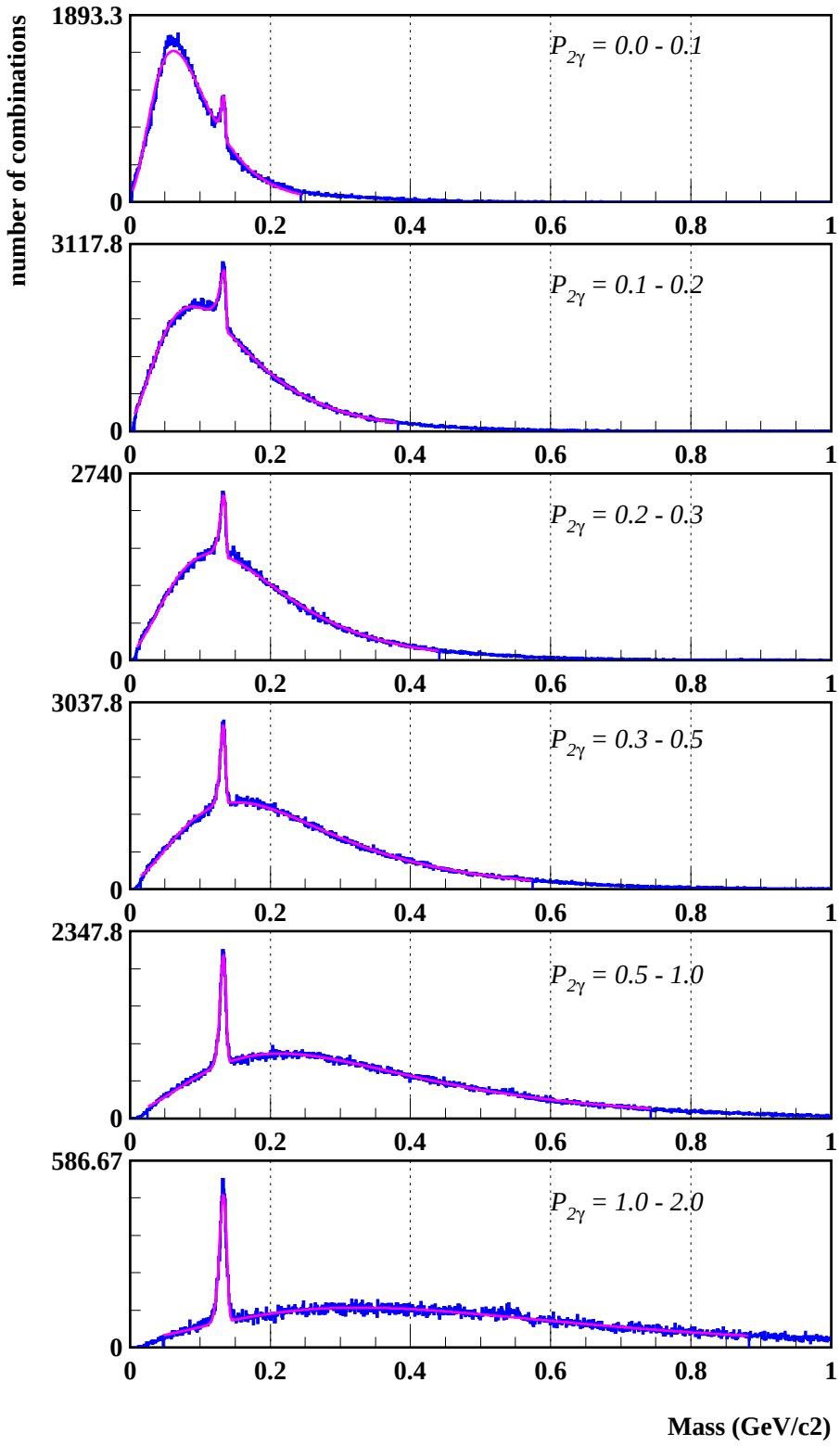

Figure 7.6: Invariant mass $M_{\gamma\gamma}$ distribution of any combination of 2 γ clusters for each momentum region ($0 - 0.1$, $0.1 - 0.2$, $0.2 - 0.3$, $0.3 - 0.5$, $0.5 - 1.0$, $1.0 - 2.0$ GeV), for $B\bar{B}$ generic events. The number of generated events is 25,000.

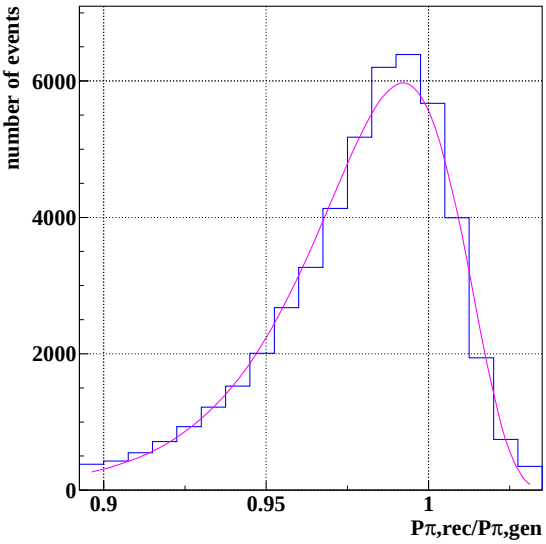

Figure 7.7: π^0 momentum distribution (reconstructed momentum/generated momentum) for all momentum regions with logarithmic Gaussian fit.

We calculated the invariant mass $M_{\gamma\gamma}$ and its associated momentum $P_{\gamma\gamma}$ for any combination of 2 γ clusters in one event. The distribution of $M_{\gamma\gamma}$ is plotted in Fig. 7.6 for each region of $P_{\gamma\gamma}$. The π^0 mass peak around 135 MeV [51] is clearly observed for all momentum regions. The distribution is fitted by Gaussian + logarithmic Gaussian. The normal Gaussian corresponds to the π^0 mass peak and the logarithmic Gaussian explains the combinatorial background. Table. 7.2 summarizes the position of π^0 mass peak M_{π^0} and the mass resolution $\sigma_{M_{\pi^0}}$ for each momentum region. The mass resolution becomes worse at energies above 1 GeV due to the angular resolution of the cluster, but the π^0 peak is distinguishable in all momentum ranges.

7.1.4 Selection of π^0

The π^0 signal is then selected by applying a cut on the invariant mass and its reconstructed momentum with respect to the generated momentum.

- $M_{\pi^0} - 3\sigma_{M_{\pi^0}} \leq M_{\gamma\gamma} \leq M_{\pi^0} + 3\sigma_{M_{\pi^0}}$
- $\hat{R}_{\pi^0} - 3\sigma^L_{R_{\pi^0}} \leq R_{\pi^0} \leq \hat{R}_{\pi^0} + 3\sigma^H_{R_{\pi^0}}$

where $R_{\pi^0} \equiv P^{REC}_{\pi^0}/P^{GEN}_{\pi^0}$, $P^{REC}_{\pi^0}$ and $P^{GEN}_{\pi^0}$ are reconstructed and generated π^0 momentum,respectively. The second cut on R_{π^0} is to check whether the generated momentum is properly restored by the reconstruction program. For events passing

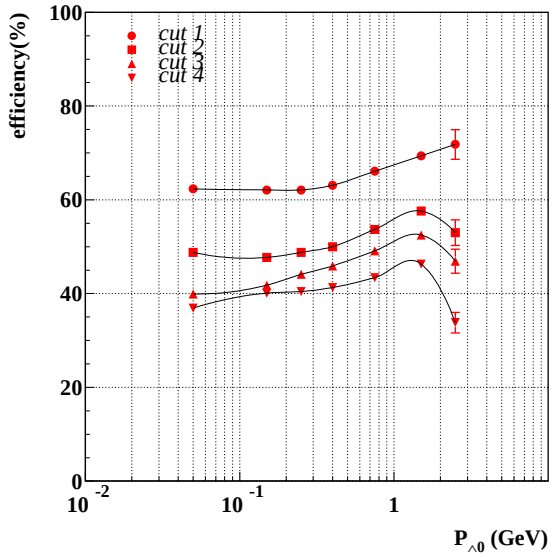

Figure 7.8: Momentum dependence of π^0 detection efficiency after each cut. (cut1 : opening angle between generated γ and the reconstructed cluster $\leq 2.5°$ for 2 γ's, cut2 : $E_9/E_{25} \geq 0.9$. for 2 γ's, cut3 : $M_{\pi^0} - 3\sigma_{M_{\pi^0}} \leq M_{\gamma\gamma} \leq M_{\pi^0} + 3\sigma_{M_{\pi^0}}$, cut4 : $\hat{R}_{\pi^0} - 3\sigma^L_{R_{\pi^0}} \leq R_{\pi^0} \leq \hat{R}_{\pi^0} + 3\sigma^H_{R_{\pi^0}}$.)

the $M_{\gamma\gamma}$ cut, we looked into the MC generator information and selected the genuine π^0 events. The distribution of R_{π^0} for such good π^0's is shown in Fig. 7.7. The distribution is fitted by the logarithmic Gaussian and the momentum resolution is determined.

The values of R_{π^0} and the resolution are summarized in Table. 7.2 for both cases of inner detector ON and OFF. The average resolution of the π^0 momentum reconstruction is 2.3 % and it varies from 3.6 % below 100 MeV to 1.9 % above 1 GeV.

7.1.5 π^0 Detection Efficiency

The π^0 particle is identified if a particular combination of two gamma clusters satisfied all the cuts. The number of such events for each momentum region is counted and is divided by the total number of π^0's generated at all the angles in the same momentum region. This gives the π^0 detection efficiency. The results is given in Fig. 7.8 where the reduction after each cut is demonstrated as a function of the momentum and summarized in Table. 7.2. The detection efficiency improves towards higher momentum. But it starts decreasing above 1 GeV because the angle between two γ's becomes too close at high momentum. If the separation of two γ's becomes less than 1 counter size, the detection of π^0 is difficult. In this case, we need the special treatments to separate

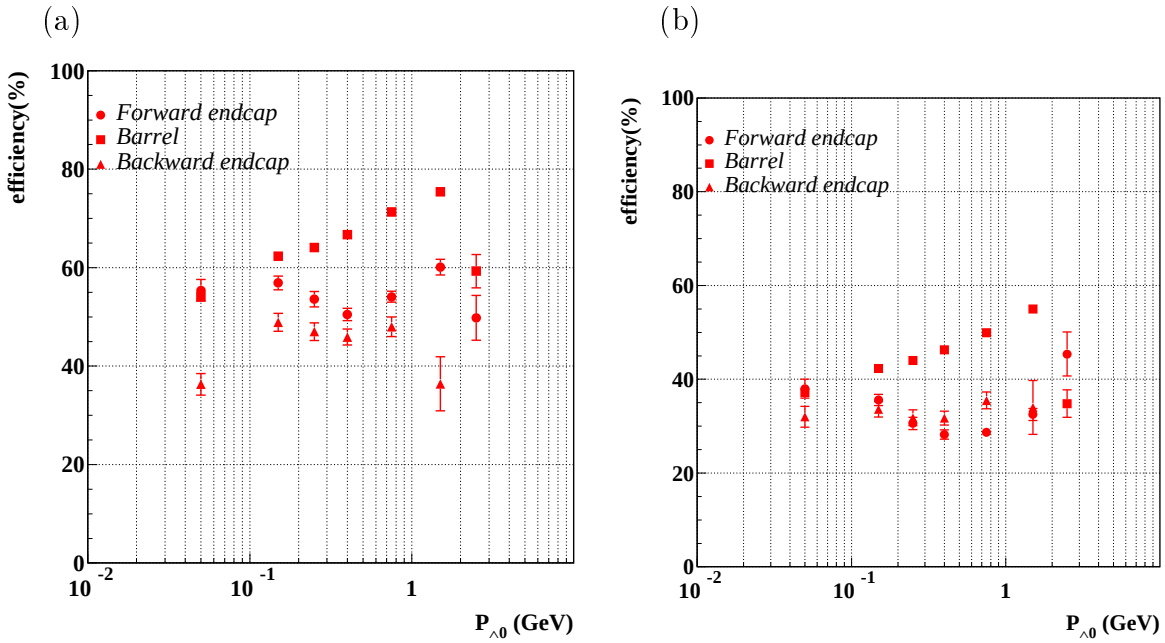

Figure 7.9: Momentum dependence of π^0 detection efficiency for (a)inner detector OFF and (b)ON. The efficiency is shown for Barrel and Forward, Backward endcap calorimeter separately.

them into two γ's.

The π^0 detection efficiency depends on the θ region. Fig. 7.9 shows the efficiency for the barrel and the endcap calorimeter separately.

7.1.6 S/N Ratio

As shown in Fig. 7.6, the reconstructed π^0's include many fake candidates from the combinatorial background. The signal to noise ratio (S/N) is estimated by the following procedure.

For all the combinations of 2 gamma clusters passing the 3 cuts, we looked into the generator information and distinguished the genuine pair of γ's coming from the π^0 (= S) and the fake pairs coming from the combinatorial background (= N). The S/N ratio for each momentum region is listed in Table. 7.2. The S/N ratio becomes better at high momentum and for the case of inner detector OFF as expected.

7.1.7 Summary

Table. 7.2 lists the summary of the π^0 detection performance. The BELLE electromagnetic calorimeter has 65 % efficiency for the γ of a energy 200 MeV and 40 % efficiency for the $\pi^0$of momentum of 100 MeV. These efficiencies are estimated for γ's and π^0's in the $B^0\bar{B}^0$ and B^+B^- decays. These efficiencies might be improved in some amounts by updating the current clustering programs. Those efforts are in progress now.

(a)

π^0 momentum P_{π^0} (GeV)	π^0 mass M_{π^0} (MeV)	π^0 mass resolution $\sigma_{M_{\pi^0}}$ (MeV)	R_{π^0}	momentum resolution $\sigma_{R_{\pi^0}}/R_{\pi^0}(\%)$	S/N	detection efficiency $\eta(\%)$
all	133.1	4.0	0.99	2.3	0.44	41.6 ± 0.2
0.0-0.1	133.5	2.9	0.99	3.6	0.22	36.9 ± 0.6
0.1-0.2	133.9	4.7	0.99	2.8	0.21	40.1 ± 0.4
0.2-0.3	133.6	4.1	0.99	2.4	0.41	40.4 ± 0.5
0.3-0.5	133.0	3.8	0.99	2.2	0.93	41.3 ± 0.4
0.5-1.0	133.1	4.1	0.99	2.0	2.16	43.4 ± 0.4
1.0-2.0	133.2	5.1	0.99	1.9	2.63	46.3 ± 0.7

(b)

π^0 momentum P_{π^0} (GeV)	π^0 mass M_{π^0} (MeV)	π^0 mass resolution $\sigma_{M_{\pi^0}}$ (MeV)	R_{π^0}	momentum resolution $\sigma_{R_{\pi^0}}/R_{\pi^0}(\%)$	S/N	detection efficiency $\eta(\%)$
all	133.2	4.0	0.99	2.3	0.54	53.9 ± 0.7
0.0-0.1	133.4	3.3	0.99	3.3	0.34	59.9 ± 0.5
0.1-0.2	133.7	3.7	0.99	2.5	0.32	60.2 ± 0.5
0.2-0.3	133.3	3.9	0.99	2.3	0.58	61.3 ± 0.4
0.3-0.5	133.1	3.8	0.99	2.2	1.24	64.3 ± 0.4
0.5-1.0	133.3	4.2	0.99	2.0	2.88	67.2 ± 0.7
1.0-2.0	133.1	5.1	0.99	1.9	3.95	60.0 ± 2.6

Table 7.2: π^0 detection performance of BELLE CsI(Tℓ) calorimeter for (a) Inner detector ON and (b) OFF.

Chapter 8

Conclusion

Our purpose in the B-factory is to know the mechanism of the CP violation by using B meson decays. We constructed the BELLE detector for that purpose. The electromagnetic calorimeter is the important part of BELLE to detect electrons and photons.

In order to build a calorimeter with good performance, we chose the CsI(Tℓ) crystal and 8736 counters are produced in total. We got all the counters stable and uniform in performance. The size of the crystals are manufactured within +0.2 −0.5 mm of the design values. The light output and the uniformity of all the counters were measured by cosmic ray muons. The average light output is 4969 electron-hole pairs/MeV and the average non-uniformity is 9 %. The light output was stable within ± 1 % over 6 months.

We carried out a beam test by using the photon beam at the Budker Institute of Nuclear Physics (BINP), Russia in autumn, 1997 to confirm the performance of our electromagnetic calorimeter and to establish the analysis and calibration methods of the calorimeter data. The beam test was successfully completed.

The electronics noise which is most effective for the energy resolution is kept minimum during the beam test. As a result, we obtained the energy resolution as follows;

$$\frac{\sigma}{E} = \frac{0.066(\%)}{E} \oplus \frac{0.81(\%)}{E^{1/4}} \oplus 1.34(\%), \quad E \text{ in GeV}. \tag{8.1}$$

It is 4 % at 20 MeV and 1.5 % at 5.4 GeV. To our knowledge, this result is better than any other similar detectors constructed, or being constructed all over the world. Most of the results have good agreement with Monte Carlo simulations and it means that we proved the GEANT simulation well reproduces the electromagnetic shower in the CsI(Tℓ). A properly tuned GEANT simulation will be a useful tool to understand the BELLE experimental data.

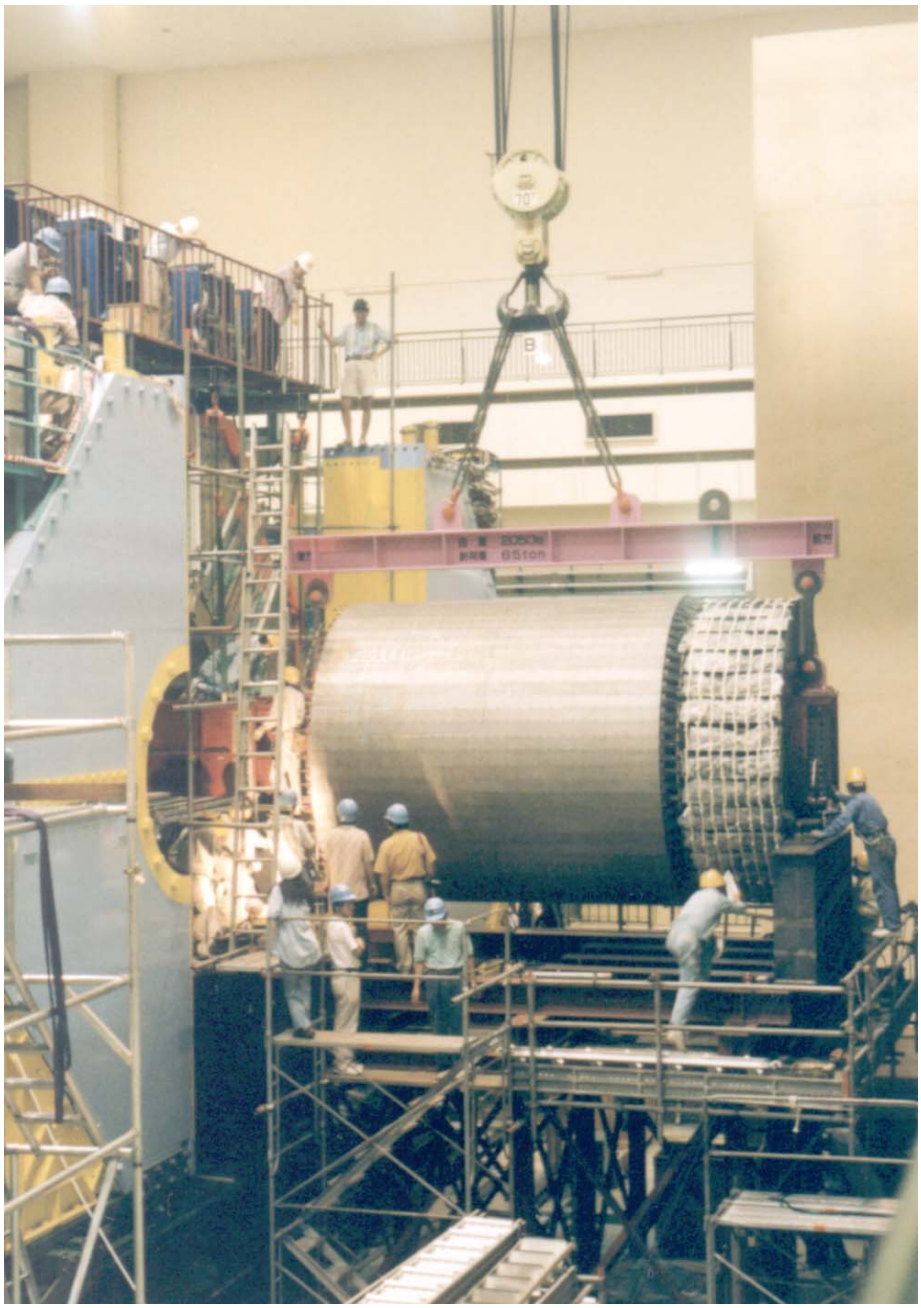

Figure 8.1: Installation of the BELLE calorimeter.

The energy linearity of the calorimeter is -3 ± 2 % for energies from 20 MeV to 5.4 GeV with the central value of $-$ 3 % which is due to the average shower leakage. The GEANT simulation did not reproduce the linearity at the lower energies than 100 MeV. The difference is almost 2 % and it looks there is still some effect that is not included in GEANT at the low energy. It is emphasized that this is the first measurement of the linearity for such a wide energy range by the photon beam. We observed that it is not necessary to correct the electronics non-linearity because our electronics has an excellent linear response. Non-uniformity of light output affects the linearity but it is only within $\pm$ 1 %.

In analyzing the beam test data, we established a clustering method. We used the sum of 5×5 counters with 0.5 MeV threshold to obtain the cluster energy with good resolution and linearity described above. It helps us to detect the electron, γ, and also π^0 with good efficiency. We estimated the average detection efficiency of 63 % for γ and 41.6 % for π^0 for γ's and π^0's from $B\bar{B}$ decays by the GEANT simulation.

We installed the barrel calorimeter into BELLE and started the system test by using the cosmic ray in October 1998. The signal from all counters are checked. It was confirmed that all counters and electronics work correctly except two out of 6624 counters which have no response from one of the two preamplifiers. Fig. 8.2 is an example of the cosmic ray triggered event and recorded by the barrel calorimeter. A clear energy deposit caused by a cosmic ray is seen and there are no strange hits in other counters. We measured the noise level of all the counters. The average noise is 217.0 ± 33.09 keV as shown in Fig. 8.4[71]. We confirmed the whole system is healthy now and will work well in the BELLE experiment which will start from April 1999.

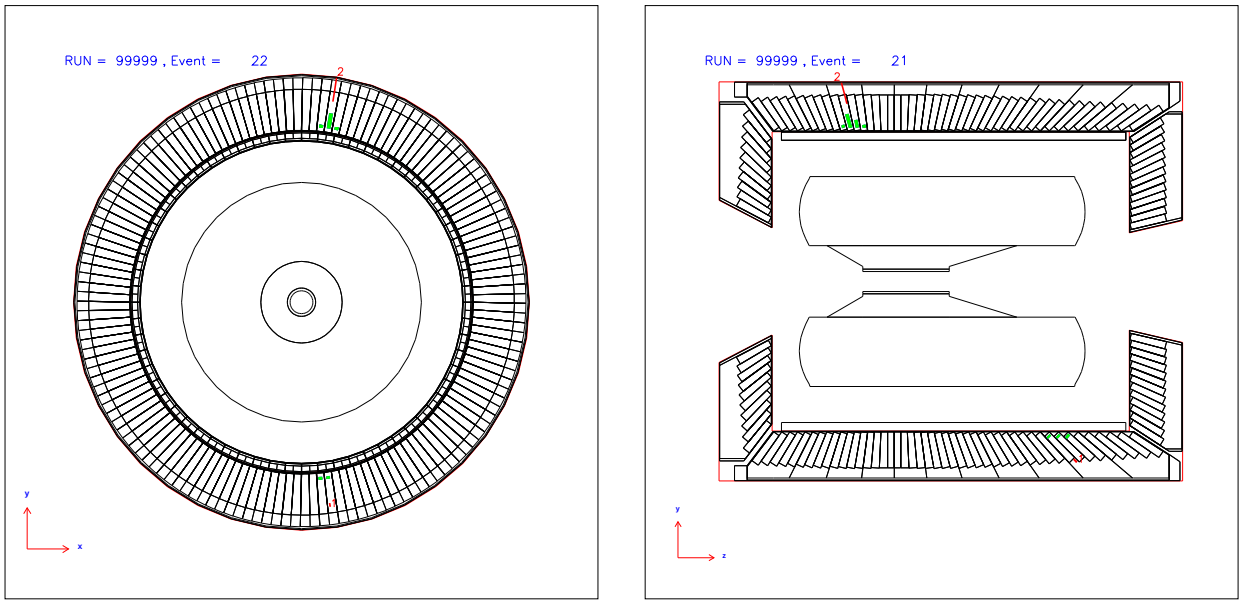

Figure 8.2: The first cosmic ray event seen after installation of the CsI(Tℓ) calorimeter into the BELLE detector (Oct. 1998)

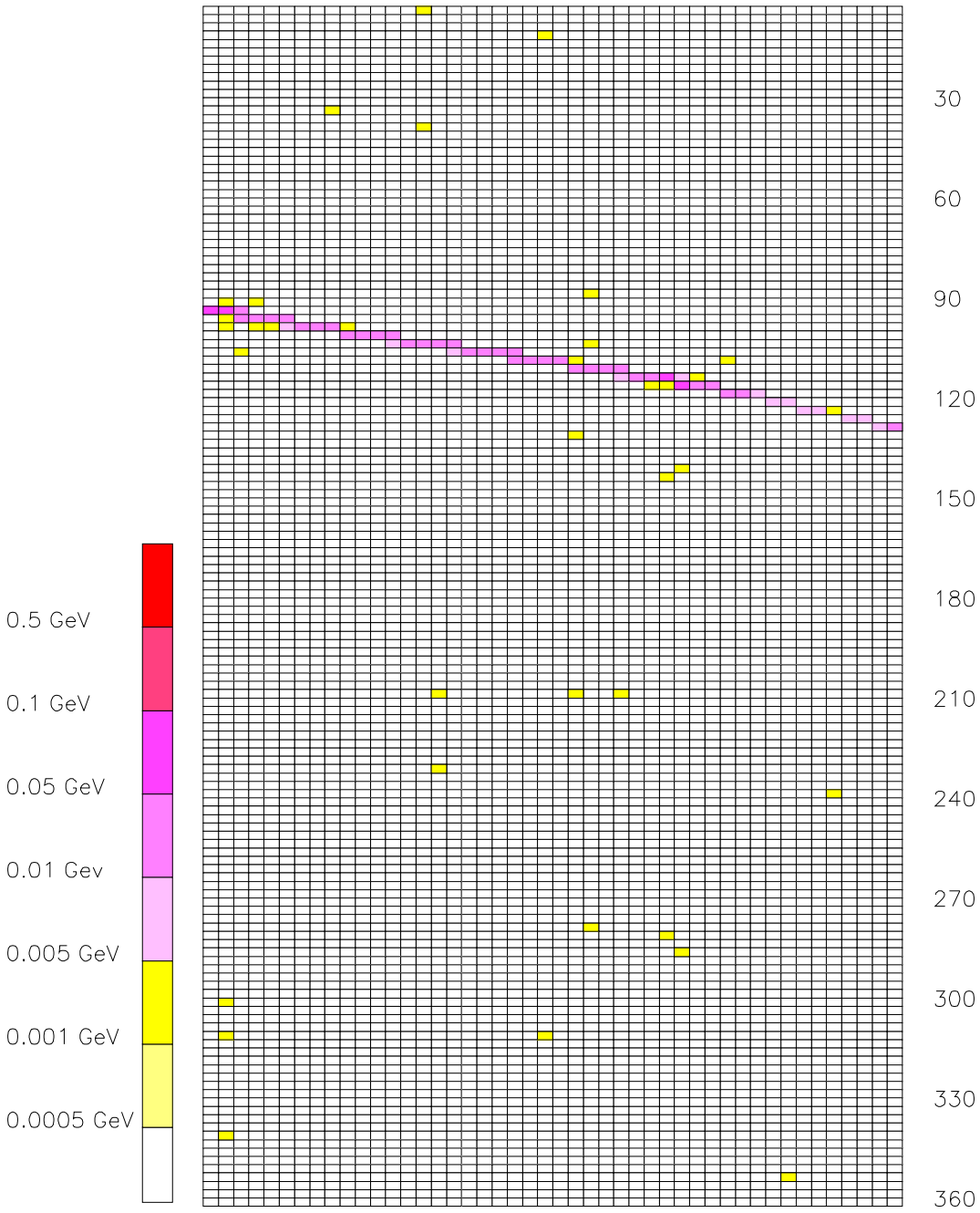

Figure 8.3: The first cosmic ray event seen after installation of the CsI(Tℓ) calorimeter into the BELLE detector (Oct. 1998)

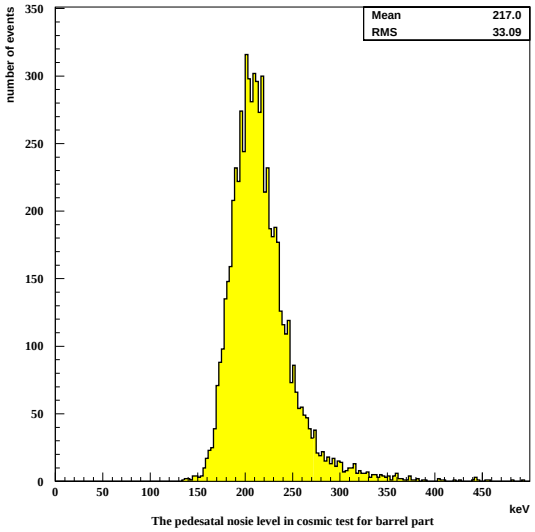

Figure 8.4: Distribution of the noise level for all the barrel counters after installation.

Appendix A

Chronicles of CsI(Tℓ) Crystal Production for BELLE *

RU : Production effort in Russia and Ukraine.

Institute for Single Crystals (ISC) in Kharkov produced crystal ingots and made a mechanical processing. Raremetal Factory (RMF) in Novosibirsk supplied CsI powder. Ise Chemical in Japan supplied the Iodine. Hydrogen iodide (HI) was produced in Galogen in Ural mountains. Budker Institute for Nuclear Study (BINP) in Novosibirsk was in charge for the overall organization of above mentioned enterprises. (see Fig. A.1(a))

CH : Production effort in China.

The Crystal production R/D was performed by Shanghai Institute of Ceramics (SIC) and by Beijing Glass Research Institute (BGRI). The most of crystal production was done by SIC. Institute for High Energy Physics (IHEP) in Beijing participated in the initial stage of organization. Raw CsI and TlI materials were supplied by Chemetall (CM) in Germany. (see Fig. A.1(b))

*This record was prepared with the help of M.Fukushima and M.H.Lee who worked for the management and technical coordination of the crystal production for BELLE.

(a)

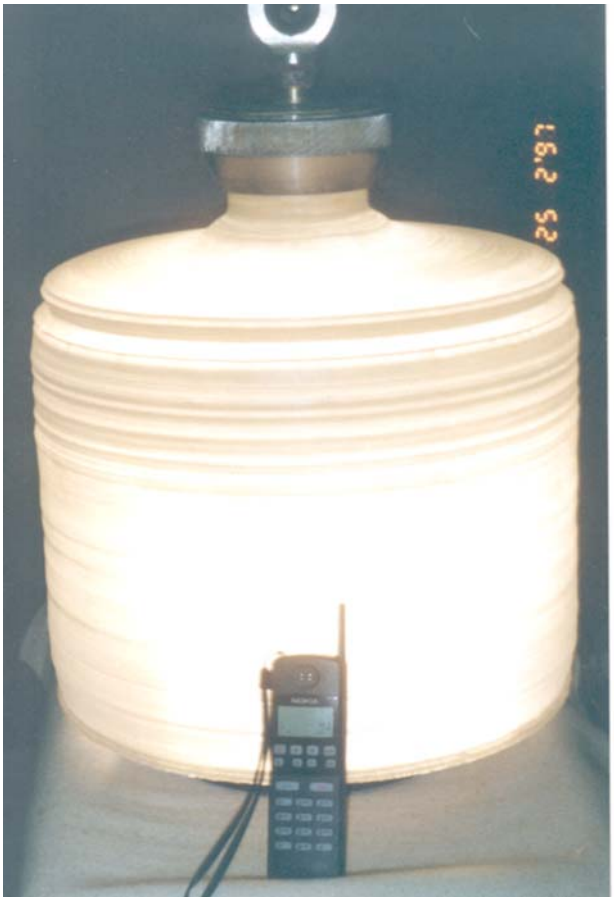

(b)

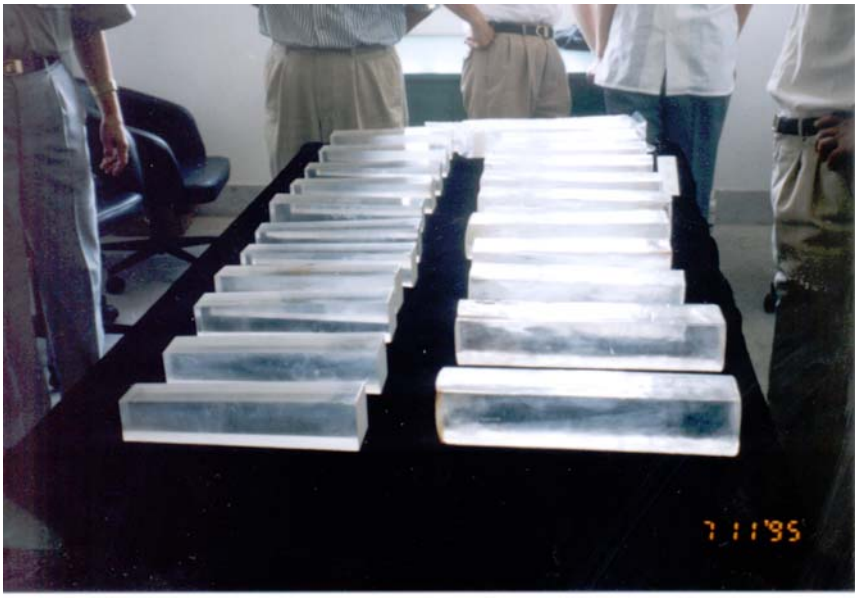

Figure A.1: Ingots of CsI(Tℓ) crystals produce by (a) Institute for Single Crystals in Ukraine and (b)Shanghai Institute of Ceramics. The Chinese crystals are grown by the Bridgman method. The Ukrainian crystals are produced by the Czochralski method. The growth speed of the crystal is $\sim$ 1 mm/hour in either method.

FR : Production effort in France.

Crystals were grown by Quartz et Silice (QS) company in France. Later the company changed the name to Crismatec/Bicron.

KE : Activity at KEK.

Most of commercial and logistic problems between KEK and producers in RU, CH and FR were handled by Toyota Tsusho Corporation (TTC) in Tokyo.

****

1992 Sep	FR	KEK made a purchase order of 120 pcs to QS.
1992 Nov	FR	First 10 pcs delivered from QS and tested at KEK. Some crystals had pink color, polycrystalline boundaries in the middle of the crystal, and wide pedestal values due to phosphorescence.
1992 May	FR	Nine crystals were replaced by QS due to boundaries and non-uniformity.
1992 May	CH	Visit to IHEP and crystal producers in Beijing. This is the first contact with Chinese crystal growers.
1992 Jul	RU	Visit to BINP and ISC. This is the first contact with Russian and Ukrainian crystal suppliers.
1992 Oct	RU	First 10 test pcs delivered from BINP. All had yellowish colors and the light output (LO) was 40% of specification. This was improved for the subsequent production.
1993 Aug	FR	Delivery of 120 pcs by QS completed.
1993 Dec	RU	Production baseline for barrel crystals agreed between BINP, ISC and KEK.

1994 May	CH	R/D in China for CsI(Tℓ) production started at SIC and BGRI.
1994 Aug	CH	First large CsI(Tℓ) sample from SIC. Bubbles, brown coloration and opaqueness observed. LO was half of specification.
1994 Oct	RU	First mass produced 120 pcs from BINP delivered to KEK. LO and uniformity specification mostly satisfied. Mechanical tolerance was problematic. Lots of mechanical damages were caused on the crystal during the transport from BINP to KEK.
1995 Feb	CH	Transparency of SIC crystals improved but still LO is 80% of specification.
1995 Apr	CH	Three pcs with good uniformity delivered from SIC. LO is 93% of specification.
1995 Aug	RU	Severe damages were caused on the crystal surface by water condensation for 100 pcs from BINP during the transport between BINP-KEK.
1995 Nov	RU	First beam test at BINP. Data taking was repeated in March, 1996.
1995 Sep	CH	Twenty pcs delivered from SIC. Good uniformity but LO is 86% of specification. Severe radiation damage observed by ^{60}Co irradiation for SIC crystals. Decrease of LO by 19% after 10 rad irradiation.
1995 Oct	CH	Small test crystals grown with scavenger were reported significantly radiation harder by Igarashi (KEK) and Zhong (IHEP).
1995 Nov	CH	Growth of large CsI(Tℓ) crystals with scavenger decided by SIC.
1996 Jan	FR	First 55 pcs for the other of 900 barrel crystals delivered by QS. Specifications satisfied.

1996 Jan	CH	Discussion on radiation hardness at SIC. CsI powder quality, baking temperature dependence, use of vacuum furnace (at BGRI) etc. were discussed.
1996 Feb	CH	Five pcs from SIC with scavenger were found to satisfy radiation hardness specification. Contamination of dirt by scavenger was noticeable for these crystals but it gradually improved for later production.
1996 Jul	CH	Lumping of CsI powder from CM caused severe loss in crystal production yield at SIC. Inefficient baking of lumped material was suspected.
1996 Sep	RU	CsI(Na) problem for BINP crystals was disclosed. Certain fraction of BINP crystals from BINP was known to show double photopeaks for 662 keV gamma rays from ^{137}Cs. The problem was traced that a part of CsI crystal block has only small amount of Sodium impurity and no Thallium activator doped. All crystals delivered to KEK from BINP (2700 pcs) were checked and about 200 pcs were found bad.
1996 Oct	CH	Mass production started at SIC.
1997 Feb	CH	Twenty pcs out of 239 pcs delivered from SIC returned for replacement. These are mostly by bad uniformity and cracks.
1997 Mar	FR	Delivery of 900 pcs from QS completed.
1997 Mar	RU	Total 216 pcs were shipped back to BINP for replacement. They were mostly CsI(Na) contaminated crystals.
1997 Aug	RU	Second beam test at BINP until November 1997. During the beam test, the silicone rubber glue joint was found unstable against temperature change.
1997 Dec	KE	Regluing of 6000 barrel crystals by epoxy glue took until February 1998.
1998 Feb	KE	Installation of barrel crystals into the support structure continued until May 1998.

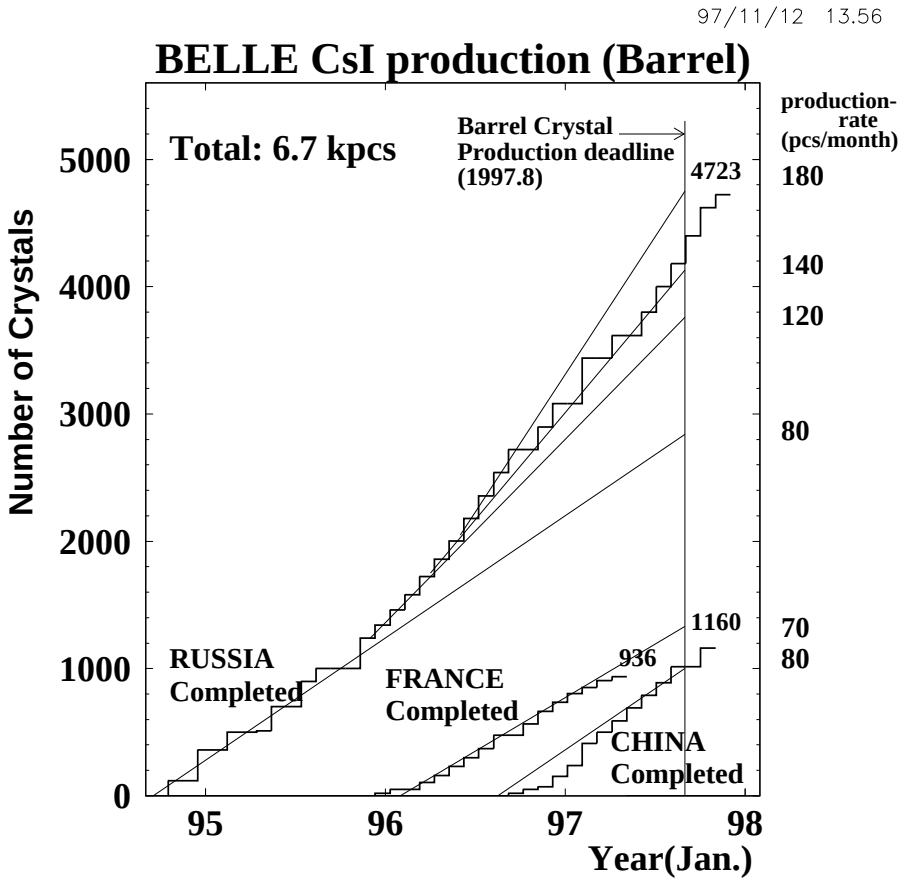

Figure A.2: Crystal delivery for BARREL.

1998 Feb	CH	"Pink" crystals and low LO caused by the change of material processing method at CM. Only 30% yield was achieved by these materials.
1998 May	KE	Break down of completed barrel calorimeter support structure.
1998 Jul	CH	The last crystals from SIC were delivered to KEK.
1998 Aug	KE	Delivery of new barrel support structure. Reinstallation of barrel counters was done in less than 50 days.
1998 Sep	RU	The last crystals from BINP were delivered to KEK.
1998 Sep	KE	Installation of barrel calorimeter to BELLE.

Appendix B

CsI(Tℓ) Crystal Size

Crystal No.	No.1	No.2	No.3	No.4	No.5	No.6	No.7	No.8
A(mm)	66.962	66.953	66.916	66.853	66.768	66.659	66.528	66.376
B(mm)	66.962	67.018	67.109	67.176	67.216	67.232	67.221	67.188
H(mm)	54.500	67.690	67.652	67.589	67.502	67.391	67.258	67.104
a(mm)	53.870	53.870	53.871	53.871	53.872	53.872	53.873	53.873
b(mm)	53.870	53.923	54.027	54.131	54.234	54.336	54.435	54.533
h(mm)	54.500	54.513	54.513	54.513	54.513	54.513	54.512	54.512
α(deg)	0.0000	0.0275	0.0821	0.1366	0.1905	0.2436	0.2957	0.3467
β(deg)	1.2500	1.2503	1.2490	1.2455	1.2395	1.2313	1.2208	1.2083
β'(deg)	1.2500	1.2491	1.2455	1.2395	1.2313	1.2209	1.2083	1.1938
γ(deg)	0.0000	1.2581	1.2545	1.2485	1.2402	1.2296	1.2170	1.2023
Volume(cc)	987.8	1112.2	1112.4	1112.2	1111.5	1110.4	1108.8	1106.8
Weight(kg)	4.455	5.016	5.017	5.016	5.013	5.008	5.001	4.992

Table B.1: Barrel crystal size 1.

Crystal No.	No.9	No.10	No.11	No.12	No.13	No.14	No.15	No.16
A(mm)	66.204	66.015	65.808	65.588	65.354	65.108	64.854	64.590
B(mm)	67.131	67.051	66.951	66.830	66.692	66.538	66.368	66.186
H(mm)	66.931	66.739	66.531	66.308	66.071	65.823	65.565	65.299
a(mm)	53.873	53.874	53.874	53.875	53.875	53.875	53.876	53.876
b(mm)	54.628	54.720	54.810	54.896	54.979	55.060	55.135	55.209
h(mm)	54.512	54.511	54.511	54.511	54.510	54.510	54.509	54.509
α(deg)	0.3963	0.4448	0.4917	0.5369	0.5801	0.6221	0.6618	0.7002
β(deg)	1.1938	1.1774	1.1592	1.1395	1.1184	1.0959	1.0725	1.0481
β'(deg)	1.1774	1.1592	1.1395	1.1184	1.0960	1.0725	1.0482	1.0230
γ(deg)	1.1858	1.1675	1.1477	1.1264	1.1039	1.0802	1.0557	1.0303
Volume(cc)	1104.4	1101.7	1098.6	1095.3	1091.6	1087.8	1083.7	1079.4
Weight(kg)	4.981	4.969	4.955	4.940	4.923	4.906	4.887	4.868

Table B.2: Barrel crystal size 2.

Crystal No.	No.17	No.18	No.19	No.20	No.21	No.22	No.23	No.24
A(mm)	64.320	64.044	63.765	63.483	63.200	62.918	62.635	62.355
B(mm)	65.991	65.787	65.574	65.354	65.127	64.896	64.662	64.426
H(mm)	65.026	64.748	64.466	64.181	63.896	63.610	63.325	63.042
a(mm)	53.877	53.877	53.877	53.877	53.877	53.878	53.878	53.878
b(mm)	55.278	55.344	55.406	55.466	55.521	55.573	55.623	55.669
h(mm)	54.509	54.508	54.508	54.507	54.507	54.506	54.506	54.506
α(deg)	0.7539	0.7713	0.8037	0.8348	0.8639	0.8910	0.9170	0.9409
β(deg)	1.0166	0.9971	0.9709	0.9441	0.9172	0.8902	0.8631	0.8362
β'(deg)	0.9971	0.9708	0.9441	0.9172	0.8902	0.8632	0.8362	0.8094
γ(deg)	1.0042	0.9778	0.9508	0.9237	0.8965	0.8693	0.8421	0.8151
Volume(cc)	1075.0	1070.5	1065.9	1061.2	1056.5	1051.8	1047.1	1042.4
Weight(kg)	4.848	4.828	4.807	4.786	4.765	4.744	4.722	4.701

Table B.3: Barrel crystal size 3.

Crystal No.	No.25	No.26	No.27	No.28	No.29
A(mm)	62.077	61.803	61.533	61.267	61.006
B(mm)	64.189	63.951	63.715	63.480	63.247
H(mm)	62.762	62.485	62.212	61.944	61.682
a(mm)	53.878	53.879	53.879	53.879	53.879
b(mm)	55.713	55.752	55.790	55.826	55.859
h(mm)	54.505	54.505	54.505	54.504	54.504
α(deg)	0.9638	0.9849	1.0047	1.0234	1.0406
β(deg)	0.8093	0.7829	0.7567	0.7309	0.7055
β'(deg)	0.7829	0.7566	0.7309	0.7055	0.6805
γ(deg)	0.7884	0.7620	0.7359	0.7104	0.6854
Volume(cc)	1037.7	1033.1	1028.5	1024.1	1019.7
Weight(kg)	4.680	4.659	4.639	4.619	4.599

Table B.4: Barrel crystal size 4.

Crystal No.	No.1	No.2	No.3	No.4	No.5	No.6	No.7	No.8
A(mm)	56.514	56.764	53.464	53.638	53.714	53.714	53.464	75.880
B(mm)	58.740	58.990	55.728	55.978	55.978	55.978	55.728	79.456
C(mm)	60.333	60.333	62.483	62.492	60.456	62.483	60.465	61.072
D(mm)	60.333	60.333	60.465	62.492	62.483	60.456	62.483	63.321
a(mm)	49.656	49.906	46.884	47.068	47.135	47.135	46.884	66.458
b(mm)	51.614	51.864	48.870	49.120	49.120	49.120	48.870	69.592
c(mm)	53.048	53.048	54.836	54.845	53.057	54.836	53.066	53.501
d(mm)	53.048	53.048	53.066	54.845	54.836	53.057	54.836	55.471
H_{aA}(mm)	3.707	3.707	3.882	4.010	3.883	3.882	3.883	4.061
H_{dD}(mm)	3.497	3.497	3.360	3.359	3.359	3.360	3.359	4.825
dg13(mm)	73.328	73.501	71.465	72.938	72.931	71.626	72.766	86.497
dg24(mm)	73.328	73.501	72.766	72.938	71.626	72.931	71.465	87.771
dg57(mm)	83.425	83.598	81.458	83.113	83.106	81.619	82.942	98.750
dg68(mm)	83.425	83.598	82.942	83.113	81.619	83.106	81.458	100.205
α_1(deg)	91.057	91.057	93.235	91.072	88.910	93.234	88.910	91.633
α_2(deg)	88.943	88.943	88.928	88.928	88.928	88.928	88.928	86.745
α_3(deg)	88.943	88.943	88.928	88.928	88.928	88.928	88.928	89.988
α_4(deg)	91.057	91.057	88.910	91.072	93.234	88.910	93.235	91.633
Volume(cc)	923	927	894	914	898	897	894	1308
Weight(kg)	4.16	4.18	4.03	4.12	4.05	4.05	4.03	5.90

Table B.5: Forward endcap crystal size 1.

Crystal No.	No.9	No.10	No.11	No.12	No.13	No.14	No.15	No.16
A(mm)	76.130	76.130	75.880	71.360	71.610	66.926	67.176	62.366
B(mm)	79.707	79.707	79.456	74.866	75.116	70.486	70.736	66.143
C(mm)	63.328	61.072	63.321	60.667	60.667	60.769	60.769	63.663
D(mm)	61.072	63.328	61.072	60.667	60.667	60.769	60.769	63.663
a(mm)	66.708	66.708	66.458	62.378	62.628	58.397	58.648	54.322
b(mm)	69.842	69.842	69.592	65.444	65.694	61.504	61.754	57.614
c(mm)	55.478	53.501	55.471	53.046	53.046	53.047	53.047	55.483
d(mm)	53.501	55.478	53.501	53.046	53.046	53.047	53.047	55.483
H_{aA}(mm)	4.061	4.061	4.061	3.942	3.942	3.988	3.988	4.211
H_{dD}(mm)	4.825	4.825	4.825	4.603	4.603	4.380	4.379	4.145
dg13(mm)	87.970	86.693	87.771	83.043	83.236	80.035	80.223	78.792
dg24(mm)	86.693	87.970	86.497	83.043	83.236	80.035	80.223	78.792
dg57(mm)	100.404	98.947	100.205	94.989	95.182	91.707	91.895	90.433
dg68(mm)	98.947	100.404	98.750	94.989	95.182	91.707	91.895	90.432
α_1(deg)	91.633	91.633	91.633	91.656	91.656	91.679	91.678	91.700
α_2(deg)	89.988	86.746	89.988	88.344	88.344	88.321	88.322	88.300
α_3(deg)	86.746	89.988	86.745	88.344	88.344	88.322	88.322	88.300
α_4(deg)	91.633	91.633	91.633	91.656	91.656	91.678	91.678	91.700
Volume(cc)	1312	1313	1307	1190	1195	1107	1112	1075
Weight(kg)	5.92	5.92	5.89	5.37	5.39	4.99	5.02	4.85

Table B.6: Forward endcap crystal size 2.

Crystal No.	No.17	No.18	No.19	No.20	No.21	No.22	No.23	No.24
A(mm)	62.616	57.981	58.232	53.661	53.710	53.913	53.913	53.661
B(mm)	66.394	61.642	61.892	57.369	57.620	57.620	57.620	57.369
C(mm)	63.663	60.968	60.968	64.366	64.382	61.073	64.366	61.089
D(mm)	63.663	60.969	60.968	61.089	64.382	64.366	61.073	64.366
a(mm)	54.572	50.413	50.664	46.579	46.654	46.830	46.830	46.579
b(mm)	57.864	53.598	53.848	49.800	50.050	50.050	50.050	49.800
c(mm)	55.483	53.046	53.046	55.920	55.935	53.059	55.920	53.074
d(mm)	55.483	53.046	53.046	53.074	55.935	55.920	53.059	55.920
H_{aA}(mm)	4.211	4.077	4.077	4.326	4.549	4.324	4.325	4.324
H_{dD}(mm)	4.145	3.905	3.905	3.664	3.664	3.664	3.664	3.664
dg13(mm)	78.969	74.269	74.445	71.669	73.917	73.906	71.827	73.743
dg24(mm)	78.969	74.269	74.445	73.743	73.917	71.827	73.906	71.669
dg57(mm)	90.611	85.388	85.564	82.525	85.087	85.075	82.682	84.911
dg68(mm)	90.611	85.389	85.564	84.911	85.087	82.682	85.075	82.525
α_1(deg)	91.700	91.721	91.720	95.240	91.740	88.239	95.239	88.239
α_2(deg)	88.300	88.279	88.280	88.261	88.260	88.261	88.261	88.261
α_3(deg)	88.300	88.280	88.280	88.261	88.260	88.261	88.261	88.261
α_4(deg)	91.700	91.720	91.720	88.239	91.740	95.239	88.239	95.240
Volume(cc)	1080	957	961	917	949	923	921	919
Weight(kg)	4.87	4.32	4.34	4.14	4.28	4.16	4.15	4.14

Table B.7: Forward endcap crystal size 3.

Crystal No.	No.25	No.26	No.27	No.28	No.29	No.30	No.31	No.32
A(mm)	74.160	74.410	74.410	74.160	67.747	67.998	61.335	61.586
B(mm)	79.958	80.209	80.209	79.958	73.437	73.688	67.153	67.404
C(mm)	60.263	63.940	60.263	63.928	61.230	61.230	64.221	61.316
D(mm)	63.928	60.263	63.940	60.263	61.230	61.230	61.328	64.221
a(mm)	64.320	64.570	64.570	64.320	58.667	58.918	53.040	53.290
b(mm)	69.349	69.600	69.600	69.349	63.596	63.846	58.073	58.324
c(mm)	52.279	55.470	52.279	55.459	53.044	53.044	55.568	53.055
d(mm)	55.459	52.279	55.470	52.279	53.044	53.044	53.067	55.568
H_{aA}(mm)	4.466	4.466	4.466	4.466	4.308	4.308	4.521	4.521
H_{dD}(mm)	5.120	5.120	5.120	5.120	4.735	4.735	4.350	4.351
dg13(mm)	84.732	87.039	84.929	86.838	80.899	81.089	76.810	78.649
dg24(mm)	86.838	84.929	87.039	84.732	80.900	81.089	78.471	76.983
dg57(mm)	97.686	100.314	97.883	100.113	93.404	93.594	88.795	90.894
dg68(mm)	100.113	97.883	100.314	97.686	93.404	93.594	90.716	88.969
α_1(deg)	92.636	92.637	92.637	92.637	92.664	92.662	95.386	89.987
α_2(deg)	84.739	89.988	84.739	89.988	87.336	87.338	87.314	87.313
α_3(deg)	89.988	84.739	89.988	84.739	87.338	87.338	87.313	87.312
α_4(deg)	92.637	92.637	92.637	92.636	92.662	92.662	89.988	95.388
Volume(cc)	1281	1283	1286	1278	1140	1145	1050	1057
Weight(kg)	5.78	5.79	5.80	5.76	5.14	5.16	4.74	4.77

Table B.8: Forward endcap crystal size 4.

Crystal No.	No.33	No.34	No.35	No.36	No.37	No.38	No.39
A(mm)	61.586	61.335	73.337	73.588	73.337	64.956	65.206
B(mm)	67.404	67.153	81.303	-	81.303	72.757	73.008
C(mm)	64.221	61.328	61.618	61.633	64.177	61.444	61.444
D(mm)	61.316	64.221	64.177	61.633	61.618	61.444	61.444
a(mm)	53.290	53.040	63.364	63.614	63.364	56.050	56.300
b(mm)	58.324	58.073	70.250	-	70.250	62.785	63.036
c(mm)	55.568	53.067	53.255	53.270	55.465	53.043	53.043
d(mm)	53.055	55.568	55.465	53.270	53.255	53.043	53.043
B_7=B_9(mm)	-	-	-	40.858	-	-	-
b_2=b_4(mm)	-	-	-	35.321	-	-	-
H_{aA}(mm)	4.521	4.521	4.679	4.679	4.679	4.492	4.492
H_{dD}(mm)	4.351	4.351	5.271	5.272	5.272	4.729	4.729
dg13(mm)	76.983	78.471	85.302	85.507	86.800	79.578	79.765
dg24(mm)	78.649	76.810	86.800	85.507	85.302	79.578	79.765
dg57(mm)	88.969	90.716	98.714	98.921	100.449	92.203	92.390
dg68(mm)	90.894	88.795	100.449	98.921	98.714	92.202	92.390
α_1(deg)	95.388	89.988	93.613	93.613	93.613	93.639	93.640
α_2(deg)	87.312	87.313	84.588	-	88.186	86.361	86.360
α_3(deg)	87.313	87.314	88.186	-	84.588	86.360	86.360
α_4(deg)	89.987	95.386	93.613	93.613	93.613	93.640	93.640
α_2'(deg)	-	-	-	91.785	-	-	-
α_3'(deg)	-	-	-	91.785	-	-	-
α_9(deg)	-	-	-	169.203	-	-	-
Volume(cc)	1054	1052	1293	1316	1290	1106	1111
Weight(kg)	4.76	4.75	5.83	5.94	5.82	4.99	5.01

Table B.9: Forward endcap crystal size 5.

Crystal No.	No.1	No.2	No.3	No.4	No.5	No.6	No.7	No.8
A(mm)	59.870	60.120	55.740	55.944	55.990	55.990	55.740	77.984
B(mm)	61.610	61.860	57.576	57.826	57.826	57.826	57.576	80.864
C(mm)	64.566	64.566	66.702	66.709	65.085	66.702	65.092	63.837
D(mm)	64.566	64.566	65.092	66.709	66.702	65.085	66.702	65.588
a(mm)	49.722	49.972	45.915	46.126	46.165	46.165	45.915	63.774
b(mm)	51.170	51.420	47.428	47.678	47.678	47.678	47.428	66.130
c(mm)	53.673	53.673	55.010	55.017	53.677	55.010	53.684	52.225
d(mm)	53.673	53.673	53.684	55.017	55.010	53.677	55.010	53.657
H_{aA}(mm)	5.515	5.515	5.913	6.057	5.913	5.913	5.913	6.124
H_{dD}(mm)	5.148	5.148	4.994	4.994	4.993	4.994	4.993	7.239
dg13(mm)	73.655	73.826	71.131	72.292	72.287	71.290	72.125	83.317
dg24(mm)	73.655	73.826	72.125	72.292	71.290	72.287	71.131	84.247
dg57(mm)	88.642	88.813	86.292	87.664	87.659	86.451	87.497	101.866
dg68(mm)	88.642	88.813	87.497	87.664	86.451	87.659	86.292	103.002
α_1(deg)	90.773	90.773	92.463	90.808	89.153	92.463	89.152	91.267
α_2(deg)	89.227	89.227	89.192	89.192	89.193	89.192	89.193	87.493
α_3(deg)	89.227	89.227	89.193	89.192	89.192	89.193	89.192	89.975
α_4(deg)	90.773	90.773	89.152	90.808	92.463	89.153	92.463	91.266
Volume(cc)	990	995	945	962	949	949	945	1305
Weight(kg)	4.47	4.49	4.26	4.34	4.28	4.28	4.26	5.88

Table B.10: Backward endcap crystal size 1.

Crystal No.	No.9	No.10	No.11	No.12	No.13	No.14	No.15	No.16
A(mm)	78.234	78.234	77.984	72.170	72.420	66.518	66.768	61.008
B(mm)	81.114	81.114	80.864	75.221	75.472	69.722	69.972	64.366
C(mm)	65.593	63.837	65.588	66.125	66.125	66.653	66.653	67.180
D(mm)	63.837	65.593	63.837	66.125	66.125	66.653	66.653	67.180
a(mm)	64.024	64.024	63.774	58.535	58.786	53.506	53.756	48.672
b(mm)	66.380	66.380	66.130	61.010	61.260	56.086	56.336	51.354
c(mm)	53.662	52.225	53.657	53.664	53.664	53.662	53.662	53.658
d(mm)	52.225	53.662	52.225	53.664	53.664	53.662	53.662	53.658
H_{aA}(mm)	6.124	6.124	6.124	6.389	6.389	6.654	6.654	6.917
H_{dD}(mm)	7.239	7.239	7.239	6.964	6.962	6.664	6.664	6.339
dg13(mm)	84.443	83.512	84.247	80.318	80.505	76.684	76.863	73.339
dg24(mm)	83.512	84.443	83.317	80.319	80.505	76.684	76.863	73.339
dg57(mm)	103.198	102.061	103.002	99.001	99.187	95.291	95.470	91.869
dg68(mm)	102.061	103.198	101.866	99.000	99.187	95.291	95.470	91.869
α_1(deg)	91.266	91.266	91.266	91.322	91.321	91.377	91.377	91.432
α_2(deg)	89.974	87.493	89.975	88.678	88.679	88.623	88.623	88.568
α_3(deg)	87.493	89.974	87.493	88.679	88.679	88.623	88.623	88.568
α_4(deg)	91.266	91.266	91.267	91.321	91.321	91.377	91.377	91.432
Volume(cc)	1309	1310	1304	1210	1215	1113	1118	1027
Weight(kg)	5.91	5.91	5.88	5.46	5.48	5.02	5.04	4.63

Table B.11: Backward endcap crystal size 2.

Crystal No.	No.17	No.18	No.19	No.20	No.21	No.22	No.23	No.24
A(mm)	61.258	55.625	55.720	55.875	55.875	55.625	75.884	76.134
B(mm)	64.616	59.136	59.386	59.386	59.386	59.136	81.310	81.561
C(mm)	67.180	70.668	70.681	67.714	70.668	67.727	64.965	68.201
D(mm)	67.180	67.727	70.681	70.668	67.714	70.668	68.191	64.965
a(mm)	48.922	44.018	44.144	44.268	44.268	44.018	59.650	59.900
b(mm)	51.604	46.800	47.050	47.050	47.050	46.800	63.916	64.167
c(mm)	53.658	56.009	56.022	53.668	56.009	53.681	51.094	53.642
d(mm)	53.658	53.681	56.022	56.009	53.668	56.009	53.631	51.094
H_{aA}(mm)	6.917	7.473	7.789	7.472	7.473	7.472	7.613	7.613
H_{dD}(mm)	6.339	5.988	5.987	5.988	5.988	5.987	8.417	8.417
dg13(mm)	73.510	70.297	72.218	72.208	70.448	72.051	80.088	82.001
dg24(mm)	73.510	72.051	72.218	70.448	72.208	70.297	81.805	80.281
dg57(mm)	92.040	88.748	91.130	91.120	88.900	90.963	101.862	104.241
dg68(mm)	92.040	90.963	91.130	88.900	91.120	88.748	104.044	102.055
α_1(deg)	91.432	94.516	91.486	88.455	94.516	88.455	92.307	92.307
α_2(deg)	88.568	88.514	88.514	88.514	88.514	88.514	85.420	89.966
α_3(deg)	88.568	88.514	88.514	88.514	88.514	88.514	89.966	85.419
α_4(deg)	91.432	88.455	91.486	94.516	88.455	94.516	92.307	92.308
Volume(cc)	1032	975	1005	980	979	977	1274	1277
Weight(kg)	4.65	4.40	4.53	4.42	4.42	4.40	5.74	5.76

Table B.12: Backward endcap crystal size 3.

Crystal No.	No.25	No.26	No.27	No.28	No.29	No.30
A(mm)	76.134	75.884	68.318	68.568	60.939	61.190
B(mm)	81.561	81.310	73.837	74.088	66.660	66.910
C(mm)	64.965	68.191	66.362	66.362	66.808	66.808
D(mm)	68.201	64.965	66.362	66.362	66.808	66.808
a(mm)	59.900	59.650	53.293	53.544	47.198	47.448
b(mm)	64.167	63.916	57.602	57.852	51.634	51.884
c(mm)	51.094	53.631	51.814	51.814	51.810	51.810
d(mm)	53.642	51.094	51.814	51.814	51.810	51.810
H_{aA}(mm)	7.613	7.613	7.593	7.593	7.801	7.801
H_{dD}(mm)	8.417	8.417	7.822	7.821	7.198	7.199
dg13(mm)	80.281	81.805	75.858	76.041	71.564	71.736
dg24(mm)	82.001	80.088	75.858	76.041	71.564	71.736
dg57(mm)	102.055	104.044	97.203	97.386	92.333	92.507
dg68(mm)	104.241	101.862	97.202	97.386	92.334	92.507
α_1(deg)	92.308	92.307	92.384	92.383	92.454	92.454
α_2(deg)	85.419	89.966	87.616	87.617	87.546	87.546
α_3(deg)	89.966	85.420	87.617	87.617	87.546	87.546
α_4(deg)	92.307	92.307	92.383	92.383	92.454	92.454
Volume(cc)	1279	1272	1128	1133	1012	1016
Weight(kg)	5.77	5.74	5.09	5.11	4.56	4.58

Table B.13: Backward endcap crystal size 4.

Appendix C

Compton Fitting Function

We used the convolution of logarithmic Gaussian and the CsI response function for the fitting of the energy distribution of the backscattered Compton photons as follow;

$$\begin{aligned} F(\varepsilon) \;=\; N\,\frac{1}{E_c^3}\,\frac{\sigma_E}{\eta}\,\sigma_0\,\{\,(\,\frac{E_c^2}{2}\;-\;E_c\,(\,\varepsilon\;-\;\frac{\sigma_E}{\eta}\,)\;+\;(\,\varepsilon\;-\;\frac{\sigma_E}{\eta}\,)^2\,)\,f_1(\varepsilon) \\ +\,(\,\exp(1.5\sigma_0^2)\,\frac{\sigma_E}{\eta}\,(\,-E_c\;+\;2\,(\,\varepsilon\;-\;\frac{\sigma_E}{\eta}\,)\,)\,f_2(\varepsilon) \\ +\,(\,\exp(4\sigma_0^2)\,(\,\frac{\sigma_E}{\eta}\,)^2\,)\,f_3(\varepsilon)\,\} \\ +N_B\,(\,1\;-\;\frac{\varepsilon-E_c}{E_c}\,) \end{aligned} \tag{C.1}$$

$$\sigma_0 = \frac{1}{\sqrt{ln4}} sinh^{-1}(\sqrt{ln4}\eta) \tag{C.2}$$

$$f_1(\varepsilon) = erf(\frac{ln(1-\frac{\varepsilon-E_c}{\sigma_0}\eta)-\sigma_0^2}{\sqrt{2}\sigma_0})\;+\;erf(\frac{ln((1-\frac{\varepsilon}{\sigma_0}\eta)-\sigma_0^2}{\sqrt{2}\sigma_0}) \tag{C.3}$$

$$f_2(\varepsilon) = erf(\frac{ln(1-\frac{\varepsilon-E_c}{\sigma_0}\eta)-2\sigma_0^2}{\sqrt{2}\sigma_0})\;+\;erf(\frac{ln((1-\frac{\varepsilon}{\sigma_0}\eta)-2\sigma_0^2}{\sqrt{2}\sigma_0}) \tag{C.4}$$

$$f_3(\varepsilon) = erf(\frac{ln(1-\frac{\varepsilon-E_c}{\sigma_0}\eta)-3\sigma_0^2}{\sqrt{2}\sigma_0})\;+\;erf(\frac{ln((1-\frac{\varepsilon}{\sigma_0}\eta)-3\sigma_0^2}{\sqrt{2}\sigma_0}) \tag{C.5}$$

$$erf(x) = \frac{2}{\sqrt{\pi}}\int_0^x exp(-t^2)dt \tag{C.6}$$

where normalization factor N, Compton edge energy E_c and background N_B are for CsI response. And resolution σ_E and asymmetry η come from the logarithmic Gaussian.

Acknowledgment

I want to thank everyone who helped me.

I express my gratitude to my supervisor of Prof. S. Noguchi, Prof. H. Hayashii and Prof. N. Fujiwara for their understanding and support for my work. They guided me since I was under graduate student, and help to keep my interest in physics. I could not have joined the BELLE experiment and enjoyed the work in this group without their encouragement.

Since I have worked mainly at KEK, I have been under the care of the KEK staffs. Heartfelt thanks go to Prof. M. Fukushima. He was my adviser at KEK for over 5 years. He taught me how to do experiments, and admonished my way of thinking and working. I cannot find words to thank him. I will never forget his advises even after parting.

Dr. M. H. Lee has been my good adviser since the first year of my work at KEK. His honest opinions were very helpful.

I thank all of the Calorimeter group members of KEK, NWU, TIT and many foreign institutes. I am grateful to Prof. K. Tamai, Dr. H. Sagawa, Dr. T. Tsukamoto, Dr. B. G. Cheon, and Dr. K. Kaneyuki for their useful comment, suggestion and instruction. I want to thank BINP collaborators; Prof. A. E. Bondar, Prof. B. A. Shwartz, Dr. A. S. Kuzmin, Dr. L. V. Romanov and Dr. V. N. Zhilich for their kind help and hospitality during our beam test at Novosibirsk. And I thank for the discussion about the analysis.

Finally, I give my thanks to all the students who shared the office in Tsukuba Hall, for their friendship, encouragement and stimulation. I especially thank Mr. S. Ichizawa and Mr. C. S. Park for their help on software tasks. If they were not here, I could not smoothly finish anything. And I don't forget Mr. A. Satpathy's friendship as well as his physicistship. I wish all of you success in future.

Bibliography

[1] S. Weinberg, Phys. Rev. Lett.**19**(1967) 1264.

[2] A. Salam, 'Elementary Particle Theory', ed. N. Svarthholm(Almqvist and Wiksell, 1968).

[3] S. L. Glashow, J. Illiopoulos and L. Maiani, Phys.Rev.**D2**(1970) 1285.

[4] Eur. Phys. J. **C3**(1998) 117.

[5] M. Kobayashi and T. Maskawa, Prog. Theor. Phys. **49**(1973) 652.

[6] A. Carter and I. Sanda, Phys. Rev. Lett. **64**(1980) 952.

[7] A. Carter and I. Sanda, Phys. Rev. **D23**(1981) 1567.

[8] I. Bigi and A. Sanda, Nucl. Phys. **B193**(1981) 851.

[9] Letter of intent, KEK Report 94-2(1994).

[10] B Study of CP Vioration in B Messon Decays Technical Design Report (1995) KEK Report 95-1.

[11] BaBar Collab., Technical design report for the BaBar detector (1995).

[12] BaBar Collab.,Letter of intent, SLAC-443(1994).

[13] HERA-B Proposal, DESY-PRC 94/02.

[14] T. D. Lee and C. N. Yang, Phys. Rev.**104** (1956) 254.

[15] C. S. Wu, E. Ambler, R. W. Hayward, D. D. Hoppes and R. P. Hudson, Phys. Rev. **105**(1957) 1413.

[16] M. Goldhaber, L. Grodzins and A. W. Sunyar, Phys. Rev. **109** (1958) 1015.

[17] J. H. Christenson et al., Phys. Rev. Lett. **13** (1964) 138.

[18] L. Wolfenstein, Phys. Rev. Lett. **51** (1983) 1945.

[19] I. I. Bigi and A. I. Sanda, Phys. Lett. **194** (1987) 307.

[20] N. Cabbibo, Phys. Rev. Lett. **10** (1963) 531.

[21] H. Leutwyler and M. Roos, Z. Phys. **C25** (1984) 91.

[22] M. Bourquin et al., Z. Phys. **C21** (1983) 27.

[23] A. Sirlin, Phys. Rev. **D35** (1987) 3423.

[24] H. Abramowicz et al., Z. Phys. **C15** (1982) 19.

[25] S. Stone 'PROSPECTS FOR B-PHYSICS IN THE NEXT DECADE' HEPSY 96-01.

[26] R. Fulton et al., Phys. Rev. Lett. **64** (1999) 16.

[27] H. Albrechet et al., Phys. Lett. **B234** (1990) 409.

[28] S. Stone 'Semileptonic B Decay' World Scientific, Sigapore (1994) 349.

[29] M. Gaillard and B. Lee Phys. Rev. **D10** (1974) 897.

[30] J. Hagelin, Phys. Rev. **D20** (1979) 2893.

[31] A. Ali and A. Aydin, Nucl. Phys. **B148** (1979) 165.

[32] T. Brown and S. Pakvasa, Phys. Rev. **D31** (1985) 1661.

[33] S. Pakvasa, Phys. Rev. **D28** (1985) 2915.

[34] I. Bigi and A. Sanda, Phys. Rev. **D29** (1984) 1393.

[35] G. Buchalla, A. J. Buras and M. K. Harlander, Nucl. Phys. **B337** (1990) 313.

[36] I. I. Bigi and A. I. Sanda, Nucl. Phys., **B281** (1987) 41.

[37] M. Yamauchi, BELLE note No.116 (1996).

[38] KEKB B-FACTORY DESIGN REPORT (1995) KEK Report 95-7.

[39] BELLE Progress Report 1996 April - 1997 March (1997).

[40] Technical Design Report of BELLE SVD (1998).

[41] W. S. Huang et al., BELLE note No.94 (1995).

[42] R. Akhmetshin, BELLE note No.239 (1998).

[43] E. Bloom and C. Peck, Ann. Rev. Nucl. and Part. Sci.**33**,(1983) 143.

[44] M. A. Akrawy et al., Nucl. Inst. and Meth. **A290** (1990) 76.

[45] H. Burkhardt et al., Nucl. Inst. and Meth. **A268** (1988) 116.

[46] W. Hoffman et al., Nucl. Inst. and Meth. **163** (1979) 77.

[47] M. A. Schneegans et al.,Nucl. Inst. and Meth. **193** (1982) 445.

[48] C. Fabjan and R. Wigmans, Rept. Prog. Phys. **52** (1989) 1519.

[49] J. V. Allaby et al., Nucl. Inst. and Meth. **A281** (1989) 291.

[50] IEEE Trans. Nuclear Science **35** (1988) 105.

[51] Review of Particle Physics (1998) 156.

[52] GRACE in electronics Catalog.

[53] K. Kazui et al., Nucl. Inst. and Meth. **A 394** (1997) 46.

[54] '1992 Progress Report on B Physics Task Force Activities' KEK report 93-1.

[55] S. Gunji et al., Nucl. Inst. and Meth. **A 295** (1990) 400

[56] K. Tamai 'Results of Photo-diode Inspection'.

[57] M. Tanaka et al., IEEE Trans. Nucl. Sci., **41** (1994) 1208; KEK-Preprint 93-156.

[58] K. Tamai 'Preamprifier Inspection' (1997).

[59] LeCroy MQT300 manual.

[60] LeCroy OPERATOR'S MANUAL 'MODEL 1877S 96 CHANNEL FASTBUS TDC.

[61] K. Kazui 'Bachelor Thesis' (1995).

[62] T. W. Hur et al., BELLE note No.107 (1995).

[63] O. C. Allkofer et al., Phys. Let. **36B** (1971) 425.

[64] Y. Takeuchi et al., Nucl. Inst. and Meth. **328** (1993) 526.

[65] Nucl. Inst. and Meth. **A410** (1988) 179.

[66] W. R. Leo 'Techniques for Nuclear and Particle Physics Experiments'.

[67] E. Blucher et al, Nucl. Inst. and Meth. **A249** (1986) 201.

[68] CLEO collaboration Nucl. Inst. and Meth. **A379** (1992) 66.

[69] E. Aker et al, Nucl. Inst. and Meth. **A321** (1992) 69.

[70] V. Zhilich private communication.

[71] H. K. Jang private communication.

List of Figures

List of Tables